On the Connection Between the Gamma-ray and (Sub-)mm Emission in Active Galactic Nuclei

BALENDERAN, SHANGKARI

On the Connection between the γ-ray and (Sub-)mm Emission in Active Galactic Nuclei

Shangkari Balenderan

Abstract

This research investigates the connection between the submillimetre (sub-mm), millimetre (mm) and γ-ray emission in a sample eight blazars (consisting of high- and intermediate-frequency peaked BL Lacertae Objects (HBLs and IBLs respectively) as well as Flat Spectrum Radio Quasars (FSRQs)) and one radio galaxy. Light curves using both short-term (~ 6 days to ~ 3 months) and long-term (5.5 - 12 years) observations at γ-ray and (sub-)mm wavebands are presented. Long-term light curves at (sub-)mm wavelengths show evidence that emission at these wavelengths is source class dependent. Similarities in emission patterns and flux variability were observed between FSRQs and IBLs. The correlation between emission at 1.35 mm and the 100 MeV to 100 GeV γ-ray wavebands was studied both qualitatively and statistically using the discrete correlation function (DCF) method. Results from the DCF analysis showed that while all sources exhibit different behavioural patterns at different epochs, some general trends can be drawn based on the source type. It was found that IBLs behaved more like FSRQs than HBLs, although IBLs are classified as BL Lacertae objects, with HBLs showing the weakest correlation and variability at both emission bands and FSRQs showing the strongest evidence for correlation and variability within this sample set. This provides further evidence for the hypothesis of the unified Active Galactic Nuclei model, in which these objects evolve from FSRQ type blazars into IBLs and then into HBLs. This is because IBLs exhibit behavioural patterns of both FSRQs and BL Lacertae objects. In addition to this, time delay analysis of 3C 454.3, BL Lacertae and 3C 273 in the correlation study yielded separation distances between the emission regions ranging between ~ 0.1 pc to ~ 19 pc in the rest frame of the observer. These are in agreement with other studies in the literature (e.g. (214; 42)). However, much greater separation distances were observed for 3C 279 and OJ 287 (> 70 pc). These findings suggest that the nature and geometry of blazar jets are highly complex and vary from epoch to epoch. It was concluded that extensive consis-

tent long-term multiwavelength studies of a larger sample of sources from all blazar subclasses would help further constrain the location of the wavelength-dependent emission regions in the jet.

On the Connection between the γ-ray and (Sub-)mm Emission in Active Galactic Nuclei

Shangkari Balenderan

A thesis submitted to Durham University
in accordance with the regulations for
admittance to the Degree of Doctor of Philosophy.

Department of Physics
Durham University
December 2016

A seeker of Truth looks beyond the apparent and contemplates the hidden.

Rumi

I dedicate this work to my loving parents and sister whose support and faith have allowed me to dream for the stars and to believe that those dreams will be fulfilled. I also dedicate this work to the Teachers of the world whose dedication and passion for knowledge, growth and expansion have inspired and continue to inspire every one of us. In this web of the human experience, we individually form a unique part of a whole, both contributing towards and as a result being affected its continuous expansion.

Contents

List of Figures

List of Tables

Declaration

The work described in this thesis was undertaken between 2011 and 2016 while the author was a research student under the supervision of Prof. P. M. Chadwick, Dr. T. J. L. McComb and Dr. A. M. Brown in the Department of Physics at Durham University. This work has not been submitted for any other degree at Durham University or any other university.

Acknowledgements

It is at the end of a journey that we often ponder over its beginnings, and with this comes a conscious and profound feeling of gratitude towards the people and events that have led to this path and consequently made it possible.

I would like to start by thanking my academic supervisors, Prof. Paula M. Chadwick and Dr. T. J. Lowry McComb who had first given me the opportunity to pursue one of my childhood dreams. I greatly treasure their guidance, support and tutelage through which this work was successfully completed. They have inspired a truly enriching experience both intellectually and emotionally. From them I have learnt the many facets of academic work and the exemplary qualities of a true academic. I would also like to extend my sincere gratitude to Dr. Anthony M. Brown who I have had the opportunity to work with and learn from in the last three years of my study. I am indebted to Dr. Brown for all the guidance, advice and encouragement he has offered me during the final years of this work.

I am also very grateful to my collogues in the Durham University γ-ray Group, Dr. M. Daniel, Dr John Osborne, Dr. S. Nolan, Dr. Lazar Staykov, Jon Harris, Nikki Peceur, Cameron Rulten, Angeliki Kalogirou, Tom Armstrong, Maialen Arrieta, Rosemary Coogen and Jamie Graham whose company, delightful conversation and thoughtful help have truly made a difference.

I would like to extend my gratitude to the people who took the time to help me with matters concerning the various instruments used in this work. I would especially like to thank Dr. Iain M. Coulson who had taken the time to schedule additional observation time with the SCUBA-2 to observe MRK 421 during an unscheduled outburst in April 2013. He had also provided me with ample help and assistance during my early stages of this project. I would also like to thank Dr. Mark Gurwell who had given me permission to use the SMA calibration datasets as part of my research.

Throughout my life, my parents and sister have been a great pillar of support and strength. I thank them, most sincerely for everything they have done and continue to do for me. They have made this pursuit not only possible but enjoyable and especially rewarding.

Finally and on a very happy note, this work could not have been possible without

the very many people I have come to meet and know during my stay in Durham. They have seen me through some of the more challenging times of my life and have given me reason to smile. I would like to especially thank Maha, Shwetha, Aalia, Matthieu, Amjed, Habiba and Vangelis who have made me laugh more times than I can count, taught me so many wonderful, priceless life-lessons and helped me realise that sometimes all one needs is the support of very good company.

Chapter 1

Active Galactic Nuclei and Extragalactic Jets

Active galactic nuclei (AGN) are the sources of some of the most energetic phenomena seen in the observable universe. These objects represent the compact central regions of galaxies which far outshine their host galaxies. AGN are thought to contain supermassive black holes (SMBH), ranging between 10^6 to 10^9 solar masses, which generate enough energy to collimate and sustain jet outflows transporting energy, momentum and angular momentum over vast distances (up to megaparsec (Mpc) scales) from the central region of the galaxy (156). These extragalactic relativistic jets form a crucial subject of multiwavelength studies, as part of an ongoing effort to understand the nature, composition, particle acceleration and energy generation mechanisms in AGN.

The first observation of a jet was recorded by Curtis in 1918 (21) within the elliptical galaxy Messier 87 (M 87). These observations show a straight ray appearing to emanate from the nucleus, connected by a thin line of matter. Continuous advancement in radio instrumentation techniques and interferometry, post World War II, allowed for instruments with better angular resolution and lower noise, resulting in the discovery of several radio sources exhibiting similar features, i.e. extended radio emission with a compact high-temperature nuclear component, jets, radio hot-spot complexes and lobes (156).

Studies of the multiwavelength emission of these radio sources has led to the understanding that synchrotron emission is the primary process responsible for emission from these continuum radio sources. This understanding came about when optical counterparts of these radio sources were identified, revealing the highly polarised nature of the optical emission (319; 285). Baade & Minkowski (285) detected the optical linear polarisation from the jet of M 87 and the diffuse component of the Crab Nebula (a supernova remnant in the Milky Way), presenting evidence that the linearly polarised nature of the

optical counterpart suggested that both these non-thermal broadband optical-to-radio components may arise from synchrotron processes, which Oort & Wolraven (331) had also used to explain the non-thermal emission from the Crab Nebula. Alfvén & Wolraven (256), had also suggested in 1950 that the radio emission of Cygnus A (now identified as a radio galaxy) resulted from cosmic ray electrons gyrating in the object's magnetic field, producing synchrotron emission. In addition, Shklovsky (316) went on to suggest in 1953 that the continuum emission in the radio and optical wavelengths from the Crab Nebula could only be the result of relativistic electrons moving in magnetic fields after suggesting that the radio and optical emission were part of the same synchrotron spectrum. This then led to further research into synchrotron models for the radio-to-optical emission observed from AGN. In 1956, Burbidge (18) investigated the parameters of this synchrotron process which produces the high luminosities ($L_{bol} \sim 10^{43} - 10^{58}$ erg s^{-1}) observed from the central nucleus and the jet of AGN. Burbidge found that in order to produce the observed synchrotron luminosities, a total energy of $10^{58} \sim 10^{60}$ ergs was required. However, these values were far greater than the total energy in the form of cosmic radiation and magnetic field in the galaxy alone (a mass-equivalent of 100 to 1000 solar masses) or the energy content in the radio lobes (18).

In the 1950s, when the synchrotron nature of the radio sources was discovered and modelled, these radio sources were thought to be stars with a jet component rather than extragalactic objects (315). The discovery of the cosmological redshift, z of 3C 273B ($z = 0.158$) of one of the two bright components of 3C 273, by Schmidt in 1963, suggested that this object was in fact extragalactic (315). This marked the beginning of studies into the radio bright components of the central nucleus and the relativistic jets of extragalactic radio sources. Waggett et al. (185) published the first example of a well-collimated stable jet spanning a distance of several kiloparsecs in the radio galaxy NGC 6251. It was later found that the radio jets occurred in radio-loud AGN of all sizes and powers, thanks to the 27-element Very Large Array (VLA) which began operation in the late 1970s (156). The VLA had the required sensitivity and angular resolution necessary to distinguish these jets from the bright unresolved emission from the AGN and separate jets from other extended radio sources (156). Bridle & Perley (296) and Bridle (15) then suggested the quantitative criteria (e.g. structural details including the collimation, freedom and confinement of the jet, velocity of the jet, difference in brightness between the core and

the lobes) which were then used to identify radio jets.

It is widely accepted that these relativistic jets as well as hot spots and lobes are powered by the prodigious amounts of energy arising from the central region of the active galaxy. The potential energy in the gravitational field of the SMBH and the rotation of the SMBH itself are thought to generate the energy necessary to continuously power these jets to megaparsec scales (156).

Multiwavelength observations of these sources are particularly useful, as they reveal the behaviour of the different components of the jet. In Chapter 2, the physical mechanisms which lead to the production of multiwavelength emission observed from these sources are discussed. In Chapter 3, the motivation behind investigating the γ-ray and (sub-)millimeter (henceforth referred to as the (sub-)mm regime as it comprises both the mm and sub-mm regimes) energy regimes are discussed. This thesis particularly concerns γ-ray and (sub-)mm observations of blazars over time periods from several days to ~ 12 years. Results from these studies are presented in Chapters 5, 6, 7 and 8.

1.1 Understanding Active Galactic Nuclei

Throughout the years, the observed phenomenological (e.g. bolometric luminosities, mass of the SMBH) and spectral (e.g. emission lines of the optical spectra) properties of AGN have been catalogued and used as parameters for classifying and understanding their nature and physics.

Today, under the current AGN paradigm, it is widely accepted that the central engine of an AGN comprises a SMBH-accretion disc system that powers the AGN system and the relativistic jet (1). Observations at optical and ultraviolet (UV) wavelengths of the nuclear activity are often obscured either by the torus or warped gas and dust well outside the accretion disc and broad line regions, when the source is viewed at particular angles (e.g. the central engine is obscured by the torus when viewed edge-on, see Figure 1.1).

The Current AGN Paradigm - The Standard AGN Model

It is generally accepted that while AGN are divided into separate classes, all AGN are essentially made up of the same components. These include a central engine which powers

the system by the accretion of surrounding matter from an accretion disc, a relativistic jet which transports energy from the central system out into the galactic and extragalactic environment, broad and narrow line regions of gas clouds surrounding the central engine including the jet, and an optically-thick dust torus which surrounds the accretion disc, extending up to 100 pc from the central SMBH. The following sections describe these components in greater depth.

1.1.1 The Central Engine

One of the key components when dealing with AGN is its energy generation mechanism (i.e. the central engine) which drives and sustains the AGN system. In the early 1960s, Hoyle & Fowler (248) suggested that the launch of the relativistic jet might be possible with the gravitational contraction of matter around a stellar-like nucleus with up to 10^8 solar masses. This mechanism would be able to release gravitational potential energy which may be stored in toroidal magnetic field lines during the accretion process by conservation of angular momentum.

Development of this scenario of energy generation by Zel'dovich & Novikov in 1965 (288) suggested that the production of jets had to be coupled with the processes of a black hole ($> 10^6$ solar masses) in the form of the potential energy found in the gravitational field of the black hole and the rotation of the black hole itself in order to generate the energy output observed from these radio sources. In 1969, Lynden-Bell (274) further developed the idea that the accretion of matter onto a rotating compact object (such as matter accretion onto a rotating Kerr SMBH) provides the deep gravitational potential well necessary to launch and sustain the gyroscopic stability of these jets over Mpc scales.

The dynamical interaction between the SMBH and the accretion disc which continually feeds the SMBH forms an important aspect of understanding the features of the central engine. The accretion disc-SMBH system and its dynamics are highly complex and have been the subject of extensive research. A review of accretion disc physics can be found in e.g. Melia (282). Matter in-falling into the central nucleus loses angular momentum through viscous and turbulent processes. The velocities of matter in the accretion disc are dependent on its radius from the nuclear region. Matter in the inner regions of the accretion disc will have higher velocities compared to matter moving in the outer regions of the disc. This leads to energy loss via friction which subsequently causes ther-

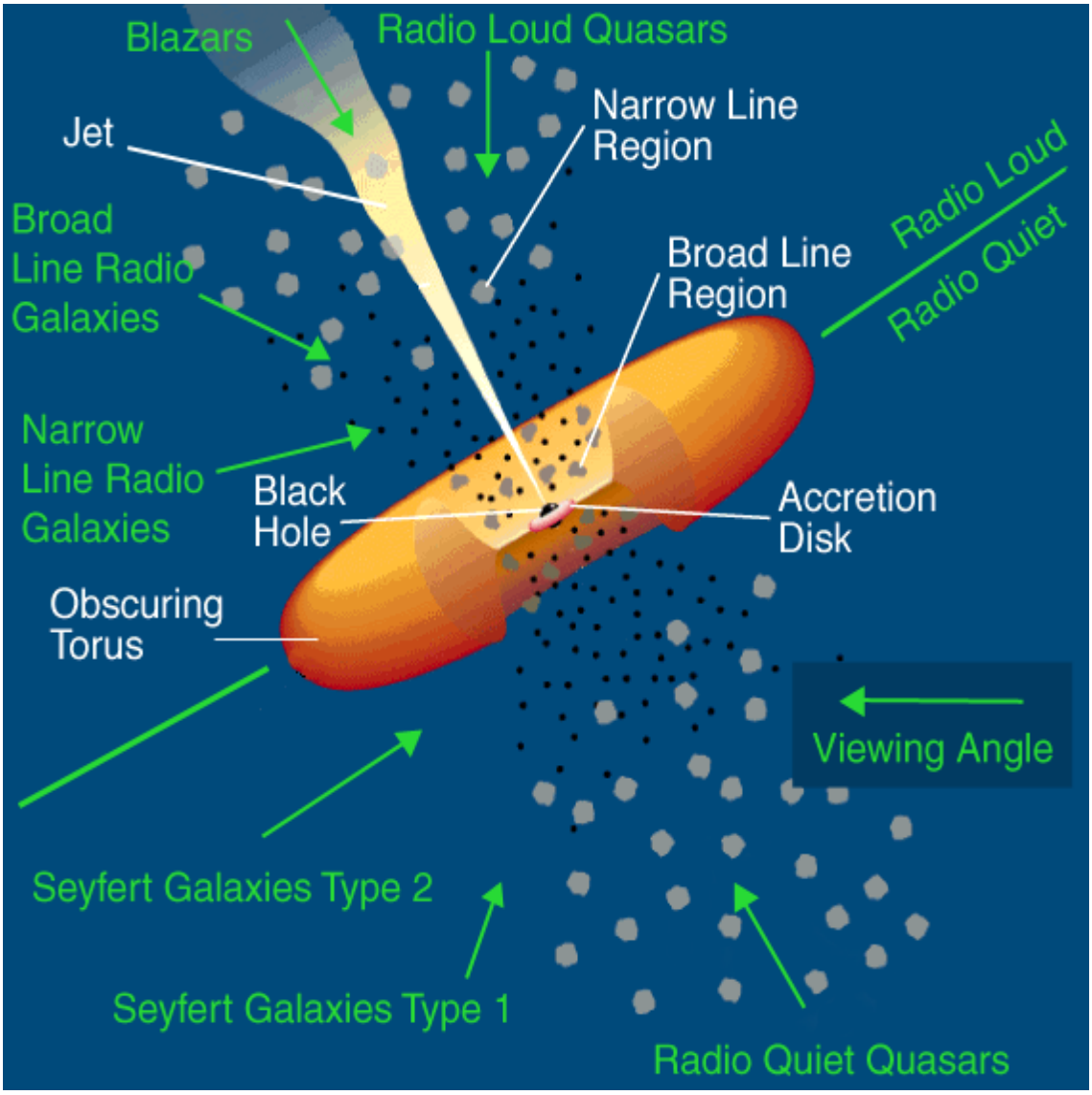

Figure 1.1: This diagram shows the active galactic nuclei (AGN) classification scheme. This classification scheme is based on observational, phenomenological and spectral properties including the orientation of the AGN with respect to the observer, such as the jet aligned blazar class. The green arrows indicate the viewing angle which is used to determine the various AGN sub-classes. The image is based on the unified AGN model by Urry & Padovani (290).

mal radiation at IR, optical and UV wavelengths. The loss of kinetic energy in the inner regions of the accretion disc also enables matter to be accreted onto the SMBH as angular momentum is transported out of the accretion disc. Another important aspect of the accretion disc system is that it radiates at different wavelengths, both thermally and non-thermally. This radiation produces seed photons which are re-radiated by particles in other regions of the central nucleus (e.g. broad and narrow line region gas clouds). Photons produced from emission in the accretion disc also feature as seed photons in jet emission models. These will be addressed in Chapter 2.

1.1.2 The Relativistic Jet

The relativistic jet is the collimated outflow of energetic particles occurring along the poles of the disc or torus (Figure 1.1). The jet comprises relativistic plasma carrying matter and energy to locations remote from the central engine. In the current AGN paradigm, jets are thought to originate in the vicinity of the SMBH and are powered by the SMBH-accretion disc system. The physical processes which lead to the formation and collimation of the jet are still the subject of great debate. The primary questions pertain to the mechanisms through which plasma is accelerated to relativistic speeds and collimated into jets with opening angles as small as few degrees (277).

The physical geometry, composition and emission processes which occur within the jet and as part of the jet phenomena is a subject in and of itself. A comprehensive look into various aspects of the relativistic jet system can be found in Boettcher et al. 2012 (156). In this section, a brief account of the jet is given. Relativistic jets have extended conical structures, launched to Mpc scales, outward from the central engine. Jets appear to be made of compact components (typically referred to knots) which move downstream at apparent superluminal speeds $> 25c$ (where c is the speed of light) (212; 221). Relativistic jets also show curvature within the compact region and between the parsec-scale and kiloparsec-scale jet (277). In 2001, Jorstad et al. (212) found that 43% of their 42 γ-ray bright AGN sources exhibited jet bending angles of $> 20^{\circ}$ at parsec scales. These were noted to be consistent with amplification by projection effects of modest actual changes in the position angle component (212).

The studies of blazars often concern the structures and dynamics of jets. This is because blazars are categorised based on the close alignment of their jets to the line-of-

sight. This causes the blazar emission spectrum to be dominated by the non-thermal emission of the jet rather than thermal emission from gas or dust either from the accretion disc, torus or the broad and narrow line region gas clouds surrounding the jet. Due to this, modelling the structure, magnetic fields, and jet plasma forms an intrinsic aspect of blazar emission models. The current relativistic jet paradigm, including its parameters and structure will be discussed in further detail in Section 2.5.

The ubiquitous nature of relativistic jets as part of the AGN phenomenon provides a wealth of information on the central engine. Observations of the jet at different wavelengths allow researchers to probe the activity of the central engine by monitoring features such as flux variability timescales, spectral indices and radio morphologies.

An important aspect which arises when studying the physics and physical properties of relativistic jets is the jet composition. The elements within the jet produce the necessary environments which result in the broadband emission observed from these sources. This jet composition is primarily important when modelling emission models (these are discussed in Chapter 2).

1.1.3 The Torus

The torus is a geometrically symmetrical toroidal structure comprising of gas and dust surrounding the accretion disc, at distances between 30 pc and 100 pc from the central engine (110) (see Figure 1.1). The torus is optically thick and reprocesses a fraction of UV radiation from the inner regions of the AGN (i.e. accretion disc) and emits this reprocessed radiation at infrared (IR) wavelengths. In the unified AGN paradigm, this dust torus is responsible for obscuring emission from the central regions including the broad line region gas clouds when AGN are viewed edge-on. The notion of obscuring material surrounding the nucleus was initially used to explain the anisotropic distribution of emission features (i.e. the absence of broad high-ionisation lines in the spectra in Type 2 AGN) (290).

1.1.4 The Broad and Narrow Line Region Gas Clouds

In the vicinities above and below the accretion disc, gas 'clouds' are heated by radiation from the accretion disc. These regions produce emission lines which can be divided into two types: (i) the broad line region (BLR) produces broad emission lines and, (ii)

the narrow line region (NLR) produces narrow emission lines. It was suggested that the difference in the widths of the permitted emission lines may be a result of the differential Doppler shifts due to motions from individual clouds within the BLR and NLR regions (265).

As shown in Figure 1.1, the BLR clouds are located closer to the central engine at distances of $\lesssim 1$ pc (286). This proximity ensures that the BLR clouds are hot (with temperatures derived from thermal motion alone reaching $\sim 10^9$ K) and denser with electron densities reaching up to $N_e \sim 10^9$ cm^{-3} moving at velocities between 1000 km s^{-1} and 25 000 km s^{-1} (298). Due to the high temperatures and its proximity to the central engine, the permitted emission lines from the BLR are very luminous and the BLR are constantly fed by the UV radiation of the nuclear region.

The NLR is located further from the central engine than the BLR, reaching distances of up to 1 kpc (286). Gas clouds in the NLR have lower temperatures (≈ 15000 K) (289) and velocities ($v \lesssim 500$ km s^{-1}) (298). The electron density of this regions is also considerably lower ($N_e \sim 10^2$ - 10^6 cm^{-3}) compared to the BLR (298).

The BLR and NLR clouds are particularly important in the study of blazars as these regions interact with the relativistic jet in several different ways. In blazar emission models (see Section 2.6), seed photons from the BLR and NLR clouds are inverse Compton scattered to higher energies producing the high-energy component observed in blazar spectral energy distributions. It is also possible that these 'clouds' move into regions of the jet, increasing particle densities in that particular region, (or a precessing jet moves into matter rich BLR or NLR regions) causing particle interaction with matter outside the jet.

1.2 The AGN Classification Scheme

AGN are generally classified based on their observational, phenomenological and spectral properties. On the first level of sub-classification (as summarised in Figure 1.2), AGN are divided into two basic categories based on their radio-loudness, R. This property represents the measure of the ratio of the radio flux at 5 GHz to the optical flux in the B-band, $S_{radio}/S_{optical}$ (139; 140). A source is considered radio loud when $R \gtrsim 10$. As such, this results in two groups: (i) radio-loud AGN, and (ii) radio-quiet AGN. The second level of

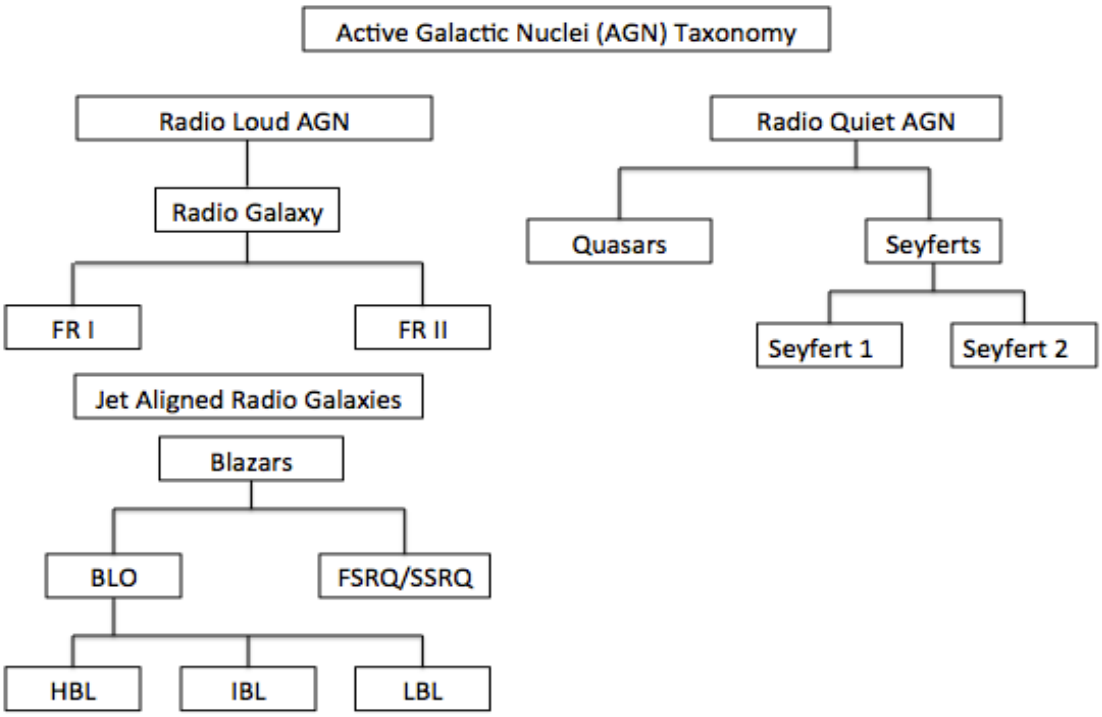

Figure 1.2: This diagram shows the active galactic nuclei (AGN) classification scheme. This classification scheme is based on observational, phenomenological and spectral properties including the orientation of the AGN with respect to the observer, such as the jet aligned blazar class.

division then comes about based on the observational angle of the source (AGN) to the line-of-sight, as well as spectral properties of the optical emission and phenomenological properties of the source (such as the wavelength-dependent flux variability timescales).

1.2.1 Quasars

Quasars are a type of high-luminosity AGN in which the brightness of the nucleus often far outshines the host galaxy. Quasars have been identified in both radio-loud and radio-quiet categories, with 10% of quasars being radio-loud. Radio-loud quasars have a stronger radio component than their radio-quiet counterparts, thought to be due to a brighter jet component.

Radio-loud quasars are further sub-categorised into Flat Spectrum Radio Quasars (FSRQs) and Steep Spectrum Radio Quasars (SSRQs). The former consists of radio-loud

quasars which have a flat and compact radio spectrum, commonly represented by $\alpha_r < 0.5$, where α_r is the radio spectral index[1] (290; 291), while the latter (SSRQs) have steeper and more extended radio spectra with $\alpha_r > 0.5$ (290). It must be noted that FSRQs are also a subset of blazars (see Section 1.2.4) due to their jet being aligned close to the line-of-sight.

1.2.2 Seyfert Galaxies

Seyfert galaxies are distinguished from other AGN by their strongly ionised emission lines. Approximately 90% of these galaxies are radio-quiet. There are in general two broad Seyfert galaxy categories: Seyfert 1 and Seyfert 2.

Seyfert 1 galaxies exhibit both broad and narrow emission lines in their spectra. The broad emission lines are thought to originate from high density ionised gas moving at velocities of up to 10^4 km s^{-1}. The narrow line emission, on the other hand, is thought to originate from lower density ionised gas moving at velocities of 10^3 km s^{-1}. Due to this, Seyfert 1s are thought to be AGN observed at lower inclination angles whose spectra contain emission from the BLR clouds which travel at much higher velocities than the NLR clouds.

The spectra of Seyfert 2 galaxies however exhibit only narrow emission lines, suggesting that these galaxies are observed at higher inclination angles than the Seyfert 1s, in order to account for the narrow emission lines observed at lower densities and velocities. It must be noted that some Seyfert 2 galaxies also exhibit weak broad narrow line emission, which are strongly polarised

It can be noted here that both Seyfert galaxies and quasars exhibit observational similarities with the quasars being brighter than Seyfert galaxies. The higher luminosities of quasars can be explained by higher accretion rates of the central engine compared to Seyfert galaxies. The observational similarities (i.e. the similarities in the spectra) from Seyfert galaxies provides further evidence for the unification scheme of AGN.

1.2.3 Radio Galaxies

This group of AGN are particularly known for their strong radio brightness and extended radio emission in the form of jets. In 1974, Fanaroff & Riley (310) discovered that

[1]The spectral index α is based on $S_\nu \propto \nu^{-\alpha}$, where S_ν is the observed flux at a given frequency ν (290).

there were different regions within these radio-loud sources which exhibited different luminosities, leading to the definition of two types of radio galaxies known as FR I and FR II. FR I sources are less luminous and have brighter nuclei while FR II are more luminous and have precessing bright radio lobes which dominate the radio spectrum (310). This distinction hinted at a difference in the emission mechanism of the central engine and the total kinetic power present in the jet (6), such that FR I with their brighter nuclear regions have jets with stronger kinetic energy compared to their radiative energy output, while the FR II galaxies have a smaller amount of bulk kinetic energy present in the jet[2].

1.2.4 Blazars

Under the AGN paradigm, blazars are a subset of radio-loud AGN with their jets closely aligned to the line-of-sight, at angles of $< 10^{\circ}$ between the jet axis and the observer (e.g. (4; 290)). Blazars are known and identified based on their characteristic properties. These include rapid variability, strong continuum emission extending from the radio up to TeV γ-ray energies, high optical polarisation, apparent superluminal motion of the jet, core-dominant radio morphologies and flat radio spectra with $\alpha_r < 0.5$ (where α_r is the radio spectral index) (290; 291).

Blazars are also interesting as they are astrophysical laboratories of high energy phenomena, dominating the extragalactic high-energy sky. These sources have been detected at γ-ray energies (> 100 MeV) with the EGRET telescope (e.g. (200; 134)) and *Fermi*-LAT[3] (e.g. (27; 58)), and at VHE γ-ray energies with H.E.S.S. (33) and VERITAS (210) among others[4]. The relativistic plasma which makes up the jet can have a bulk Lorentz factor, Γ, reaching ~ 50 (291; 156; 41; 159). As such, blazars are extreme variable sources of γ-ray emission detected at TeV energies using ground based atmospheric Cherenkov telescope arrays (13). Observations of blazars are dominated by the non-thermal emission from the jet. This leads to the interpretation that the observed blazar

[2]Fanaroff & Riley (310) showed that radio sources with total power exceeding 2.5×10^{26} W Hz^{-1} (at 178 MHz) almost exclusively have FR II morphologies, while radio sources with FR I morphologies had total powers of $< 2.5 \times 10^{26}$ W Hz^{-1}.

[3]*Fermi*-LAT has detected over 1000 blazars which are included in the recent 3LAC catalogue (66).

[4]H.E.S.S. has observed ~ 45 blazars (33) while VERITAS has observed over 130 blazars at high energy (HE) and very high energy (VHE) energies (210).

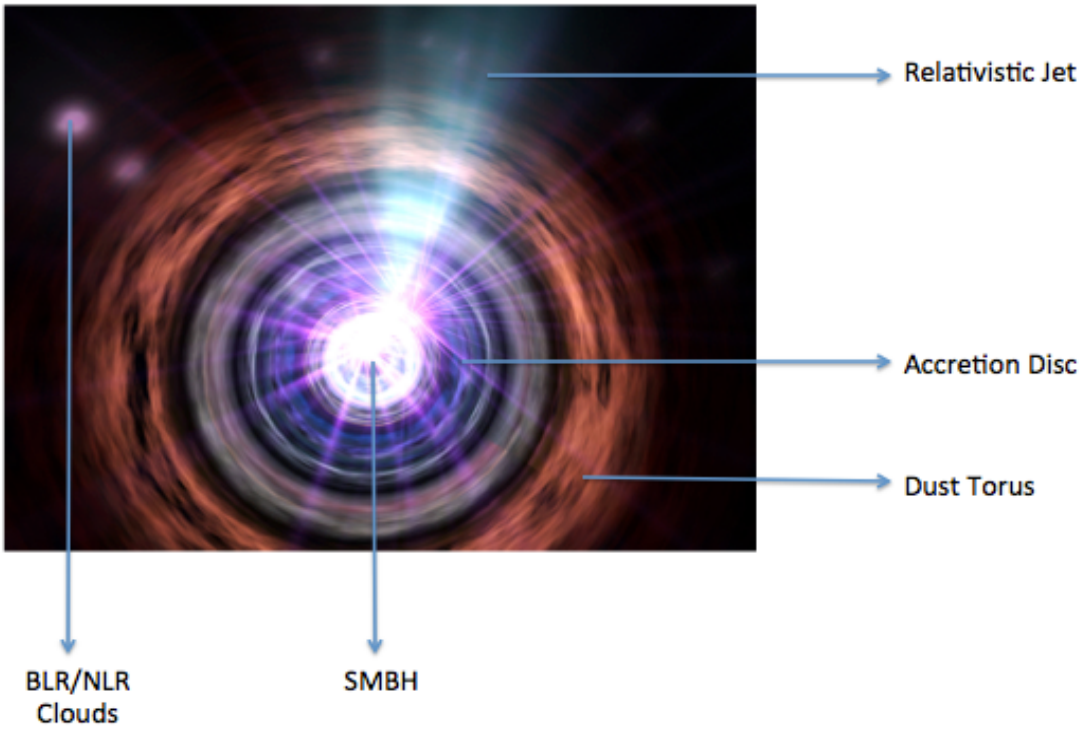

Figure 1.3: An illustration of a blazar as observed directly down the jet along with its various AGN components. Image credit NASA (www.nasa.gov, last viewed: 23/03/2016).

spectral energy distributions (see Section 1.3) are therefore strongly Doppler boosted due to the relativistic motion of the jet material. This apparent relativistic boosting of the spectrum (see Section 2.5.1) explains the extreme characteristics of this source type, namely rapid variability at all frequencies and on different timescales (13).

It has been observed that many of the blazars that have been detected emit the bulk of their bolometric luminosities at γ-ray energies (13). This could be due to the Doppler shifting of the emission to higher energies as the emitting regions are aligned with the line-of-sight. Observations using radio interferometry often show a one-sided jet[5] with apparent superluminal motion (13; 156).

[5]The appearance of a one-sided jet, instead of a two-sided jet, is also attributed to the effects of relativistic beaming which strongly beams the jet component moving towards the observer while de-beaming the jet component moving away from the observer (156).

1.3 Blazar Spectral Classification and the Blazar Spectral Energy Distribution (SED)

Due to their orientation relative to the observer, observations of blazars probe regions within the jet, depending on the wavelength of observation. Studying the observational properties of jets give an insight into the processes that occur within these jets and, through the unification scheme, other AGN. Blazars are typically sub-categorised into two classes, BL Lacertae objects (BLOs), which are generally thought to be the 'beamed' counterparts of high and low luminosity radio galaxies (FR I galaxies) and γ-ray loud FSRQs (high luminosity FR II galaxies). BLOs have generally featureless optical spectra with weak or absent emission or absorption lines. FSRQs on the other hand, have strong broad emission lines (290; 291; 165; 106).

A typical aspect of the study of blazars concerns the blazar spectral energy distribution (SED) which shows the power per logarithmic frequency band (νFν) (see Figure 1.4). Blazar SEDs are generally known for their two broad components which span the entire electromagnetic spectrum. The first component occurs at lower energies, typically between radio to UV or X-ray frequencies. This component is generally attributed to synchrotron emission from the relativistic particles interacting with magnetic field lines (see Section 2.6). The second component occurs at higher energies, namely between X-ray and TeV γ-ray frequencies. This component is usually modelled as inverse Compton emission from a source of seed photons, although the origin of this high-energy component is still a matter of debate. In blazar SEDs, the high and low energy components peak at different frequencies for different sources. This particular aspect of the blazar SED is used as a means to differentiate between the blazar subsets. This was particularly useful in distinguishing between the the different BLO classes and establishing the blazar sequence (13).

Based on the peak frequencies of the synchrotron component of the blazar SED, BLOs can be further sub-categorised into three different classes, namely HBLs, IBLs and LBLs (30). High-frequency-peaked BL Lacertae Objects, more commonly referred to as HBLs, are sources with synchrotron peaking at frequencies $\nu_{pk}^{sy} > 10^{15}$ Hz. Intermediate-frequency peaked BL Lacertae Objects (IBLs) have synchrotron peaks between $\nu_{pk}^{sy} \sim 10^{14}$ Hz and $\nu_{pk}^{sy} \sim 10^{15}$. Low-frequency peaked BL Lacertae Objects (LBLs) have synchrotron

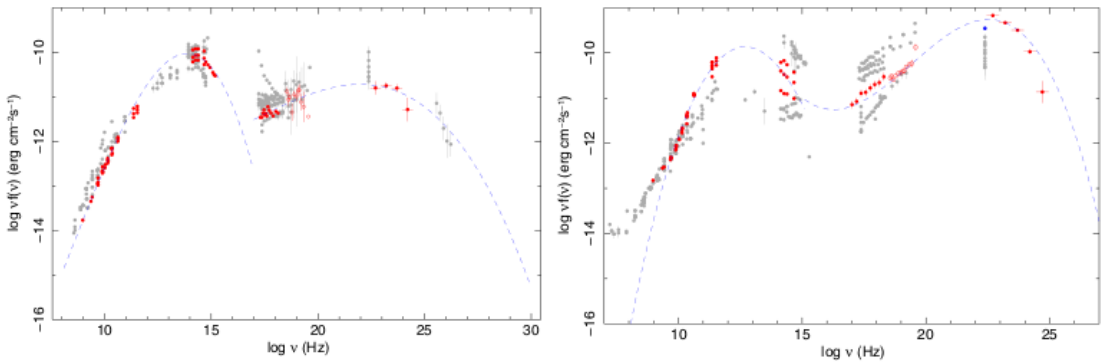

Figure 1.4: SED of PKS 1510-089, based on both quasi-simultaneous (large filled red symbols) and non-simultaneous archival (open grey points) radio to γ-ray observations, while the dashed lines represent best fits to the synchrotron and inverse Compton components based on observational parameters including the radio spectral index, peak frequency and peak flux of the synchrotron component and the peak frequency and peak flux of the inverse Compton component (29).

frequencies $\nu_{pk}^{sy} < 10^{14}$ Hz (30). It must be noted that almost all FSRQs also have synchrotron peaks at $\nu_{pk}^{sy} < 10^{14}$ Hz. This particular feature leads to the notion of there existing a sequence of blazar sub-classes often called the Blazar Sequence.

1.4 The Blazar Sequence

The blazar sequence suggests that there may be a link between the different blazar subclasses based on the increasing $\nu F\nu$ peak frequencies and decreasing dominance of the γ-ray flux over the low-frequency emissions together with decreasing bolometric luminosity (see Fossati et al. (93)). This link was first described as an anti-correlation between the observed bolometric luminosity at the synchrotron peak and the frequency of this peak. The sequence revealed a trend that followed from the low-synchrotron peaked FSRQs $\rightarrow$ LBLs $\rightarrow$ IBLs $\rightarrow$ HBLs with their high-frequency synchrotron peaks, decreasing dominance of the γ-ray flux over the low-frequency emission, and decreasing bolometric luminosities (93; 13). Figure 1.5 shows the observed trend as described by the blazar sequence scheme. The SEDs from three different blazar sub-classes fit by leptonic jet models are shown to distinguish between the observed peak frequencies of the synchrotron component. The SED of 3C 279 (an FSRQ) shows synchrotron peak fre-

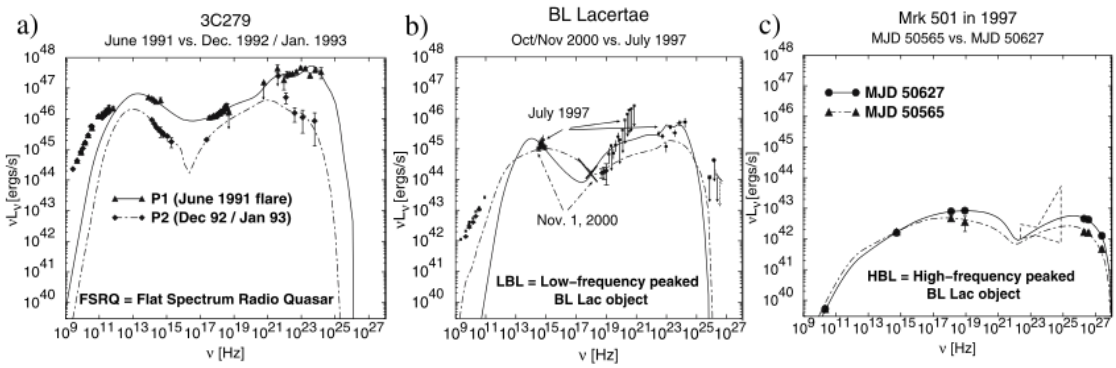

Figure 1.5: This figure illustrates the trends depicted in the blazar sequence using the SEDs of three different blazar sub-classes. The first (a) is the SED of 3C 279 (202), an FSRQ, (b) is BL Lacertae (157), an archetype of the IBL/LBL category and (c) is MRK 501 (300), a HBL. The SEDs are model fits using leptonic jet models based on observations conducted at two different epochs. Image courtesy of Boettcher (13).

quencies between 10^{11} to 10^{13} Hz, not dissimilar to the synchrotron peak frequencies of BL Lacertae (an intermediate between an LBL and IBL). MRK 501 (a HBL) shows the highest synchrotron peak frequency (13).

While this may be evidence for an intrinsic trend in the evolution and unification of the blazar scheme, the existence of this sequence has recently been brought into question. Padovani et al. (196), Padovani (291), Giommi et al. (188; 189; 190) have suggested that the blazar sequence may be the effect of a selection bias and flux-limited samples. A review of the different studies conducted can be found in Finke (247).

In this thesis, the aim will be to understand the temporal properties of the (sub-)mm emission and how it relates to the γ-ray emission observed in a selection of eight blazars from each different blazar sub-class. Does the behaviour of the source at both these wavebands depend on the blazar class and is emission in both these wavebands related?

In Chapter 2, the primary physics which concern the radiative processed in AGN and blazar jets will be presented. Here, an introduction into the jet structure and properties will be discussed as this forms a very important aspect of blazar emission, due to its spectrum being jet dominated. In Chapter 3 the motivation behind multiwavelength campaigns and the significance of the γ-ray and (sub-)mm regimes will be discussed. Also, in this chapter, a brief introduction on the properties and historical and observational background of the sources analysed in this research will be presented. Chapter

4 will detail instrumentation and analysis methods for two of the instruments used to obtain the observations presented in this thesis. These are SCUBA-2 and *Fermi*-LAT. In Chapter 5, results from short-term, targeted SCUBA-2 and *Fermi*-LAT observations of PKS 2155-304 and MRK 421, both of which are HBLs will be presented and discussed. Chapter 6 will detail the long-term (sub-)mm observations (using the Submillimeter Array) and study of eight sources (two HBLs, two IBLs, three FSRQs and a radio galaxy). In Chapter 7, a qualitative analysis of the relationship between the long-term (sub-)mm observations along with simultaneous γ-ray observations using *Fermi*-LAT will be discussed. In Chapter 8, this relationship will be analysed quantitatively using the discrete correlation function (DCF) method. In this chapter, the presence or absence of correlation will be discussed for each source and its implication to the blazar sequence will be presented.

The aim will be to study the properties and behaviour of blazars in the (sub-)mm waveband and how this behaviour relates to emission in the γ-ray band. Another aspect will be to investigate the implications of the presence or lack of correlation to the type of emission produced in the jet, the emission regions and subsequently how this may related to the jet structure. The study of a select sample of well-known blazars allow direct comparisons and archived observations recorded over the similar periods of the long-term study presented in this thesis. It is also an efficient way of obtaining a better understanding of AGN under the current AGN paradigm and unification scheme, as it provides a particularly unique perspective of the jet.

Chapter 2 | *The Physics of Blazars*

Observations of blazars are dominated by emission from their relativistic jets due to the jets being oriented to the line-of-sight. This then determines the type of emission that is observed. Radiation processes from these relativistic jets are generally non-thermal, and are produced by the relativistic motion of the particles within the jet. Studying these processes and the interaction of these particles with either the fields within the jets or other particle populations also within or immediately outside the jet, gives rise to several types of scenarios leading to emission at different wavelengths.

This chapter will first introduce the types of particle interaction and radiation processes within the blazar environment which lead to their characteristic SEDs and then continue to examine how these are used to develop emission models which aim to explain the overall radiation output of blazar jets.

2.1 Radiative Processes and Particle Acceleration within the Jet

Particle-particle interaction and particle-field (e.g. magnetic field) interaction processes within the jet environment are generally accepted to be responsible for the characteristic double-peaked SEDs observed from blazars.

This section describes the fundamental processes which occur within the relativistic jets of blazars, the synchrotron and inverse Compton processes. In addition, pair and pion production processes, which refer to the production of γ-rays in particular, will also be considered.

2.1.1 The Synchrotron Process

The synchrotron process occurs when a charged particle, moving relativistically, interacts with magnetic field lines (Figure 2.1). This interaction causes the particle to be accelerated, resulting in the charged particle moving helically around the field line.

The power radiated via the synchrotron emission process is derived based on Larmor's theorem, and applied to a relativistic charged particle. In the following steps, the approach taken to relate the fundamental concepts of the synchrotron process is adapted from Longair (272).

First, consider the frequency of the helical motion as the charged particle propagates along the magnetic field line. This is known as the Larmor frequency or, more commonly, the gyrofrequency. For an electron of rest mass energy, $m_e c^2$, where m_e is the mass of the electron, γ is the Lorentz factor[1], and c is the speed of light, the gyrofrequency, ω_g can be written as:

$$\omega_g = \frac{eB \sin \phi}{\gamma m_e} \tag{2.1}$$

where B is the strength of the magnetic field, and ϕ is the angle between the velocity vector of the electron and the direction of the magnetic field, known as the pitch angle.

The total energy loss rate of the electron is given by:

$$-\left(\frac{dE}{dt}\right)_{sync} = 2\sigma_T c U_{mag} \left(\frac{v}{c}\right)^2 \gamma^2 sin^2\phi \tag{2.2}$$

where $U_{mag} = \dfrac{B^2}{2\mu_\circ}$ is the energy density of the magnetic field (**B**-field), $\sigma_T = \dfrac{e^4}{6\pi\epsilon_\circ^2 c^4 m_e^2} = \dfrac{8\pi r_\circ}{3}$ is the Thomson cross section. Here, $r_\circ = \dfrac{e^2}{4\pi\epsilon_\circ m_e c^2}$ is the classical radius of the electron; $\epsilon_\circ$ and $\mu_\circ$ represent the permittivity and permeability of free space respectively.

The energy loss rate given in Equation 2.2 applies for electrons of a specific pitch angle, ϕ. If the electrons of a particular energy, E and Lorentz factor, γ, have an isotropic distribution of pitch angles, then the average energy loss rate can be obtained by averaging over an isotropic distribution of the pitch angle, $p(\phi)\, d\phi = \dfrac{1}{2} \sin\phi d\phi$. Thus, the average energy loss rate becomes:

$$\left(\frac{dE}{dt}\right)_{sync} = \frac{4}{3} c \sigma_T \left(\frac{v}{c}\right)^2 \gamma^2 U_{mag} \tag{2.3}$$

The amount of energy per unit time emitted by a particle is inversely proportional to the square of the mass of the relativistic particle. For an electrically neutral plasma, synchrotron radiation produced by electrons will most likely dominate the synchrotron

[1]The Lorentz factor, γ is defined as $\gamma = \left(1 - \frac{v^2}{c^2}\right)^{-1/2}$, where v is the speed of the relativistic particle.

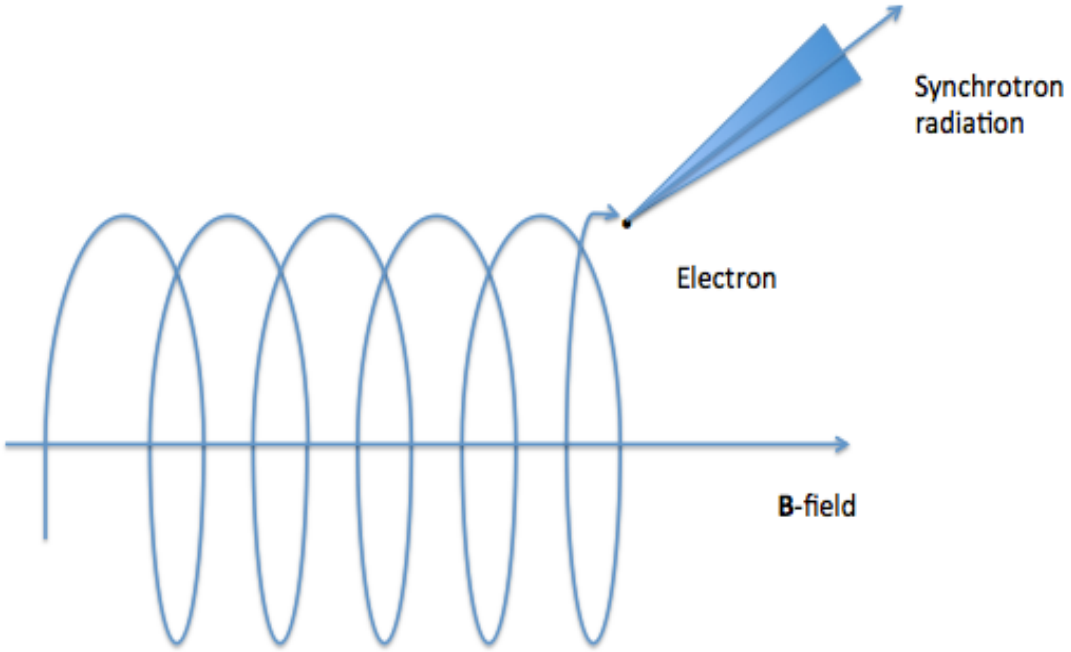

Figure 2.1: This schematic represents the trajectory of the synchrotron emission as it gyrates about a uniform stationary magnetic field line. This motion results in the synchrotron emission appearing as a cone emitted in the tangential direction to the motion of the particle.

emission when no other processes occur (i.e. processes that can be attributed to the acceleration of protons to relativistic speeds, see Section 2.8)

In the classical limit, as the electron gyrates about the magnetic field line, it emits a dipole radiation pattern (Figure 2.2). However, at relativistic speeds, this pattern is altered primarily due to the effects of relativistic aberration between the frame of reference of the moving electron and the frame of reference of the observer. This leads to the dipole emission being strongly beamed in the direction of motion as shown in Figure 2.2. The beamed radiation features as a conical beam with an half opening angle of $\alpha = \pm\frac{1}{\gamma}$ and is linearly polarised. As this beam sweeps past the observer in the observer's frame, a pulse of radiation is observed. The Fourier transform of this pulse results in the observed synchrotron spectrum.

The characteristic angular frequency of the synchrotron radiation is given by:

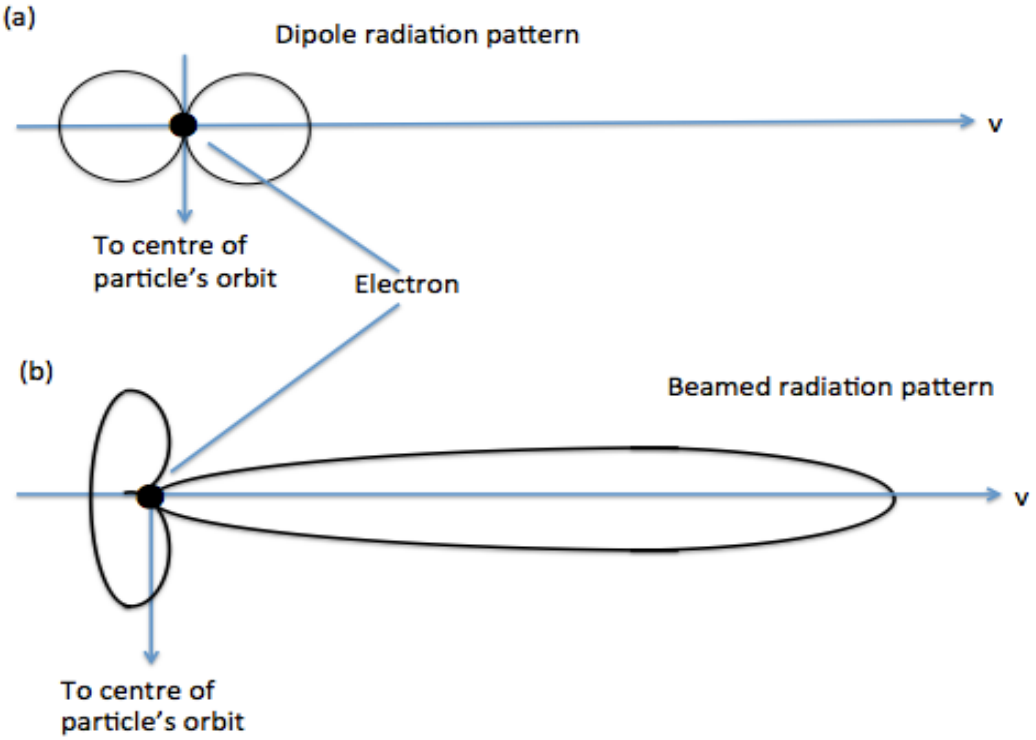

Figure 2.2: This schematic represents the typical dipole radiation of non-relativistic particle emitting synchrotron radiation and the beamed emission in the direction of motion when this particle moves at relativistic speeds.

$$\nu_{syn} = \frac{1}{2\pi}\gamma^2 \frac{qB}{m} \sin\phi \tag{2.4}$$

However, the power radiated by a single relativistic electron orbiting in a magnetic field consists of a range of frequencies including ν_{syn} (14). This is observed as a distribution of the power over the range of frequencies with a peak frequency given by $\nu_{peak} = 0.44\nu_{syn}$ and a critical frequency given by $\nu_c = 1.5\nu_{syn}$. The critical frequency observed in the power spectrum of a single electron is is given by:

$$\nu_c = \frac{3}{2}\gamma^2 \nu_g \sin\phi \tag{2.5}$$

where $\nu_g = \dfrac{eB}{2\pi m_e}$ is the non-relativistic gyrofrequency. ν_{syn} characterises the frequency range of the rapid descent of the radiated power spectrum for a single electron orbiting in a magnetic field.

Another important feature of the synchrotron process which has implications on the

particle acceleration mechanisms is the cooling timescale of the charged particle. This is given by:

$$t_{cooling} = \frac{\gamma m_e c^2}{\frac{dE}{dt}_{sync}} \tag{2.6}$$

Based on this, the more energetic electrons would cool more quickly which is an important consideration when assessing blazar jet emission at different wavelengths (i.e. γ-ray flux would decay more quickly than (sub-)mm emission, see Chapters 7 and 8). For continuous emission from these particles, it must follow that there needs to be acceleration mechanisms within the jet environment which function to continually accelerate these particles to the energies needed for further synchrotron and inverse Compton processes. These will be discussed in Section 2.4.

The synchrotron emission is believed to be the process responsible for the lower energy peak of blazar SEDs, evidenced by the polarisation observed from the non-thermal emission in blazars (e.g. (272; 173)).

2.1.2 The Inverse Compton Process

The inverse Compton process describes the interaction of a charged particle with a photon in which the charged particle transfers some of its energy to the photon, upscattering the latter to higher energies (Figure 2.3). This is the opposite process to Compton scattering whereby the photon imparts energy to the electron during interaction, while itself losing energy. The Compton process is thought to be responsible for producing the high energy peak of the SED.

Inverse Compton scattering relies on the transformation of the energy and frequency of the photon during interaction between the moving frame of the electron (i.e. in this frame the electron is at rest) and the laboratory (observer) frame in which the electron and the scattered photon appears to be moving. The energy boost to the photon in the observer's frame occurs as a consequence of the two transformations. The first is from the observer's frame to the rest frame of the electron and the second transforms the energy and frequency of the scattered photon back into the rest frame of the observer.

Consider a charged particle, i.e. an electron, moving relativistically with energy $\gamma m_e c^2$ interacting with a photon of frequency ν', then in the rest frame of the electron, the frequency of the photon, ν_e, will appear to be given by the following.

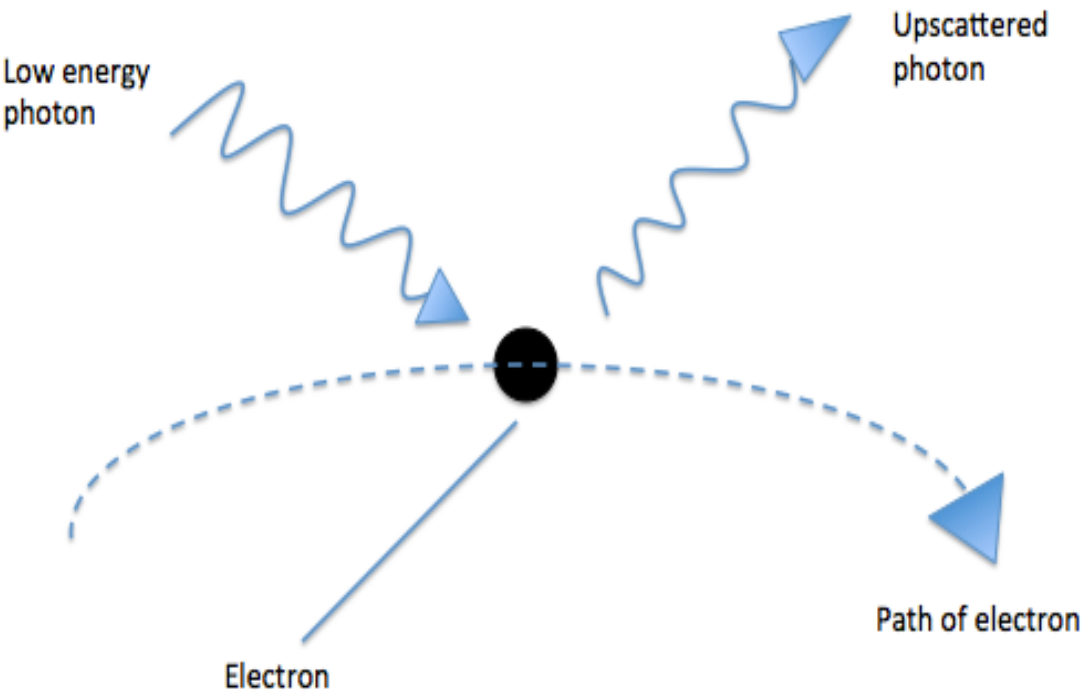

Figure 2.3: This schematic represents inverse Compton process where the charged particle interacts with a lower energy photon, resulting in the photon being upscattered to higher energies.

$$\nu_e = \nu' \gamma \left(1 + \beta \cos\theta\right) \tag{2.7}$$

where γ is the Lorentz factor, θ is the angle between the incident and scattering directions. In the rest frame of the electron, the photon is backscattered and thus moves with slightly less energy. However, in the rest frame of the observer, the energy and frequency of the photon appears much higher as a result of the transformation from the rest frame of the electron to the rest frame of the observer. The scattered energy of the photon in the rest frame of the observer is given by:

$$h\nu \approx 4\gamma^2 h\nu \tag{2.8}$$

This expression is valid if the incident photon energy in the rest frame of the electron is $\ll mc^2$. This is known as inverse Compton scattering in the Thomson regime. Interactions take place in the Klein-Nishina regime when the incident photon energy in the rest

frame of the electron $\gg mc^2$. For the latter, the resulting energy of the scattered photon in the rest frame of the observer is given by:

$$h\nu \approx \gamma m_e c^2 \tag{2.9}$$

The interaction cross-section will change between the Thomson and Klein-Nishina regimes depending on the energies of both the interacting photon and electron. In the following sections the IC process in these two regimes will be discussed.

Emission in the Thomson Regime

As discussed, the interaction occurs in the Thomson regime when the energy of the photon in the rest frame of the electron is $h\nu \ll \gamma m_e c^2$. In the classical limit, the IC process is dominated by the Thomson cross-section in which the classical radius of the particle becomes an important aspect of the interaction. First, consider the Thomson scattering cross-section, σ_T:

$$\sigma_T = \frac{8\pi}{3} r_e^2 \tag{2.10}$$

$$\sigma_T = \frac{8\pi}{3} \left(\frac{e_2}{4\pi\epsilon_\circ m_e c^2} \right)^2 \tag{2.11}$$

where $r_e = \dfrac{e^2}{4\pi\epsilon_\circ m_e c^2}$ represents the classical radius of the electron.

The total energy loss rate for an electron in the Thomson regime is:

$$\left(\frac{dE}{dt} \right)_{IC} = \frac{4}{3} \sigma_T c U_{rad} \left(\frac{v}{c} \right)^2 \gamma^2 \tag{2.12}$$

where U_{rad} is the energy density of the photon radiation field.

A characteristic feature of interaction in the Thomson regime is that the photons are scattered isotropically over a wide range of angles in the rest frame of the electron. In addition, the energy of the photon increases by γ^2. In the Thomson regime, the relativistic electrons only transfer a small fraction of their energy during interaction and thus, a single relativistic electron may undergo several IC interactions.

Emission in the Klein-Nishina Regime

The interaction occurs in the Klein-Nishina regime if the energy of the low-energy photon in the rest frame of the electron approaches $m_e c^2$. In the Klein-Nishina (K-N) regime, the incident photon must have energy that fulfils the criterion such that $2\gamma h\nu \gg m_e c^2$ in the rest frame of the electron. Thus, the quantum relativistic cross-section for scattering must be applied. This also occurs when the photons are of low energy, i.e. $h\nu \ll m_e c^2$ but the electrons move ultra-relativistically with $\gamma \gg 1$. The latter is more typical of the blazar jet environment.

Both these cases lead to a scattering cross-section given by the following:

$$\sigma_{K-N} = \pi r_e^2 \frac{1}{x}\left(\ln 2x + \frac{1}{2}\right) \tag{2.13}$$

where $x = \frac{h\nu}{m_e c^2}$ and r_e is the classical electron radius. In the K-N regime, the IC scattering of the photons is anisotropic and the gain in energy is only by a factor of γ, unlike the energy gain of a factor γ^2 in the Thomson regime. In addition, σ_{K-N} is smaller than σ_T. The decrease in the interaction cross-section in the K-N regime reduces the efficiency of the IC process in this regime. The electron, on the other hand, loses a larger fraction of its total energy during interaction and as such undergoes only one IC interaction.

The similarity between the total energy loss rates in the synchrotron and IC processes (Equations 2.3 and 2.12 respectively) is a result of the energy loss rates being dependent on the electric field that accelerates the electrons in its rest frame, regardless of the origin of that field. The difference between the total energy loss rates in both processes is the energy density of the magnetic field, U_{mag} which affects the synchrotron process and the energy density of the radiation field, U_{rad} which affects the IC process. This feature is particularly important when considering the processes and emission produced in different leptonic emission scenarios (see Section 2.6).

2.2 γ-Hadron Interactions

In the highly-energetic regime of relativistic jets, with the presence of dense radiation fields, the interactions between relativistic hadrons and photons become an important part of the processes which occur within the jet environment.

2.2.1 Photo-Pion Production

Relativistic jets of active galactic nuclei are thought to be the production site of the highest energy cosmic rays observed from Earth at energies reaching $E \gtrsim 10^{20}$ eV (156). Any such cosmic ray particles, generally protons, must possess Lorentz factors of $\gamma \gtrsim 10^{11}$ (156). These ultra-relativistic protons can then interact with low-energy photons to produce either neutral or charged pions ($\pi^{\pm,\circ}$), following the interaction below:

$$p + \gamma \rightarrow p + \pi^0 \tag{2.14}$$

Another mode of pion production is via the proton-proton or proton-neutron interaction which is shown below:

$$p + p \rightarrow \pi^{+,0} + 2N \tag{2.15}$$

$$p + n \rightarrow \pi^{\pm,0} + 2N \tag{2.16}$$

where N represents a nucleon and is either a proton, p or a neutron, n (i.e. $2N = p+n$ or $2N = p + p$ based on the charge of the π produced).

For an interaction with target photons of energy much less than the pion rest-mass energy of $m_\pi c^2 \approx 140$ MeV, the interacting proton must be highly relativistic in order to reach the threshold for pion production.

Then the decay of neutral pions via the electromagnetic force produces two γ-rays:

$$\pi^0 \rightarrow 2\gamma + e^+ + e^- \tag{2.17}$$

This process is of much interest as it is thought to play an important role in the production of the high-energy photons observed from some AGN (156) (see Section 2.8).

2.3 $\gamma\gamma$ Pair Production

This process describes the interaction of a very-high-energy photon with either the field of a nucleus, another photon or a magnetic field resulting in its conversion into an electron and positron pair, as shown in Equation 2.18. The inverse of this process is the electron-positron annihilation which results in the production of two photons.

$$\gamma + \gamma \rightarrow e^{+}e^{-} \tag{2.18}$$

Within the vicinity of the jet emitting regions, in which the VHE γ-rays are thought to be generated either by leptonic or hadronic emission processes (see Section 2.6), the γ-γ interactions may occur with the VHE γ-ray photon along with a low-energy photon. This process has been suggested as a method for attenuating VHE photons within the emitting source and in regions external to the source.

The γ-γ interaction mechanism is also a process involved in hadronic models. This process may occur as a consequence of π° - decay cascades (see Section 2.8).

2.4 Fermi Processes and Shocks

As observed in the above sections, the energy loss by an electron population undergoing synchrotron and inverse Compton processes will result in rapid cooling. Thus, consideration must be given to how these particle populations maintain their energy. It follows that these particles must be constantly accelerated to continuously produce a power-law distribution.

The relativistic jet is believed to be composed of highly magnetised plasma. For such a case, the Fermi acceleration processes can be considered to be responsible for particle acceleration within the jet environment. These were first proposed by E. Fermi in 1949 (246), in which particles are accelerated through the energy transfer between magnetised plasma regions. This will occur when the charged particles interact and are reflected by means of 'magnetic mirrors' present in the region of a plasma blob. This then results in the individual particles gaining or losing kinetic energy. There are two Fermi acceleration processes known as First-order and Second-order Fermi Acceleration respectively. In the First-order process, particles may travel across a shock front. As shock waves are thought to possess moving magnetic inhomogeneities, the particles will diffuse back and

forth across the shock front resulting in a net gain in the particles' energy. In the Second-order process, the particles may interact with moving 'magnetic mirrors' resulting also in a net-gain of energy. This is because a head-on particle - 'magnetic mirror' collision is more probable than a head-tail collision (246). The accelerated particles from both these processes will have a power law distribution (7).

A second mode of particle acceleration within the jet is through a model known as Diffusive Shock Acceleration (DSA). This was proposed by Anthony Bell in 1978 (8; 9). In the high-energy regime of blazar jets, there is strong evidence for the presence of shocks moving through and interacting with the turbulent magnetic fields. These are observed as 'knots' from radio to X-ray wavelengths (305). It is generally accepted that these shocks and their movement along the jet promote particle acceleration processes via the DSA model. Bell (8; 9) built on the initial premise by Fermi (246) by considering the effects on highly-relativistic charged particles when the plasma bubbles encompassing these particles overtake the shock, when the particles are considered to be moving with respect to the plasma. The particles moving within the plasma will continuously lose energy by means of collisions with Alfvén waves and decelerate until they become at rest with respect to the plasma (332). During the interaction between the plasma and the shock, the latter would overtake the plasma as the particles would be decelerating as described above, thus resulting in the shock eventually overtaking the plasma. When this occurs, the particles would begin to accelerate due to the wake of the turbulent shock. This will lead to the particles being caught between the Alfvén waves and the wake of the shock, crossing and recrossing the shock. There will be a net gain in energy by the particles as a result of this (e.g. (8; 9; 305)).

Another way of particle acceleration is through magnetic reconnection events. This process can occur in conducting plasmas within the highly turbulent regions within blazar jets. These events can be caused by several factors within and outside of the jet. Within the jet environment, the highly turbulent magnetic field lines make magnetic reconnection a very likely scenario. Differential rotation in the accretion disc is another possibility. The result of these magnetic reconnection events is that magnetic energy is converted into bulk kinetic and thermal energy and hence particle acceleration as magnetic field lines are rearranged (100; 320). Magnetic reconnection events can deposit more than 50% of energy dissipated from shocks into non-thermal leptons, given

that the energy density of the magnetic field in the bulk flow is larger than the rest-mass energy density (216). The accelerated particles from the DSA and magnetic reconnection events will produce a power-law distribution (272; 156).

2.5 Relativistic Jets and Acceleration

2.5.1 Jet Parameters

The idea of the jet being comprised of highly magnetised plasma with charged particles moving at relativistic speeds provides the fundamental premise for modelling the jet and its parameters. The key property that must be first considered is the relativistic motion of the plasma which introduces a Doppler factor. In the following steps, the approach taken to understand how Doppler factors relate the observed flux and luminosity to the intrinsic flux and luminosity is adapted from Urry & Padovani (290) and H. Bradt (14).

In such cases where relativistic beaming occurs, the observed flux needs to be corrected for this effect using the Doppler factor, δ (290; 277). For a variable emission region moving within the jet, δ is given by:

$$\delta = [\gamma(1 - \beta \cos\theta)]^{-1} \tag{2.19}$$

where γ is the Lorentz factor, $\beta = v/c$ and θ is the angle between the jet axis and the line-of-sight.

When a source, moving at relativistic speeds approaches the observer, the time intervals measured in the observer's frame, t_{obs} are contracted compared to that observed in the source's frame, t_{src}, such that (290):

$$t_{obs} = \delta^{-1} t_{src} \tag{2.20}$$

The frequency of the emission is blue-shifted in the observer's frame as shown in Equation 2.21:

$$\nu_{obs} = \delta \nu_{src} \tag{2.21}$$

The Doppler factor is also used to relate the intrinsic flux of the source with the observed flux. For a source moving at relativistic speeds, the Doppler factor enhances the specific intensity, I_{obs} (with units J m^{-2} s^{-1} sr^{-1}) through the following relation (270):

$$I_{obs}(\nu_{obs}) = \delta^3 I_{src}(\nu_{src}) \tag{2.22}$$

where I_{src} (with units J m^{-2} s^{-1} sr^{-1}) is the intensity in the source frame, and ν_{obs} and ν_{src} are the Doppler shifted frequency in the observer's frame and the frequency in the rest frame of the source respectively.

The δ^3 term shown in Equation 2.22 is produced from the following transformations between the source and observer's frame (14):

1. The solid angled is transformed into the rest frame of the observer as $d\Omega_{obs} = \delta^{-2} d\Omega_{src}$. This results in the power increasing by a factor of of δ^2 per unit solid angle in the rest frame of the observer thus increasing the intensity by the same power.

2. The frequency of the individual photons are boosted by a factor of δ resulting in the increase of the energy of the observed photon and the intensity, I_{obs} by a factor of δ.

3. The time interval for the arrival of a group of photons is compressed by a factor of δ. This results in the increase in the rate of detected photons and thus the intensity by a factor of δ.

4. The frequency bandwidth in the rest frame of the source increases proportionally with photon frequency (by a factor of δ). This results in the reduction of the intensity (i.e power per unit frequency interval) by a factor of δ^{-1}.

For isotropic emission in the source rest frame and a power-law spectrum of the form $S_{src,\nu} \propto (\nu_{src})^{-\alpha}$, the observed flux density, at a given frequency, $S_{obs,\nu}$ transforms in the same way as the specific intensity (Equation 2.22):

$$S_{obs,\nu}(\nu) = \delta^{3+\alpha} S_{src,\nu}(\nu) \tag{2.23}$$

where δ^α is the ratio of the intrinsic power-law fluxes at the observed and emitted frequencies. Based on Equation 2.23, the broadband fluxes are obtained by integrating over the frequency range, $d\nu_{obs} = \delta d\nu_{src}$, introducing another factor of δ to the observed flux:

$$S_{obs} = \delta^4 S_{src} \tag{2.24}$$

Given the above arguments, the luminosity at the source for a variable emission region moving within the jet, can now be corrected for relativistic beaming effects:

$$L_{src} = S_{obs}\delta^{-4}4\pi D_L^2 \tag{2.25}$$

where L_{src} is the luminosity at the source and D_L is the distance between the observer and the source.

For a source or emission zone moving with a bulk velocity βc, the bulk motion[2] is entirely described by δ as given by Equation 2.19. However, now the Lorentz factor, γ, is represented by Γ which is referred to as the bulk Lorentz factor (312). Both the bulk Lorentz factors and relativistic δ of blazar jets have been estimated at values > 10 or even ~ 50 (41; 159; 105).

Other parameters that are usually included in the modelling of blazar jets are the magnetic field structure and the strength of the field (e.g. (130)) and its implications for the type of models used to describe the jet scenario. In addition, models include the radiating particle energy distribution and the size of the opening angle of the jet (e.g. (184; 160)).

These parameters are varied and constrained based on the model used for different objects or the modelling of a particular event observed from the source, such as flares and outbursts. In the following sections, some of these models are presented and discussed as a description of either the fundamental modes of emission (i.e. the synchrotron and inverse Compton processes) or the relativistic jet as a whole.

2.5.2 Jet Structure and Emission

Relativistic jets from blazars are commonly described as an extended linear structure consisting of plasma which transports energy, momentum and angular momentum (304; 306; 313) and particles from the central engine of the AGN out to kiloparsec (kpc) or even Mpc distances (e.g. (297)). The origin of these jets is still unknown. However, they are

[2]The bulk property refers to the average property (i.e. velocity or Lorentz factor) of the entire emission region (e.g. plasma 'blob') within the relativistic jet as opposed to the property of a single particle which has been used to explain emission processes up to this point.

thought to occur as a result of material being accreted onto a spinning SMBH. These jets are highly collimated and launched at right angles to the spin axis of the SMBH from the core.

The current understanding of these jets is drawn from the fundamental idea of the interaction of plasma with turbulent magnetic fields within the jet environment (334; 295). The orientation of these magnetic fields and the type of interactions which occur, including the activity of the SMBH, determine the type of output that is observed.

The standard jet model was first proposed by Blandford & Rees (307). They described relativistic jets as collimated, gas dynamical flows within which collisionless relativistic plasmas are threaded by a dynamically unimportant magnetic field. These plasmas move at bulk velocities close to the speed of light.

In the standard model (Figure 2.4), assuming that the jet is free, confined only by its own inertia, the visible part of the jet is structured as a cone with an opening half-angle of ψ. The apex of this conical structure is marked R_g and represents the visible core identified in most studies as the VLBI (Very Long Baseline Interferometry) core. VLBI images [3] show that this core is followed by a series of 'knots' (knots are individual emission components as observed in VLBI images. In some cases concerning blazars, these knots move at apparent superluminal velocities[4] due to their relativistic motion with respect to the observer) extending in the direction of the jet and becoming more diffuse the further out they are. It is thought that these knots are formed during the early stages of a shock which occurs close to the VLBI core. The core itself is thought to be highly variable containing the highest density and magnetic field strength of the conic portion of the jet. This causes it to appear stable or stationary with variations occurring in newly created knots (277).

As discussed previously, there is strong evidence for the presence of shocks in jets (305)(see Section 2.4). Within the jet paradigm, these are proposed to be caused by disturbances in the jet flow which cause a shock to form and propagate down the jet, asso-

[3]These images were published using a hybrid mapping technique with results that support the relativistic jet model (39; 277). This initial model was developed in the following years by e.g. Blandford & Koenigl 1979 (262), Reynolds 1982 (309)(276; 263).

[4]The apparent superluminal speeds of knots have been measured to exceed $25c$ using VLBI observations of jet components moving outward from the VLBI core (55; 212; 221). The apparent speed of a jet is an important parameter as it helps place a lower limit on the bulk Lorentz factor (290; 55).

ciating these shocks with the observed superluminal knots (262). Further studies then went on to show that these shocks could reproduce details of the structural, spectral and polarisation variability in blazars (e.g. (277; 258; 249; 183)). These studies further led to the development of shock-in-jet models (see Section 2.6).

Another important feature of the jet is that although predominantly described and understood as linear, jets appear to bend considerably (209; 132). There are several factors which may cause jets to bend. In papers by Hardee (255; 287), the jet-bending phenomenon was described to be caused by macroscopic fluid instabilities. When a beamed jet propagates in a uniform ambient medium, it can be confined and collimated by its cocoon pressure. Any changes in that field, e.g. a non-uniform ambient particle field, will result in an asymmetric cocoon. This may lead to a deflection of the light beam (229; 20; 10). The bending of a jet may affect observational features, such as the changes in multiwavelength variability over time and the apparent superluminal speeds of regions within the jet (277).

Jets are known to be highly variable at all wavelengths, as described in Section 3.2. As discussed above, the jet is composed of a highly turbulent plasma stream (or blobs, depending on the jet model chosen), traversing through the jet at apparent superluminal speeds and interacting with the similarly turbulent magnetic fields. This interaction will cause variations in the intensity of emission produced. In addition, the possibility that the flow of these plasmas will be disturbed by shocks or the injection of new plasma, suggests another cause for the flux variability observed. This fundamental premise forms the basis for multiwavlength monitoring campaigns of blazar sources. Variability observations also allow constraints to be made on the size of the emission region. The smallest constraint that can be placed is determined by the light-crossing time argument. Based on the timescale of the variability observed at any given wavelength, this provides a lower-limit on the parameter space of the emission region. A simple example of this is represented by Equation 2.26 below, which constrains the δR parameter space of the emission region from which the particular wavelength of emission is observed.

$$R \leq \frac{c\Delta t\delta}{1+z} \tag{2.26}$$

Here, c represents the speed of light, Δt is the observed variation in time, δ is the Doppler factor and z is the redshift of the source (see Section 3.2 for further details).

Another aspect of the jet that must be mentioned is the mechanics of the inner jet. This is the region where the collimation of the jet is thought to occur. Begelman, Blandford & Rees (158) discussed that it is more likely that the collimation of the jet occurs close to the central engine, which would also involve the twisting of magnetic fields caused by the differential rotation of the accretion disc, to produce opening angles as small as 1° to 3°. This is because external pressure gradients alone will not result in jet opening angles as small as this (277). The effects of the mechanisms that focus and collimate the inner jet, either through the partial contribution of pressure gradients or a magnetic dynamo mechanism (273; 334; 277) will eventually determine the acceleration mechanism of the particles streaming down the jet (e.g. (277)).

The next important factor that must be recognised is the type of radiation that might be produced by the inner jet. If particle acceleration processes occur in regions closest to the central engine, this will lead to the synchrotron emission (i.e. UV, optical and IR radiation) being produced in these same regions (e.g. (276; 309; 97; 40; 147)). In this region, the highest energy electrons will emit only at lower frequencies, due to radiative and adiabatic losses. It must be noted, however, that observations of the inner regions of the jet are limited by frequency-dependent synchrotron opacities due to synchrotron self-absorption processes[5]. Synchrotron opacity causes synchrotron emission produced in the inner jet to be observed further downstream, rather than in its actual production site (262; 36). This will be discussed further in Section 3.6.1.

Next, the higher energy emission (i.e X-ray and γ-ray emission), often considered to occur as a result of the inverse Comptonisation of UV and optical photons, can be considered in the regions of the inner jet. Dermer, Schlickeiser & Mastichiadis (57), Begelman & Sikora (317) and Melia & Koenigl (264) suggested that inverse Compton reflection of optical and UV photons from the accretion disc takes place in the synchrotron emission region of the inner jet. This will produce γ-rays in the deepest region followed by X-rays further downstream of the inner jet. Even further downstream will see the occurrence of the non-thermal optical and radio emissions as a result of the delay caused by synchrotron self-absorption processes. An example of this structure can be seen in Figure 2.4.

[5]Synchrotron self-absorption is the absorption of photons by relativistic electrons in a magnetic field. This process is dependent on photon frequency such that the opacity due to synchrotron self-absorption rapidly increases with decreasing frequency.

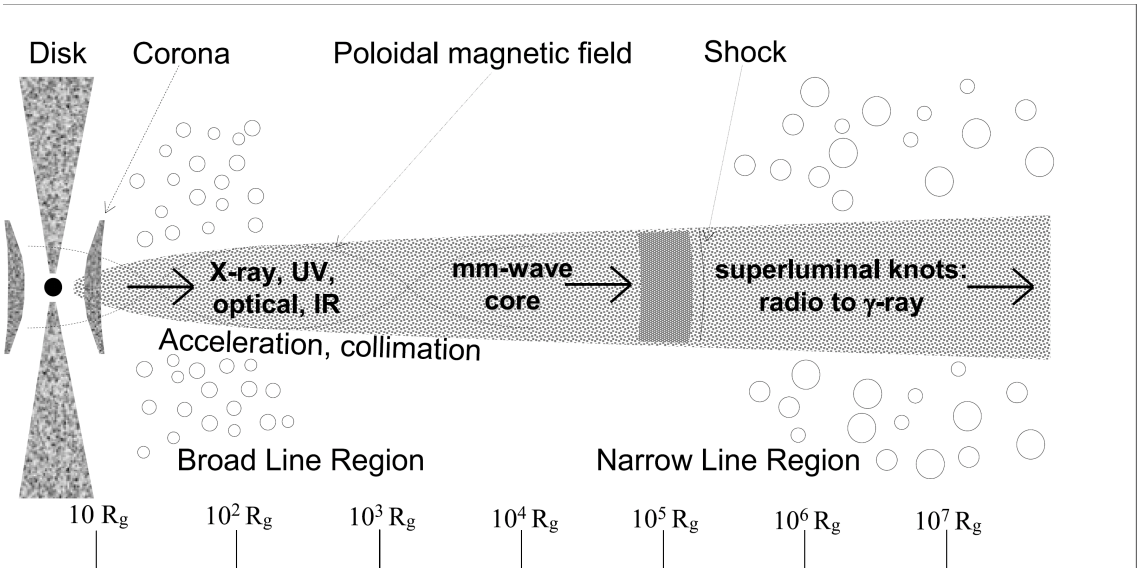

Figure 2.4: Schematic of a quasar jet and regions from which emission at different wavebands is thought to originate. R_g represents the gravitational or Schwarzschild radius of the SMBH ($R_g \sim \frac{GM}{c^2}$, where G is the gravitational constant, M is the mass of the SMBH, and c is the speed of light). For an SMBH of $\sim 10^9$ solar masses, R_g is estimated at $\sim 5 \times 10^{-5}$ pc. The scale in the figure is logarithmic beyond 10 R_g. At distances of 10^3 R_g, the jets become visible at radio wavelengths. The broad line region (BLR) typically lies within the sub-parsec region of the jet, while the NLR regions lie at distances > 1 pc (286). It must be noted that other jet models exist which place the location of the γ-ray emission region closer to the central engine (16; 208). Image based on the schematic adapted from Marscher 2005 (278) and Lobanov 2007 (271). Image credit Karouzos et al. (169).

While several models exist for the structure and dynamical properties of the relativistic jets, there is much that still remains unknown. For instance, do the emission regions producing the higher and lower frequency flux coincide? Does the same mechanism that produces the higher energy emission produce the lower energy emission? Are there contributions from regions external to the jet? All these questions require extensive and comprehensive research into all aspects of the blazar jet. First, the theoretical platforms can be considered and following this, observational evidence which will then support or place further constrains on the parameters used to model these properties. In the following section, some of these properties will be explored in order to outline a basic

understanding of how jets are described and studied.

2.6 Emission Models

Emission models can be loosely sub-categorised into two classes, leptonic models and hadronic models. Leptonic models are currently the most widely held scenario in describing blazar physics due to their efficacy in fitting blazar broadband multiwavelength observations. The general premise for modelling blazar emission stems from the composition of the jet material interacting with the photon and magnetic fields present within the jet. It is generally accepted that the low-energy component is attributed to synchrotron emission from relativistic electrons and positrons. The origin of the high-energy component however is still uncertain. Both leptonic and hadronic scenarios have been used to explain the high-energy component based on jet composition (308). In the following sections, both these scenarios will be presented and discussed with a greater emphasis given to leptonic scenarios as they are currently more favoured in the literature.

Other models involve determining the type and extent of emission zones within the relativistic jet. These begin with homogeneous single-zone SSC models as well as the more recent multi-zone emission models. Both of these and their variations rely on leptonic scenarios. However, it must be noted that there are hadronic models which are sometimes invoked to describe a certain blazar behaviour (e.g. orphan flares (217)) and these models cannot be fully discounted. The reason leptonic scenarios are favoured compared to their hadronic counterparts is that it is easier to accelerate electrons to relativistic energies compared to protons.

2.6.1 The Synchrotron Self-Compton (SSC) Model

In this model, the population of relativistic electrons which produces the synchrotron photons then up-scatter the same photons to higher energies via the inverse Compton process. Emissivity by synchrotron radiation is linearly dependent on the electron distribution (i.e. the electron number density), such that for a given magnetic field strength, the synchrotron flux (S_{syn}) is proportional to the electron number density (n_e), $S \propto n_e$. The flux of the inverse Compton process (S_{IC}) is proportional to the product of the syn-

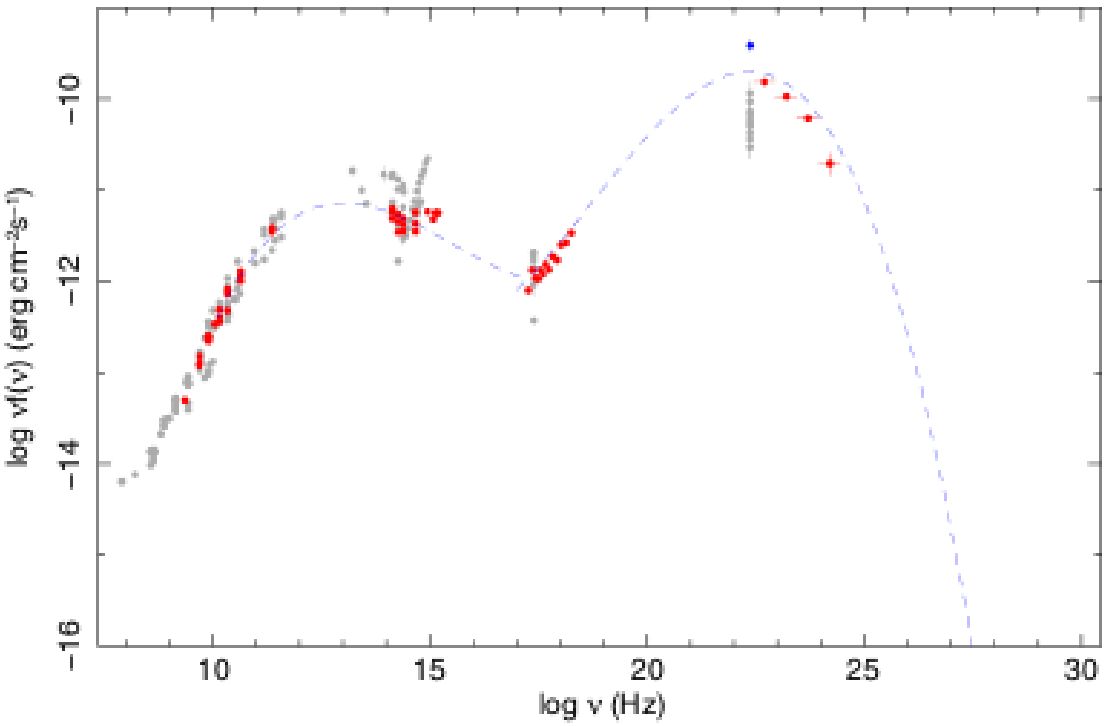

Figure 2.5: The SED of PKS 1510-089 (an FSRQ) showing two broad peaks. The lower energy peak represents the synchrotron emission while the higher energy peak is attributed to the IC process. The source of the seed photons which are upscattered (often up to TeV energies) is a subject of great interest especially in the development of emission models. Image credit (29).

chrotron flux and the electron number density, $S_{IC} \propto n_e S_{syn}$. Thus, the flux due to the inverse Compton upscattering depends on the square of the synchrotron flux, $S_{IC} \propto S_{syn}^2$. Thus a small change in the electron number density within a certain volume or the synchrotron flux will result in a considerable increase in the inverse Compton flux.

The ratio of the radiation losses due to the inverse Compton and synchrotron processes, η can be described as follows:

$$\eta = \frac{\left(\frac{dE}{dt}\right)_{IC}}{\left(\frac{dE}{dt}\right)_{sync}} \tag{2.27}$$

$$\eta = \frac{U_{photon}}{\left(\frac{B^2}{2\mu_\circ}\right)} \tag{2.28}$$

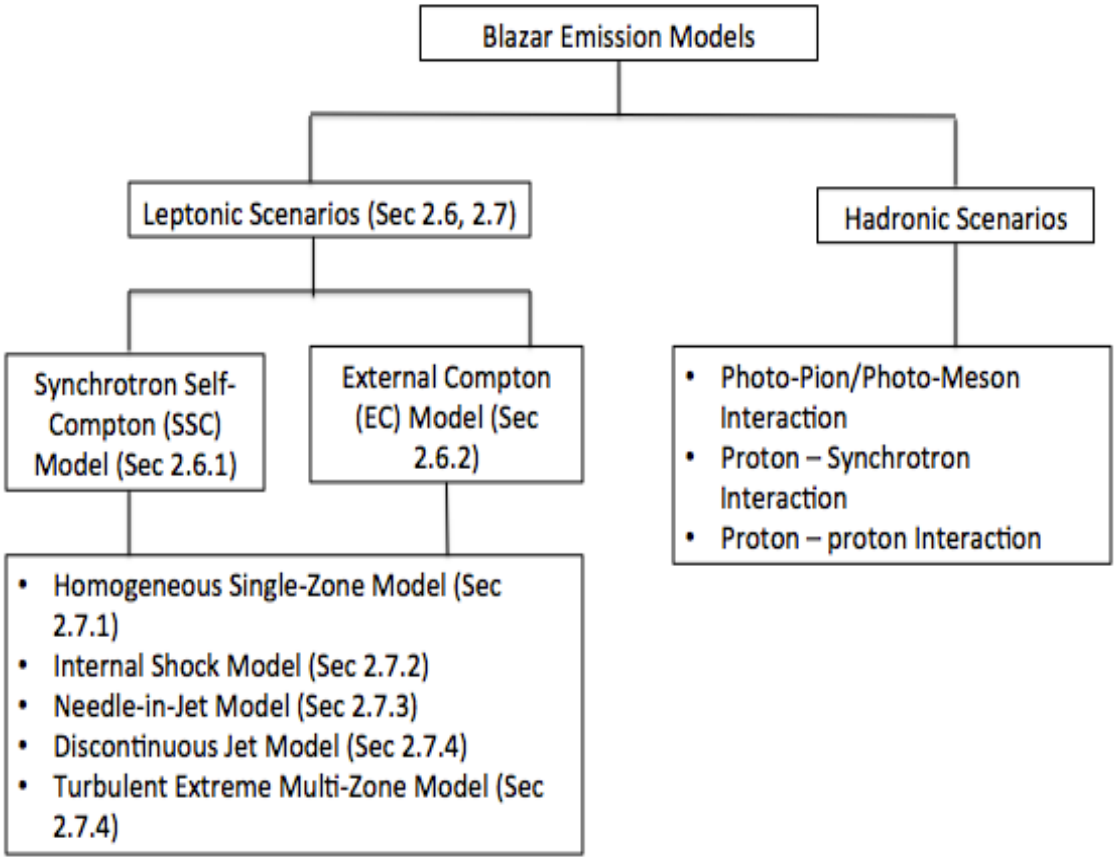

Figure 2.6: A comprehensive summary of the leptonic emission models used to model blazar multiwavelength observations based on the blazar SEDs and the composition of jet material. Although not discussed in this thesis, some examples of the hadronic emission framework are given based on reviews of hadronic scenarios found in Reimer (308) and Boettcher (13).

where U_{photon} is the energy density of the photon field and $\frac{B^2}{2\mu_\circ}$ is the energy density of the magnetic field. For $\eta > 1$, the energy density of the inverse Compton photons is greater than that of the synchrotron photons, in which case the electrons undergo greater losses by scattering x-ray photons to γ-ray energies. Thus, in order to maintain the energy output of the source, the electrons must be constantly accelerated perhaps under the influence of diffusive shocks or varying magnetic fields (see Section 2.4).

This model makes a very important prediction. Since the population of synchrotron photons is bumped up to higher energies by the population of electrons which has produced them, then the inverse Compton emission must in some way reflect the syn-

chrotron emission spectrum. The way to determine this is by using multiwavelength variability studies (see Chapter 3). In other words, variability in the synchrotron aspect of the blazar emission should lead to a similar variability in the inverse Compton aspect of the emission. Although the timescales of the emission might vary, the general features of the wavelength specific emission should reflect similar characteristics.

The synchrotron self-Compton process would result in a smooth broadband spectrum. This is primarily due to the fact that the synchrotron seed photon field has a broad distribution in energy. Thus, there is a wide range of combinations of seed photon energy and electron energy which can produce the IC photons. It must be noted that, towards high energies, the Klein-Nishina effects dominate and inverse Compton scattering is gradually suppressed. However, in the Thomson regime, the peak of the synchrotron spectrum, $\epsilon^{obs}_{sy,pk}$ can be directly related to the peak of the inverse Compton spectrum, $\epsilon^{obs}_{IC,pk}$ such that:

$$\epsilon^{obs}_{IC,pk} \sim \epsilon^{obs}_{sy,pk}\gamma^2 \tag{2.29}$$

where γ is the bulk Lorentz factor.

It must be noted however, that there is evidence which challenges this simple view. Recent observations show complex correlation patterns between VHE and emission at lower frequencies. Also observations of 'orphan' VHE flares with no associated increase in the synchrotron X-ray emission, contradicting the second prediction, and the presence of flux variability on very short timescales (hours or less) motivate a closer look into the emission mechanisms of blazar jets (86; 168; 85; 49), and in particular the formulation of the external Compton model and modifications to the simple SSC model.

2.6.2 The External Compton Model

In the external Compton (EC) model, instead of the seed photons being sourced from the synchrotron process, the seed photons are sourced externally. This model was first proposed by Begelmen & Sikora (317) in 1987.

The model varies from the SSC only by the source of the population of seed photons producing the synchrotron and IC emission. Both the SSC and EC models are built upon the same premise, in that they require a relativistic, non-thermal population of electrons to produce synchrotron photons responsible for the lower energy peak. The second peak

is again an effect of inverse Comptonisation by the same electrons, only this time the seed photons which are Comptonised are sourced external to the jet.

There are many thoughts on where these secondary seed photons originate from. The more widely accepted of these are thermal photons from the accretion disc (173)(57)(314), thermal radiation from the dusty torus (281), disc radiation reprocessed by the broad line clouds (173; 269) or by wind photo-ionisation of the accretion disc (173)(65). Later models by Georganopoulos & Kazanas (260), Ghisellini, Tavecchio & Chiaberge (322) and Ghisellini & Tavecchio (323) have suggested that emission from a slowed-down outer layer of the jet may be inverse Compton-scattered by the relativistic electrons in the more active inner regions of the jet.

An important aspect of radiation fields external to the jet is the transformation of the external radiation field into the emission region rest-frame (i.e. the jet). This will affect the result of the EC peak emission. When the external radiation field enters the jet, the radiation is either red-shifted or blue-shifted in the rest frame of the emission region, depending upon the direction of the EC radiation field with respect to the emission region. This aspect of the transformation becomes crucial when the EC radiation field goes from either the Thomson to the K-N regime or vice versa, affecting the number of interactions which may occur (see Section 2.1.2). Another feature that must also be accounted for is the change in the energy density of the external radiation fields when it enters the jet region. As an external radiation field enters the jet, the energy density of the field may be increased or decreased depending on the angle between the external radiation field and the jet axis. A detailed explanation of the transformations and the resulting Compton spectra from external radiation fields can be found in Dermer & Menon (283). In order to test the EC model, we expect that there will be a correlation between a rise in the seed photon flux and that of the VHE flux e.g. (65)(245). The type of correlation observed will be more complex than if it was produced following the SSC model.

It is suspected that both the SSC and EC models contribute to the overall broadband SED with one process dominating the other. As discussed earlier, the energy losses for an electron undergoing synchrotron/IC emission differ from each other by the magnitude of the radiation field energy densities. Assuming that the energy lost in the interaction is in effect the power of the radiation emitted, the dominant mechanism can be determined by considering the ratio $\frac{U_{mag}}{U_{rad}}$ (303)(137). If U_{mag} is greater than U_{rad}, then the SSC model

becomes the dominant mode of emission. The EC mode dominates when U_{rad} is greater than U_{mag}.

In addition to the SSC and EC scenarios, there are several other emission models that have been developed either to explain a particular blazar phenomenon, to account for the broadband blazar emission or light curve variability. A general review of these will be discussed in the following sections.

2.7 Extension to the Basic Leptonic Scenarios

While the SSC scenario is more easily tested, the more realistic consideration for the multiwavelength emission of blazars is far more complex. The complex and intricate structure of the relativistic jet and spatial regions of the particle population would result in a good probability of there being more than one contribution to the jet emission.

While both the synchrotron self-Compton and External Compton scenarios provide a basic model for blazar emission, numerous multiwavelength monitoring campaigns and investigations into blazar behaviour have shown that this view might not be the most accurate. Often, the blazar lightcurves or emission spectra have complex features calling for extensions to the basic model. Both the SSC and EC platforms including models of the jet structure suggest that there must be some underlying correlation between the synchrotron and IC emission of blazar sources (see Section 2.5). However, the strength of this correlation, the nature of the time lag observed between multi-wavelength observations suggest a more complex emission process. This has led to the development of different scenarios, including multi-component jet scenarios, which are developed and tested under the framework of either the SSC or EC scenarios. In the following sections, some of these models are discussed.

Multi-Zone Models

Multi-zone models are generally built on the understanding that the jet might be made up of various 'emission regions'. These regions contain the plasma that produces the observed radiation. Emission regions can take on various sizes and features and models are proposed based on the characteristic feature of these emission regions.

In this section, some of these models will be presented along with the framework

upon which they were built. The observational aspect of the study will also be explained.

2.7.1 The Homogeneous Single Zone SSC Model (Paggi et al. 2009 (49))

This involves the specific modelling of BL Lac SEDs based on the homogeneous single zone synchrotron self-Compton (HMZ SSC) model. The main goal of the study was to predict correlations in the γ-ray regime with variabilities observed at optical to X-ray energies, using SSC modelled parameters. A log-parabolic distribution of relativistic electrons was assumed as it provided a more accurate fit in the optical and X-ray bands and uniformly low residuals throughout a wide energy range (e.g. (206)(76)(64)(77)).

In general, it is thought that variations in the SED flux occur due to changes within the emitting region (see Chapter 3). The kinematics of each region rely on 'source parameters'[6] and the particle acceleration process (e.g. whether interactions occur in either the Thompson or the K-N regimes) present in that region.

The HSZ SSC model was able to reproduce the SEDs from LBLs and IBLs within the Thompson regime and HBLs within the Klein-Nishina regime. γ-ray variability was attributed to dominant root-mean-square particle energy variations and magnetic field changes. This was similar to the conclusion drawn by Marscher et. al. (48), ascribing the overall spectral variability to fluctuations in the magnetic field strength and particle densities at the base of the jet, possibly due to instabilities in the magnetic field of the accretion disc. This was also described a possible cause of superluminal knots (48).

It was also noted that the model worked for general flares but was unable to reproduce fast/strong flares in the TeV range which require a sudden acceleration of emitting electrons. Possible alternatives involve more elaborate scenarios such as decelerated relativistic outflows or sub-jet scenarios (250)(251)(67).

2.7.2 Internal Shock-in-Jet Models (Spada et al. 2001) (174)

In 2001, Spada et al. (174) introduced the 'internal shock scenario' in which shocks in jets are formed by a random collision of accelerating shells of plasma with different masses, energies and velocities. By simulating the evolution of shells within a jet, from birth to

[6]The source parameters include the size of the emission region (which are wavelength dependent, see Chapter 3), the magnetic field strength, the Doppler factor ($\delta \sim 10 - 50$ (41; 159)) and the number density of particles within the emitting region.

propagation and finally collision (e.g. Figure 2.7), the authors construct the overall spectral energy distribution along with the time dependent spectra and light curves. Further analysis includes characterising the predicted variability at any frequency, studying the correlations between emission at different frequencies and specifying the contribution of each region of the jet to the total emission. This final aspect was adopted in many later papers, e.g. (151). This study also sought to find correlations between flares at high energies and the birth of superluminal knots, a factor central to an observational paper discussed in the following section (48)(213).

The model proposed by Spada et. al. 2001 was qualitatively compared to the properties of 3C 279 resulting in the conclusion that there exists a global agreement in terms of the spectra and temporal evolution. However further work was necessary in order to further investigate constraints of this model. This will include studies into the onset of superluminal knots and/or radio flares and the propagation and dissipation of the jet on larger pc scales.

2.7.3 Needle-in-Jet Scenario (Ghisellini & Tavecchio 2008) (323)

For the particular case of PKS 2155-304, Ghisellini & Tavecchio (323) investigate the rapid variability of PKS 2155-304 during an overall active state of the source showing variability on timescales of three to five minutes. In order to accommodate this ultrafast variability, the authors critically analyse the implications of emitting regions with a very high Bulk Lorentz Factors, $\Gamma \sim 50$. The aim of the paper was to assume this Γ existed within an emitting region as small as 3×10^{14} cm, in order to reproduce variability timescales of 200 seconds. This was applied to the accepted one zone-SSC, EC and needle-in-jet models. Parameter model fits show that the most favourable model is the needle-in-jet scenario suggesting that there are small active regions or 'needles' of matter inside a larger jet, oriented in different directions, moving faster than the rest of the plasma and occasionally pointing to the observer, leading to rapid variability. Another scenario would be that the emitting regions are 'shells' corresponding to an intermittent activity of the central engine much like the internal shock model proposed by Spada et. al. (174).

The authors go on to suggest that simultaneous observations in the UV-X-ray and TeV bands would help distinguish between the SSC, EC and needle-in-jet scenarios. If observations show simultaneous variability within these bands, the needle-in-jet model

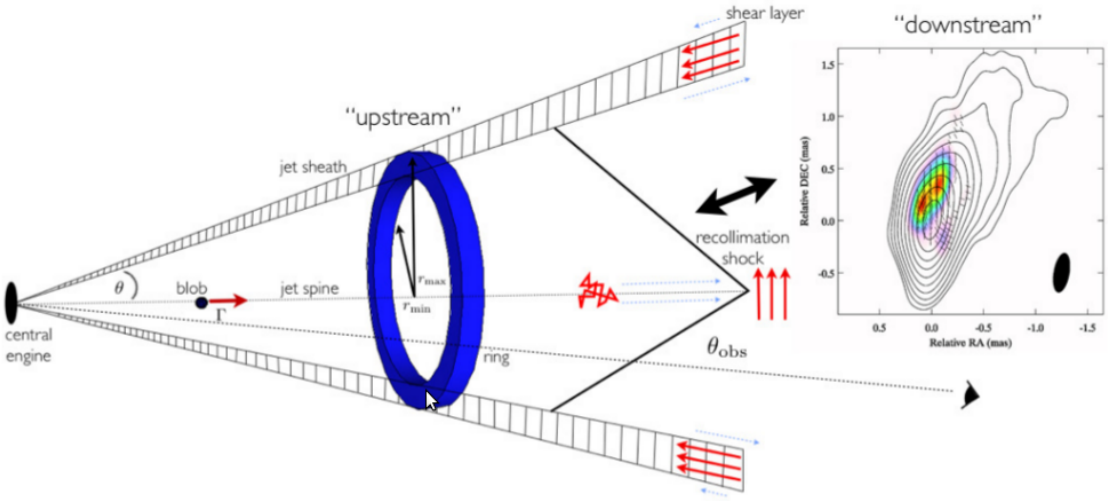

Figure 2.7: Schematic of the internal shock-in-jet model based on a shocked sheath plasma ring (blue ring) along with the location of the radio core shown by the 'downstream' diagram of stacked radio images of PKS 1510-089. Based on the model proposed by MacDonald et al. (182), the ring is located at a distance of ~ 4 pc from the central engine, while the radio core is located at a scale of 10 pc from the central engine. Based on the model, the radio core, thought to be associated with a recollimation shock, orders the tangled magnetic field (given in red between the ring and the radio core) to be oriented perpendicular to the jet (red arrows located to the right of the recollimation shock). The blue arrows denote relative velocity vectors causing velocity shear between the sheath and ambient medium. This then aligns magnetic field lines on the outer edges of the jet to be approximately parallel to the jet axis, resulting in the spine-sheath polarisation. Image credit MacDonald et al. (182).

is favoured indicating that the X-rays and UV rays are being produced by the entire jet while the TeV flux could be originating from the 'needle' component.

2.7.4 Discontinuous Jet Model (Blobs-in-Jet Scenario) (e.g. Rachen et al 2010) (137)

This discontinuous jet model describes blazar jets as a series of discontinuous blobs, referred to as plasmons, and models how they evolve with time and distance to finally form a continuous jet flow at larger scales.

The motivation behind this particular model was to accommodate instabilities in the

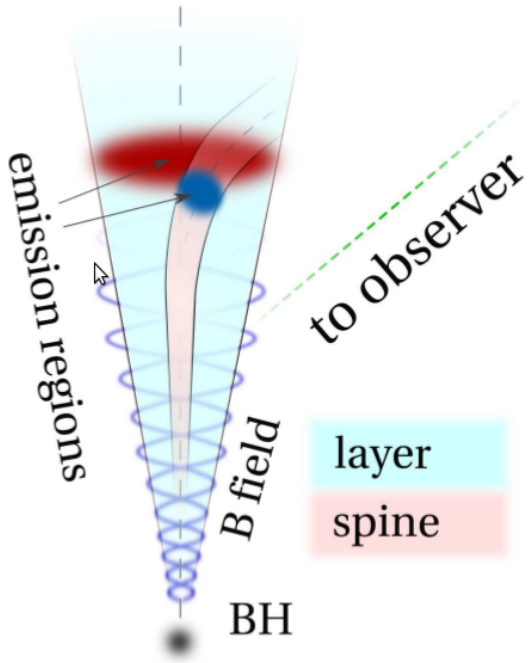

Figure 2.8: Schematic of the needle-in-jet model also referred to as a spine-sheath model. The needle-in-jet scenario suggests that the jet geometry is made of a faster, wiggling 'needle' region and a slower moving outer layer surrounding the needle. Image credit Janiak et al. (167).

highly relativistic regions close to accreting black holes. The jet starts off as a series of plasma blobs created near the black hole (see Figure 2.9). The blobs, being unconfined, begin to expand in all directions. This leads to an opening angle of the discontinuous jet. At this stage, when relativistic gas dominates the pressure, the expansion decreases with distance from the black hole leading to an apparent collimation of the jet. The process continues assuming conical expansion and eventually merges into a continuous jet after the expansion has filled up the gaps between them.

This model was fitted to radio data between 2.7 GHz and 43 GHz along with data from the Submillimeter Array at 230 GHz and 345 GHz for the 2005/06 flare of 3C 454.3. Results show that the temporal evolution of the flare was represented very well with slight discrepancies at higher energies. It was indicated that data at frequencies greater than 350 GHz ($\sim 860\ \mu$m would help further constrain the parameters used in this model.

A vital aspect of this model is the suggestion that collisions between plasmons of various energies cause the production of shocks over a range of scales, existing only

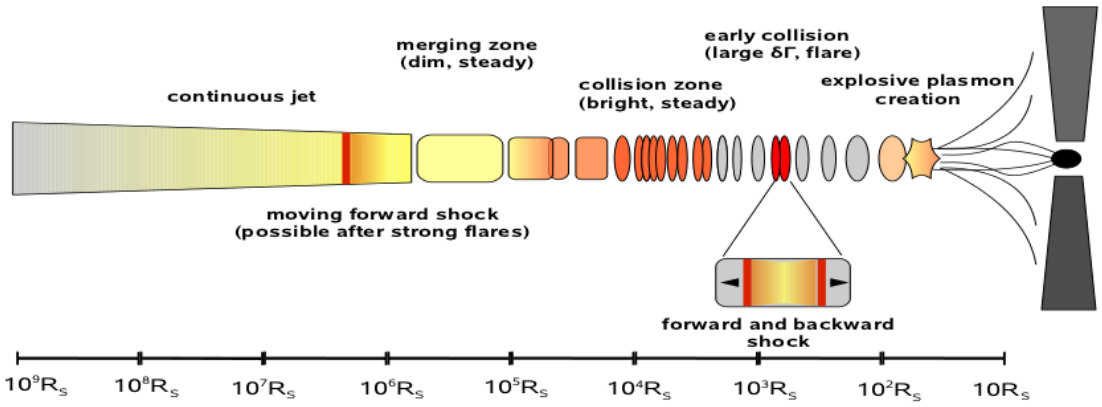

Figure 2.9: Schematic of the discontinuous jet model developed by Rachen et al. (137) which depicts that the jet begins as a series of blobs known as plasmons (137).

temporarily. This is similar to the idea presented in an earlier paper by Ghisellini & Tavecchio (323). This provides further evidence for a multi-zone emission model within the SSC/EC framework. Marscher (279; 280), on the other hand, proposed the idea of a Turbulent Extreme Multi-Zone (TEMZ) model, which is an extension of both the blob-in-jet and discontinuous jet scenarios. In the TEMZ model, the jet is modelled as a structure with many individual turbulent cells. A plasma, with its own magnetic field and relativistic electrons (and positrons, if any), move through each the turbulent cells, which in turn introduces a turbulent component to the injected plasma affecting its speed and direction. This model was developed to account for the rapid variability observed in blazar spectra and produce more accurate calculations compared to models with significantly fewer emission zones (280)(see Figure 2.10). It was noted, however, that this model failed to reproduce the ratio of the γ-ray to X-ray luminosities observed in major blazar outbursts (44).

Another aspect of importance is the necessity for sub-mm data in tandem with γ-ray observations for the discontinuous jet model. This paper (280), unlike the previous internal shock model by Spada et. al. (174) which accounts for the production of γ-rays and rapidly varying light curves, instead only focusses on the radio/sub-mm regime. Although the general temporal evolution of the flare agrees with observation, discrepancies exist in the model at very high energies. This provides strong motivation for quasi-simultaneous HE γ-rays/(sub-)mm study.

In summary, we note the importance of an extension to the simple SSC/EC scenarios

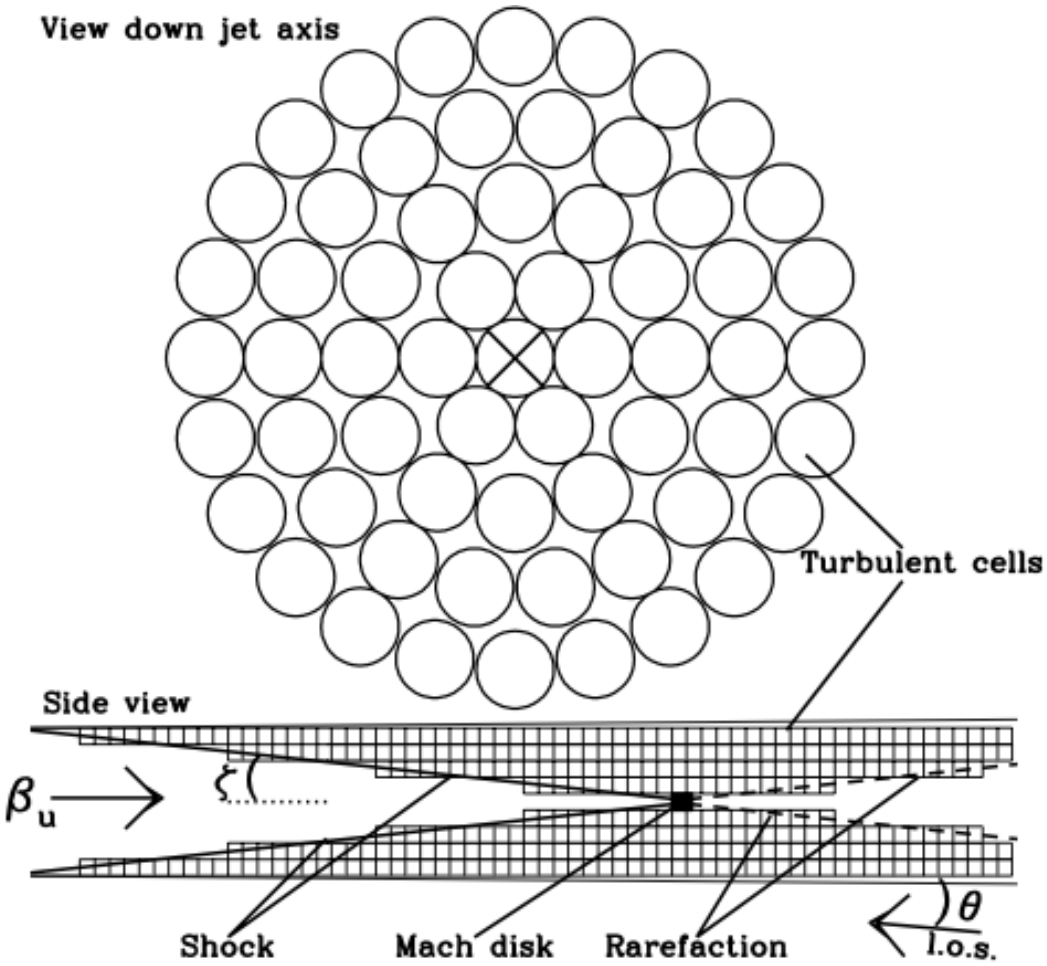

Figure 2.10: Schematic of the discontinuous jet model developed by Marscher (279; 280) which depicts a single plasma blob, with its own magnetic field and population of relativistic electrons moving through a jet comprising of individual turbulent cells. The turbulent cells affect the injected plasma by inducing a turbulent component to its speed and direction (280).

to explain the rapid variability and flaring activity observed at TeV energies. Theoretically, it is clear that a more complex model is required to explain blazar properties. Thus, we set our sights on a coordinated long-term multiwavelength observational strategy in an attempt to further discriminate between the various scenarios.

2.8 Hadronic Emission Models

As discussed in the beginning of Section 2.6, emission models are developed based on the composition of the jet material involved in producing the emission seen in blazar SEDs. While leptonic scenarios rely on relativistic electrons and positrons producing the synchrotron and inverse Compton emission either through the SSC or EC models, hadronic scenarios are based on the premise that relativistic protons and electrons are both involved in producing the high energy component of the SED. Blazar jets are known to be electrically neutral (308), suggesting that if part the energy in the jet is used to accelerate protons to relativistic speeds, there will be a hadronic contribution to the blazar emission spectrum. It is generally understood that both hadronic and leptonic scenarios play a role in producing the broadband SED observed from blazars. However, it is vital to determine which of these two scenarios dominate the spectrum.

Some of the more common hadronic scenarios are shown below based on three different types of interactions:

- between protons and photon fields, described in photo-pion models
- between protons and magnetic fields, invoked in proton-synchrotron models
- between protons and ambient matter

While hadronic processes form an aspect of the blazar emission scenario, the work presented in this thesis will only consider variations of leptonic models. As such, details of the hadronic framework will not be described in this thesis.

A complete review of the different hadronic emission models of blazars can be found in Boettcher (12) and Reimer (308).

Chapter 3

Blazar Multiwavelength Campaigns

3.1 Blazar Multiwavelength Studies

In this chapter, the motivation behind multiwavelength campaigns on blazars is discussed in detail.

Multiwavelength studies offer a wealth of information which can be used to explore various aspect of blazars, from the types of emission mechanisms involved in producing the extreme characteristics typical of blazars to the physical geometry of the jet. Extensive multiwavelength campaigns are used to investigate blazar jet properties including variability timescales, duty cycles, correlation studies between different wavelength regimes, and the temporal evolution of emission states produced by the dynamic emission of the jet as well.

Multiwavelength studies may also be used to distinguish between current blazar jet emission models (see Section 2.6 for a discussion of the current blazar jet framework). They also provide information which further improves constraints on model parameters such as Doppler factors, δ, bulk Lorentz factors, Γ, and magnetic field strengths, B. Improvements on these constraints could refine these emission models and further pave the path to a better understanding of the dominant factors which lead to the complex emission patterns observed from blazars.

An important aspect of multiwavelength studies is the search for correlation between multiple spectral wavebands. For example, as described in Section 2.6.1, a strong correlation between the wavebands attributed to the synchrotron and IC emission would suggest that SSC processes dominate emission within the jet, whereas a lack of correlation would suggest that EC processes dominate. Alternatively, a lack of correlation could also

suggest that emission at different wavebands is not co-spatial and a multi-zone model would be appropriate. If evidence of correlation exists, any time-delay between emission events at different energies suggests that the emission regions are separated from each other, and the disturbance propagating along the jet may cause an increase in flux in a particular waveband.

The variability and temporal evolution of emission states as well as multiwavelength correlation properties will be explored as part of the research conducted in this thesis.

3.2 Variability Studies

The variability of a particular source can be broadly described as the difference in the flux output of the source over a given period of time. Blazars are known to be highly variable sources, often exhibiting variability from radio to VHE γ-ray wavelengths, where variability at longer wavelengths is observed to occur on much longer timescales than that at higher energies. The reason for this can be understood in terms of how emission occurs within the relativistic jet. Within the jet paradigm described in Section 2.5, relativistic electrons are accelerated in the region of the inner jet, producing emission in the optical, IR and UV energies. It is thought that seed photons from this process are then upscattered to higher energies, i.e. X-rays and γ-rays, through the inverse Compton process, with X-ray emission occurring further down the jet from γ-ray emission. As the electrons move along the jet, radiative and adiabatic losses cause the particles to lose energy. This can explain the longer variability timescales at longer radio wavelengths (277).

Blazars are known for exhibiting variability on very short (hours to minutes) to very long timescales (years) (156). This variability is an intrinsic feature of the jet observed due to its alignment to the line-of-sight of the observer (see Section 2.5.1).

Variability studies bring two primary properties to light, as follows:

- The nature of the intrinsic properties of blazar jets (e.g. flares, outbursts and high states)

- Size of the emission region

3.2.1 Intrinsic Properties of Blazars: The Different Emission States

Multiwavelength variability studies of blazars produce fairly complex light curves due to the extreme nature of these sources. These light curves, varying on different timescales at different wavelengths, are used to infer the intrinsic properties of the jet based on the the different emission states present. Emission states, typically characterised as flares, outbursts, high states and flickering, are generally defined based on flux variability timescales and amplitudes. However, due to the nature of variability timescales which are dependent on the wavelength of observations, it is particularly challenging to define the emission states in general terms as to be applicable to all wavelength regimes simultaneously. Most studies on blazars indicate that emission at higher wavelengths varies on shorter timescales compared to emission at longer wavelengths (326). This would mean that flux doubling timescales, which are generally used to define flares, would be shorter at higher frequencies compared to that of lower frequencies. While this would not be a problem when comparing flux varying times and the different emission states between different epochs at a particular wavelength, it will not apply when comparing emission states between two different wavelengths (e.g. the γ-ray regime with the optical regime or the γ-ray regime with the (sub-)mm regime). Thus, due to the dependence of the variability timescale on the observational frequency, a specific definition of each emission state as it applies to the wavelength of emission will be given separately for γ-ray observations and (sub-)mm observations in this thesis (see Section 6.3 for a definition of states in the (sub-)mm waveband and Section 7.1 for a definition of states in the γ-ray waveband).

Another important emission state which sets the baseline for all other emission states and must thus be defined in accordance with them is the quiescent state. In broad terms, this is the period in which the source is at its lowest flux levels without exhibiting any significant activity. A quiescent state may typically involve flickering which is broadly defined as low-level flux variability, i.e. the flux increases and decreases on short timescales without doubling in amplitude.

In the following sections, the overall features of each emission state will be discussed.

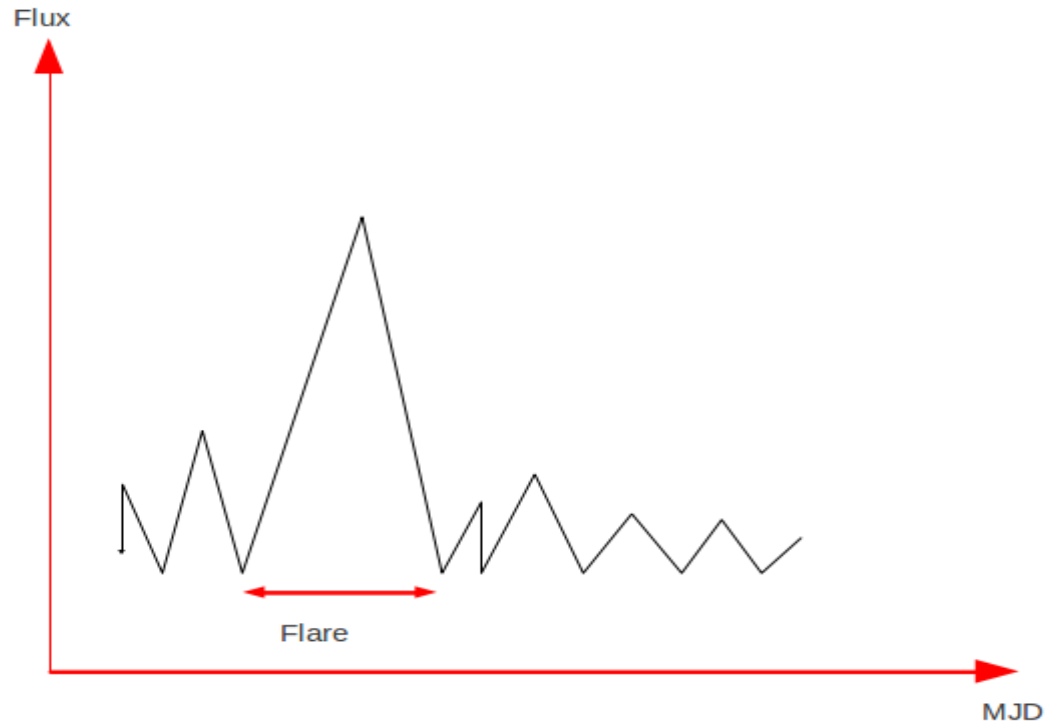

Figure 3.1: Schematic of a flare.

Flare

A flare is typically described as a rapid increase in flux, typically quantified by a doubling timescale (which is the time period it takes for the flux to double at the onset of the flare) (Figure 3.1). Flares can be observed occurring independently or in conjunction with an outburst during which flares may occur recurrently. Flares typically have a definitive structure given by an onset phase in which flux levels rapidly double or triple, a peak in which flux levels reach a maximum and a decay phase which follows the peak. While the timescales of each flare may vary from one to another at a particular wavelength, flares at higher frequencies tend to have shorter lifetimes compared to flares observed at lower frequencies. It can also be observed that at higher frequencies, the rising time of the flare (i.e. between the onset and the peak of the flare) is usually similar to the decay timescales. This is not the case at lower frequencies in which rising timescales are much shorter than the decay timescales of the flare. This trend in the rise and decay timescales is also observed for the case of an outburst.

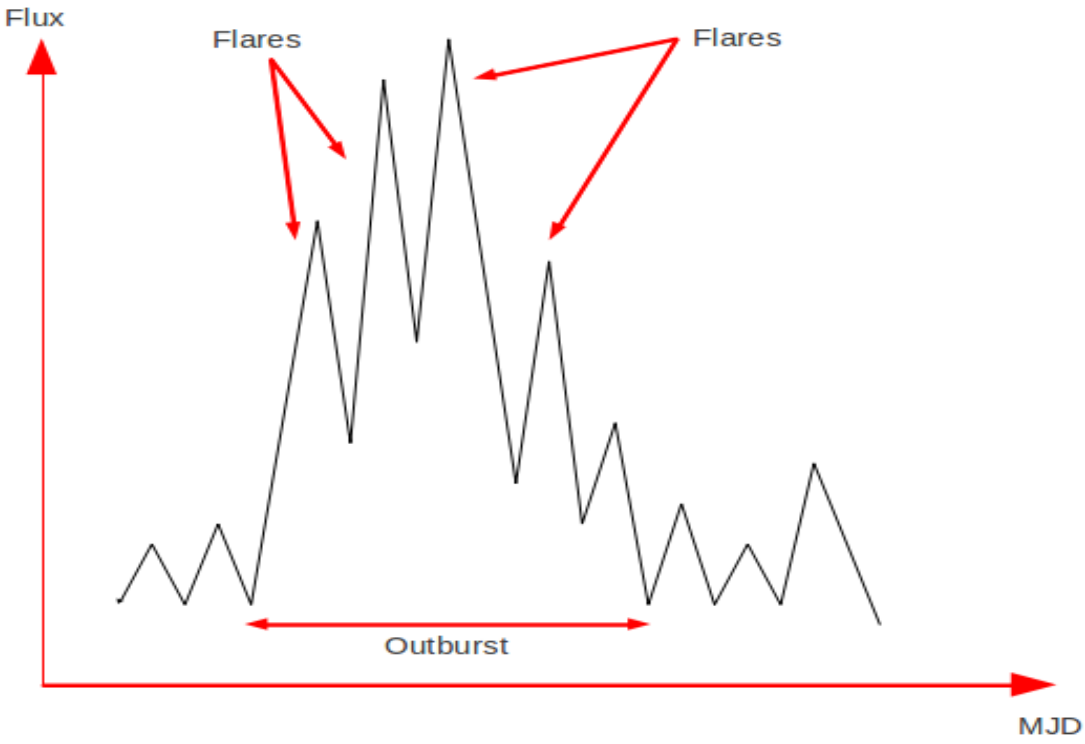

Figure 3.2: Schematic of an outburst.

Outburst

An outburst is defined as a period of intense activity where the onset is marked by a rapid increase in flux (often doubling or tripling) followed by the occurrence of several consecutive flares (see Figure 3.2). These flares may be superposed, such that the subsequent flare begins before the initial flare subsides.

High State

High states are generally defined as periods of subdued activity such that the flux rises gradually (as opposed to the rapid doubling timescales of the onset of a flare) to levels which are double or triple the quiescent level flux, and plateaus at this level for a given duration (see Figure 3.3). During this plateau phase, the flux may flicker (see Figure 3.4), or remain without significant flux variability until the flux levels gradually fall back to quiescence or begin to rise into a flare or outburst. High states may mark the beginning or end of an outburst. It must be noted that high states are particularly challenging to quantify and compare in terms of variability timescales and amplitudes.

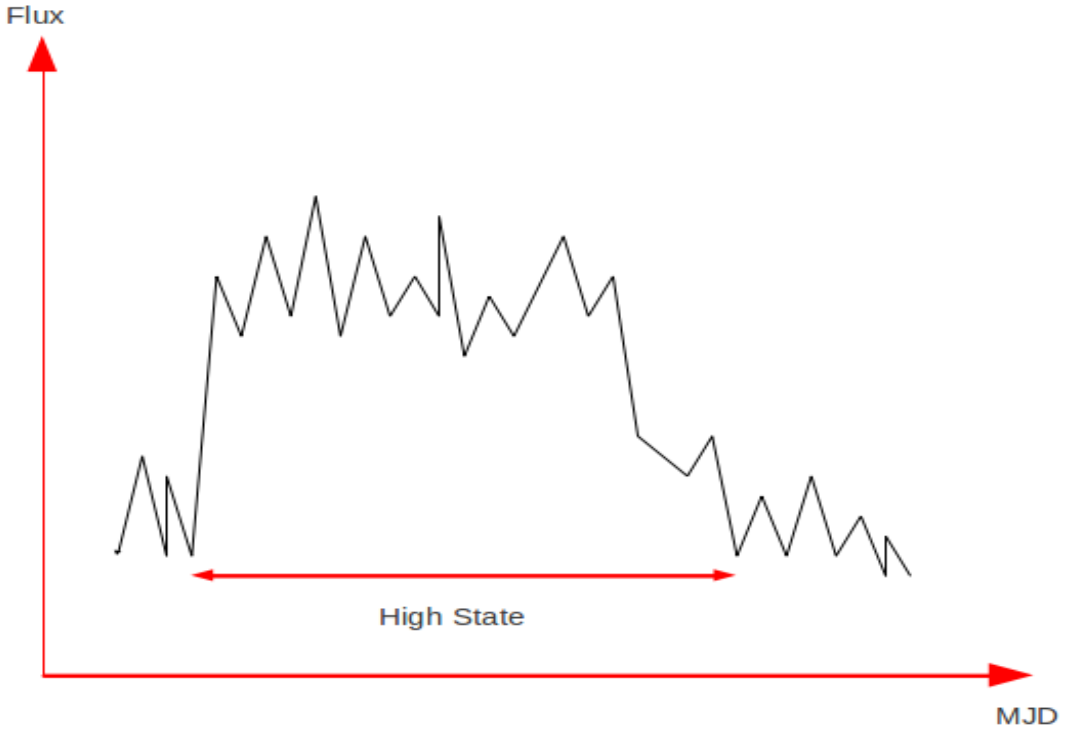

Figure 3.3: Schematic of a high state.

This is due to the difference in timescales at different wavelengths. For example, a high state observed in the γ-ray regime may well be a flare in the (sub-)mm regime, since the doubling timescales of the flare in the lower energy bands are much longer compared to the doubling timescales observed in the higher energy bands. Thus, caution must be exercised when defining and comparing high states between different emission bands.

3.2.2 The Physical Significance of Variability and Emission States

The different emission states can be interpreted as different processes occurring within the jet. While the general modes of emission and particle acceleration processes leading to the observation of the overall broadband emission are described throughout Chapter 2, it is necessary here to outline the particular dynamics of the jet which may lead to the variability and temporal dependence of the different emission states outlined above.

It is generally considered that the production of flares and outbursts can be understood to have been produced by shocks propagating downstream along the axis of the jet. These propagating shocks produce long-term outbursts, which can occur on timescales

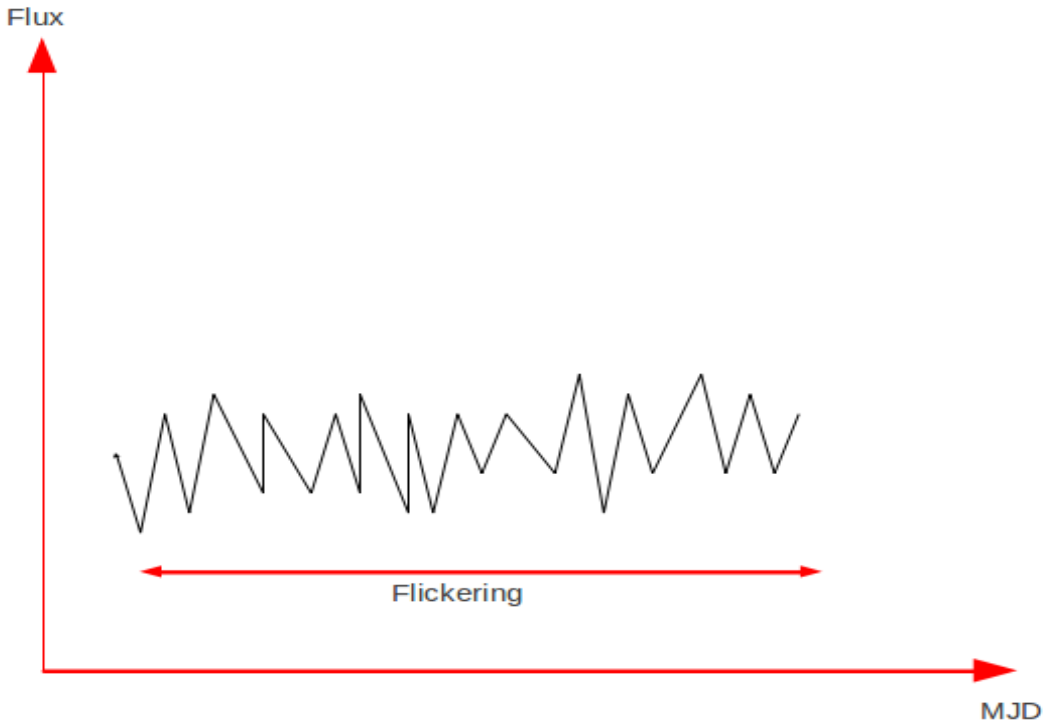

Figure 3.4: Schematic of flickering activity which may occur during both high and low emission states.

of months to years (249; 183). It is also possible that the onset of flares may be triggered by the collision of relativistic shocks propagating along the jet with another compression moving more slowly along the jet (174). Alternatively, the relativistic shock may also come into contact with the stationary core (typically the radio core observed in Very Long Baseline Interferometry observations) (53). It was also noted in Sokolov et al. (53) with reference to the generally-accepted jet models by Blandford & Koenigl (262), Marscher & Gear (249) and Hughes et al. (183), that the quiescent state emission may involve contribution from emission produced in the accretion disc, hot corona and dust torus; however, this contribution to the overall emission may not affect the more rapidly varying components of emission (typically the X-ray and γ-ray regimes).

If the assumptions proposed by the SSC and EC emission models (see Section 2.6) are true, then a strong correlation in the emission observed in the synchrotron component and higher energy component may suggest that both synchrotron and IC components are produced in the same location within the jet (115; 46). Alternatively, the nature of the emission regions within the primary jet may be complex and oriented in different

directions with respect to the observer. The onset of several different consecutive flares may be the result of partially co-spatial emission regions aligned differently with respect to the observer's line of sight, resulting in the 'flares' observed delayed with respect to one another. A thorough analysis of the different emission states and the nature of the transition between each state is an important aspect of blazar variability studies and a crucial aspect of this thesis. It helps bring to light some of the possible emission scenarios present in blazar jets.

3.2.3 Constraining the Size of the Emission Region

Variability studies provide constraints on the size of the emission region. With the assumption that the extended source is not optically thick to synchrotron self-absorption or γ-ray absorption through the $\gamma\gamma$ pair production process, light travel time causality arguments determine the variation of the observed emission. This can be characteristically expressed as $\Delta t_{em} \sim R/c$ where R is the characteristic size scale of the emission region and Δt_{em} is the observed variability timescale in the rest frame of the emission region. When the observed emission region is moving relativistically, the Doppler effect must be accounted for. As a result the time interval in any co-moving frame of the emission region will appear contracted in the rest frame of the observer by a factor of $\Delta t_r = \Delta t_{em}\delta^{-1}$, where Δt_r is the variability timescale in the stationary rest frame of the observer. This will lead to the following for a relativistically-moving source of size, R, in the rest frame of the observer:

$$\Delta t_r \geq R\delta^{-1}c^{-1} \tag{3.1}$$

where δ is the Doppler factor, and t_r is the minimum variability timescale of the relativistically moving emission region in the rest frame of the observer.

Since the Doppler factor is not always known, an estimate of this must be assumed for most models. In the current AGN paradigm, most studies point to $\delta \sim 10$ (156). Without making this assumption, variability studies provide constraints on the δR parameter space.

3.3 Quantifying Variability

Variability timescales and the 'strength' or level of variability at different wavelengths allow constraints to be made on current emission models as well as improving our understanding on the current relativistic jet paradigm. The presence or amplitude of variability can be established using several variability tests. These include the simple χ^2 test and a variability amplitude parameter known as the variability index, V. Both of these parameters give an overall idea of the type of variability present in the source at a given wavelength. They also facilitate comparison between sources and with studies present in the literature.

In order to establish the presence of variability for a sample with limited data, a simple χ^2 test of the flux measurements over the duration of the observation period can be performed. This χ^2 analysis is conducted based on the null hypothesis that the flux remains constant at the average flux value throughout the duration the observation period.

The other parameter that can be used to quantify an aspect of variability other than the timescale is called the variability index (222). This is a measure of the 'strength' or amplitude of the variability. This is given by:

$$V = \frac{(S_{max} - \sigma_{S_{max}}) - (S_{min} + \sigma_{S_{min}})}{(S_{max} - \sigma_{S_{max}}) + (S_{min} + \sigma_{S_{min}})} \tag{3.2}$$

where S_{max} and $\sigma_{S_{max}}$ are the maximum flux measurement and its corresponding measurement error while S_{min} and $\sigma_{S_{min}}$ are the minimum observed flux along with its corresponding measurement error.

The variability index represents the ratio of the difference in the minimum amplitude of a flux output to the maximum amplitude in the flux output over the given duration of observation. It must be noted that this parameter is heavily affected by the number and frequency of observations (222; 175). A variability index of $V \sim 1$ indicates that strong variability is present. This parameter is used as an estimate to compare the level of variability between the observed γ-ray and (sub-)mm wavebands for the different source classes and the different behaviour they exhibit throughout the monitoring period.

Variability amplitudes can also be measured using other methods, for instance the 'fractional root-mean-square variability amplitude' parameter (219). This method of es-

timating variability amplitudes is usually used for flux emissions at higher energies (i.e. γ-ray, X-rays, optical etc. e.g.(86; 235)) and extensively at γ-ray energies e.g.(86; 234; 121; 122). However, as the particular work shown in this thesis concerns the (sub-)mm regime, the variability index, V, as described in 3.2 will be used to determine the variability at the mm and sub-mm wavebands. This is more reflective of the method employed in (222; 45) (and references therein) and will thus facilitate comparisons between research in this thesis and that present in the literature.

3.4 γ-ray Emission from AGN

For the particular case of blazars, studying the HE γ-ray emission on daily timescales can be used as part of multiwavelength campaigns to determine whether γ-ray emission is produced through inverse Compton processes within the region of the jet. In order to test this, one can compare the light curves produced between the radio-IR regime with light curves at γ-ray energies. The radio-IR regime represents emission from the synchrotron process.

3.4.1 Probes the High Energy Spectrum of the Blazar Jet

Blazars are sub-categorised into two broad classes: BL Lacertae objects (BLOs) and Flat Spectrum Radio Quasars (FSRQs). The sub-categories that BL Lacertae objects are divided into are LBLs, IBLs, and HBLs (see Sections 1.2.4 and 1.3). As discussed, these sources exhibit their higher-energy peak at different γ-ray wavebands. Thus, when studying the γ-ray emission from these objects, much importance must be given to addressing the peak emission. Since most of the sources considered in this study are IBLs and FSRQs, the MeV to GeV γ-ray regime becomes of crucial importance. This is the energy regime that *Fermi*-LAT observes, providing consistent and frequent monitoring of the objects chosen for this study.

3.4.2 Localising the γ-ray Emission Zone

Investigating the high-energy spectra of blazars also provides information on localising the emission region where the majority of γ-ray photons are produced. In the current blazar jet paradigm there are two broad possibilities for the location of the γ-ray emis-

sion. A concise summary can be found in (146). In this section, some of these points will be discussed.

The first is speculated to be in regions close to the central engine (SMBH). These are regions either within the BLR (see Figure 1.1) or regions close to the accretion disc, within a few hundred Schwarzschild radii (269). This ties in with the standard relativistic jet model presented in Section 2.5. If we assume that the γ-ray production site is the ultra-compact region that spans the entire cross-section of a conical jet, observations of rapid variability at timescales of minutes to hours at MeV/GeV energies (e.g. (92; 145; 56)) support this scenario. Theoretical leptonic emission models are then used to describe the production of γ-rays from the inverse Compton upscattering of seed photons from the BLR and accretion disc (23).

The second possible location is at larger distances further out along the jet, greater than a few parsecs (~ 14 pc (114)) from the central engine (215; 90). There are several conditions within the jet that may lead to the production of γ-rays at these locations. First, regions in which radio shocks occur or regions in which shock-shock interactions occur are possible sites for the production of γ-rays. Alternatively, if the inner regions of the jet that are made up of turbulent multi-layer emission zones (see Section 2.6), these multi-layer zones will move at different velocities with respect to other zones within the jet, producing emission at different wavelengths (e.g. (212; 47; 214; 114; 89; 56; 170; 62)).

Observational data suggest both these cases might form part of the blazar γ-ray emission framework and should be investigated further. One method of doing this is to study γ-ray emission with respect to emission at other wavelengths. The presence of correlation between emission at γ-ray energies with emission at other energies may suggest co-spatial emission regions or similar emission mechanisms (producing emission at different wavebands) which will further constrain the location of the emission regions within the jet or provide constraints on the emission mechanisms involved.

3.5 Sub-Millimetre and Millimetre Astronomy

(Sub-)mm observations in general provide information on the synchrotron component of blazars. Standard models of emission from the inner jet show that this region is the site of the production of synchrotron emission, beginning at ultraviolet to optical fre-

quencies. As the population of synchrotron emission producing particles moves further along the jet, losing energy, and producing emission at longer wavelengths, the emission will now fall within the regime of the sub-mm, mm and cm radio bands. Until recently, the (sub-)mm waveband was poorly sampled, but with the advent of instruments such as SCUBA-2, SMA and ALMA, observations can now be made at (sub-)mm wavelengths which can consistently monitor blazars simultaneously or quasi-simultaneously with other instruments.

An important aspect of blazars is the dynamic nature of the light curves. Due to the alignment of the jet being close to the observer's line-of-sight, the emission from the jet is greatly amplified causing variations in flux to become more prominent for the blazar sub-class. As a result, the various emission states in blazars are more readily observed compared to other AGN sources. One particularly interesting case is the evolution of flares. It is thought that while most flares begin at higher frequencies and then propagate to lower frequencies, there is the possibility that flares could also begin simultaneously over a range of frequencies and either continue to propagate to lower frequencies or not propagate at all. In addition to this, there is the possibility that some flares may begin at sub-mm, mm and cm wavelengths (72; 101). In this thesis, this aspect of the sub-mm emission will be studied by comparing daily monitoring data between the γ-ray and (sub-)mm wavebands. Results from this study will be presented in Chapters 7 and 8.

3.6 Studying the Connection Between the γ-ray, Sub-millimetre and Millimetre Wavebands in Blazars

Due to the nature of the turbulent jet environment, it is possible that both scenarios, namely, the co-spatial higher and lower-energy emission zones along with the multi-zone emission scenario can exist simultaneously (e.g.(191)). The case of 'orphan' γ-ray flares not observed at lower energies is one example of this, while the correlated behaviour observed during radio/γ-ray monitoring campaigns (e.g. (129; 222)) suggest that γ-rays can be produced in regions where lower-energy emission is observed.

Since both these possibilities may be part of the same blazar jet paradigm, it is important now to establish the extent to which this connection between the higher energy wavebands and lower energy wavebands exists. An empirical approach to this is to de-

termine the 'strength' of correlation using discrete correlation function methods. In order to obtain an unbiased study, it is crucial to investigate correlation properties regardless of the activity of the source, i.e. consistently over long monitoring periods, during both quiescent and high states. This is the motivation behind this thesis.

In the past it has been shown that the connection between emission at lower frequencies and higher frequencies differ between the blazar classes, namely FSRQs and BL Lacertae objects (HBLs, IBLs and LBLs) (96; 152; 128; 78). This may be a result of the underlying differences in the jets of the various BLOs and FSRQs (237). Giommi et al. 2012 (190) suggested that a misclassification of a BLO as an FSRQ could occur when the non-thermal optical continuum was prominent and high enough to swamp the broad emission line in the optical spectral range (292), and as the continuum emission weakens the object could once again be classified as an FSRQ. This is a very important aspect of the study as it affects the blazar sequence (see Section 1.2).

A way in which the connection between the γ-ray emission and the (sub-)mm emission can be studied is through investigating time delays present between the multiwavelength light curves. This is characterised as an intrinsic delay between events observed in one waveband and events observed in another waveband. However, before correlation statistics and time delays are explored, it must be cautioned that the emission of blazars is intrinsically complex. For example, often, it will be observed that the superposition of flares is common and this usually occurs during a period of outburst (see Chapter 6 and 7). This feature of the multi-wavelength light curves makes it difficult to ascertain the magnitude of the correlation observed, or if correlation is present at all. Another complexity that arises when considering observations at longer wavelengths like the sub-mm and mm regimes is that the flares which occur often rise and decay on different timescales compared to their the higher-energy counterparts. It is possible that these features (flaring events) are not interpreted accurately when correlation statistics are considered. In order to take this into consideration, a qualitative assessment of the observations is employed in Chapter 7, when studying the connection between the MeV to GeV γ-ray and (sub-)mm light curves, before employing a statistical approach.

3.6.1 The Physical Significance of Time Delay Measurements

As will be described in Chapter 8, the DCF method will measure the level of correlation between the γ-ray and mm emission wavebands based on the time delay observed between flaring events. This measured time delay parameter can be used to understand the physical properties of the jet. In order to understand these properties, some of the factors which may lead to the observation of time lags between emission at different wavebands should be explored.

Based on the jet structure described in Section 2.5, observations of the inner regions of the jet are limited by the frequency-dependent synchrotron opacity, such that the radio/mm wave cores are optically thick to synchrotron emission up to its frequency dependent radius (262). For instance, the mm-wave core is located at a r_{mm} distance from the central engine, where $r_{mm} \propto \nu^{-1}$, where ν is the frequency of observation (262). In other words, the observable emission region is dependent on the wavelength of observation (i.e. the radio mm-wave and sub-mm wave cores are located at distances closer to the central engine compared to the radio cm-wave core). While the exact location of the production of γ-ray photons is still a subject of debate, based on this model (262), γ-ray photons can be thought of as being produced in regions upstream from the mm-wave core. A disturbance (e.g. shock) may cause emission in both the γ-ray and (sub-)mm regions. If it is assumed that the emission at both the mm and γ-ray wavelengths are boosted by the same Doppler factor (this also implies that the orientation of both emission regions are in close alignment with the observer), then a certain level of correlation may be expected between the two wavelengths observed.

Based on this assumption, and the direction of propagation of the disturbance, i.e. downstream along the jet axis, then a non-significant time delay can be expected from emission at the different energy regimes. As γ-ray photons escape immediately from the jet, it would take time (days to months depending on the wavelength of emission monitored, redshift and the AGN source class (36)) for the disturbance in the jet to propagate further downstream, resulting in emission at other wavebands. Due to synchrotron opacity, the rise in flux caused by the disturbance only becomes observable when the perturbation in the flow reaches the surface or the mm-wave core where emission is no longer limited by synchrotron opacity. The different positions of the mm wave core and the site of production of γ-rays as employed in jet models by Marscher 2005 (278) and

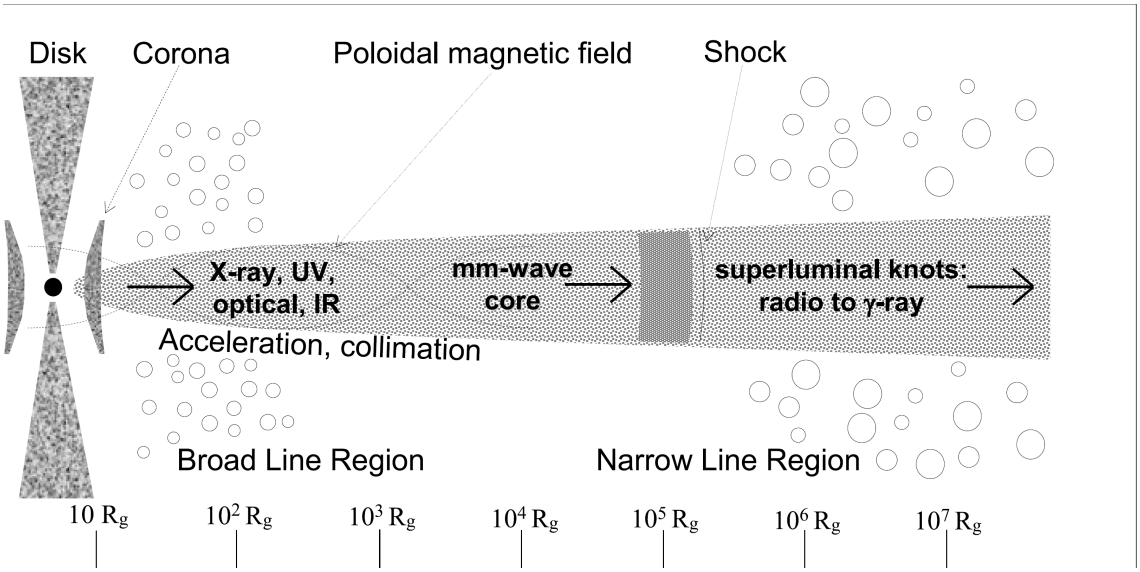

Figure 3.5: Schematic of a quasar jet and regions from which emission at different wavebands is thought to originate. This is based on the schematic adapted from Marscher 2005 (278), Lobanov 2007 (271). Image credit: Karouzos et al. (169).

Lobanov 2007 (271) can be seen in Figure 3.5.

Thus, when the observed time delay is corrected to a measured time delay in the source's frame using Equation 3.4, the distance between the γ-ray emission zone, r_γ and the mm-wave core, r_{mm} can be calculated. The distance, Δr is given by (36):

$$\Delta r = r_{mm} - r_\gamma = \frac{\delta \Gamma \beta c \Delta tl^{obs}_{mm-\gamma}}{(1+z)} \tag{3.3}$$

where r_{mm} and r_γ and the distances of the emission zones from the SMBH. δ, Γ and β_c are the Doppler factor, Lorentz factor and intrinsic jet speed respectively and z is the redshift of the object. $\Delta tl^{obs}_{mm-\gamma}$ is the measured time lag between emission at the two wavelengths studied (in this case the mm and γ-ray wavebands) in the reference frame of the observer. In 2007, Cohen et al. (161) described the relationship between the Doppler factor and the apparent angular speed of the jet, β_{app} (see Cohen et al. (161) for details on obtaining this relationship). Applying this to Equation 3.3, along with the redshift corrected time-delay, $tl^{src}_{mm-\gamma}$, given by:

$$\Delta tl^{src}_{mm-\gamma} = \frac{\Delta tl^{obs}_{mm-\gamma}}{(1+z)} \tag{3.4}$$

where $\Delta tl^{src}_{mm-\gamma}$ is the measured time lag between emission at the two wavelengths

studied (in this case the mm and γ-ray wavebands) in the reference frame of the source, the following expression is obtained:

$$\Delta r = \frac{\beta_{app} c \Delta t l^{src}_{mm-\gamma}}{(\sin\theta)} \tag{3.5}$$

where $\sin\theta$ is the viewing angle between the jet axis and the observer. Given θ and β_{app}, the time delay can therefore be used to estimate the distance between the γ-ray and 1.35 mm emission regions. This method will be used in Chapter 8 to analyse the distance between the 1.35 mm and γ-ray emission sites based on measured time lags from the DCF analysis.

In this thesis, the connection between the high-energy and low-energy emission will be studied statistically using the discrete correlation function (DCF) method. First, the calibration data from the Submillimeter Array will be used to produce light curves for the eight sources presented in this study. These light curves will depict flux output at 1.35 mm and 870 μm, the former monitored consistently (typically on daily timescales when the source is above the horizon) for most sources over the period of ~ 12 years. The light curves will be analysed to obtain variability indices, and studied for features such as flares, outbursts, high states and flickering.

Following this, the *Fermi*-LAT light curves will be presented and analysed for the same characteristics of flares, outbursts, etc. The γ-ray light curves will then be compared to the SMA light curves. The onset, development and decay of the spectral features will be analysed. It must be noted that, due to the difference in the type and temporal features of emission at γ-ray and (sub-)mm wavebands, the characteristic features (flares, outbursts, etc.) of the light curves will take on different definitions. This will be presented and discussed in Chapter 6 and 7.

Finally, the connection between the γ-ray and mm wavebands will be studied statistically using the DCF method (see Chapter 8). Results from this will be compared to discussions from the qualitative study presented in Chapter 7. This approach will provide insights into the mechanisms of blazar jets and how this varies with respect to the source type.

The important aspects of this thesis relates to the following:

- does correlation exist between the γ-ray and (sub-)mm wavebands?

Name	RA (hh:mm:ss)	dec. (deg:min:sec)	z	Type
PKS 2155-304	21:58:53	-30:13:18	0.116	HBL
MRK 421	11:04:27	+38:12:32	0.031	HBL
MRK 501	16:53:52	+39:45:37	0.034	HBL
OJ 287	08:54:49	+12:06:31	0.310	IBL/LBL
BL Lacertae	22:02:43	+42:16:40	0.069	IBL/LBL
3C 273	12:29:07	+02:03:09	0.158	FSRQ
3C 279	12:56:11	-05:47:22	0.536	FSRQ
3C 454.3	22:53:58	+16:08:54	0.859	FSRQ
NGC 1275	03:19:48	41:30:42	0.018	Radio Gal.

Table 3.1: A summary of the blazar sources included in this study and details on right ascension (RA), declination (dec.), redshift (z) and the blazar type.

- if it does, then how strong is this correlation?
- does the correlation (if observed) follow a particular trend?
- is the existence or absence of correlation source-class dependent?
- if they are source-class dependent, then what does this mean for blazar unification schemes?
- how does this fit into the overall AGN unification?
- further prospects of extensive monitoring with CTA

3.7 The Blazar Sample

In this section, a brief description of the eight blazars and one radio galaxy which form the core of this thesis will be presented. These objects are all well studied and were chosen to represent three blazar sub-classes, namely, HBLs, IBLs, and FSRQs. It is understood that while these blazars are all oriented to the line-of-sight, the behaviour of these objects differs between sub-classes. In addition to the blazars, a well-known radio galaxy, NGC 1275, is added to the study to provide a different perspective.

3.7.1 PKS 2155-304

PKS 2155-304 is located at a redshift of $z = 0.117$ (244). The source was observed during a period of outburst in November 1997, detected in X-rays and γ-rays with EGRET (328; 144). This led to detection of VHE γ-rays above 300 GeV by the Durham group (193; 194). While the source was detected to be in a low state in 1998 at X-ray energies, there was no evidence for TeV γ-ray emission (19).

PKS 2155-304 is a particularly interesting source forming part of various multiwavelength campaigns (151; 242; 69) which target the source at both flaring and quiescent states from the lower energy regimes (infrared/optical/UV (151)) to TeV regimes (e.g. (243)). The first of several multiwavelength campaigns (84), with observations including H.E.S.S. (High Energy Stereoscopic System) at VHE γ-ray energies, ROTSE at optical energies, RXTE/PCA at X-ray energies and at radio energies using the Nançay Radio Telescope (NRT) between 19 October and 26 November 2003, showed no evidence for correlation between any of the wavelengths observed during this short-term observation. However, intranight variability was observed at VHE γ-ray energies, along with variability (on kilosecond timescales) in the X-ray and optical bands (84). Other studies by Aharonian et al. (87) in 2009, conducted during a low state, revealed again no correlation between the X-ray and VHE γ-ray emissions, However, there was some level of correlation between the VHE and optical bands.

Longer-term observations during active states, however, showed slightly different results. In 2012, Abramowski et al. (243) published results of VHE observations of PKS 2155-304 during two exceptional flares in July 2006. This was part of a long term multiwavelength campaign which included X-ray, optical and radio observations between 2004 and 2008. They found correlation between the X-ray and VHE γ-ray emission during the observed flaring period. However, there was no direct correlation between the higher (VHE γ-ray and X-ray) emission and the lower energy (optical, radio) emission during the flaring period (243).

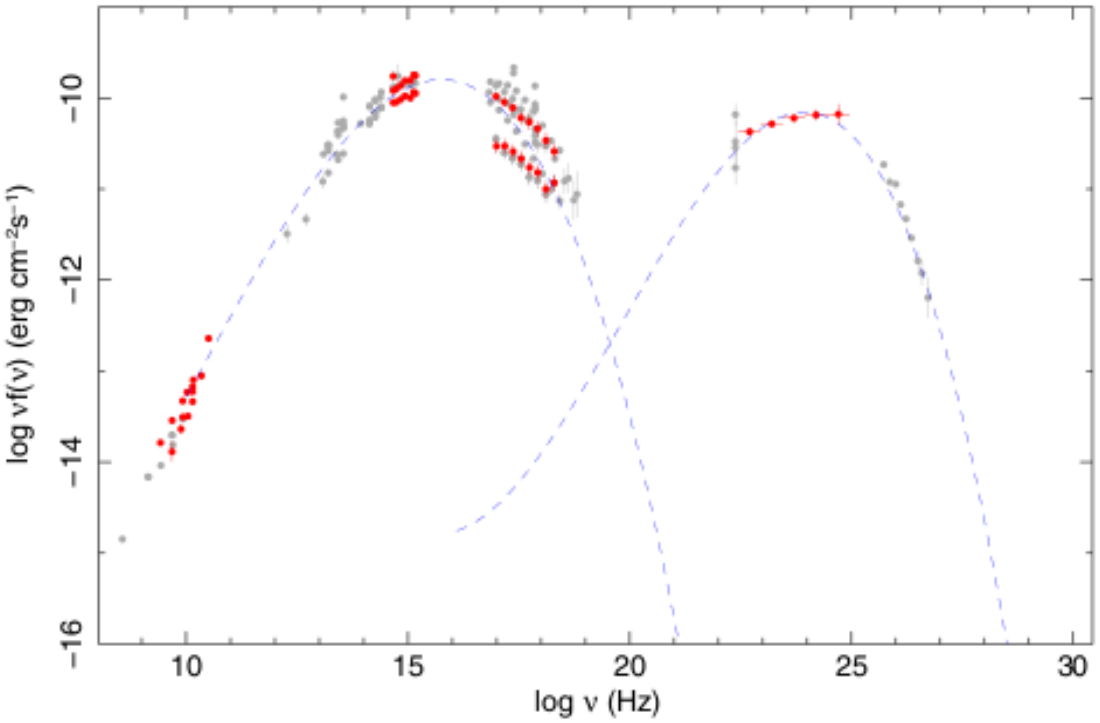

Figure 3.6: SED of PKS 2155-304, based on both quasi-simultaneous (large filled red symbols) and non-simultaneous archival (open grey points) of radio to γ-ray observations, while the dashed line represent best fits to the synchrotron and inverse Compton components based on observational parameters including the radio spectral index, peak frequency and peak flux of the synchrotron component and the peak frequency and peak flux of the inverse Compton component (29).

3.7.2 Markarian 421 (MRK 421)

MRK 421 is one of the brightest and closest BLOs in the northern hemisphere, and is located at a redshift of $z = 0.031$ (22). It was classified as a BLO due to its nucleus showing polarisation properties and a featureless spectrum (162), and then classified as a HBL due to its synchrotron peak being located at energies > 0.1 keV (162; 102). An example of MRK 421's SED can be seen in Figure 3.7 based on model fits to multiwavelength observations (95).

It was first discovered at TeV energies by Punch et al. in 1992 (171) and at GeV energies with EGRET (241; 186). This source is also monitored at lower wavelengths, typically at optical (284), IR and at radio wavelengths (112; 113). MRK 421 has been

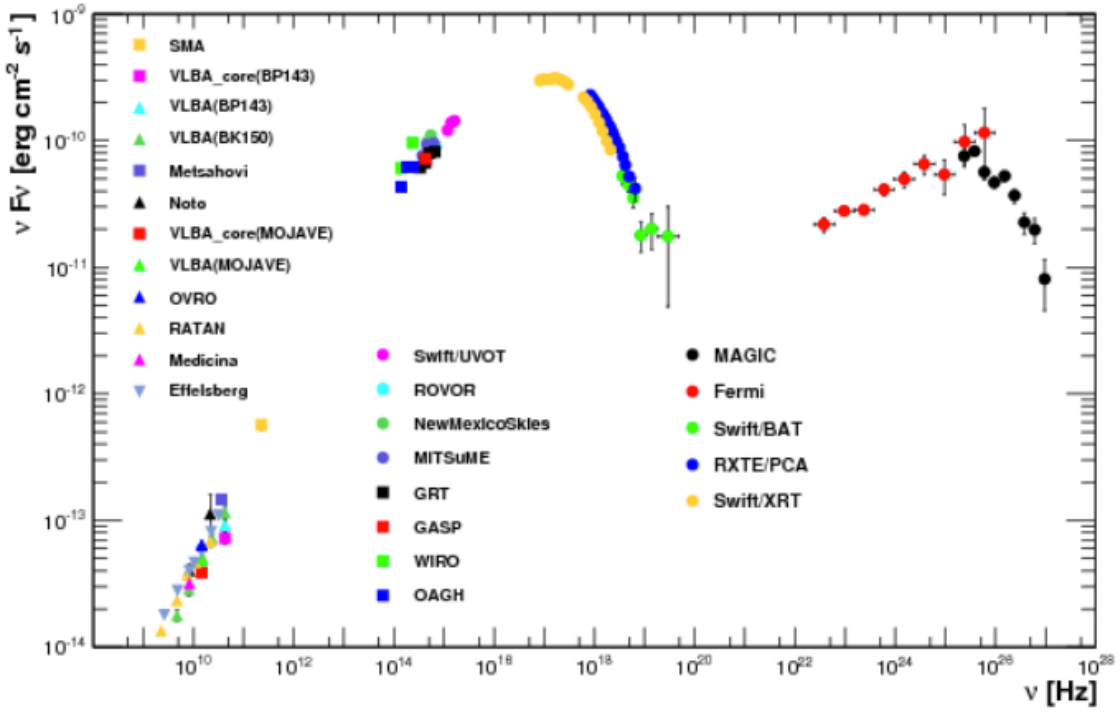

Figure 3.7: This figure shows the SED for MRK 421 based on multiwavelength observations obtained between 19 January 2009 (MJD 54850) and 1 June 2009 (MJD 54983). Image obtained from Abdo et al. (31).

the target of countless simultaneous multiwavelength monitoring campaigns (231; 187; 94; 95). Studies in the optical regions show strong variability (284; 88) and at TeV γ-ray energies on timescales as short as $\sim$ 10 minutes (116). Work has been done to look for correlated variability between emission at different wavelengths. Some of these include the search for variability between the X-ray and near infrared wavebands (38), while a correlation between X-ray and TeV γ-ray variability is noted in (148; 94). Results from these studies suggest that the SSC framework (323) might apply in explaining the level of correlation observed between the energy bands.

Most recently, in April 2013, MRK 421 entered a high state (257) resulting in unprecedented flaring activity which was detected with MAGIC, VERITAS, Swift and NuSTAR (155). This prompted ToO observations with SCUBA-2 which will form part of the research in this thesis (see Section 5.3).

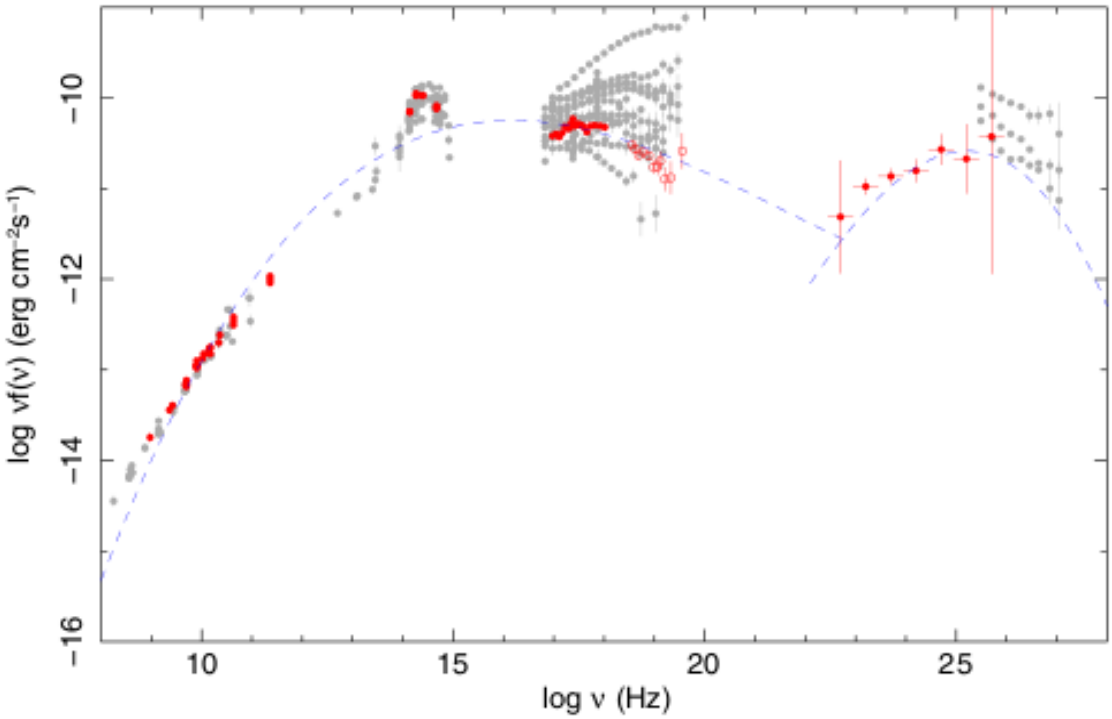

Figure 3.8: SED of MRK 501, based on both quasi-simultaneous (large filled red symbols) and non-simultaneous archival (open grey points) of radio to γ-ray observations, while the dashed line represent best fits to the synchrotron and inverse Compton components based on observational parameters including the radio spectral index, peak frequency and peak flux of the synchrotron component and the peak frequency and peak flux of the inverse Compton component (29).

3.7.3 MRK 501

MRK 501, with a redshift of $z = 0.034$ (233), is the third HBL included in this study. It was first detected at VHE energies by the Whipple collaboration in 1996 (131). An example of the MRK 501 SED is shown in Figure 3.8 (29). In 1997, this source entered a strong outburst state when observed at γ-ray energies (82) and at X-ray energies (79). The object then entered another high state in 2005. Observations by the MAGIC collaboration at this time revealed flux doubling timescales of only a few minutes (118).

As with other HBLs emitting at TeV energies, much of the multiwavelength campaigns have been organised to coincide with the high VHE states (104; 91). However, there are campaigns covering the low-activity states of the VHE emission (125; 207). Mul-

tiwavelength correlation studies by Aleksic et al. (123) have found evidence of positive correlation between the VHE and X-ray bands with zero time lag; similar time lags have also been observed by (104; 91; 253; 118). However, observations of lower energy bands, show little evidence of correlation between the lower-energy component and higher energy component (211; 301).

Intermediate/Low Frequency Peaked BL Lacertae Objects (IBL/LBL)

3.7.4 OJ 287

OJ 287 is a BLO at a redshift of $z = 0.31$ (143). This source, like the others, has also been part of extensive multiwavelength campaigns which aim to investigate correlation and variability between the higher-energy and lower-energy emission. A SED of OJ 287 is shown in Figure 3.9 depicting SSC model fits to multiwavelength data from radio, optical, X-ray and γ-ray observations ((111) and references therein). These studies have been conducted over decades (321; 230).

One particular aspect of much interest is the periodic or quasi-periodic nature of the optical outbursts, detected every ~ 12 years, when optical data spanning over 100 years were inspected (51). Further studies later confirmed this periodicity (52). Another intriguing aspect of these optical outbursts is that they consist of a double peak, with an interval of ~ 1.2 years (318). It must be noted that this periodicity and the occurrence of the double peak may change according to the sampling rate and binning timescales of the observations (52; 318).

OJ 287 is classified as a intermediate to low frequency peaked BLO, which means its synchrotron emission peaks at sub-mm to optical energies (252). This particular aspect makes this source an ideal target for long-term (sub-)mm observations.

In November 2005, OJ 287 entered an outburst period in the optical regime (166; 178). A second flare, according to the double-peak outburst trend of (318), was expected in May to June of 2007 (166). This flare actually occurred between November and December 2007 and was closely monitored at different wavelengths, part of a multiwavelength campaign involving MAGIC and Suzaku. Results from this campaign showed a significant increase in flux from the radio to the X-ray band. However, no significant increase in flux was measured with MAGIC (163).

In 2009, results from the first three months of bright AGN sources by the *Fermi*-LAT

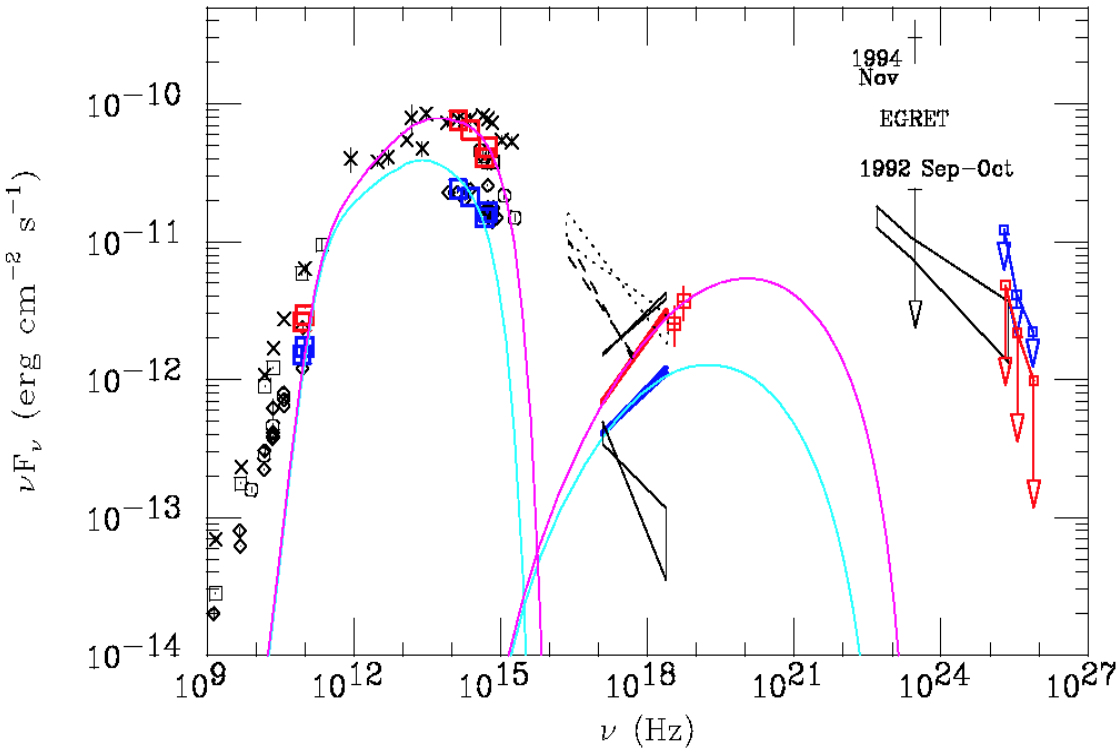

Figure 3.9: SED of OJ 287, obtained from Seta et al. (111) based on multiwavelength campaigns with data from radio to γ-rays. The squares represent radio and optical data, and the bow-ties represent X-ray data. The downward arrows are the upper limits of the VHE γ-ray spectrum. Radio optical and γ-ray data from non-simultaneous observations are shown with black points, while the dotted, dashed and solid lines show X-ray data from EXOSAT, ROSAT and ASCA respectively (see (74; 181). The *Fermi*-LAT γ-ray spectrum is also given by the bow tie (25). A model fit to the simple one-zone SSC model during a quiescent state and flaring state is shown by the light blue and magenta lines respectively (111).

instrument was reported (25), showing that the measured γ-ray flux of OJ 287 exceeded the simple SSC scenario when observations were made during its quiescent period, suggesting that there is an external Compton radiation to the γ-ray emission (163). This further motivates the search for the connection between the γ-ray and (sub-)mm energy bands and the extent of the correlation between these wavebands.

3.7.5 BL Lacertae

This source is the archetypal BLO located at a redshift of $z = 0.069$ (135) and is classified as a low-frequency peaked BLO (LBL) (5). It has been extensively observed at all wavelengths (Figure 3.10), exhibiting variability at all wavelengths ((62) and references therein). Observations also indicate a correlation between the variability observed at optical energies and that observed at radio wavelengths (103). A trend in which the lower frequency radio emission lags that at higher radio frequencies was also observed using cross-correlation methods (103). This is interpreted such that the higher radio frequencies are produced at regions close to the inner jet while the longer radio wavelengths correspond to emission produced further out from the central region (103).

BL Lacertae has also been a part of several multiwavelength campaigns, especially that of the Whole Earth Blazar Telescope (WEBT) program (60; 180; 62). An interesting aspect of this source is the observation of a rapid (minute-scale) TeV γ-ray flare on 28 June 2011 (5). Investigations of the correlation between the high-energy γ-ray emission by *Fermi*-LAT and radio bands were difficult to determine due to the undersampling of the source at radio wavelengths.

Investigations into correlated variability between the optical and radio bands suggest a delay of 100 days (with radio lagging optical emission), explaining these variations as a result of emitting plasma flowing along a rotating helical path within a curved jet (180). Other studies by (157) have also shown weak correlations between the optical and radio bands[1] when the object was transitioning between a quiescent and flaring state[2]. This is an important feature as the level of correlation might depend on the state of the object (i.e. outburst or quiescent). Part of the aim of this study is to determine the extent to which this is true.

[1] Observations were conducted over a ~ 6 month period in the second half of 2000.

[2] The flaring state of BL Lacertae began in September 2000 and continued for the rest of the year.

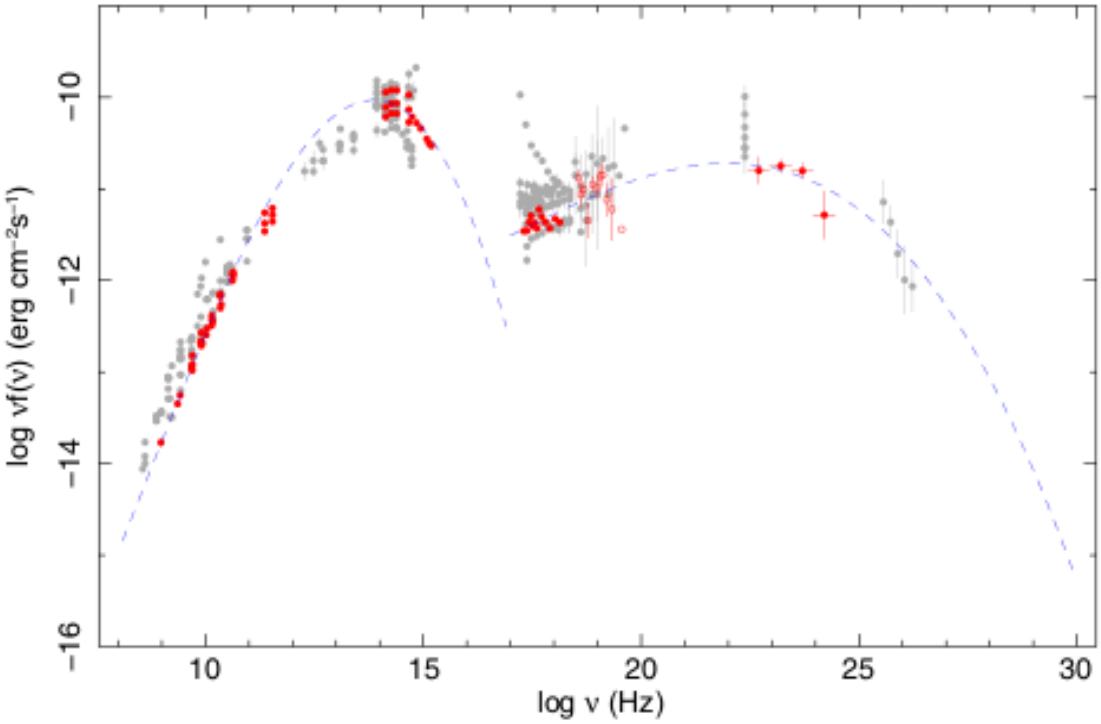

Figure 3.10: The SED of BL Lacertae, based on both quasi-simultaneous (large filled red symbols) and non-simultaneous archival (open grey points) of radio to γ-ray observations, while the dashed line represent best fits to the synchrotron and inverse Compton components based on observational parameters including the radio spectral index, peak frequency and peak flux of the synchrotron component and the peak frequency and peak flux of the inverse Compton component (29).

Flat Spectrum Radio Quasars (FSRQ)

3.7.6 3C 273

3C 273 is located at a redshift of $z = 0.158$ (315) and has been observed for over 100 years at optical wavelengths and for over 50 years at radio wavelengths (329). Databases exist containing over 30 years of observations and light curves covering over 16 orders of magnitude in photon energy (176; 218). Results from these monitoring campaigns can be found in (225; 226), with more recent studies in (218; 149). An example of the SED of 3C 273 is shown in Figure 3.11.

Flares at radio through mm to infrared and optical domains are attributed to the synchrotron mechanism (177; 73), while it has been suggested that the X-ray to γ-ray

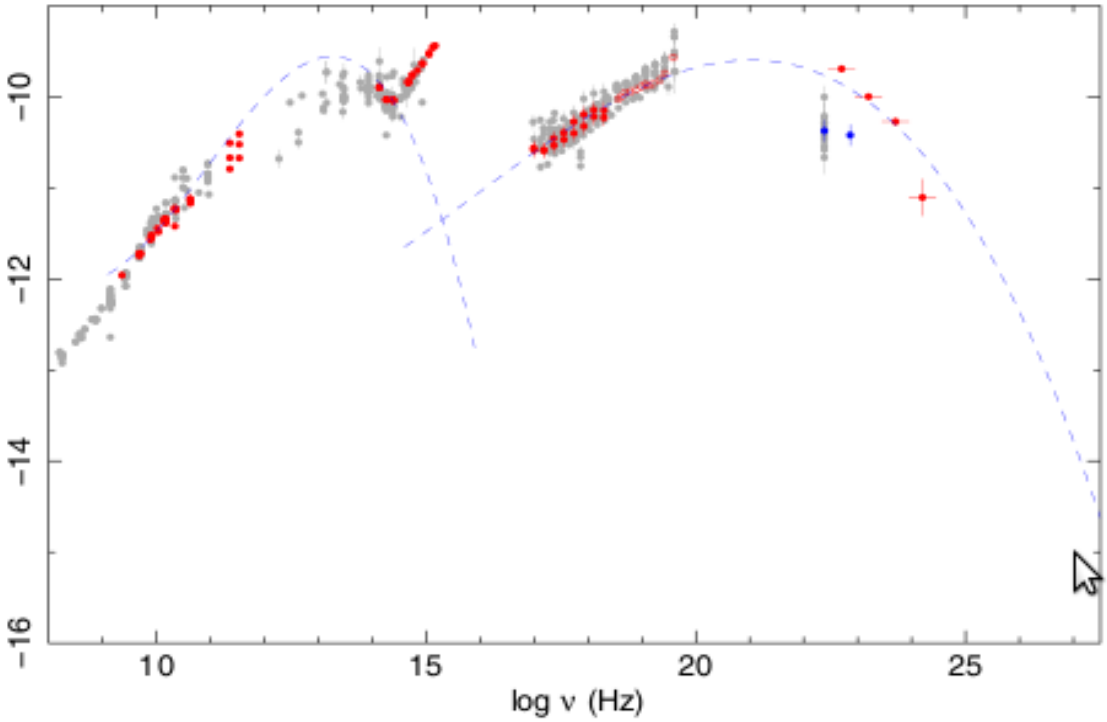

Figure 3.11: The SED of 3C 273, based on both quasi-simultaneous (large filled red symbols) and non-simultaneous archival (open grey points) of radio to γ-ray observations, while the dashed line represent best fits to the synchrotron and inverse Compton components based on observational parameters including the radio spectral index, peak frequency and peak flux of the synchrotron component and the peak frequency and peak flux of the inverse Compton component (29).

emission is produced by inverse Comptonisation of the thermal plasma in the accretion disc or in a corona (typical of a dominant EC scenario) and of a non-thermal component associated to the jet (126; 294). Later studies building on this understanding have shown that emission within the same waveband, between the hard and soft X-rays for instance, or HE and VHE γ-rays, exhibit temporal variability on different timescales (218), This suggests that even within the same waveband, different modes of emission are present. Soldi et al. (218) also observed no clear correlation between the X-ray and radio-mm wavebands, again suggesting that this behaviour may be attributed to *two* separate components (a Seyfert-like component and a blazar-like component) producing emission at the energy range below and above ~ 20 keV. A short-term study performed by Pacciani et al. (149) also revealed no significant correlation, this time between the near-infrared

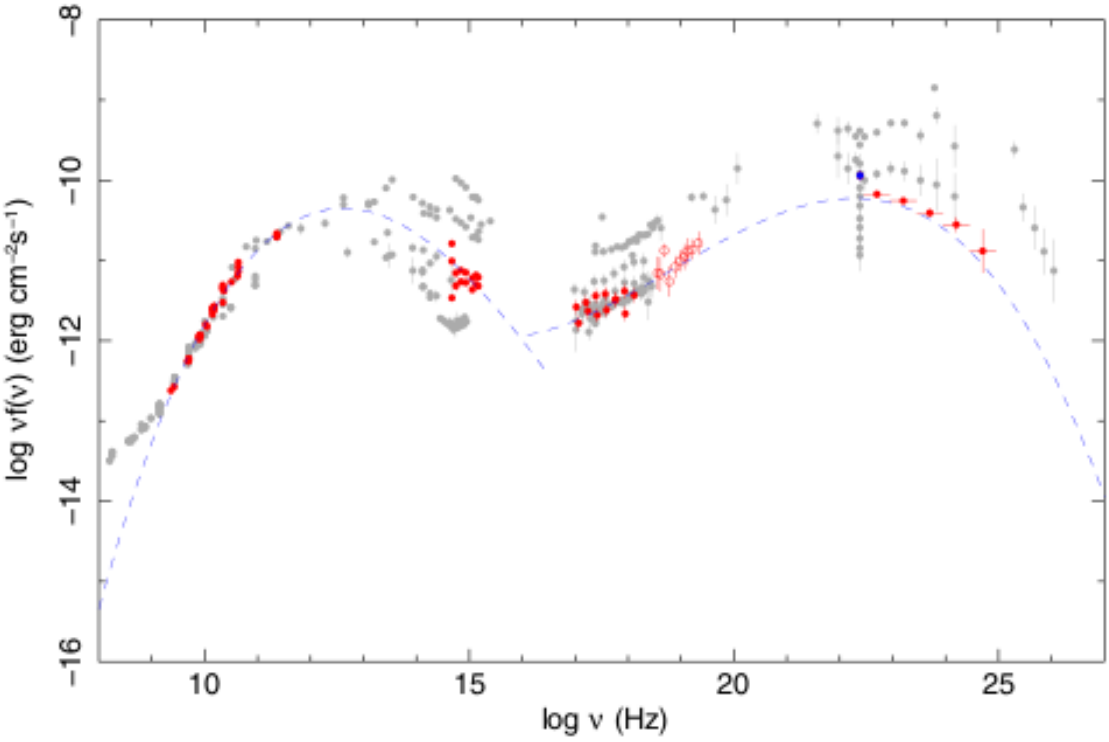

Figure 3.12: This figure shows the SED for 3C 279. Image obtained from Abdo et al. (29) based on both quasi-simultaneous (large filled red symbols) and non-simultaneous archival (open grey points) of radio to γ-ray observations, while the dashed line represent best fits to the synchrotron and inverse Compton components based on observational parameters including the radio spectral index, peak frequency and peak flux of the synchrotron component and the peak frequency and peak flux of the inverse Compton component (29).

to γ-ray regimes. However, an anti-correlation was observed from emission in the X-rays and γ-rays (149). Vol'vach et al. (329) have also detected the appearance of 13-year cyclicity in the optical data, motivating further long-term monitoring campaigns to further investigate this behaviour.

3.7.7 3C 279

This source is one of the brightest FSRQ at a redshift of $z = 0.536$ (63; 17). It was the first quasar observed at γ-ray energies with the Compton Gamma Ray Observatory (CGRO) (199). An example of 3C 279's SED can be seen in Figure 3.12.

This source has been part of extensive multiwavelength observations (164; 119; 201; 204) including radio, optical, sub-mm, infrared, X-ray, HE γ-ray and VHE γ-ray. This source most recently entered a flaring state between 2013 and 2014 which was studied by Hayashida et al. (164) and between the specific periods of March and April 2014 by Paliya et al. (234).

Much of radio through to optical emission is explained by the synchrotron mechanism, while the X-ray to γ-ray emission is perhaps produced by the inverse Compton upscattering of the synchrotron photons under the leptonic scenarios. Dermer et al. (57) and Sikora et al. (173) have discussed that the most efficient way of producing the γ-ray emission is through external photon fields (see Section 2.6). An important aspect of studies in the γ-ray regime is to localise the γ-ray production site and much work is being done in order to address this question (e.g.(119)).

3.7.8 3C 454.3

This is another bright FSRQ, located at a redshift of $z = 0.859$ (275). An example of 3C 454.3's SED is shown in Figure 3.13. VLBA monitoring of the source revealed that 3C 454.3's jet has a narrow opening angle, as small as 1°, with its relativistic jet at a viewing angle of within 2° of the line-of-sight (213). This source has also been a part of extensive multi-wavelength campaigns (e.g.(44; 214; 324; 220)) over several decades. This source has exhibited flux variability over the broadband spectrum observed ((102) and references therein).

In October 2010, 3C 454.3 entered an unprecedented high state observed at all wavelengths from mm through to γ-rays ((220) and references therein). The temporal peak of the flare was observed in November 2010 at approximately 1 GeV (324; 220; 81; 24; 31). Studies continue to investigate the properties of this flaring activity. An interesting aspect discussed by Wehrle et al. (44), based on observations of the mid-IR and near-IR emission of the object, revealed a double-peaked synchrotron component in the SED (see Figure 3.14) (195). A similar condition was also noted by Raiteri et al. (61) when BL Lacs were observed, with the difference being that the double peak appeared at higher energies compared to the FSRQs.

Multiwavelength observations of this source were also used to study correlation between the radio and higher energy wavelengths, searching for delays between flares at

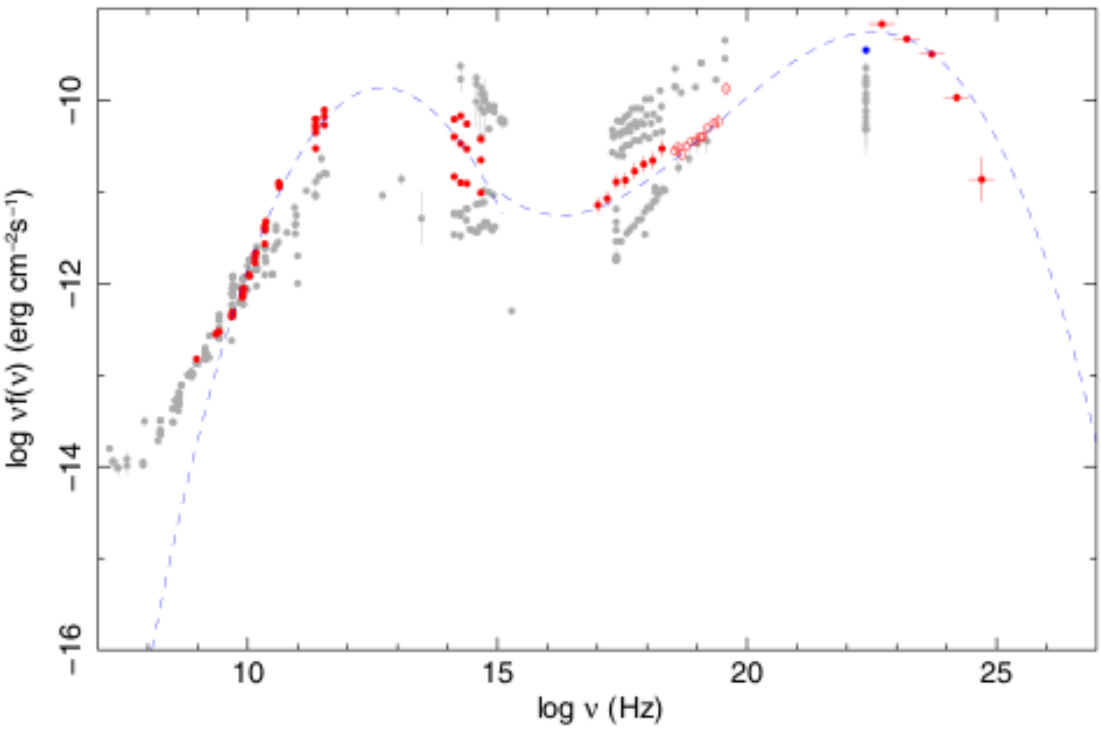

Figure 3.13: The SED of 3C 454.3, based on both quasi-simultaneous (large filled red symbols) and non-simultaneous archival (open grey points) of radio to γ-ray observations, while the dashed line represent best fits to the synchrotron and inverse Compton components based on observational parameters including the radio spectral index, peak frequency and peak flux of the synchrotron component and the peak frequency and peak flux of the inverse Compton component (29).

different wavelengths. The study by Vol'vach et al. (43) revealed that the delays vary between the wavelengths observed.

Radio Galaxy

3.7.9 NGC 1275

NGC 1275 is a well known radio galaxy of the Perseus cluster (Abell 421), and is located at a redshift of 0.018 (70). Radio observations of this source reveal a bright compact core, known as 3C 84, which dominates emission at radio wavelengths. VLBI observations (203; 330; 138) show that alongside this bright core are asymmetrical jets at both parsec (138) and kiloparsec scales (50), so that the object appears to be a Fanaroff Riley type 1

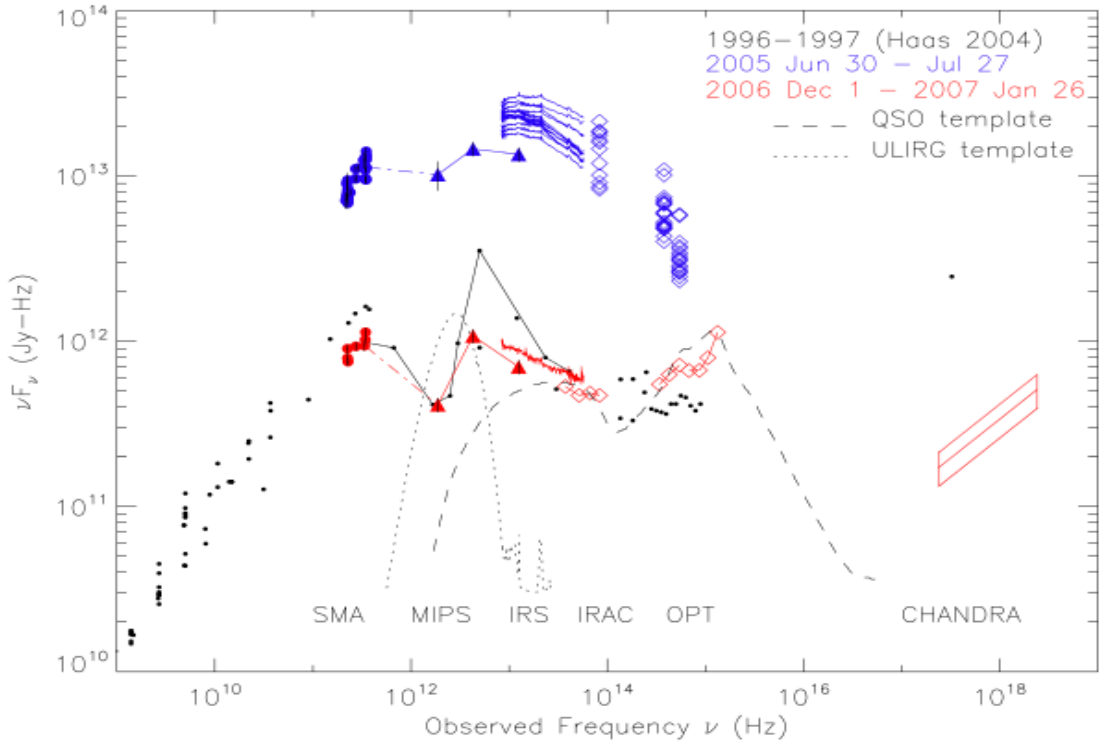

Figure 3.14: The double-peaked synchrotron component of 3C 454.3 at IR and sub-mm wavelengths in both low and high states as proposed by Ogle et al. (195). The triangles show *Spitzer* MIP photometry data at 160, 70 and 24 μm. The solid lines represent *Spitzer* IRAC 3.6 μm data, while the diamond points represent optical photometry data. The small black points are radio and optical photometry obtained between 1979-1995 from the NED database. The dashed line represents the mean SED for 3C 454.3 from Richards et al. (99) and the dotted line represents the mean SED template of ultraluminous purely star forming infrared galaxies from Rieke et al. (98). Observations of 3C 454.3 are incompatible with the SEDs from Richard et al. and Rieke et al.. The IR bump present in the plot, which does not fit into the SED profiles given, suggests that there is a dominant non-thermal component contribution from the jet in this energy regime (195).

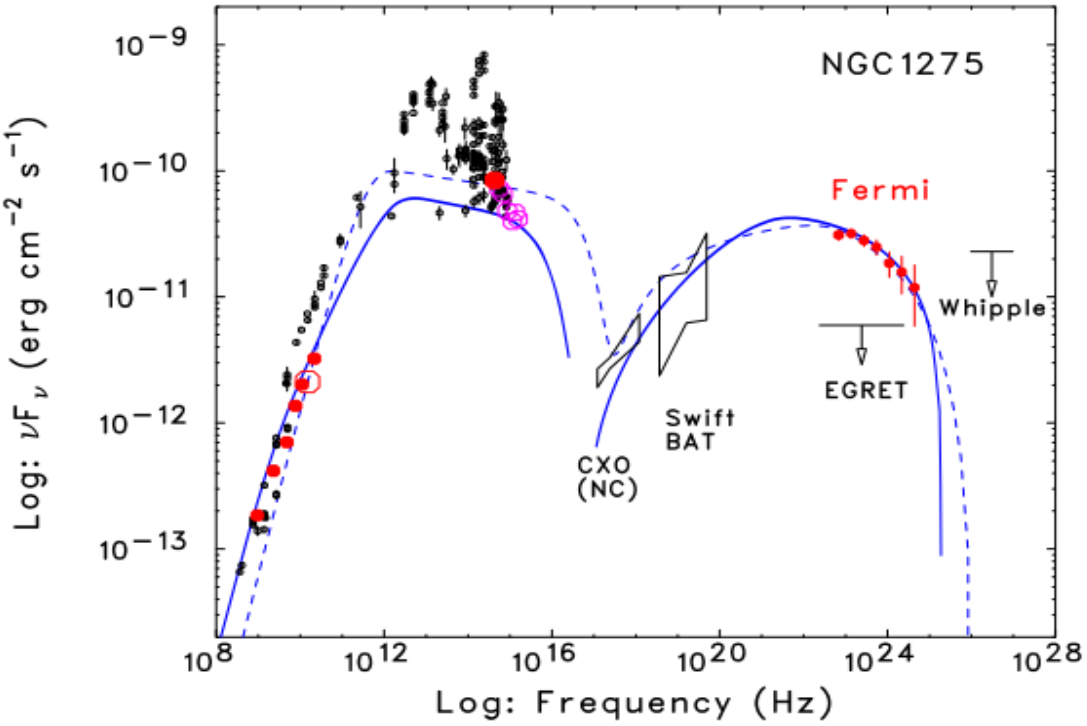

Figure 3.15: The SED of NGC 1275, based on multiwavelength data from radio to γ-rays fitted with a single-zone SSC model (blue dashed curve) along with a decelerating flow model by Georganopoulos & Kazanas(259) (26).

radio galaxy with one of the jets pointing close to the line of sight, at an angle of $\leq 14.4°$ (228), and the second jet located at an angle of $30° - 55°$ in the core region. Another interesting feature observed in the radio is the evidence for jet bending (50; 205).

NGC 1275 has been monitored over the years in the X-ray, HE γ-ray and VHE γ-ray regimes. Emission observed in the X-ray regime are primarily thermal in nature e.g. (71; 37) with a non-thermal component (71; 54; 154; 293). In the HE γ-ray regime, the object has been observed to vary on very short (a week) timescales, suggesting a very compact emission region (2; 127),

Observations by Nagai et al. (107), show that the source is currently undergoing a period of outburst, which began in 2005. Further observations at subparsec scales reveal the emergence of a new component close to the core in 2007, growing in flux as it travels away from the core (107; 108).

Recent work on correlation studies between the γ-ray and 1.35 mm wavebands have been conducted by Dutson et al. 2014 (141), revealing a positive correlation at $\sim +800$

days and ~ -450 days, and an anti-correlation at $\sim +1100$ days. The long delay present in the correlation analysis between the γ-ray and 1.35 mm wavelengths coupled with the variability on shorter timescales (days to weeks) at γ-ray energies compared to the lack of significant variability on similar timescales at 1.35 mm wavelengths suggests a more extended mm emission region or that the 1.35 mm emission is being self-absorbed (141). It was also observed by Dutson et al. (141) that there is a lack of significant variability at 1.35 mm during flaring periods observed at γ-ray wavelengths. This is indicative of a lack of change in the electron population producing the synchrotron emission. It was also suggested that changes in the electron population are dependent on the structure of the emission region further indicating that variations in one wavelength might not always lead to variations at other wavelengths. A further discussion of this in the context of correlation studies and variability will be given in Chapter 8 as results from Dutson et al. (141) will be compared to research conducted for this thesis on NGC 1275.

Other multiwavelength studies (120), however, have found evidence for positive correlation at a significance level of 4 to 5 σ between the optical and GeV γ-ray energy bands. It was suggested that this correlation could be attributed to the optical emission being dominated by the optical counterpart of the γ-ray emitting region. Due to the particular alignment of this source (leading to its classification as a radio galaxy rather than a jet aligned blazar), the observed emission may not be completely dominated by the non-thermal emission of the jet. The broadband spectrum of this source could be a result of a contribution of the non-thermal component of the jet along with the emission from extended thermal structures in the host galaxy. It will be observed later (in Chapters 6, 7 and 8), that the light curves obtained from NGC 1275 have a different structure when compared to the other seven blazar sources presented in this thesis.

Chapter 4

The Fermi-LAT and SCUBA-2 Instrumentation and Data Reduction Techniques

4.1 Introduction

In this chapter, the details including the instrumentation, observation and data reduction processes of *Fermi*-LAT and SCUBA-2 will be discussed. The observation techniques in general will be covered, including a general description of the data reduction processes.

4.2 The JCMT SCUBA-2 Instrument

The James Clerk Maxwell Telescope[1] is located at 19° 49′ 22.2″ N 155° 28′ 37.0″ W close to the summit of Mauna Kea, Hawaii. The telescope has a primary reflector with a diameter of 15 m and is the largest telescope operating at sub-mm wavelengths. The telescope is protected from the elements by a carousel which co-rotates with the antenna. The carousel has a membrane which is deployed in front of the antenna at all times and

[1]The introductory details of the telescope site and instrument specifications along with observation techniques were obtained from http://www.eaobservatory.org/jcmt/ (last viewed:23/03/2016). A detailed description of the instrumentation can be found in Holland et al. (240). The details of on-sky calibration are discussed in Dempsey et al. (136) and information on the data reduction techniques are presented in Chapin et al. (75).

is transparent at mm and sub-mm wavelengths. This membrane also functions to reflect visible and near-IR radiation (providing protection from the solar heat which could damage the antenna). This enables daytime astronomical and direct solar observations. The JCMT has a number of receivers located either in one of the bays of the Cassegrain cabin or on the two Nasmyth platforms located at the ends of the elevation bearing. The SCUBA-2 receiver is located at one of the Nasmyth platforms.

The Submillimetre Common User Bolometer Array 2 (SCUBA-2) is a 10,000 pixel sub-mm receiver. It consists of two focal planes, each containing 5120 pixels grouped in four separate sub-arrays of 1280 bolometers which are butted together to give a full field of view. The SCUBA-2 detector operates simultaneously at 450 μm and 850 μm, with both wavelengths sharing the same field of view of 42 arcmin^2.

The bolometers are made up of eight arrays of transition edge sensors (TES) built on 3″ silicon wafers, with each wafer containing 1280 TES bolometers. The signal is read out by a Superconducting Quantum Inteference Device (SQUID) multiplexer. A total of four TES arrays (consisting of 5120 bolometers) along with their corresponding SQUID multiplexers operates at each wavelength of observation (240; 75).

4.3 Observing with the SCUBA-2

Blazars are point sources and fall under the category of small-field observations. In such observations, the DAISY 3-arcminute scanning mode is used, in which the telescope is kept moving at a constant speed in order to maintain the astronomical signal at a constant frequency (240). This mode requires the telescope to move in a pseudo-circular pattern keeping the target coordinate on the arrays throughout the integration (see Figure 4.1). This mapping pattern functions to maximise the exposure time in the centre of the image.

SCUBA-2 operates at 450 μm and 850 μm simultaneously; both wavebands are within the atmospheric transmission windows between 300 μm and 1 mm. The main concern with ground-based sub-mm observations is the attenuation and distortion undergone by the incoming radiation as it passes through the atmosphere. The primary cause of attenuation to the sub-mm signal is the absorption by water vapour in the atmosphere. This is represented by the precipitable water vapour (PWV) at 225 GHz, generally obtained

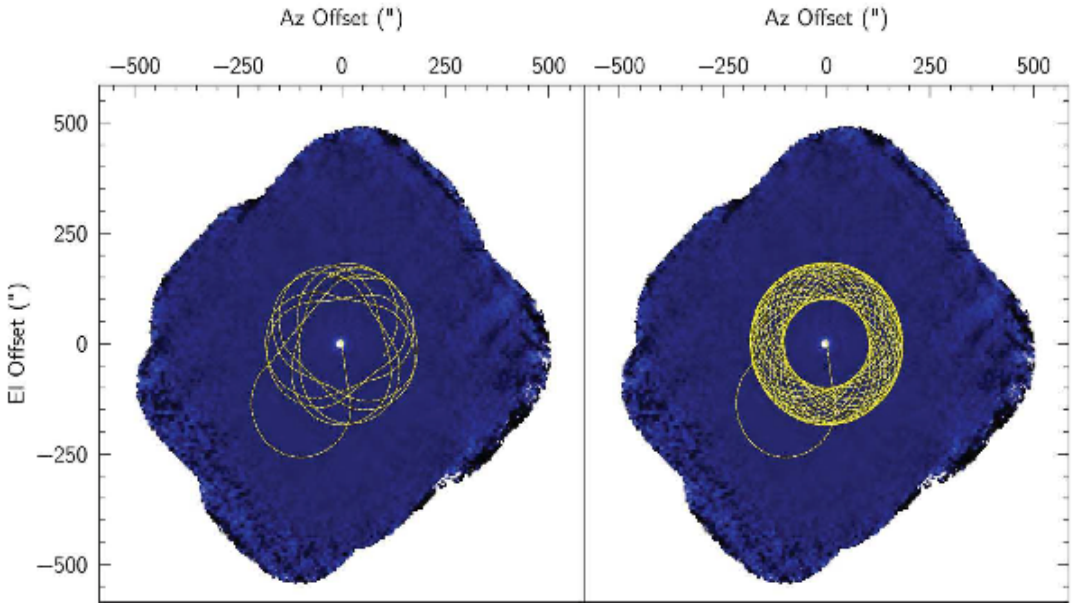

Figure 4.1: This shows the DAISY 3-arcminute mapping pattern. The track pattern on the left shows a single rotation of the DAISY pattern while the track pattern on the right represents multiple rotations of the DAISY pattern based on a 3-arcminute diameter. The x and y axes represent the azimuth and elevation offsets (in arcminutes) of the DAISY pattern while the blue area represents the total area of sky covered during an observing pattern (240).

from the nearby 225 GHz radiometer at the nearby Caltech Submillimeter Observatory.

4.3.1 On-Sky Calibration Processes

Effects of Water Vapour on Calibrating the SCUBA-2 Receiver

As noted in the previous section, attenuation in the 450 μm and 850 μm windows depends primarily on the precipitable water vapour (PWV) in the atmosphere. This effect can be seen in Figure 4.2, which shows the difference in atmospheric transparency in three different Weather Bands (see Table 4.1), corresponding to different values of the extinction coefficients at 225 GHz (136). The comparative transparency at 850 μm is higher than that at 450 μm at any given Weather Band.

The atmospheric transmission, assuming a plane-parallel atmosphere for a given sub-mm wavelength, is described by Equation 4.1.

Weather Grade	PWV (mm)	τ_{225}
1	< 0.83	< 0.05
2	0.83 - 1.58	0.05 - 0.08
3	1.58 - 2.58	0.08 - 0.12
4	2.58 - 4.58	0.12 - 0.2
5	> 4.58	> 0.2

Table 4.1: The variation of Weather Grades with respect to the precipitable water vapour (PWV) and the resulting extinction coefficient, τ_{225} at 225 GHz.

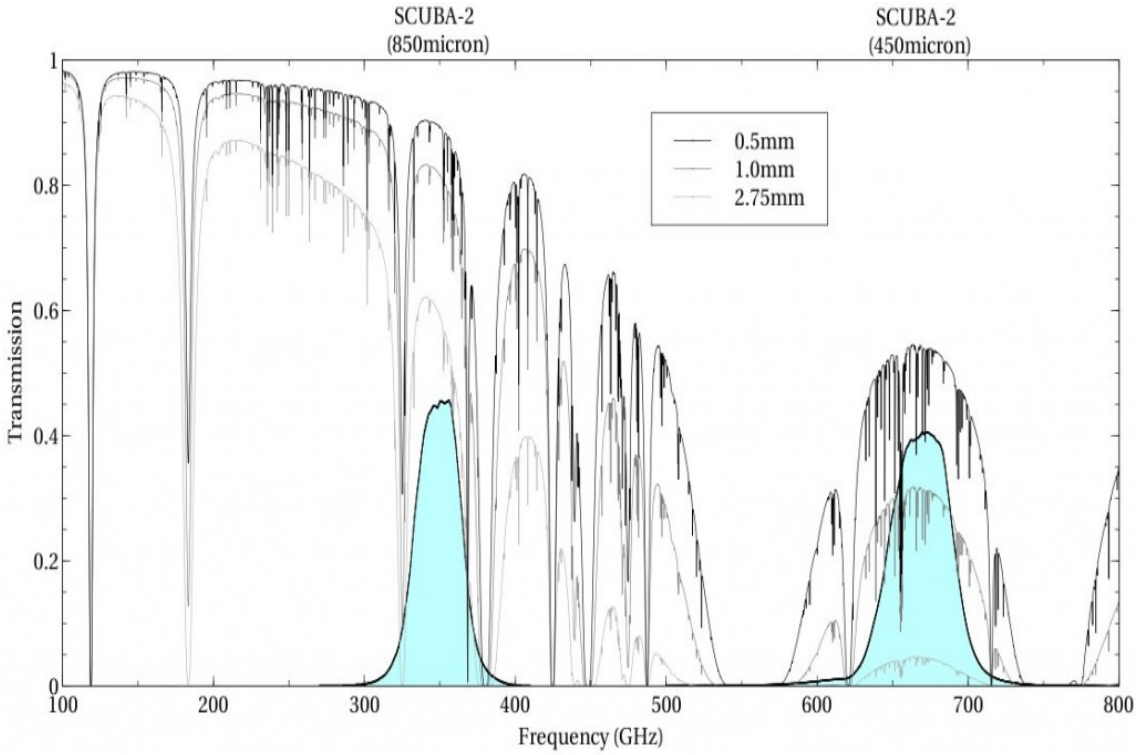

Figure 4.2: This shows the measured SCUBA-2 450 μm (blue) and 850 μm (blue) band-pass filters with respect to the 0.5 mm, 1.0 mm and 2.75 mm of precipitable water vapour transmission windows (black/grey). This shows that the transmission windows decrease when levels of the precipitable water vapour increases. It also suggests that the 450 μm observations are affected to a greater extent by atmospheric absorption than the 850 μm observations. Image obtained from the JCMT website.

$$I_m = I_\circ e^{-\tau A} \tag{4.1}$$

where I_m and $I_\circ$ represent the measured signal at the telescope and the measured signal at the top of the atmosphere respectively, τ is the extinction coefficient and A represents the airmass (117). In order to obtain the unattenuated signal, I_m, the extinction coefficient, τ must be determined for each observing waveband.

There are two ways in which the extinction coefficient is determined. The first is from the 225 GHz fixed azimuth tipping radiometer at the Caltech Submillimeter Observatory. This instrument completes a skydip every 15 minutes and calculates the zenith opacity based on a plane-parallel atmospheric model. Another measurement of the extinction coefficient, τ is obtained via measurements from the 183 GHz water vapour monitor (WVM) at the JCMT. This instrument measures the precipitable water vapour along the telescope's line-of-sight every 1.2 seconds, providing better temporal resolution. This method also no longer requires the assumption of a plane-parallel atmosphere as measurements are obtained in the line-of-sight of the JCMT. The PWV along the line-of-sight can then be adjusted to its zenith value by dividing it by the airmass, given by Equation 4.2. Since the airmass is determined by the declination, δ, of the source, the opacity measurements used are those obtained closest in time to the science observations. It is noted here that both the 225 GHz CSO WVM and the 183 GHz JCMT WVM are used to measure τ values during observations. The reason behind this is that, although the JCMT WVM monitors the PWV at different positions in the sky with a better temporal resolution compared to the CSO WVM, the former is occasionally subject to glitches producing noisy spikes in the signal. During these periods, the CSO WVM results are used. In general, the τ values recorded during observations is quoted at 225 GHz as this facilitates comparisons with previous observations in the literature. These are then accounted for during the data reduction process.

The air mass also affects the data quality and must be accounted for during the SCUBA-2 observations. This is done by adjusting the integration time spent on an observation of a source at a given declination. The air mass, A is given by:

$$A = \frac{1}{0.9cos[\frac{\pi}{180}(\delta - L_{JCMT})]} \tag{4.2}$$

where δ is the source declination measured in degrees and L_{JCMT} is the latitude of

the JCMT ($L_{JCMT} = 19.8°$). Finally, 0.9 represents an approximation for the average zenith angle of the source during the 4 hours near transit.

Based on the measurements of PWV obtained from either the 225 GHz CSO WVM or the 183 JCMT WVM, a relation to the opacity at a given sub-mm wavelength (τ_λ), can be determined based on a least-squares algorithm fitted to the PWV measurements (Equation 4.3). The fits produced for 450 μm and 850 μm are represented by Equation 4.4 and 4.5. Here, τ_{450} and τ_{850} are the extinction coefficients at 450 μm and 850 μm respectively. PWV is measured in millimetres. a and b represent the coefficients of the fit based on PWV measurements. These values are accounted for in the final flux calibration measurements (see Section 4.4.2.)

$$\tau_\lambda = a(PWV + b) \tag{4.3}$$

$$\tau_{450} = 1.014(PWV + 0.142) \tag{4.4}$$

$$\tau_{850} = 0.179(PWV + 0.337) \tag{4.5}$$

The extinction coefficients, τ_{450} and τ_{850} consequently determine the observing conditions and the integration time of each observation run. Based on Figure 4.2, seeing is better at 850 μm compared to 450 μm. The wavelength-dependent extinction coefficients, τ_{450} and τ_{850} can also be described in terms of the 225 GHz extinction coefficient, τ_{225} based on the following equations:

$$\tau_{450} = exp(-26 \times A \times [\tau_{225} - 0.01196]) \tag{4.6}$$

$$\tau_{850} = exp(-4.6 \times A \times [\tau_{225} - 0.00435]) \tag{4.7}$$

where A is the airmass (136).

Next, it is necessary to determine the integration time of each observation run. This is dependent on the following factors:

- The air mass which is determined by the object declination
- The atmospheric extinction

- The sampling factor, which affects the sensitivity and time of observation
- The mapping or scanning mode

A Grade 4 weather is sufficient in order to determine the peak flux levels of HBLs. For a chosen source of a given declination, and an average opacity at Weather Grade 4 of τ_{225} = 0.16, with noise levels of 10 mJy beam^{-1}, the average observation time can be derived using the SCUBA-2 ITC[2] (Integration Time Calculator).

Due to PKS 2155-304 and MRK 421 being point sources, the sampling factor, f, specified for 850 μm and 450 μm is 5.0″ and 8.0″ respectively with the application of a matched-beam filter during observations. The matched-beam filter uses the full flux of the beam instead of only the peak value at the position of the source. This improves the signal-to-noise ratio. The sampling factor and default matched-beam filter pixel sizes are given by the following equation:

$$f = \frac{p_r}{p_d} \tag{4.8}$$

where p_r and p_d are the requested (with the application of the matched-beam filter) and default pixel sizes respectively. The default pixel sizes are 2″ and 4″ at 450 μm and 850 μm respectively. The sampling factor then determines the integration time of each observation run based on the following equations:

$$T_{450} = \frac{1}{f}[(\frac{689}{\tau_{450}} - 118)\frac{1}{\sigma_{450}}]^2 \tag{4.9}$$

$$T_{850} = \frac{1}{f}[(\frac{189}{\tau_{850}} - 48)\frac{1}{\sigma_{850}}]^2 \tag{4.10}$$

The resulting integration times for the sources MRK 421 and PKS 2155-304 are 10 minutes and 15 minutes respectively. This will be discussed in further detail in Chapter 5.

Flux Calibration

Flux calibration involves converting the measured signal of the source from picowatts (pW) to Janskys (Jy) using astronomical sources of known flux properties (136). These

[2]https://proposals.eaobservatory.org/jcmt/calculator/scuba2/time (viewed on 20/08/2015)

astronomical sources are observed nightly and classified as primary and secondary calibrators. Some of the primary calibrators include Uranus and Mars, while the secondary calibrators constitute of either late-type stars or compact HII regions (e.g. CRL 618, CRL 2688, Arp 220 (240; 136)). These calibrators are observed using the DAISY mode with an integration time of approximately 4 minutes. Data from each observation are reduced using the SMURF (Sub-Millimeter User Reduction Facility) MAKEMAP routine. The Dynamic Iterative MapMaker (DIMM), within the SMURF environment, uses the configuration file for a bright compact source in the data reduction process. From this, the canonical values of the flux conversion factors (FCFs) for absolute peak flux measurements of discrete sources are derived (shown by Equations 4.11 and 4.12).

$$FCF[450]_{peak} = 491 \pm 67 \text{ Jy pW}^{-1} \tag{4.11}$$

$$FCF[850]_{peak} = 537 \pm 26 \text{ Jy pW}^{-1} \tag{4.12}$$

These values are a general guide. A better approach is to apply FCF values derived from individual calibration observations taken on the day of each science observation. This will be discussed in further detail in Section 4.4.2.

There are several factors which affect the FCF. These include the optical path to the detectors, the shape of the dish and the filter profiles at each wavelength (136).

Flat-fielding and the SCUBA-2 Point Spread Functions

In this section, other important aspects of the SCUBA-2 observation process are noted briefly. The first involves 'flat-fielding'. The SCUBA-2 instrument is flat-fielded to calibrate the response of the TES sub-arrays, optimise the SQUID settings and to determine the quality of the bolometer performance (see (136) for further details of how this is conducted). This process is carried out before every science observation, removing bolometers with responsivities above or below a threshold limit. Flat-fields are usually conducted with the internal instrument shutter open as these produce better bolometer yields particularly during instabilities in the sky. Dark flat-fields, on the other hand, are conducted at the end of an array set-up to determine if the set-up was successful (136).

The SCUBA-2 point spread functions are determined from the instrument beam shape. These are obtained from two-component Gaussian fit to the beam profiles from individ-

ual observations of Uranus (136). The resulting two component fits yield a main beam Full Width Half Maximum (FWHM) of 7.9 arcseconds and 13.0 arcseconds for the 450 μm and 850 μm beams respectively (see (136) for further details).

4.4 Data Reduction using SMURF

Raw data from SCUBA-2 are sourced from the Canadian Astronomy Data Centre (CADC) JCMT Science Archive. Data reduction processes use the SMURF software package written within the Starlink Software Environment (302; 227). The following sub-sections highlight the processes involved in reducing SCUBA-2 data, including the application of flux calibration factors for each wavelength of observation.

4.4.1 Producing Maps using the DIMM Configuration

For each scan, the Dynamic Iterative MapMaker (DIMM) (75) tool is used to produce source maps from the raw data. This is followed by further reduction processes done using PICARD (Pipeline for Combining and Analysing Reduced Data)[3].

Raw data from the CADC are recorded in terms of the number of scans per sub-array separately for each observed wavelength. First, the SMURF MAKEMAP routine, using the configuration file for a bright compact source, is executed on each data stream for both wavelengths. This routine applies an iterative technique on the data by removing most of the correlated noise sources in parallel with a simplified map estimator.

Partial maps are produced for each of the four sub-arrays and finally combined into a single map. This leads to a single map for each observed wavelength, displaying the peak flux of the source.

In general, point-source detectability can be improved by applying the MATCHED _FILTER from PICARD to smooth over the image with modified point source functions. This is particularly important in order to improve detectability of the source on the 450 μm maps, because observations of the source using the SCUBA-2 450 μm filter are affected to a greater extent by atmospheric opacities compared to observations at 850 μm (see Figure 4.2). For this study, however, this method did not improve the images produced by the MAPMAKER, indicating that atmospheric opacities were too large for suffi-

[3] www.starlink.ac.uk/docs/sun258.htx/sun258.html

cient detection of the source at 450 μm.

4.4.2 Flux Calibration: FCF Values Derived from Calibration Sources

Once the raw data are reduced using the DIMM parameter file for a bright compact source, the resulting map must be flux calibrated using the SMURF KAPPA routine. This is done by first reducing data from either primary or secondary calibrators taken close to the time and position of the science observation. Calibration data are reduced using the SMURF MAKEMAP routine with a bright compact source configuration file. Next, the PICARD routine is run to calculate FCF values for the reduced calibrator data. This produces a .log file which contains the FCF_{beam} values for 450 μm and 850 μm. These values are then applied to the science reduced maps using the KAPPA routine.

4.4.3 Errors

The complete maps were further processed to produce error maps, which are in effect maps representing the uncertainty in each pixel. In addition to the uncertainties introduced to the fluxes during the mapmaking process, there is a second contribution to flux errors from instrument calibration. This is a 5% error on all observations (136).

4.5 *Fermi*-LAT: Instrument Design and Methodology

All γ-ray data for this research were obtained from the *Fermi*-LAT instrument. The first part in this section will describe the *Fermi*-LAT instrument and its components. This will be followed by how γ-rays are detected with the instrument, which includes information on how the instrument is triggered and how initial data are processed. Next, the instrument response functions will be described.

The second part concerns the *Fermi*-LAT data reduction pipeline based on a likelihood analysis method. This begins with the data selection process, followed by the computation of the number of events observed and the generation of a source model in order to perform the final light curve analysis.

4.5.1 *Fermi*-LAT Instrument Components

The Large Area Telescope (LAT) is a pair-conversion imaging γ-ray telescope on-board the *Fermi* satellite. It was launched on 11 June 2008[4] with science observations beginning on 4 August 2008 (236). *Fermi*-LAT has a wide field-of-view[5] with a large effective area. The instrument operates in its primary 'scanning' mode approximately 95% of the time (153). While in this mode, *Fermi*-LAT alternates pointing above and below the orbital plane providing complete sky coverage once the instrument has completed two orbits approximately every three hours.

Fermi-LAT is equipped with the following components, each designed to perform a particular task. Details of each *Fermi*-LAT component are described in Atwood et al. (236).

[4]http://fermi.gsfc.nasa.gov/ssc/observations/ (last viewed:13/12/2015)

[5]The *Fermi*-LAT field-of-view covers approximately 20% of the sky at any time.

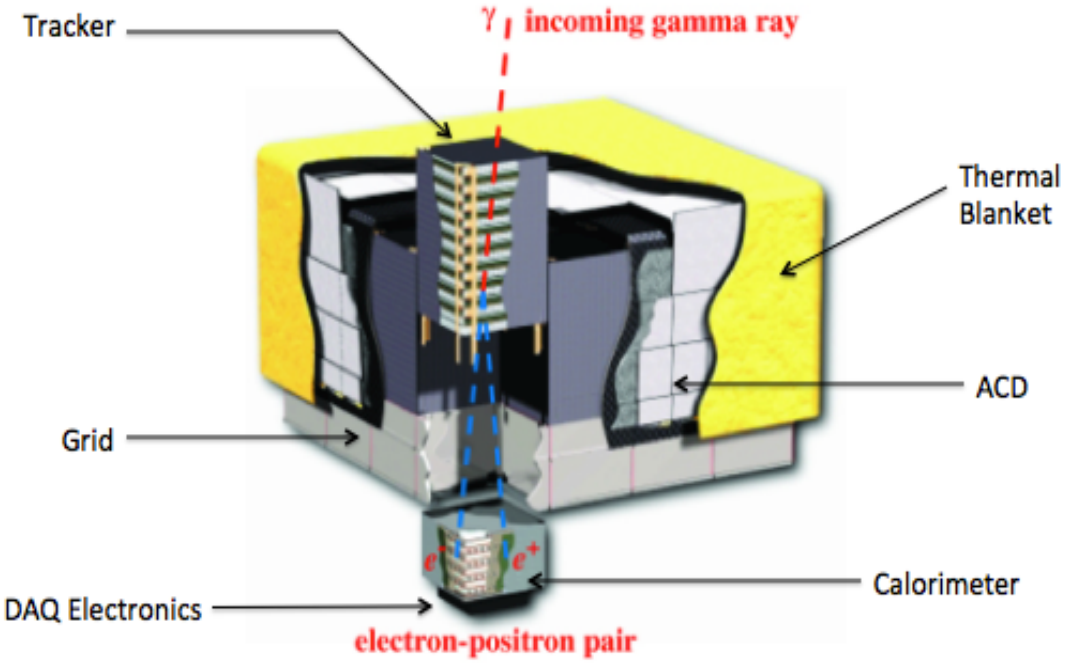

Figure 4.3: Schematic of the *Fermi*-LAT detector on-board *Fermi* and its various components. The incoming photon interacts with the converter tracker and is converted into an electron positron pair. The tracker (TKR) array is surrounded by an anti-coincidence detector (ACD). The schematic also shows the location of the calorimeter (CAL) and the data acquisition (DAQ) electronics. Heat produced by the TKR, CAL and DAQ is transferred to the thermal blanket, made up of radiators, through heat pipes in the grid. Image of the LAT was obtained from Atwood et al. (236).

Converter-Tracker (TKR)

The converter-tracker (TKR) is made of 16 tracker modules, each consisting of 18 XY[6] alternating tungsten foils and silicon strip detector planes, which promote the pair-conversion of an incident γ-ray photon into an electron-positron pair and then measures the direction of the particles resulting from pair conversion (see Figure 4.4). Of the 18 XY planes, 16 planes have tungsten converter plates of two different thickness. Of the 16 XY planes, 12 planes, which are furthest from the calorimeter, have thinner tungsten converter plates compared to the 4 XY planes closest to the calorimeter (see Figure 4.4). The different thickness in the plates serves to balance

[6]Tungsten foil strips alternate perpendicularly in the XY plane.

between optimising the point spread function (PSF)[7] at low energies and maximising the effective area[8] which is important at higher energies. The trade off with the thicker converter plates results in a decrease in angular resolution of less than a factor of two at 1 GeV, for photons converting in that region. The aggregate of the thick layers also functions to limit the number of back-scattered particles (i.e. backsplash effect) from the calorimeter (CAL) returning into the TKR and anti-coincidence detector (ACD) in high energy events[9]. In addition to this, the thicker planes also serve to reduce background contamination in front-converting events caused by tails of showers from events entering back into the CAL. Finally, the last two of the 18 planes immediately before the CAL do not have any tungsten converter foils. This is because the TKR trigger requires hits in three adjacent XY planes making it insensitive to γ-rays which convert in the last to layers. A detailed description of this can be found in (236) and (153).

Calorimeter (CAL)

The CAL is located at the bottom of the TKR and has a mass of ~ 1800 kg (Figures 4.4 and 4.5). The CAL, like the TKR is also made of 16 modules, each consisting of 96 CsI(T1) crystals, arranged horizontally in eight layers of 12 crystals each. The CAL functions to measure the energy deposition from the electromagnetic particle shower produced by the electron-positron pair and images the shower development profile. The crystal elements are read out by photodiodes, mounted on both ends of the crystal. These photodiodes measure the scintillation light transmitted to each end of the CsI crystal. The position resolution of the energy deposition along the crystal is given by the difference in the light levels measured at each end. This position resolution scales with the deposited energy, ranging from a few millimetres (low energy deposition of ~ 10 MeV) to a fraction of a millimetre (large energy deposition of > 1 GeV).

As such, the CAL is a 3-dimensional imaging calorimeter such that each of the CsI

[7] using the thin converter plates in the first 12 XY planes (often referred to as the front section of the TKR)

[8] using four XY planes with converter plates six times thicker than the first 12 XY converter plates (often referred to as the back section)

[9] The backsplash effect refers to the Compton scattering (in the ACD) of isotropically distributed secondary particles produced in the electromagnetic shower created by an incident high-energy photon. This may then create false veto signals from the recoil electrons. (236).

crystals produces three spatial coordinates for the energy deposited within it. Two of the coordinates specify the physical location of the crystal in the array. The third is obtained by measuring the light yield asymmetry at the ends of the crystal along its long dimension. These three coordinates provide spatial imaging of the shower along with an accurate reconstruction of its direction (236; 153).

Anti-Coincidence Detector (ACD)

This surrounds the LAT and is composed of 89 plastic scintillator tiles (25 covering the top of the instrument while 16 tiles cover each of the four sides respectively) (153). This element functions to reject background signals produced by cosmic ray particles incident on the LAT. While incoming γ-ray photons pass freely through the ACD tiles, charged particles (cosmic rays) cause a flash of light. The ACD also suppresses the backsplash effect caused by the heavy (~ 1800 kg) calorimeter (236). This is achieved by the segmented design of the ACD which significantly reduces the area of the ACD which may contribute to the backsplash effect from an incident candidate photon (236; 32). The ACD is designed and tested to detect charged particles efficiently.

Data Acquisition System (DAQ)

The data acquisition system (DAQ) performs on-board preliminary filtering of background events by first collecting data from the other components (TKR, CAL and ACD). The DAQ implements a multilevel event trigger system (see Section 4.5.1) before data are sent to the ground for further processing. The filters reduce the number of downlinked events by removing the number charged-particle background events. It also maximises the rate of the events triggered by γ-ray photons. The DAQ is equipped with an on-board science analysis platform which searches for transients (see Section 4.5.2) (236).

Instrument Methodology

In this section, the basic methodology of the instrument is presented. This can be described using the path taken by a single γ-ray photon as it moves through the LAT detector components.

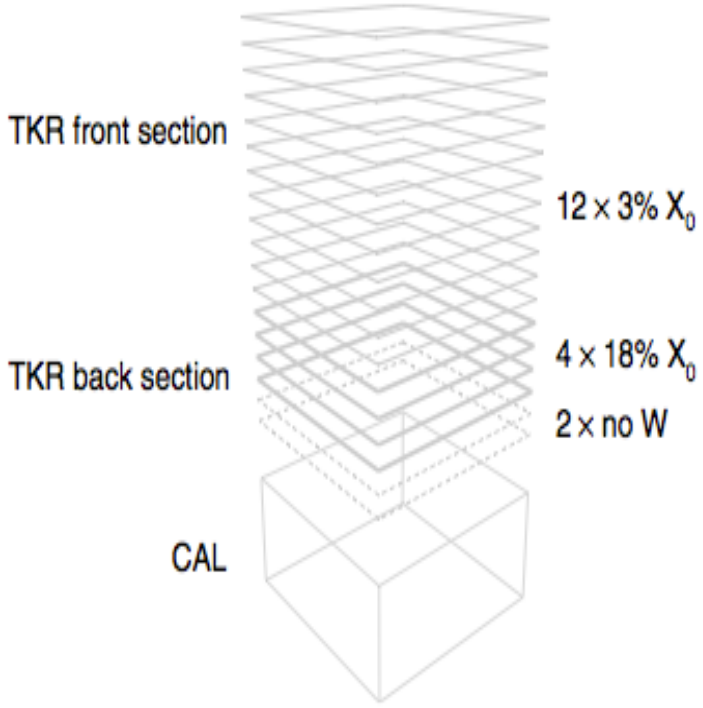

Figure 4.4: Schematic of the precision conversion-tracker (TKR) and calorimeter (CAL) on-board LAT which function to promote pair-conversion of incoming γ-ray photons as well as measuring the directions of the resulting pair-converted electrons and positrons. The TKR front section (located furthest from the CAL) is made up of 12 thinner XY planes. This is followed by the back section of the TKR which is made up of four thicker XY planes. The final two XY planes closest to the CAL do not have tungsten converter planes. Image of the LAT was obtained from Ackermann et al. (153).

When a γ-ray photon is incident on the LAT detector, it begins by travelling through the converter-tracker modules. Here, there is a high possibility that the photon will interact with the field of one of the heavy tungsten atoms in the converter planes and produce an electron-positron pair (see Section 2.3). The incoming γ-ray has energies much larger than the rest mass energies of the resulting electron-positron pair. This ensures that the charged particles continue predominantly in the direction of the incident γ-ray photon, while allowing the tracker to reconstruct the direction of that photon[10]. As a result, the reconstruction is heavily dependent on the multiple scattering of the charged

[10]The initial directions of the converted electron and positron pair are reconstructed from the conversion point based on the tracks recorded by the silicon-strip tracking detectors.

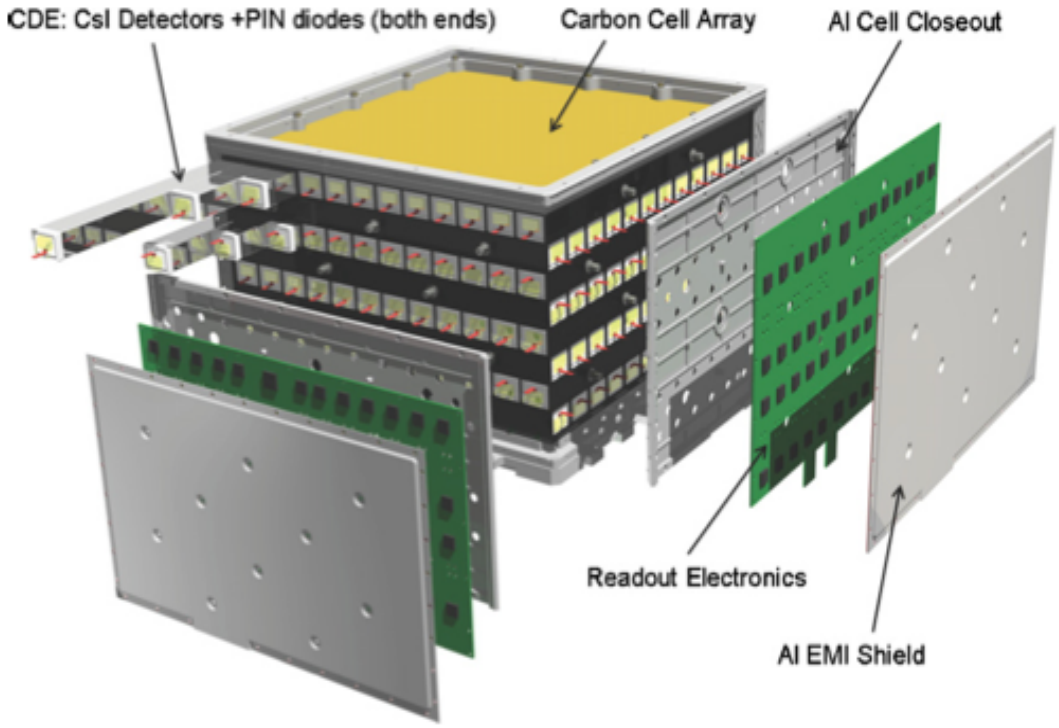

Figure 4.5: Schematic of the CAL module located below the TKR (see Figure 4.4) depicting the 96 CsI crystal detector modules arranged in eight layers and the position of the readout electronics. Image of the CAL was obtained from Ackermann et al. (153).

particles within the tracker and the spatial resolution of the tracker. Once the pairs travel through the planes of the converter-tracker modules, they reach the CAL[11]. The CAL then measures the total energy deposited onto it through the amount of scintillation light measured by the photodiodes located at both ends of each CsI crystal (see Section 4.5.1).

The output from the CAL is then passed through to the DAQ system, which reads input from the TKR, CAL and ACD to estimate the energy and direction of the incident γ-ray photon. Finally, information is transmitted to the ground for further processing.

[11]It must be noted that not all converted electron positron pairs reach the CAL, particularly for the cases in which the particles may have deposited all their energy in the TKR before reaching the CAL.

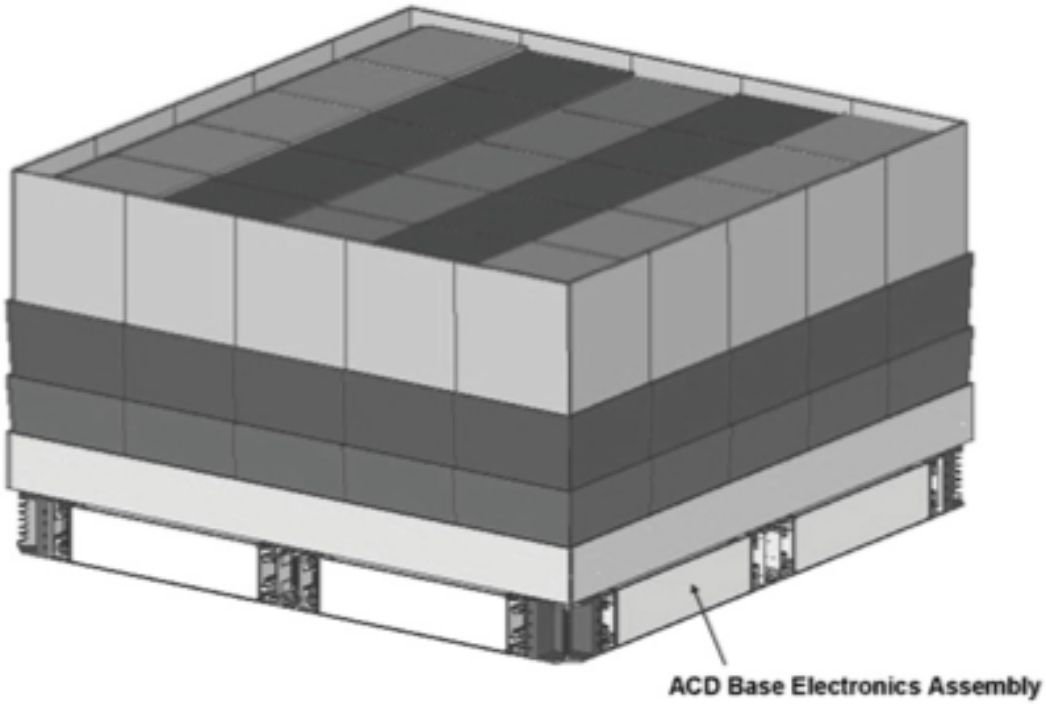

Figure 4.6: Schematic of the ACD surrounding the TKR and CAL modules with its 89 plastic scintillator tiles. In order to minimise gaps between tiles, the tiles overlap in one dimension and scintillating fibre ribbons are used to cover the remaining gaps. This is done to improve the efficiency of event triggering and filtering processes (see Section 4.5.1). Image of the ACD was obtained from Ackermann et al. (153).

4.5.2 Instrument Trigger and Event Processing

The final *Fermi*-LAT data sample is a result of the triggering and filtering processes done both on-board *Fermi* and on the ground. This begins at the DAQ level[12], after which the particle interactions are reconstructed. These events are then analysed and defined based on the various event classification scheme described further on in this section.

Before proceeding with this section, it is important to highlight the necessary terminology used when processing *Fermi*-LAT data. As a γ-ray photon is incident on the detector, there are three ways in which it may be described. These are as follows:

photon

A photon describes the discrete γ-ray particle which is incident on the detector and

[12]Contributions from all other components are present in the triggering process as stated in Section 4.5.1.

is not yet affected by the instrument response.

event

An event is characterised as the response of the instrument when it detects the particle. This can consist of two possibilities. An event could be the response of the detector on an incident γ-ray photon or charged particle. An event could also be due to the response of the detector to noise that appears as a charged particle.

count

A count is the result when an event is classified as being due to an incident γ-ray photon. The number of counts depend on the detector response, the trigger and event processing pipeline which result in the count being characterised by detector modified observables. It must be noted that there is a possibility some photons are undetected or sometimes rejected as being part of the background. At the same time, counts could also be produced by non-astrophysical background events.

The triggering and event-processing pipelines are described in detail in (153). However, a brief account of this is presented here, followed by the *Fermi*-LAT event classification procedures.

Fermi-LAT data which are transmitted to the ground have undergone triggering and filtering processes by the DAQ. The TKR modules, CAL and ACD are all involved in determining whether or not a trigger or a signal is observed and to distinguish if this trigger is a result of an incoming γ-ray photon, charged particles entering the *Fermi*-LAT from inside the field of view or backsplash events due to multiple-scattering in the TKR and CAL modules (236; 153). When the TKR detects a signal over a threshold value, this flags that a potential trigger is present in the tower. The CAL modules then distinguish if this potential trigger is at low energies, typically when the signal in any of the CAL crystal ends crosses the low-energy trigger threshold of ~ 100 MeV, or high energies, typically when the signal in the CAL crosses the high energy threshold of ~ 1 GeV (153). The triggering is then followed by the filtering process. There are three filtering algorithms, namely GAMMA, HIP and DIAGNOSTIC. The GAMMA filter algorithm filters γ-ray events. This algorithm processes events by running several tests on the triggered event. These tests are categorised into steps which will accept or reject the triggered event based on a predetermined criteria. In particular the GAMMA algorithm

accepts events which have total energy (deposited in the CAL) that is greater than the programmable threshold (set at 20 GeV) (153). The HIP and DIAGNOSTIC algorithms are designed for calibration purposes of the CAL and monitor the performance of the sensors respectively. The event filtering process includes (but is not limited to) rejecting events from cosmic rays, accepting all events which have a total energy deposited in the CAL of < 20 GeV, reject events with energy deposited in the CAL of < 100 MeV that has patterns in the TKR which are unlikely to produce a track and reject all events without at least one rudimentary track (153).

The cuts applied in the filtering process may cause the rejection of some important events, particularly events which deposit all their energy in the TKR (either because they miss the CAL or they range out before reaching the CAL), or events which do not have reconstructed tracks but have information in the CAL which enables only an estimate of the event direction, thus decreasing the angular resolution of the event due to the lack of information from the TKR[13] (153).

The next process involves reconstruction by the CAL, TKR and the ACD. The first level is the energy evaluation by the CAL reconstruction algorithms. This is followed by the TKR reconstruction that serves to reconstruct the trajectories of the events detected by the calorimeter. The ACD reconstruction then estimates the energy deposited on each of the ACD tiles and ribbons and associates this with the tracks in the TKR. At this stage, the rejection of events caused by charged particles entering the detector from within the field of view is performed. Events which have reconstructed tracks all the way to the edge of the TKR module and points to an active region of the ACD which has significant deposited energy (which are too large to be classified as backsplash from the CAL) or less sensitive areas in the ACD (corners, gaps or between tiles) are filtered and classified as background[14] (153). The rejection of the charged particle background removes $\sim 95\%$ of downlinked data, in which $\sim 10\%$ of the γ-ray sample is lost (153).

Event trigger and filtering then lead to event classification processes. There are four event classes within the PASS7REP event classification scheme used in this work. The

[13]This may be the result of γ-ray photons entering the LAT at large incident angles, missing most of the tracker or resulting in broader scattering as it interacts with a larger cross-section of the converter-tracker planes (153).

[14]It must be noted that misclassification of γ-rays as charged particles can occur during very bright solar flares due to energy deposition in the ACD from solar flare X-rays ((153) and references therein).

event classification system is nested such that each event class is a subset of the previous event class. The succeeding event class will have stricter selection cuts compared to its previous class. As such, each event class is determined fundamentally by the types of constraints placed on the reconstruction of the events. The constraints which determine these classification cuts are the quality of the energy and direction reconstruction, probability of γ-rays from various event analysis (this step follows the reconstruction process), and the overall probabilities of γ-rays from the final classification step of the event analysis (153).

P7TRANSIENT

Based on the selection criteria, this event class has the least number of cuts, hence it is the least pure of the event classes. This is only used for the analysis of transient sources such as γ-ray bursts. The cuts applied for this event class should maintain a high efficiency for γ-rays while limiting residual background rate[15] to only a few Hz (153).

P7SOURCE

This event class is a subset of the P7TRANSIENT and is used for single point source analysis over long temporal periods and thus, has more stringent constraints than the P7TRANSIENT event class. Further to this, residual cosmic ray background can be modelled as an isotropic component and thus will be accounted for in the final output. For the P7SOURCE event class a background rate of less than ~ 1 Hz in the LAT field of view is required in order to maintain a high signal-to-background ratio that would not compromise source detection and characterisation. This event class is used for the analysis of all *Fermi*-LAT data presented in this thesis.

[15]The background rate represents LAT trigger rates due to charged particles or cosmic rays (typically dominated by cosmic rays) (153).

P7CLEAN

A subset of the P7SOURCE class, this is used for the analysis of both source and diffuse γ-ray emission which require tighter cuts to reduce background contamination to ~ 0.1 Hz in the LAT field of view. This enables the background contamination to be at levels below the extragalactic γ-ray background at all energies. The contribution from the total Galactic diffuse background is ~ 1 Hz, most of which is localised along the Galactic plane (153).

P7ULTRACLEAN

As with the P7CLEAN, this is also used in the analysis of the extragalactic diffuse γ-ray emission. As such, even tighter cuts than that used for the P7CLEAN is used in order to reduce background contamination even further below the extragalactic γ-ray background rate (the residual contamination of P7ULTRACLEAN is $\sim 40\%$ lower than that present in P7CLEAN at 100 MeV)[16]. This helps avoid the presence of artificial spectral features in the data (153).

4.5.3 Instrument Response Functions

The LAT Instrument Response Functions (IRF) are largely dependent on the energy of the incident γ-ray photon and the inclination angle[17], LAT components and the accuracy of background selections, event quality selections and event reconstruction algorithms (particularly at lower energies, since the lower energy events are affected to a greater degree by systematics). The LAT IRFs (for PASS7REP data, see Section 4.5.4) can be categorically described by three aspects as presented below:

The Point Spread Functions (PSF)

In short, the instrument point spread function (PSF)[18] is given by the energy of the incident photon, its angle of inclination as it hits the detector and its event class (153; 236). Optimum results are obtained when the electron and positron directions

[16]However, it must be noted that the residual levels become more similar to each other with increasing energy and become approximately equal to each other at 10 GeV (153).

[17]The inclination angle represents the angle between the direction to the source and the instrument's z-axis.

[18]The point spread function (PSF) is defined here as the probability distribution for the reconstructed direction of the incident γ-ray photons from a point source.

are measured immediately after the conversion occurs. If this detection of passage of the charged particle through the TKR strip and the consequent recording of the strip address is missed the PSF will be lowered by a factor of two in resolution. Figure 4.7 shows the PSF as a function of energy at normal incidence at 68% and 95%[19] containment angles for the front and back sections of the TKR (see Section 4.5.1).

The *Fermi*-LAT effective area

The *Fermi*-LAT effective area is also dependent on the energy of the incident photon and its inclination angle, along with its position in the TKR. The effective area also depends on the thick and thin sections of the TKR (see Section 4.5.1), the energy dispersion and the PSF. Figure 4.8 shows that the peak effective area occurs between 1 GeV to 100 GeV. This is the same for the transient, source and diffuse event classes. At lower energies (< 300 MeV (236)), the effective area for the transient class is larger than the effective area for the diffuse class (by a factor of ~ 1.5) at normal incidence (236)). Figure 4.8 shows the effective area as a function of energy for photons which impinge on the instrument at normal incidence (i.e. cos $\theta > 0.975$).

The energy resolution of LAT

The *Fermi*-LAT energy resolution describes how well the energy of the photon is reconstructed based on the energy dispersion[20]. The energy resolution degrades at lower energies due to events which lead to energy being deposited in the TKR instead of the CAL. The energy resolution also degrades at higher energies when there is a leakage of the electromagnetic shower out of the CAL. Another factor which influences the energy resolution is the incidence angle of the incoming γ-ray photon. Larger incidence angles from the z-axis of the detector will result in broader scattering. The energy resolution improves as the incidence angle increases. For this thesis, which considers data within a relatively large energy range from 100 MeV to 100 GeV, the energy dispersion is relatively small, namely $< 5\%$

[19]The 68% and 95% containment angles refer to the angles of a cone which contain 68% and 95% of the events from a point source at a specific energy (133).

[20]The energy dispersion is the fractional difference between the reconstructed energy and the true energy of the events.

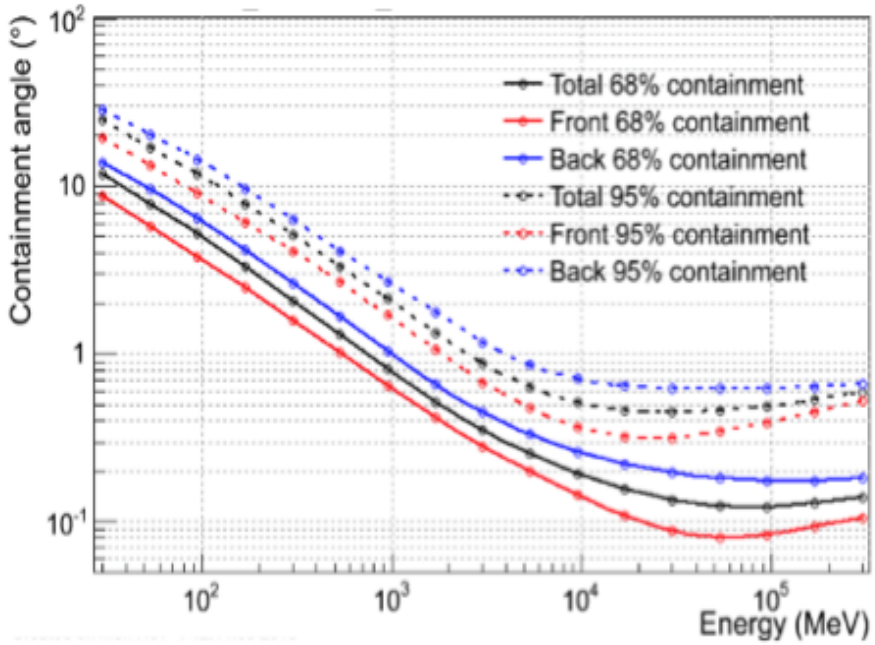

Figure 4.7: LAT PASS7REP PSF as a function of energy at normal incidence at 68% and 95% containment angles for the front (red) and back (blue) end of the TKR (see Section 4.5.1). The total PSF of the instrument as a function of energy at 68% and 95% containment is shown in black. Image obtained from (333).

above 300 MeV (153).

A detailed description of this can be found in (153) and (236)[21].

4.5.4 The PASS7REP Data Version

This research uses PASS7 Reprocessed data (PASS7REP)[22], as it was the most recent data version when the analysis was performed. It involves improvements made to the previous PASS7 data. This included updated instrument calibration constants which results in an increase of up to a few percent in the energies of the events, as well as a more accurate direction reconstruction at energies > 3 GeV. This data version also includes improvements on calorimeter event-position reconstruction (which leads to improvements of the

[21]The current LAT performance parameters are available at www.glast.slac.stanford.edu/software/IS/glast_lat_performance.htm (last viewed: 26/03/2016).

[22]PASS7 raw data were reprocessed primarily due to a bug present in the original processing code.

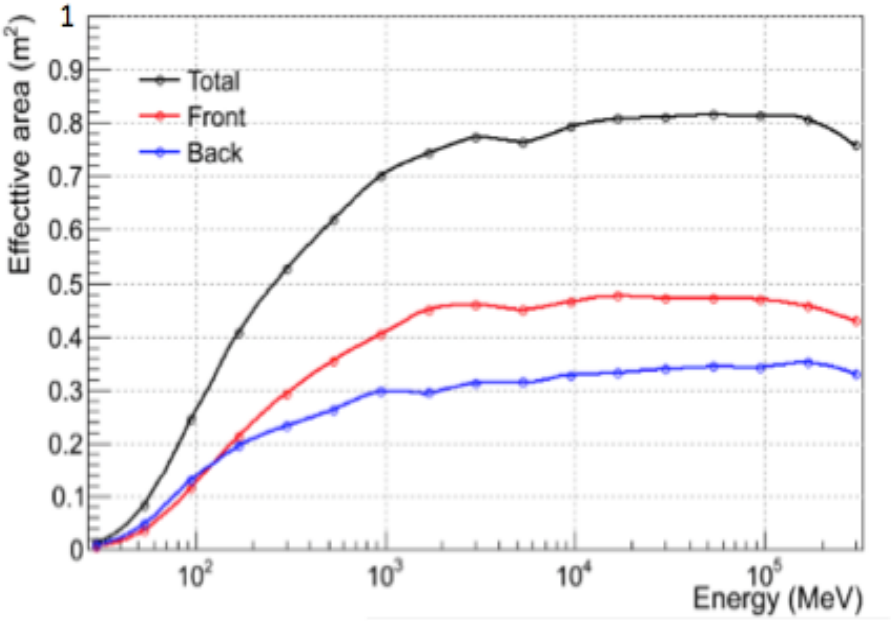

Figure 4.8: The LAT PASS7REP effective area as a function of energy for photons which impinge on the instrument at normal incidence (i.e. $\cos\theta > 0.975$). The red and blue lines show the effective area as a function of energy at the front and back of the TKR respectively, while the black line represents the total effective area vs. energy of the instrument (see Section 4.5.1). Image obtained from (333).

PSF at energies > 5 GeV), an updated galactic and isotropic diffuse models and optimisation of the IRFs used in source class analyses.

4.6 *Fermi*-LAT Data Analysis Pipeline

4.6.1 The Likelihood Analysis

The likelihood analysis (can be found in Fermi Science Tools: Cicerone)[23] is the method used to obtain the best-fit model parameters based on a likelihood constructed from a given source model (see Section 4.6.5). The model is then used to compute source flux measurements. This method is applied in the analysis of *Fermi*-LAT data to produce γ-ray light curves (Section 4.9) for each source in the source sample (Section 3.7). The

[23]http://fermi.gsfc.nasa.gov/ssc/data/analysis/documentation/Cicerone/ Cicerone_Likelihood/ (last viewed: 11/04/2016)

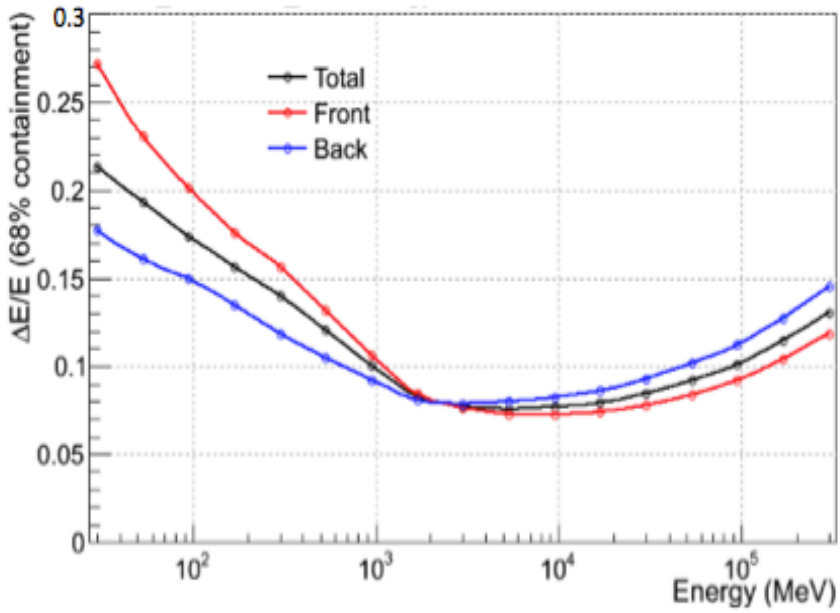

Figure 4.9: The LAT PASS7REP total energy resolution given by the 68% containment radius (energy resolution) vs. energy at normal incidence, shown with the black line. The red and blue curves represent the energy resolution vs. energy at normal incidence at the front and back ends of the TKR respectively (see Section 4.5.1). Image obtained from (333).

method and steps in which this is carried out will be described in detail in the following sections and are summarised in Figure 4.10.

In theory, the likelihood can be described as the probability of obtaining a certain data given an input model of the distribution of the γ-ray sources over the region of interest. The input model[24], which will be discussed in further detail in Section 4.6.5 consists of point sources, extended sources, a diffuse galactic and a diffuse extragalactic background, each designated by a spectral model described by several parameters (e.g. normalisation factor and spectral index).

The parameter used to determine the likelihood that the model describes the data is the Test Statistic, TS, given by:

[24]The input model, also known as the XML source model (in this thesis) describes the distribution of γ-ray sources on the sky, including information on their spectra and intensities. The data, on the other hand, represents the distribution of counts produced by the LAT.

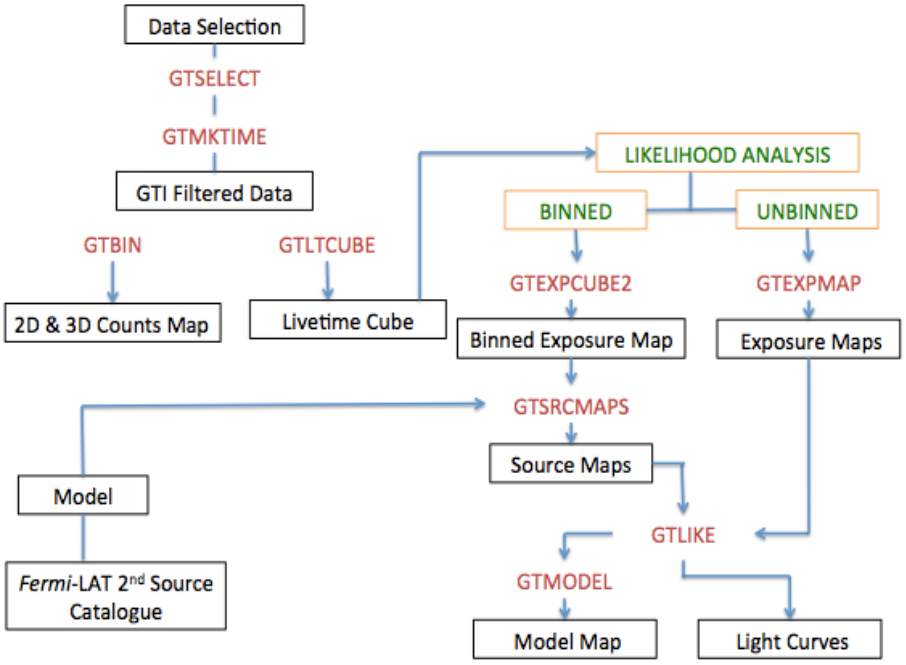

Figure 4.10: Flow chart representing the methods used in the binned (Section 4.7) and unbinned likelihood (Section 4.8) analysis from data selection to producing light curves.

$$TS = -2\ln\left(L_{max,0}/L_{max,1}\right) \tag{4.13}$$

where $L_{max,0}$ is the maximum likelihood of a model without the additional source and $L_{max,1}$ is the maximum likelihood of the model with the additional source at the specified location. The former represents the null hypothesis (133).

For a large number of counts, the TS is asymptotically distributed as $\chi^2 x$ (where χ^2 represents the distribution and x is the number of parameters of the additional source) according to Wilkes Theorem (133). As such, the TS will be drawn from the χ^2 distribution if no source is present, while the presence of a source will result in a fluctuation, such that a larger TS will suggest a source is present (rejecting the null hypothesis). The approximate significance of the detection of a given source is determined by $\sigma = \sqrt{TS}$ (133). This depends on the number of free parameters used to describe the source (see Section 4.6.5).

4.6.2 Extracting *Fermi*-LAT data

Data in the form of photon files are first obtained from the *Fermi* Science Support Centre (FSSC) data server[25]. The data for each source are downloaded by specifying the source name, the start and end times of the observation period, the energy range and the region of interest. The region of interest (ROI) specifies the area around the source that is required for the analysis. A ROI of 15° is chosen around the source. This is determined by the PSF at 100 MeV (the PSF is larger at lower energies, see Figure 4.7).

Along with this, the spacecraft data file is also obtained. The spacecraft file contains information on the instrument orientation and position at 30 second intervals. This also includes information on when the instrument was operating in the 'survey' mode which is required when performing good time selection cuts (see Section 4.6.3).

4.6.3 Performing Selections and Cuts to the Data

In order for the likelihood analysis to be carried out, data extracted from the LAT database must be processed by the application of appropriate selection cuts. These are done using the *Fermi* Science Tools. The selection cuts follow a certain procedure and format. Details of this will be discussed in the sections below.

Event Selection with GTSELECT

For source analysis, the source event class selection is applied to data from the extracted photon files. This is done by running the GTSELECT routine. GTSELECT applies the appropriate event selection cuts by filtering the extracted photon file by row, based on a specified criteria. For this thesis, a source event class (P7SOURCE) was specified within the energy range of 100 MeV and 100 GeV[26]. The ROI of 15° from the 2FGL position is used as discussed above. This selection cut also specifies the maximum zenith angle, which for PASS7REP data is 100°. The zenith angle cut removes cosmic-ray induced γ-rays from the limb of the Earth's atmosphere. In the event selection, the monitoring

[25] http://fermi.gsfc.nasa.gov/cgi-bin/ssc/LAT/LATDataQuery.cgi (last viewed: 11/04/2016)

[26] This energy range was chosen as not many events are expected at energies > 100 GeV as the number of events observed are dependent on the spectral properties of the source and the energy-dependent effective area of the instrument (see Section 4.5.3). Furthermore, the systematic errors from the detector at higher energies are larger (see Section 4.5.1).

period as well as the source position (right ascension (RA) and declination (dec)) are also specified (see Table 3.1).

The output from the GTSELECT routine is a FITS file which is then ready to be processed with the GTMKTIME routine.

Good Time Interval (GTI) Selection with GTMKTIME

Next, a good time selection (also known as the Good Time Interval (GTI)) cut is applied to the event filtered dataset. This uses the GTMKTIME routine and information from the spacecraft data to make 'good' time selection cuts during which the instrument was collecting data while in 'survey' mode and removes periods in which the source was observed close to the Earth's limb. The GTMKTIME also corrects for the rocking angle[27], with a selection cut of $< 52^{\circ}$ (DATA_QUAL==1 && LAT_CONFIG==1&& ABS(ROCK_ANGLE)<52) which eliminates data during pointed mode observations.

In effect this routine first uses the spacecraft data and generates a set of good time intervals based on the specified cuts. This is then combined to the times present in the event filtered dataset. All times that fall outside the GTI of the filtered dataset will then be removed from the output. The result is a list of new GTIs (i.e. time range when the data can be interpreted as valid) and written to the GTI extension of the final FITS output.

4.6.4 The Preliminary Analysis and Information on the *Fermi* Science Tools

Once the appropriate selection cuts are applied to the photon files, the datasets are now ready to be processed to compute the instrument exposure and γ-ray count distributions for each source. This process provides the necessary information (i.e. actual data) which the likelihood estimator uses to produce the best fit based on both model and observed data (see Section 4.6.1).

[27] *Fermi* rocks to the left and right on alternate orbits in order to enable the LAT to cover a larger fraction of the sky. The rocking angle cut will also minimise contamination from the Earth's limb (in addition to the zenith angle cut).

Producing the Counts Map and Counts Cube with GTBIN

First, the GTI filtered datasets are used to produce a counts map under the CMAP algorithm using the GTBIN tool. This process provides a 2-dimensional spatial image of the photon distribution based on the GTI filtered dataset. The output from this routine is a counts map (also referred to as a sky map) which depicts the 100 MeV and 100 GeV γ-ray photon distribution within the chosen ROI, centred on the source.

The counts cube, CCUBE is computed using the GTBIN routine. This produces a 3-D map which bins the observed counts into an X-Y position plane with a Z photon energy axis. This counts cube is represented by a square binned-region within the circular acceptance cone defined by the region of interest. The output from this is used as an input when calculating the best fit parameters during a binned likelihood analysis.

The projection method specified for the generation of both the counts map and counts cube is Aitoff [AIT] from the Hammer-Aitoff projection which represents the equatorial case of the zenithal equal area projection. This reduces distortion in the polar regions compared to other types of projections. This is the most common all-sky projection method used (254).

'Livetime' Cubes using GTLTCUBE

The 'livetime' cube is created by using the GTLTCUBE tool. This essentially represents the time during which the instrument spends observing the target source at a given inclination angle. This is because the number of counts observed from a particular source is dependent on the instrument's 'livetime'.

The 'livetime' cube is calculated from the GTI filtered dataset over the specified time range within that dataset along with instrument pointing information obtained from the spacecraft file. This produces a three dimensional 'livetime' cube which comprises the sky position and binned over the inclination angle (i.e. instrument z-axis). The resulting 'livetime' cube is a FITS file and is used as an input parameter in the likelihood analysis.

Exposure Maps with GTEXPMAP and GTEXPCUBE2

In this section, the two types of exposure maps using two different tools are presented. Exposure maps generated for the unbinned and binned likelihood analyses are done using GTEXPMAP and GTEXPCUBE2 respectively.

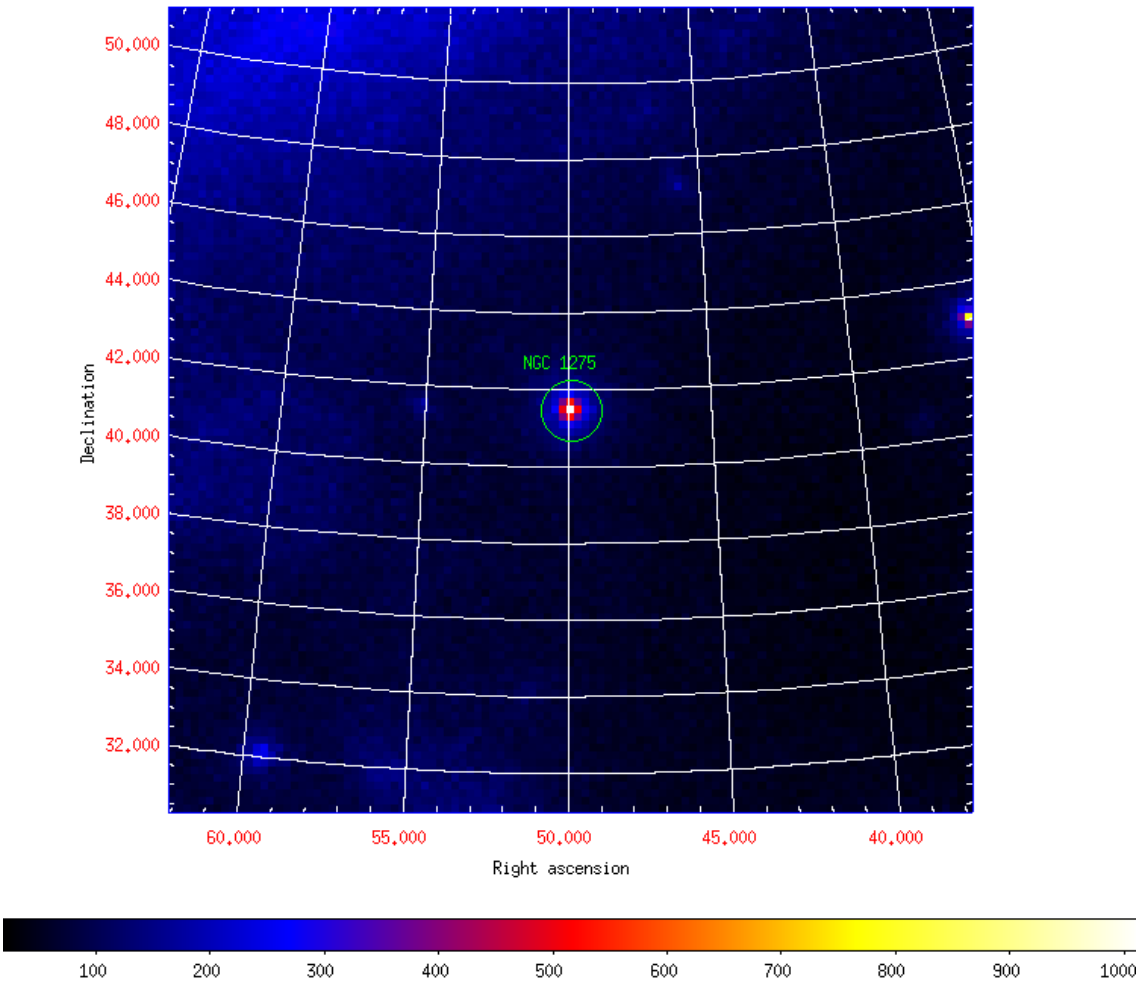

Figure 4.11: The counts map (sky map) constructed using the GTBIN tool. This shows the distribution of γ-ray photons over the ROI centred on NGC 1275 (green ring) for the observation period of 5.5 years (i.e. between 04/08/2008 - 04/02/2014). The colour scale shows the number of photon counts present in a given position in the counts map.

The exposure map generated by the GTEXPMAP tool shows the exposure of the instrument as a function of position which is used to calculate the predicted number of photon counts at a given inclination angle and a given position in the sky. As such, the exposure maps are dependent on the instrument response (i.e. effective area, energy dispersion and the PSF). The GTEXPMAP tool uses the 'livetime' cube to determine the time the instrument spends at a given inclination angle. The resulting map, is a total exposure map for the number of counts that could be observed for a specified position in the sky at a given energy.

The exposure cube is generated by the GTEXPCUBE2 tool for the purpose of carrying out the binned likelihood analysis. This map is generally an all sky exposure map. The difference between the exposure map and the exposure cube is that the latter generates different maps for a specified energy bin, and is not integrated over the energy band pass.

4.6.5 The XML Source Model

The XML source model is an input model which is needed to calculate the likelihood that the model describes the data (see Section 4.6.1). In general, the XML source model consists of point sources, the galactic diffuse emission for the P7REP_V15 data, GLL_IEM _V05_REV1.FIT and the extragalactic isotropic source model, ISO_SOURCE_V05.TXT. For certain sources (e.g. BL Lacertae), which are located close to an extended source (within the ROI), contribution from the extended source must be added to the XML file. The analysis of BL Lacertae required the addition of the Cygnus Loop source emission, obtained from the Extended Source Template Archive[28] in the XML model.

Each point source within the XML model file is given a spectral model as well as the right ascension (RA) and declination (dec) of the source. The parameters for sources within the target's ROI are allowed to vary, while parameters for sources outside this field of interest is fixed to the values published in the Second Fermi Source Catalog (192). For both the power-law and log parabola spectra, the normalisation prefactor as well as the spectral indices are allowed to vary. In this research, MRK 421, MRK 501 and OJ 287 use a power-law spectrum, while BL Lacertae, 3C 273, 3C 279, 3C 454.3 and NGC 1275 use a log parabola as given in the 2FGL catalogue. The functional form of both these

[28] www.fermi.gsfc.nasa.gov/ssc/data/access/lat/2yr_catalog/ (last viewed:23/03/2016).

spectral models is given by Equations 4.14 and 4.15.

$$\frac{dN}{dE} = N_0 \left(\frac{E}{E_0} \right)^{\gamma} \tag{4.14}$$

where $N_\circ$ is the normalisation prefactor, γ is the photon index and $E_\circ$ is the scale.

$$\frac{dN}{dE} = N_0 \left(\frac{E}{E_b} \right)^{-(\alpha+\beta \log(E/E_b))} \tag{4.15}$$

where N_0 is the normalisation prefactor, α and β are the spectral and curvature indices respectively and E_b is the scaling parameter which is usually fixed near the lower energy range of the spectrum being fit (76).

Calculating the Model Counts Map with GTSRCMAPS

This particular tool and its generated map is only used for binned likelihood analyses. The model counts maps is a product of the XML spectral model for each source and the exposure at the source position. This is then convolved with the effective PSF.

The result is a FITS data structure file with each extension corresponding to a source in the XML model file. Each extension then contains a counts map binned in space and energy for the given source.

4.7 *Fermi*-LAT Binned Likelihood Analysis in Conjunction with the XML Source Model

The binned likelihood analysis for research in this thesis is the first step in a two-stepped approach, conducted for the purpose of determining the best-fit γ-ray properties of the target sources in the sample. The binned likelihood analysis is performed over the entire monitoring period, as defined in Table 4.3 following the pipeline shown in Figure 4.10. The selection cuts used in the binned likelihood analysis is given in Table 4.2.

In order to perform the binned likelihood analysis, the data is first selected using the event and time selection cuts as described in the GTSELECT and GTMKTIME above. Then a counts map and a counts cube are created. The counts map represents all the counts summed over the photon energies while the counts cube represents the counts map this time with a z-axis representing the photon energy.

Instrument	Selection Criteria
ScienceTools Version	v9r33p0
IRF	Reprocessed PASS7 (PASS7REP)
Event Class	source
Zenith Angle Cuts	100°
Rock-Angle cut	<52°
Energy Range	100 MeV - 100 GeV
Radius of Interest	15° (centred on source)
TS Threshold	See Table 7.1
Likelihood Analysis	Binned
Binning Timescale	5 years
Start date	MJD 54682 (4 August 2008)
End Date	MJD 56692 (2 April 2014)

Table 4.2: Summary of *Fermi*-LAT instrument specification and data selection cuts for all eight sources.

Once this is complete, the 'livetime' and exposure are computed. As with the unbinned likelihood analysis, the 'livetime' cube is generated with GTLTCUBE. However, unlike the unbinned likelihood preliminary analysis, the exposure map for a binned likelihood analysis requires the generation of a complete sky exposure map for the 'livetime' computed. This represents the predicted number of counts in a certain position over the entire sky at a certain energy. This is followed by the generation of a source map with the GTSRCMAPS tool.

In order to perform the binned likelihood, the GTLIKE routine is performed. GTLIKE applies one of five optimisation algorithms to maximize the likelihood function as discussed in Section 4.6.1. For the *Fermi*-LAT analysis presented in this thesis, the MINUIT[29] algorithm was used. This algorithm determines the best fit to the spectral parameters in the XML source model. The GTLIKE tool uses output from the other tools as well as spectral information of each source from the XML source model to determine the best fit to the normalisation and spectral index parameters by maximising the likelihood that the data fits the model, given by maximising the TS value (see Section 4.6.1).

[29]http://seal.web.cern.ch/seal/snapshot/work-packages/mathlibs/minuit/ (last viewed: 10/04/2016).

Source	Purpose	Duration	Date
PKS 2155-304	quiescent-state	3 mths	11/08/2012 - 16/10/2012
MRK 421	ToO Campaign	6 days	12/04/2013 - 17/04/2013
MRK 421	long-term	5.5 yrs	04/08/2008 - 04/02/2014
MRK 501	long-term	5.5 yrs	04/08/2008 - 04/02/2014
OJ 287	long-term	5.5 yrs	04/08/2008 - 04/02/2014
BL Lacertae	long-term	5.5 yrs	04/08/2008 - 04/02/2014
3C 273	long-term	5.5 yrs	04/08/2008 - 04/02/2014
3C 279	long-term	5.5 yrs	04/08/2008 - 04/02/2014
3C 454.3	long-term	5.5 yrs	04/08/2008 - 04/02/2014
NGC 1275	long-term	5.5 yrs	04/08/2008 - 04/02/2014

Table 4.3: Observation periods over which light curves were analysed for this research. The purpose of the observation, i.e, short-term or long-term study, are also specified.

The output from the binned likelihood analysis provides the integrated flux and the associated TS value for each source present in the ROI over the duration analysed. This information is then used to refine the source model.

4.7.1 Refining the XML Source Model

The XML source model (see Section 4.6.5) is refined to include only sources with significant TS values above a threshold of 10[30]. Removing sources with $TS < 10$ will remove some of the noise as well as contribution from sources which may not be producing γ-rays during the observation period[31]. This, will then reduce the possibility of miscalculating the likelihood of how well the model describes the data.

4.7.2 Generating a model map with GTMODEL

For the purpose of testing the outcome of the binned likelihood analysis and the accuracy of the refined XML source model (containing only sources with $TS > 10$), a model map is

[30] A TS of 10 signifies detection at a $\sim 3\sigma$ level (133).

[31] Some of the sources present in the sample are variable, and as such, have periods during which they are quiet at γ-ray energies. If this occurs during the time frame used in the analysis, the XML source model may not reflect the accurate expected distribution of γ-rays in the ROI.

generated using the GTMODEL tool. This tool provides the user with a means of assessing the accuracy of the XML model. The generated model map will then be used to determine the percentage residual between the counts map and the model map.

The GTMODEL routine produces a counts map of the region of interest based on the fitted model. First, the fitted model is scaled based on the individual source maps produced with the GTSRCMAPS tool, which are then all used to produce the final model map.

Next, a percentage residual map (Figure 4.13) is created in order to compare the observed counts map (generated with GTBIN) and the expected model map (generated with GTMODEL). The percentage residual map is produced by first subtracting the model map (Figure 4.12) from the sky map (Figure 4.11). The residual is then divided by the model map to obtain a percentage residual map (see Equation 4.16 and Figure 4.13). If there is a large difference[32] between both maps, then these counts must be accounted for by refining the XML model to include the contribution of γ-ray photon counts from the source present in the counts map (which are not present in the model map). When this is complete, the GTLIKE routine is carried out again. The aim is to achieve a minimal difference between the counts map and the model map (i.e. all sources observed by *Fermi* during the observation period have been accounted for by the XML model). Once this criteria is satisfied, the source model is ready to be used in the unbinned likelihood analysis to produce source light curves.

$$\text{Percentage Residual Map} = \frac{\text{Sky Map} - \text{Model Map}}{\text{Model Map}} \tag{4.16}$$

4.8 Light Curve Analysis

The γ-ray source light curves are produced using the unbinned likelihood analysis pipeline (see Figure 4.10). The unbinned likelihood analysis is preferred and applied when the number of events per temporal bin is small (such as that required to produce a daily light curve). The steps taken in performing the unbinned likelihood analysis follow the order shown below, and is performed iteratively, to produce γ-ray photon fluxes for each time bin:

[32] This is indicated by a large number of photon counts in the percentage residual map ($> 1\%$).

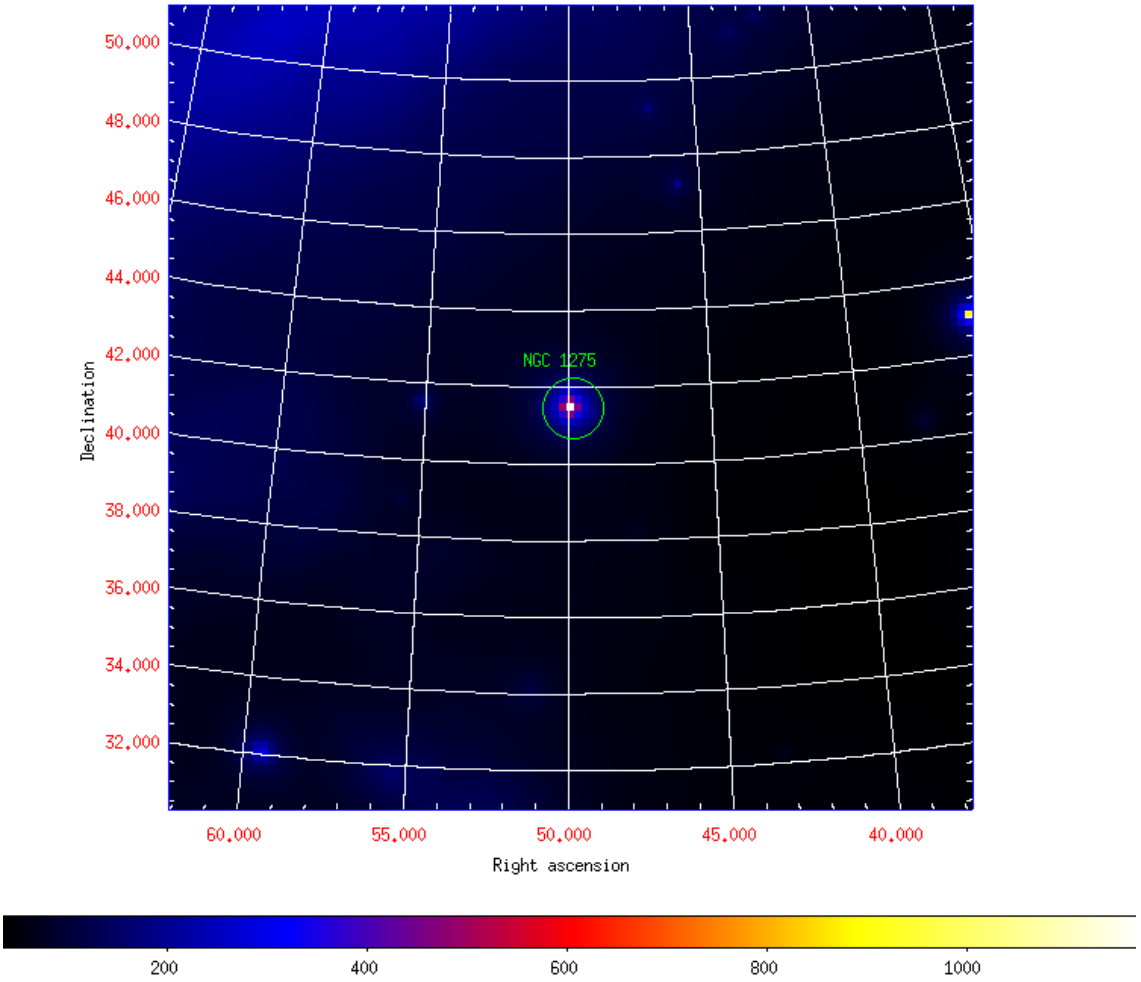

Figure 4.12: The model map of NGC 1275 constructed using the GTMODEL tool based on the fit parameters specified in the XML source model. This shows the modelled counts map based on the binned likelihood fit (as described in Section 4.7.2) for γ-ray counts produced over the ROI centred on NGC 1275 (green ring) for the 5.5 year monitoring period (i.e. between 04/08/2008 - 04/02/2014). The colour scale shows the number of photon counts at a given position in the model map.

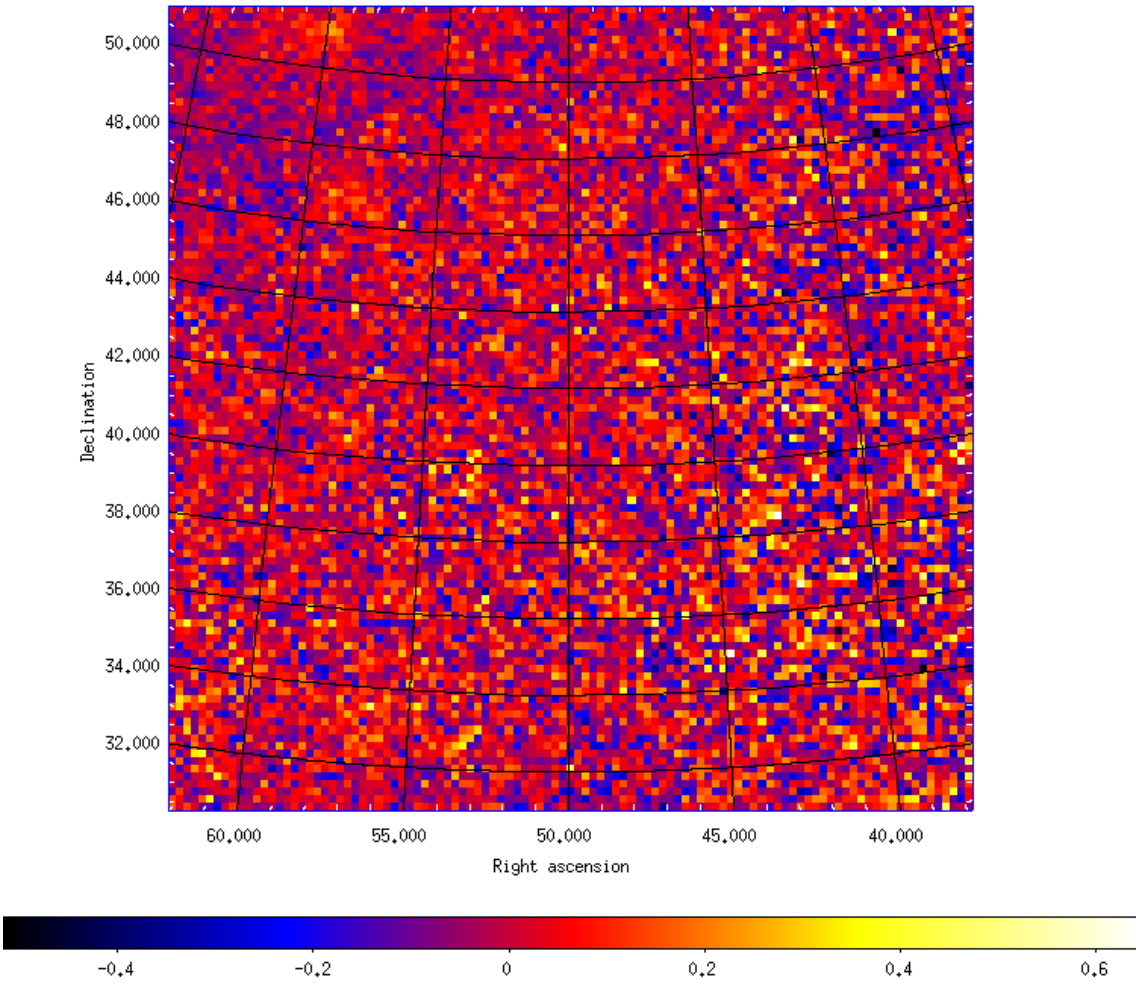

Figure 4.13: The percentage residual map of NGC 1275 obtained by first subtracting the model map (Figure 4.12) from the sky map (Figure 4.11). The resulting residual is then divided with the model map which yielded a percentage residual map (the colour scale represents the percentage residual). A large difference between the observed sky map (counts map) and the model map, given by bright pixels in the percentage residual map ($> 1\%$) may suggest the presence of source(s) unaccounted for by the XML model. In this case, the percentage residual is $< 0.6\%$, suggesting that all sources have been accounted for.

1. GTSELECT
2. GTMKTIME
3. GTBIN
4. GTLTCUBE
5. GTEXPMAP
6. GTLIKE

The GTLIKE tool[33], uses output from the other tools, spectral information for each source from the XML source model to determine the best fit normalisation and spectral index parameters by maximising the likelihood that the data fits the model (see Section 4.6.1). The final output from the unbinned GTLIKE routine is a text file with the date of observation (in Modified Julian Day (MJD)), daily flux measurements and its associated error, the corresponding TS value for the chosen source specified at the centre of the ROI. The output file also includes the spectral index α and a curvature index, β (see Equation 4.15).

4.9 Results from the *Fermi*-LAT Analysis and γ-ray Light Curves

In this section, the sky maps (counts maps), model maps and percentage residual maps, obtained from running the GTBIN and GTMODEL tools for the 5.5 year *Fermi*-LAT datasets are presented for MRK 421, MRK 501, OJ 287, BL Lacertae, 3C 273, 3C 279, 3C 454.3 and NGC 1275 in Figures 4.14, 4.15, 4.16, 4.17, 4.18, 4.19, 4.20, 4.21 respectively.

Images on the top left show the sky map of the source constructed using the GTBIN tool. This depicts the distribution of γ-rays over the ROI centred on the source between 04/08/2008 - 04/02/2014 (5.5 years).

Images on the top right represent the model maps of each source constructed using the GTMODEL tool based on the fit parameters specified in the XML source model. This shows the expected distribution of γ-rays in the ROI based on the 2FGL source catalogue (see Section 4.7.2).

[33]The unbinned likelihood analysis was performed using the *Fermi* User Contributions perl script by R. Corbet obtained from www.fermi.gsfc.nasa.gov/ssc/data/analysis/user/ (last viewed: 27/03/2014).

Images at the bottom of the page show the percentage residual map of the ROI obtained by subtracting the model map from the sky map and consequently dividing the residual by the model map. The lack of large photon counts (percentage residuals for all sources (except 3C 279) were $< 1\%$) indicates that all sources present in the sky map were accounted for by the XML source model.

For 3C 279 (Figure 4.19), it was found that the percentage residual map showed the possible presence of point sources which were not in the XML source model. This was because the five point sources present in the sky map of 3C 279 were not present in the 2FGL catalogue based on which the XML source model was generated. The additional sources were, however, present in the more recent 3FGL catalogue (LAT 4-Year Point Source Catalogue, published in 2015 (83))[34]. In order to determine if and how these sources affect the accuracy of the likelihood analysis and the resulting light curve data, a new XML source model which included the five additional sources was generated and a binned likelihood analysis was performed using the new XML model. It was found that the resulting TS for the five additional sources exceeded the 5σ detection threshold in the new model. However, the 5.5. year integrated flux of 3C 279 with the additional sources present was within error of the flux obtained when the XML model without the additional sources was used. It was also found that each of the additional sources had flux levels that were only $\sim 1\%$ of 3C 279 with an angular separation ranging between 4° and 11° from 3C 279.

Next, it was necessary to determine whether the absence of the additional sources in the XML source model affected the short term flux of 3C 279. This was done by quantifying the variability of the additional sources based on the information given in the 3FGL catalogue. It was found that four of the five additional sources were not flagged as variable sources in the 3FGL catalogue (83). However, one of the five sources, namely 3FGL J1218.0 - 0029, was flagged as a variable source in the 3FGL catalogue with a significance of 2.3σ, 5.2σ, 6.5σ, 3.0σ and 3.4σ in the energy bands 100 MeV - 300 MeV, 300 MeV - 1 GeV, 1 GeV - 3 GeV, 3 GeV - 10 GeV and 10 GeV - 100 GeV respectively (83). Based on the PSF for the PASS7REP data shown in Figure 4.7, it can be deduced that the energy band with the largest PSF ($\sim 10.5^\circ$) corresponds to the lowest energy band (i.e. 100 MeV - 300

[34]The additional sources not present in the 2FGL catalogue were identified in the 3FGL using the location of each additional source in the sky map.

MeV). Although, in this case the PSF is close to the angular separation between 3FGL J1218.0 - 0029 and 3C 279 within the 100 MeV - 300 MeV energy band, 3FGL J1218.0 - 0029 did not exceed the detection significance in this energy band. More importantly, in the energy bands where the significance of 3FGL J1218.0 - 0029 exceeds 5σ (i.e. 300 MeV - 1 GeV and 1 GeV - 3 GeV), the PSF ($\leq 4^{\circ}$ at total[35] 95 $\%$ containment, Figure 4.7) is smaller than the angular separation from 3C 279, making it unlikely that any photon counts from the tail of the distribution will affect the number of photon counts from 3C 279. Apart from this, the integrated flux of 3FGL J1218.0 - 0029 (obtained from the 3FGL catalogue (83)) was only $\sim 0.14\%$ of 3C 279 for the energy bands in which the TS exceeded the 5σ detection significance. Thus, taking into account the small photon count of 3FGL J1218.0 - 0029 when compared to 3C 279, its angular separation of $\sim 11^{\circ}$ from 3C 279 and the effects of the instrument PSF in tandem with the energy bands in which the source exceeded the detection significance threshold suggests that the result of 3FGL J1218.0 - 0029 not being present in the XML source model was not likely to affect the accuracy of the daily binned 3C 279 light curve during the 5.5 year observation period. Since the discrepancies in the flux and spectral index are within error without the presence of additional sources, the original XML source model (without the additional sources) was used to produce the γ-ray light curve for 3C 279.

Table 4.4 summarises the final TS values of each source along with the average flux over the 5.5 year observation period for the 100 MeV to 100 GeV energy range observed with *Fermi*-LAT.

Finally, daily flux measurements were obtained from the light curve analysis (see Section 4.8) to produce 100 MeV to 100 GeV γ-ray light curves for each source in the sample. The flux measurements are given by the observed photon counts per cm^2 per second (ph cm^{-2} s^{-1}). The error bars in the light curves are statistical. The *Fermi*-LAT light curve for PKS 2155-304 is presented in Chapters 5, while the *Fermi*-LAT light curves for the remaining eight sources are presented in Chapter 7.

[35]The total PSF refers to the combined PSF of the front and back sections of the TKR.

Source	TS	Average Flux	Flux Error
MRK 421	59465.1	20.08	0.03
MRK 501	10542.3	5.5	0.05
OJ 287	4858.4	8.9	0.32
BL Lacertae	18784.5	26.8	0.08
3C 273	18646.8	35.9	0.62
3C 279	39889.3	42.8	0.25
3C 454.3	353007.0	198.0	0.59
NGC 1275	31198.3	25.8	0.13

Table 4.4: The final TS value along with the average flux ($\times 10^{-8}$ ph cm^{-2} s^{-1}) and the average flux error ($\times 10^{-8}$ ph cm^{-2} s^{-1}) of the eight blazar sources over a period of 5.5 years between the 100 MeV and 100 GeV energy range observed with *Fermi*-LAT.

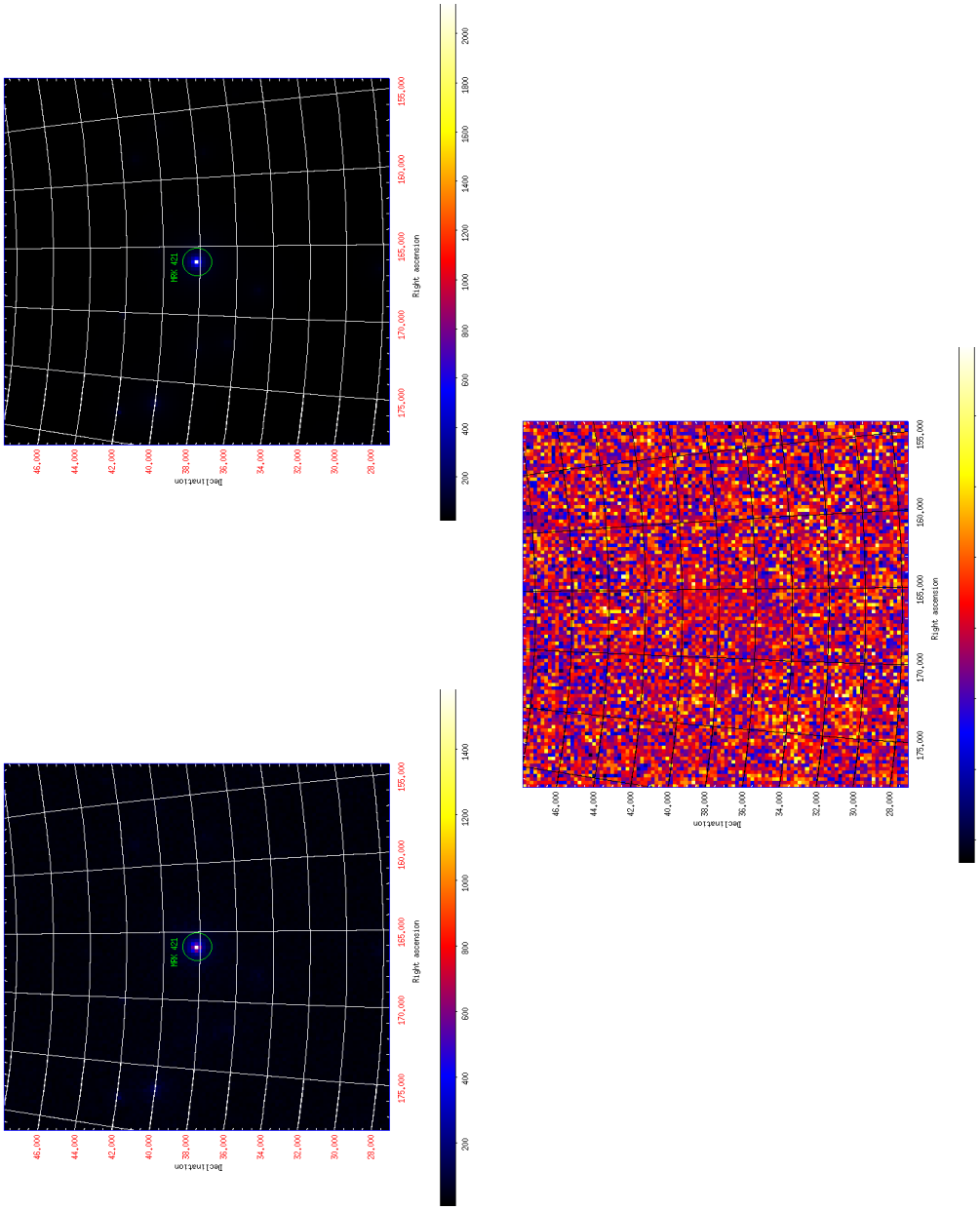

Figure 4.14: MRK 421: sky map (top left), model map (top right), residual map (bottom).

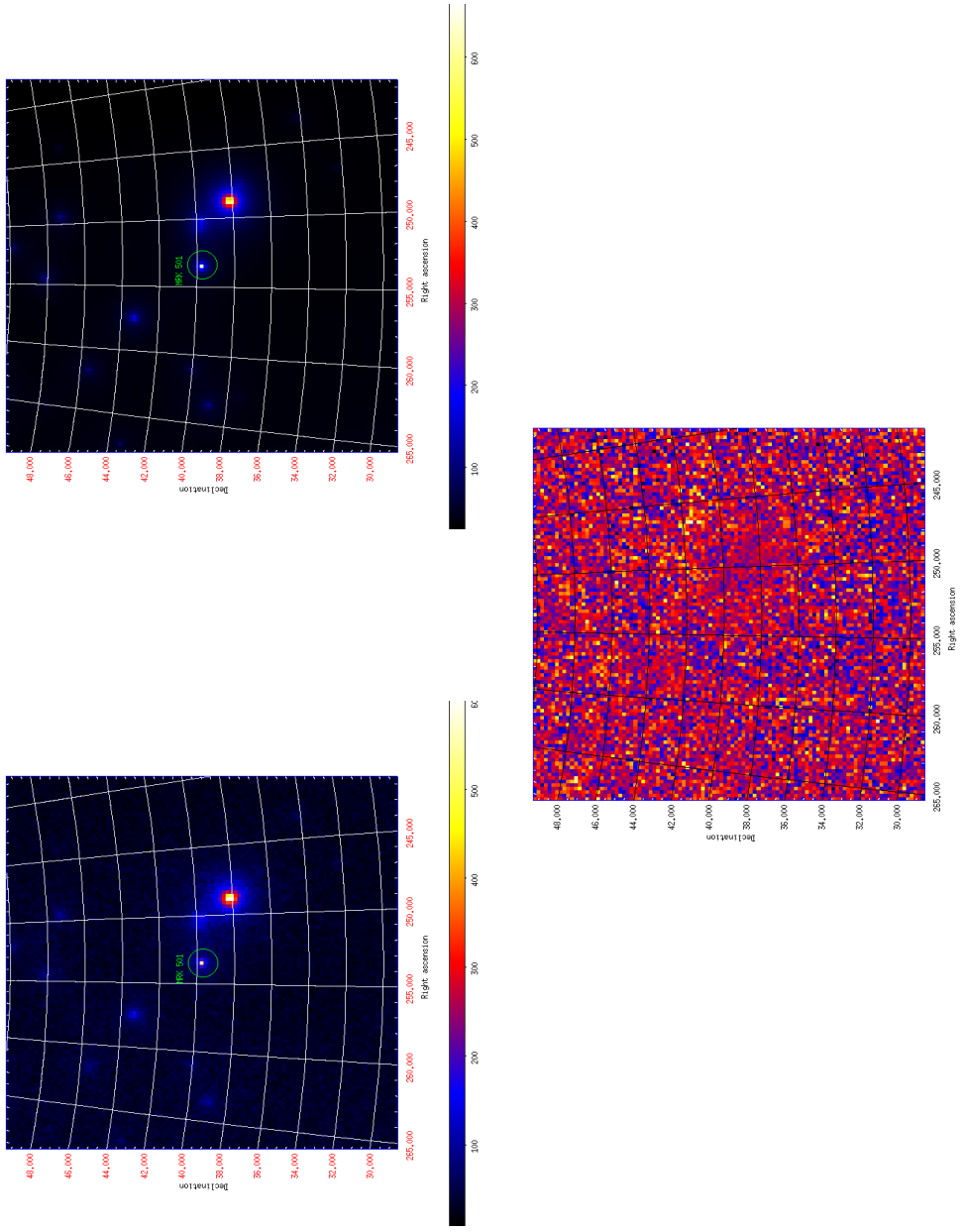

Figure 4.15: MRK 501: sky map (top left), model map (top right), residual map (bottom).

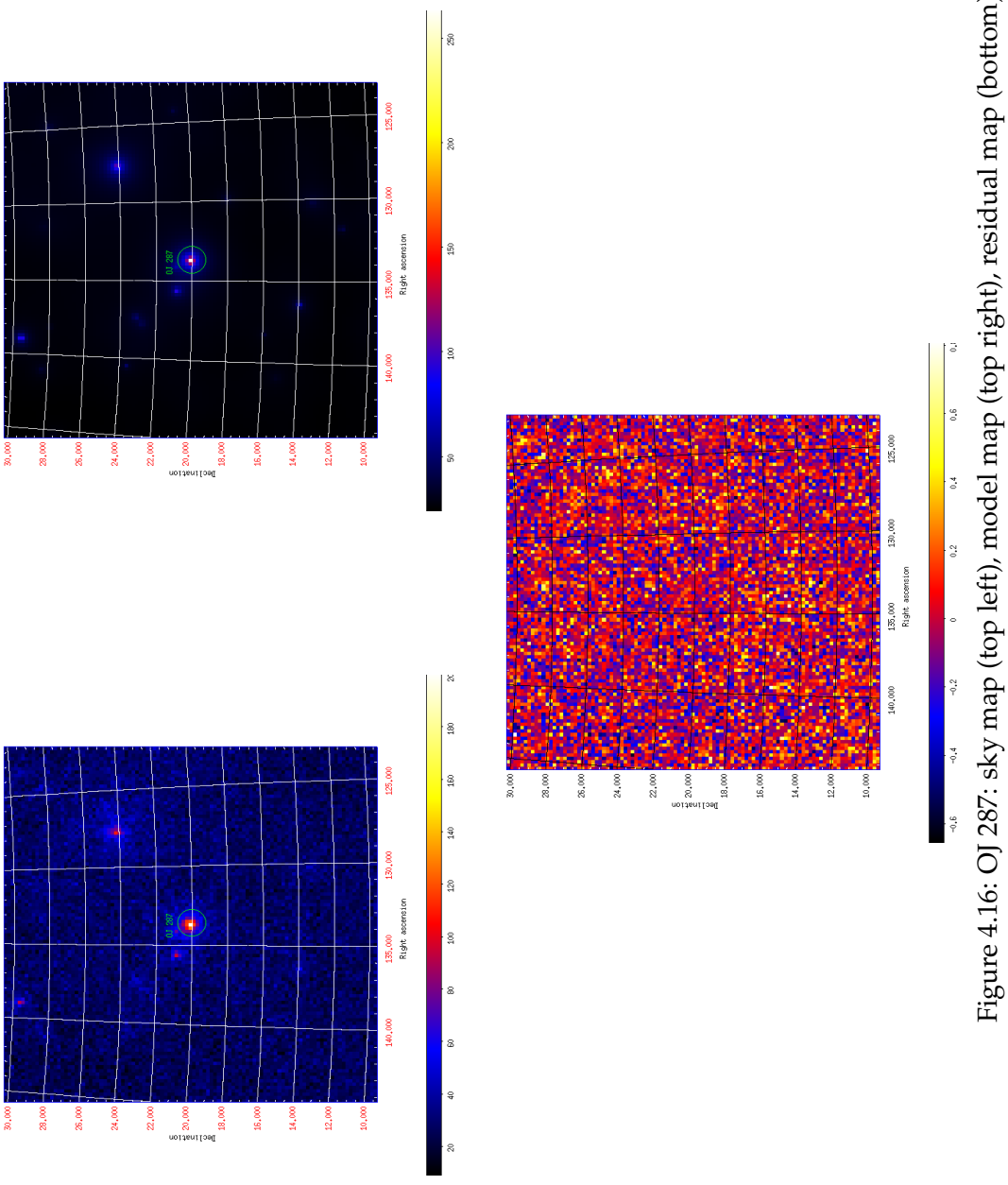

Figure 4.16: OJ 287: sky map (top left), model map (top right), residual map (bottom).

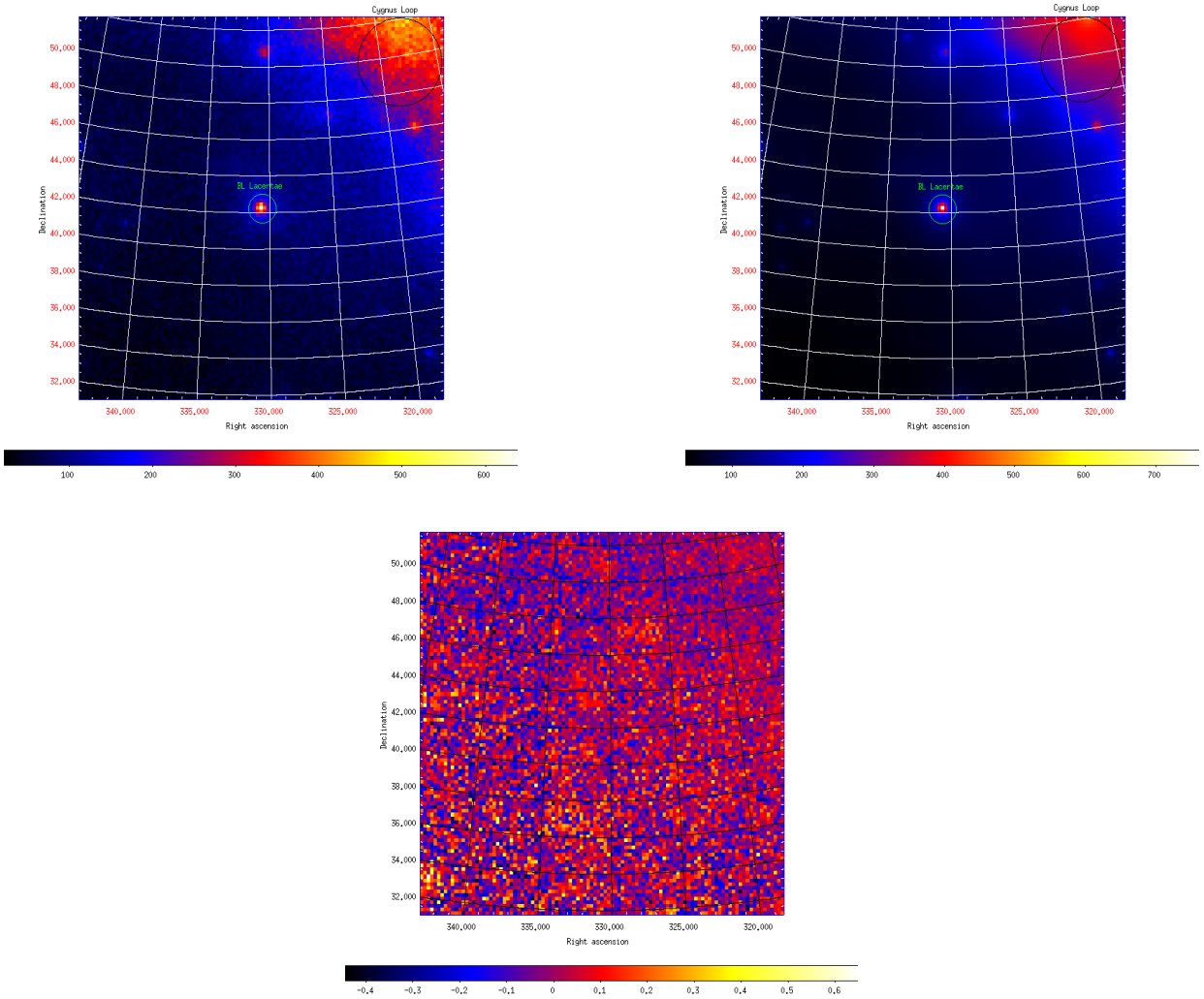

Figure 4.17: BL Lacertae: sky map (top left), model map (top right), residual map (bottom).

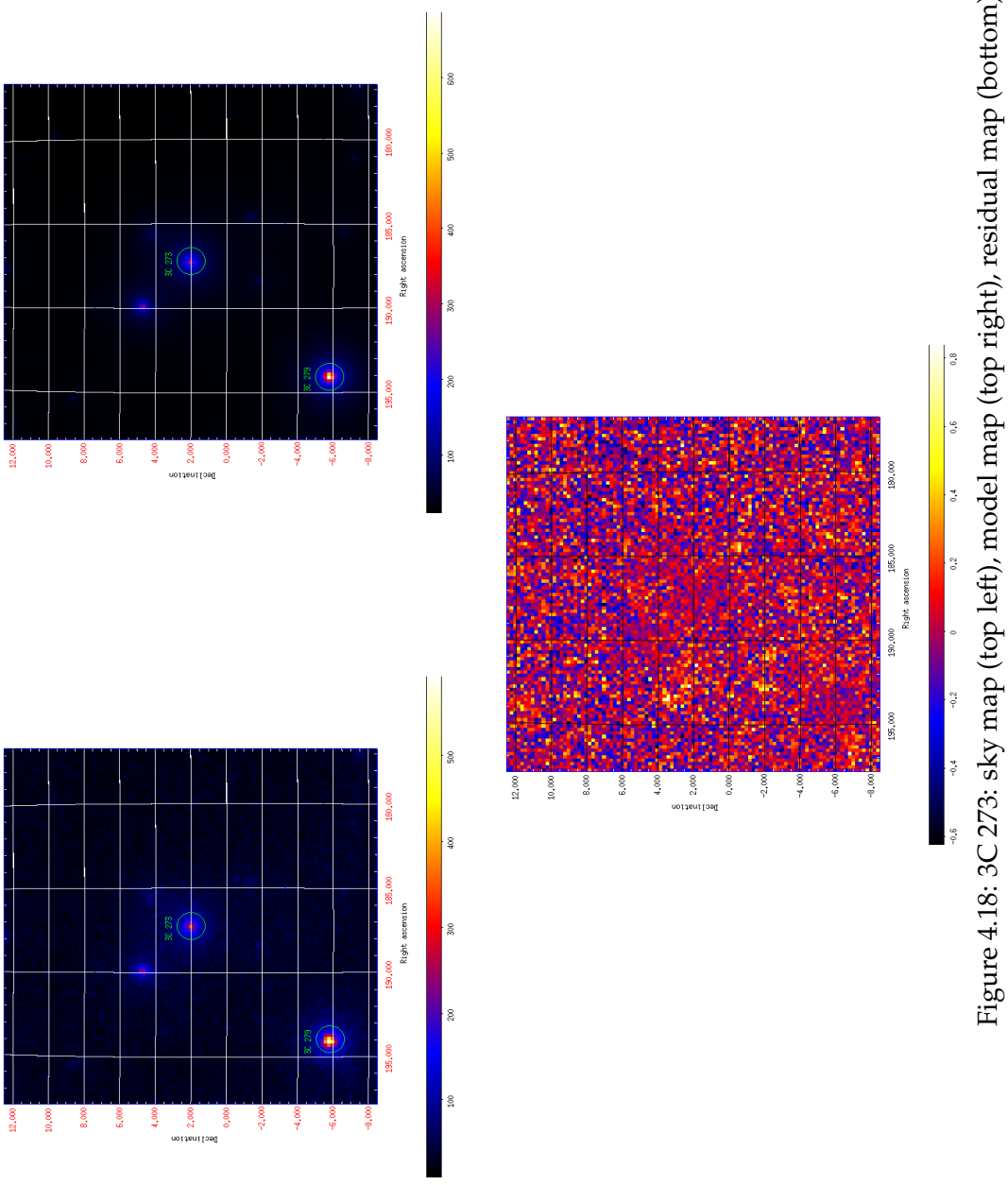

Figure 4.18: 3C 273: sky map (top left), model map (top right), residual map (bottom).

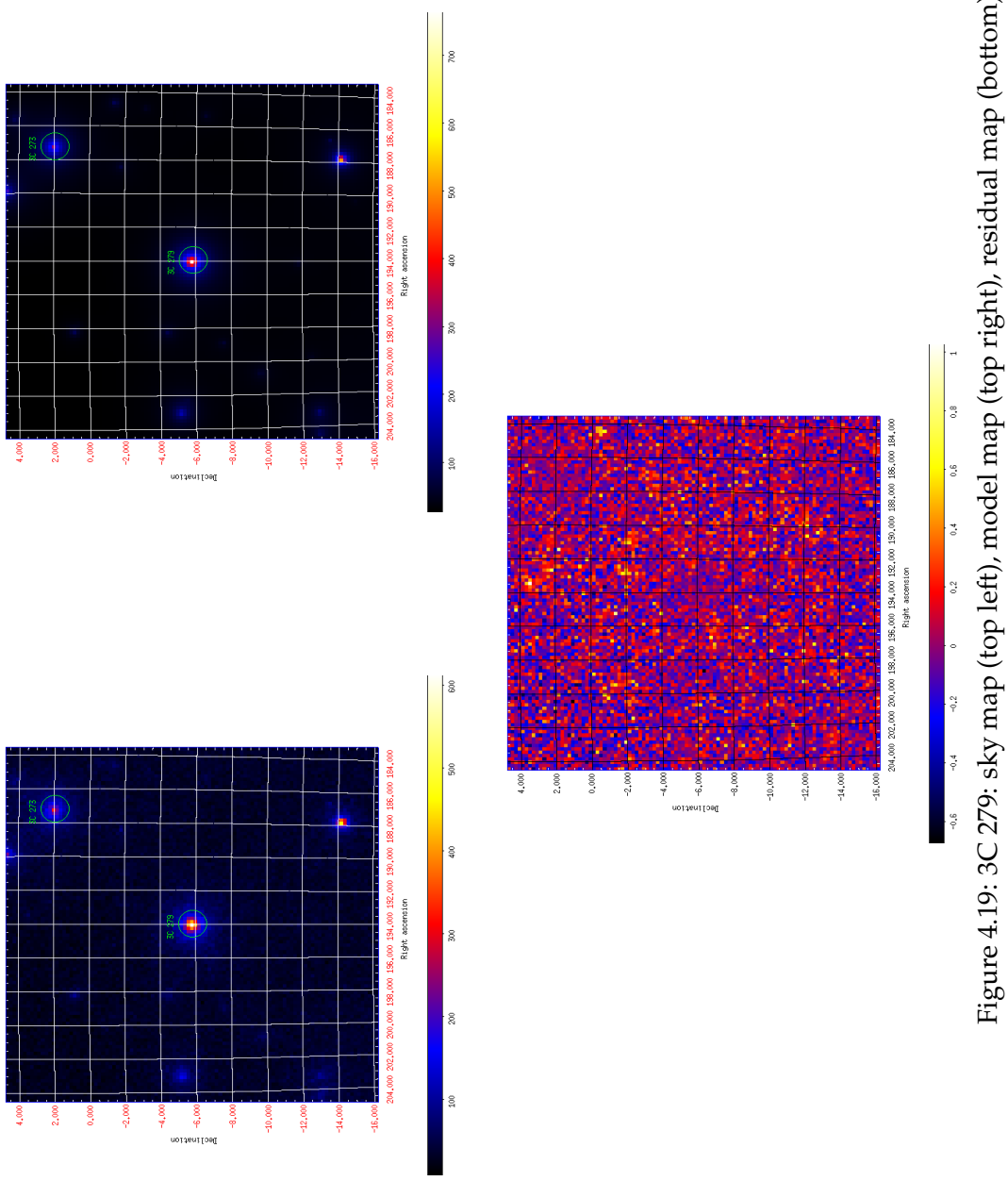

Figure 4.19: 3C 279: sky map (top left), model map (top right), residual map (bottom).

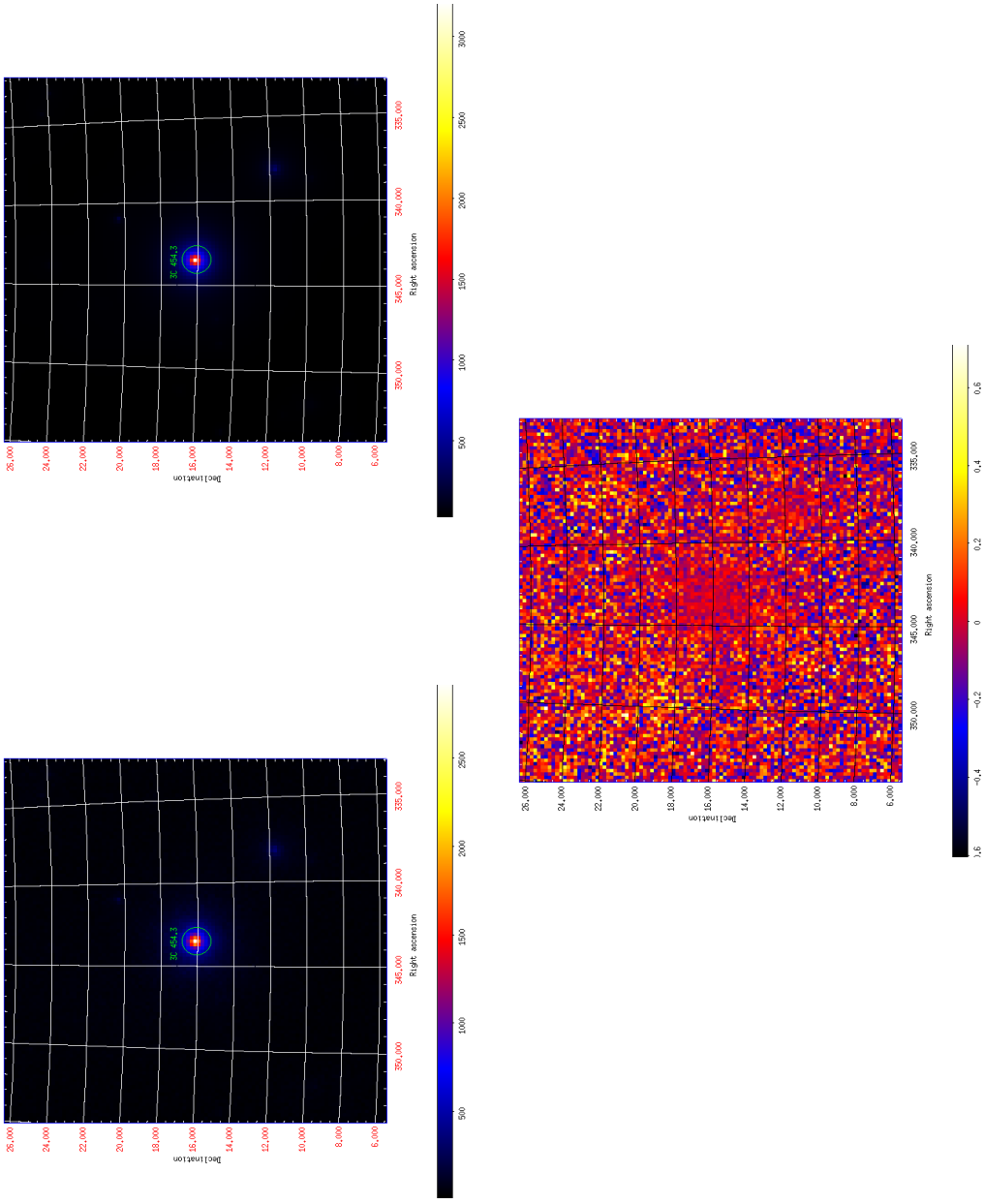

Figure 4.20: 3C 454.3: sky map (top left), model map (top right), residual map (bottom).

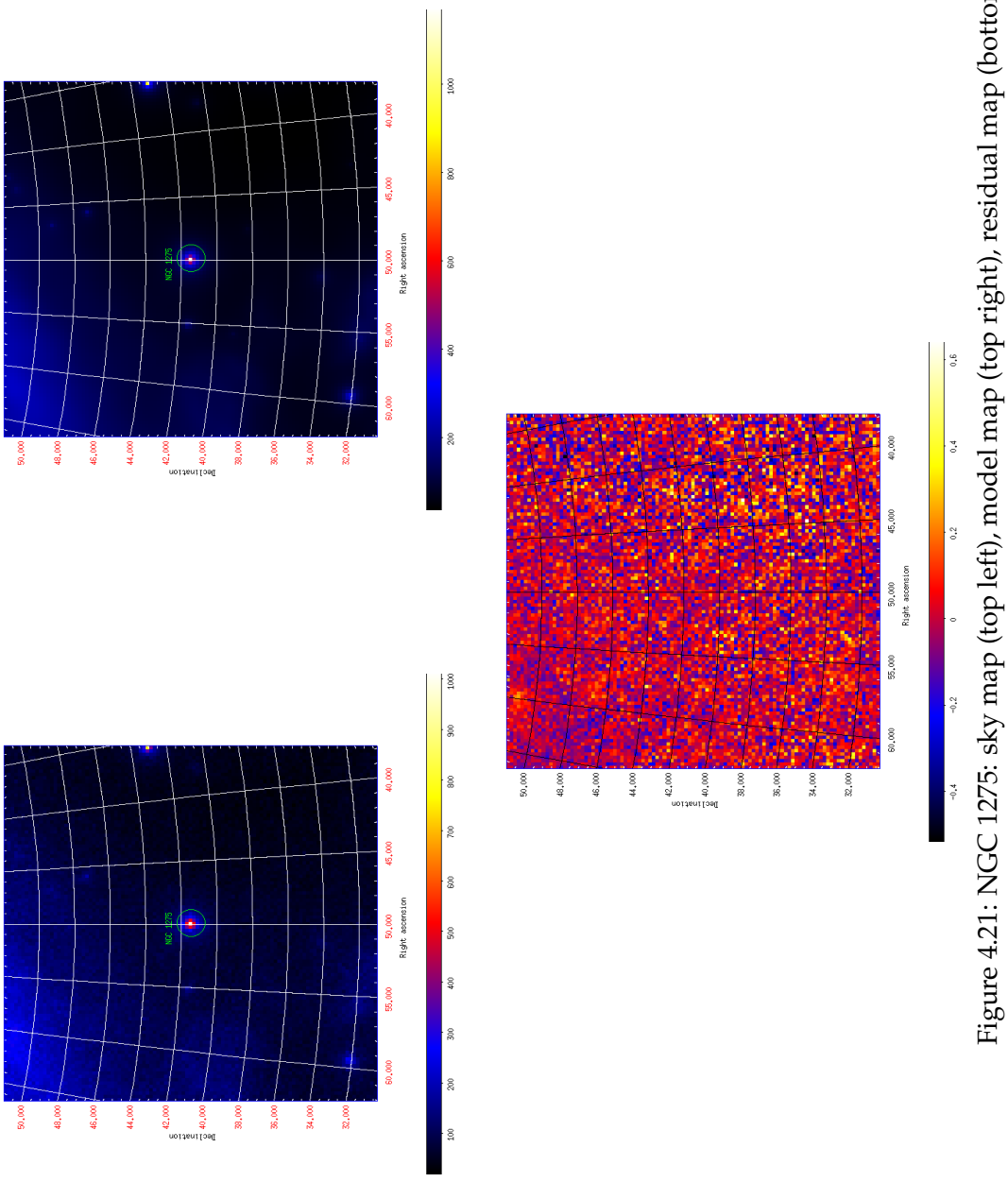

Figure 4.21: NGC 1275: sky map (top left), model map (top right), residual map (bottom).

Chapter 5

Observations of PKS 2155-304 and MRK 421 using SCUBA-2 and Fermi-LAT

This chapter highlights the sub-mm observations conducted on two HBLs, namely PKS 2155-304 and MRK 421. In the first part of this chapter, sub-mm observations of PKS 2155-304 using the SCUBA-2 instrument are presented. This observation campaign was conducted as part of a multi-wavelength endeavour to investigate the correlation between the sub-mm and γ-ray regimes during the object's quiescent state. The *Fermi*-LAT instrument was used to obtain data of the γ-ray component during the same time period. The second part of this chapter will concern the results from a Target of Opportunity campaign on the HBL MRK 421 during a period of outburst in April 2013. This study was aimed at investigating the sub-mm behaviour of this archetypal HBL source during an exceptional γ-ray flare detected by the MAGIC and VERITAS instruments (257) in early April 2013. Once again, the *Fermi*-LAT instrument was used to obtain data on the γ-ray component. For both these objects, studies in flux variability and correlation between the sub-mm and γ-ray energy bands were performed and will be discussed in detail in the following sections.

5.1 HBLs Revisited

Observations and extensive multi-instrument monitoring campaigns of HBLs form an interesting part of blazar studies. These objects exhibit extreme variability on very short timescales. This is most likely due to the Doppler boosting of the spectrum since the jets

of these objects are aligned close to the line-of-sight.

Another important aspect of blazars which drives these ongoing multiwavelength studies is the characteristic feature of the HBL SED, in which the peak of the high-energy component is observed at TeV energies, while the peak of the low-energy component is observed at X-ray energies (see Section 1.3). Based on this, the MeV to GeV energy regime forms part of the lower energy tail of the high-energy component and the sub-mm regime forms part of the tail end of the lower-energy component. Based on widely accepted leptonic scenarios, which invoke either synchrotron self-Compton (SSC) or external Compton (EC) models (see Section 2.6), the sub-mm and γ-ray emission should show evidence for correlation. A correlation between these energy bands would consequently suggest that the emission in both energy regimes could arise from the same population of electrons which, when interacting with magnetic fields within the jet, produce the synchrotron and inverse-Compton components. A strong correlation between the two energy bands would favour an SSC model, while a weaker correlation would suggest an EC scenario is more dominant, in which contribution to the emission also comes from external sources, such as the BLR region or re-radiation from the torus (see Section 2.6), or that there are different emission zones within the blazar jet (114).

Observations of HBLs are limited at sub-mm wavelengths. Recent advances in sub-mm instrumentation techniques (as described in Section 4.2) have enabled these objects to be monitored more closely and with better accuracy, thus prompting the PKS 2155-304 3-month observation campaign with SCUBA-2 in 2012.

5.2 PKS 2155-304 Observations with SCUBA-2 and *Fermi*-LAT

5.2.1 Observations with SCUBA-2

The SCUBA-2 PKS 2155-304 observation campaign was designed to study the sub-mm flux of the object over a duration of several months while the object was in a quiescent state. Based on the monitoring campaign by H.E.S.S. (High Energy Stereoscopic System), which aimed to study the object at TeV γ-ray and optical energies, this SCUBA-2 campaign was designed to obtain observations on similar timescales and over the same

duration[1]. SCUBA-2 observations were thus organised between 11 August 2012 (MJD 56150) and 16 October 2012 (MJD 56216). They were conducted at 3-day intervals, with a minimum of four observations a month. These observations were conducted simultaneously at 450 μm and 850 μm using the DAISY 3-arcminute mapping pattern (240) (see Section 4.3). The average integration time for each observation run during good weather conditions was 15 minutes. This value is derived from the atmospheric opacity, average airmass and target sensitivity calculations obtained from the SCUBA-2 Integration Time Calculator (ITC)[2]. Details of the observations are presented in Table 5.1.

SCUBA-2 raw data were analysed using the SMURF DIMM configuration for a bright compact source as described in Section 4.4. A total of 15 observations was obtained at 850 μm and only a single observation was obtained at 450 μm. This is mainly due to 450 μm observations being affected to a greater extent by atmospheric opacities compared to the 850 μm observations (see Section 4.3.1).

5.2.2 Observations with *Fermi*-LAT

Raw PASS7REP_V15 (reprocessed PASS7) *Fermi*-LAT data for the duration between 4 August 2012 (MJD 56143) and 6 November 2012 (MJD 56237) were obtained from the instrument's data server.

The *Fermi*-LAT observations were binned on daily intervals over the period stated above to correspond to the SCUBA-2 observations. This particular binning interval was chosen (instead of a three-day interval which was the interval between observations at SCUBA-2 wavelengths) because little is known of the variability timescales of the source at γ-ray energies during this observation period. Thus, choosing a binning timescale with a higher resolution will be a safe compromise which would reduce any loss of information.

The data considered for this study include all 'source' class events within a region of interest (ROI) of 15° centred on PKS 2155-304. The energy range for the photon selection was limited to the regime between 100 MeV to 100 GeV. A summary of the data selection

[1]The quasi-simultaneous observations with H.E.S.S. could not be used due to bad weather conditions at the observation site which rendered the results unreliable. Due to this, *Fermi*-LAT data were used in place of H.E.S.S. data (see Section 5.2.2).

[2]http://www.eaobservatory.org/jcmt/instrumentation/continuum/scuba-2/itc/ (last viewed: 03/11/2015)

MJD	Int. Time (s)	τ	Weather Grade	Flux (Jy)
56150	935	0.17	4	0.24 ± 0.02
56153	918	0.07	2	0.25 ± 0.02
56156	922	0.04	1	0.25 ± 0.01
56162	925	0.06	2	0.25 ± 0.02
56177	942	0.07	2	0.27 ± 0.02
56180	918	0.08	2	0.28 ± 0.02
56183	930	0.08	2	0.28 ± 0.02
56186	915	0.08	2	0.29 ± 0.02
56190	917	0.08	2	0.25 ± 0.02
56204	1787	> 0.27	> 5	0.35 ± 0.05
56207	1771	0.24	5	0.27 ± 0.03
56207	1771	0.26	5	0.33 ± 0.04
56210	1771	0.14	4	0.31 ± 0.02
56214	942	0.09	3	0.30 ± 0.02
56216	965	0.08	2	0.31 ± 0.02

Table 5.1: The 850 μm flux measurements of PKS 2155-304 obtained using the JCMT SCUBA-2 instrument over a period of 66 days between 11 August 2012 (MJD 56150) and 16 October 2012 (MJD 56216).

cuts is presented in Table 5.2. A detailed description of the *Fermi*-LAT analysis procedure is described in Section 4.6.

It was found that the *Fermi*-LAT dataset of PKS 2155-304 during the 3-month observation period was highly limited by noise present in the dataset. There are several reasons which may have caused this. PKS 2155-304 is a HBL which typically has its high energy (inverse Compton) peak at very-high-energy (VHE) γ-ray wavelengths (see Section 1.3). This results in more energy being emitted in the VHE range compared to the amount of energy emitted in the 100 MeV to 100 GeV range chosen for this study. This source was also quiescent during the observation period resulting in particularly low flux levels. As a result, it was likely that systematic uncertainties were introduced to the observed photon counts through either convolution of the observed flux with instrument response functions or the presence background noise. For example, temporal bins with low pho-

Instrument	Selection Criteria
ScieceTools Version	v9r33p0
IRF	Reprocessed PASS7 (PASS7REP)
Event Class	source
Zenith Angle Cuts	100°
Rock-Angle cut	<52°
Energy Range	100 MeV - 100 GeV
Radius of Interest	15° (centred on source)
Likelihood Analysis	Unbinned
Binning Timescale	2 Days
TS Threshold	25

Table 5.2: A summary of the *Fermi*-LAT instrument specification and data selection criteria as discussed in Chapter 4.

ton counts may possess large flux errors due to the presence of Poissonian shot noise (172). In order to reduce some of this noise the TS threshold was increased from 10 to 25 to improve the detection statistics from 3σ to 5σ (133). This removed some of the points with large error bars. In order to test the validity of the resulting light curve, a plot of $\frac{observed\ flux}{flux\ error}$ against $\frac{Npred}{\sqrt{Npred}}$ where $Npred$ is the predicted photon counts in a particular time bin, was produced. This plot showed a positive linear trend as expected which indicates that the source model used in the analysis was accurate and the limitation factor on the *Fermi*-LAT light curve was predominantly due to systematic noise.

5.2.3 γ-ray and Sub-mm Light Curves of PKS 2155-304

The light curves from both *Fermi*-LAT and SCUBA-2 observations are shown in Figure 5.1. Of the 15 observations at 850 μm, three were conducted during high atmospheric opacities (Weather Grade 5 with $\tau > 0.2$). The observation conducted on 04 October 2012 (MJD 56204) in particular was obtained at high opacities, $\tau \gg 0.2$ and was consequently removed from further analysis. The average opacity over the 66-day observation period was $\tau = 0.11$ (Weather Grade 3). The average flux obtained during the observation period was $S_{850,ave}$ = (0.28 $\pm$ 0.02) Jy. The maximum and minimum fluxes obtained over the observation period were $S_{850,max}$ = (0.33 $\pm$ 0.04) Jy (MJD 56207) and $S_{850,min}$ = (0.24 $\pm$

MJD	Flux (10^{-7} ph cm^{-2} s^{-1})
56143	0.65 ± 0.35
56145	2.09 ± 0.92
56146	1.98 ± 0.87
56180	1.26 ± 0.54
56185	1.87 ± 0.80
56192	1.69 ± 0.86
56235	1.70 ± 0.83
56237	4.10 ± 1.35

Table 5.3: The *Fermi*-LAT 100 MeV to 100 GeV observations between 4 August 2012 (MJD 56143) and 6 November 2012 (MJD 56237) of PKS 2155-304.

0.02) Jy (MJD 56150) respectively.

Fermi-LAT data consisted of a total of eight flux measurements which survived the threshold value of $TS > 25$. The average flux at 100 MeV to 100 GeV energies was $S_{\gamma,ave}$ = (1.91 $\pm$ 0.81) $\times 10^{-7}$ ph cm^{-2} s^{-1}. The maximum and minimum flux obtained over the observation period is $S_{\gamma,max}$ = (4.10 $\pm$ 1.35) $\times 10^{-7}$ ph cm^{-2} s^{-1} (MJD 56237) and $S_{\gamma,min}$ = (0.65 $\pm$ 0.35) $\times 10^{-7}$ ph cm^{-2} s^{-1} (MJD 56143) respectively.

5.2.4 Variability Studies on SCUBA-2 and *Fermi*-LAT Observations of PKS 2155-304

In order to examine the possibility of variability in both the γ-ray and sub-mm light curves, two separate tests were conducted. The first is a χ^2 test based on the null hypothesis that the flux is constant at the average flux measurement in the respective wavebands. The χ^2 test on SCUBA-2 data resulted in a χ^2 = 24.57 and yielded a reduced-χ^2 of 1.76 (degrees of freedom, d.o.f = 14) with the probability of the result being due to chance, *p*-value = 0.04 ($< 2\sigma$). This suggests that there is no evidence for variability at 850 μm. The χ^2 test using *Fermi*-LAT data resulted in a χ^2 = 34.0, yielding a reduced-χ^2 of 4.86 (d.o.f = 7). This suggests that the *Fermi*-LAT 100 MeV to 100 GeV flux shows evidence for some variability at the $\sim 4\sigma$ level. However, this result must be treated cautiously due to the faintness (i.e low photon counts) of the source at 100 MeV to 100 GeV energies.

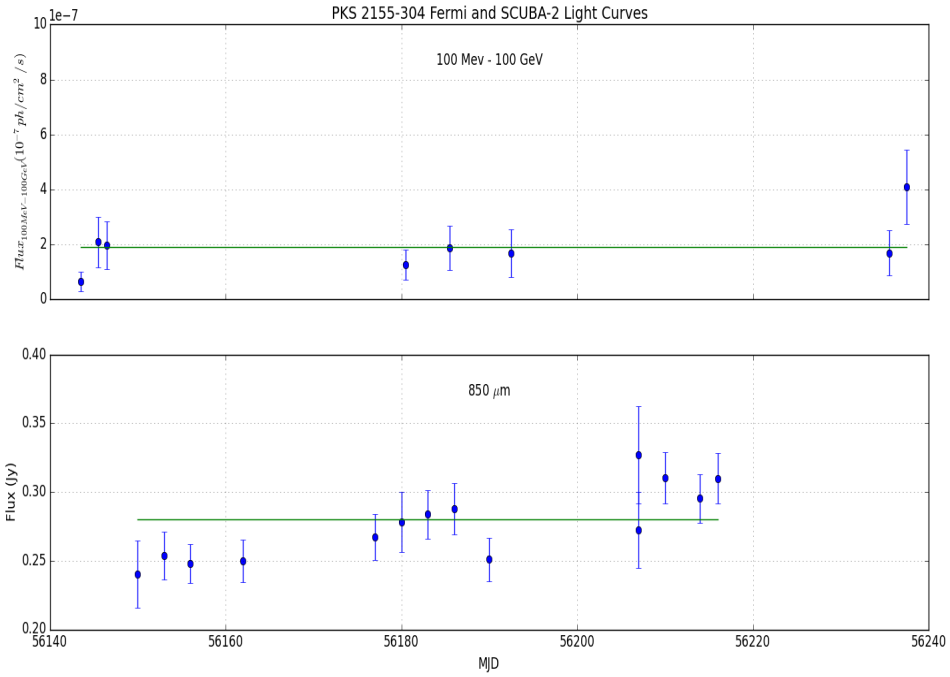

Figure 5.1: *Fermi*-LAT(top) and SCUBA-2 (bottom) observations of PKS 2155-304 between August and October 2012. The line (green) represents the average flux at γ-ray and sub-mm energies. The average *Fermi*-LAT flux is based on the individual flux measurements which exceed the $TS = 25$ presented in Table 5.3.

Secondly, the variability index, V based on the method developed by Hovatta et al. (222) was computed for each light curve (see Section 3.3). The variability index obtained based on the maximum and minimum SCUBA-2 flux measurements was V = 0.049, while the variability index based on the maximum and minimum flux measurements at *Fermi*-LAT energies was V = 0.467. These results indicate that the *Fermi*-LAT observations show a much higher possibility of variability compared to the SCUBA-2 observations. This is in agreement with the χ^2 analysis above. These results are presented in Table 5.4.

The results obtained from the χ^2 tests and variability indices of the γ-ray and sub-mm datasets of PKS 2155-304 hint at a difference in behaviour between the HE γ-ray and sub-mm regimes. However, it must be noted that both the γ-ray and 850 μm datasets were limited by the small number of observations obtained during the 66-day monitoring period.

Waveband	Ave. Flux	χ^2	Red. χ^2	V
sub-mm	(0.28 ± 0.02) Jy	24.57 ($< 2\sigma$)	1.76	0.05
γ-ray	$(1.91 \pm 0.81) \times 10^{-7}$ ph cm^{-2} s^{-1}	34.0 ($< 4\sigma$)	4.86	0.47

Table 5.4: Variability analysis and statistics of PKS 2155-304 at sub-mm and γ-ray energies.

5.2.5 Variations in Opacity

As discussed in Section 4.3.1, observations with SCUBA-2 are susceptible to bad weather conditions in which high levels of atmospheric opacity ($\tau > 0.2$ corresponding to a Weather Grade of 5) affects the measured flux levels. Due to this, it is necessary to ascertain if these fluctuations in opacity result in any correlation between the measured flux in each observation run. The opacities, obtained from the SCUBA-2 observation log, are determined for each observation run based on the method described in Section 4.3.1. The opacity is plotted against the observed flux for the whole of the observation period shown in Figure 5.2. No direct correlation is observed between these parameters.

Further investigation into weather grades show that the varying opacities do not influence the observed flux but rather introduce a larger uncertainty to flux measurements during the MAKEMAP task when the routine corrects for atmospheric extinction. This effect is particularly evident when the opacities exceed Grade 5 weather conditions. During the observation period, the flux error ranged between 0.01 and 0.05 (see Table 5.1), the latter taken during an observation where opacities exceeded $\tau > 0.2$. In total, there were three nights in which weather conditions exceeded Grade 5 conditions, resulting in measurement errors between ~ 0.3 Jy and ~ 0.5 Jy. A similar trend is observed for MRK 421 presented in Section 5.3.6.

5.2.6 Discussion of the 3-Month Observation of PKS 2155-304

During the period of SCUBA-2 observations between August and October 2012, the object was in a relatively quiescent state (124).

It was also found that the datasets presented in the analysis do not show any evidence for correlation. It was observed from Figure 5.1 that the γ-ray flux flickered against its average flux of $S_{\gamma,ave}$ = $(1.91 \pm 0.81) \times 10^{-7}$ ph cm^{-2} s^{-1}, while the 850 μm flux in-

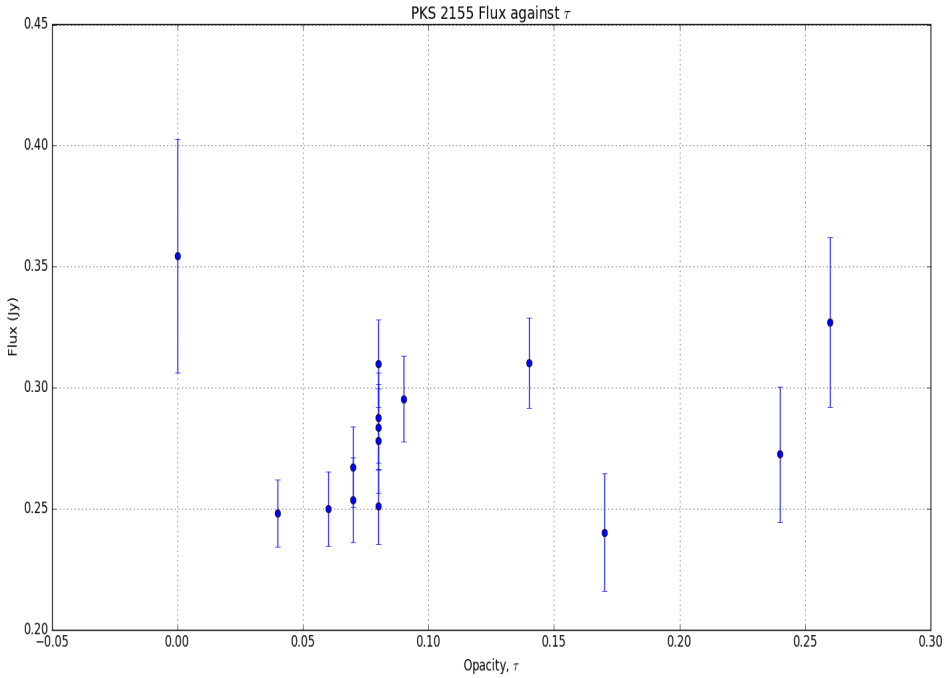

Figure 5.2: The first plot (top) represents the opacities recorded during each observation while the plot (bottom) shows the flux against opacity for each observation over the 66-day observation period.

creased from (0.24 $\pm$ 0.02) Jy to (0.31 $\pm$ 0.02) Jy (observed on 16 October 2012 (MJD 56216)) during the observation period.

Although few observations at sub-mm wavelengths are referenced, PKS 2155-304 is a very well-monitored source at higher energies. Chevalier et al. (124) summarise the variability trends that are observed at MeV to TeV energies, X-ray and optical wavelengths. They showed that the level of variability decreases with wavelength, with the highest variability observed at γ-ray and X-ray energies, while observations in the optical reveal much lower levels of variability. This study was conducted over a period of 11 years and only included data from the quiescent state of the source, and shows a trend that is in general agreement with the results found here.

Observations by Abramowski et al. (34) have also found that there are only moderate flux changes at optical (observed with ATOM) and VHE γ-ray (observed with H.E.S.S.) energies, while the object was transitioning between a flaring state into a quiescent state between the observation period of 2007 and 2009. It was also noted that Abramowski et

al. (34) could not find any universal relationship between the VHE γ-ray band and the optical band, although Abramowski et al. (243) showed that a delayed small amplitude optical echo might be present during the exceptional VHE outburst in 2006 (85).

Based on the limited γ-ray and sub-mm dataset and the lack of evidence for correlation between the γ-ray and sub-mm wavebands, more observations made consistently over a period of several years are necessary to understand the sub-mm behaviour of PKS 2155-304. It is important to determine whether the sub-mm emission behaves differently during periods of quiescence and outburst and how and to what extent this behaviour relates to the γ-ray wavebands. The next section will aim to study the latter: sub-mm observations of an HBL during an outburst and its relation to emission at γ-ray energies.

5.3 MRK 421 Target-of-Opportunity Observations with SCUBA-2 and *Fermi*-LAT during an Exceptional Flare

5.3.1 MRK 421

Between July 2012 and July 2013 MRK 421 exhibited several periods of flaring activity at gamma-ray energies (325). At approximately 12-13 April 2013 (MJD 56394 to MJD 56395), MRK 421 once again entered a high state and was closely monitored by various telescopes in the γ-ray, X-ray, optical, millimetre, IR and radio bands (257; 68; 109; 155; 80; 223; 224). During this period, Target-of-Opportunity (ToO) observations were obtained for this source using the SCUBA-2 instrument over a period of 6 days. Observations were focussed on the initial stages of the flare.

The primary objective was to use the flare event to understand the behaviour of the source at temporal resolutions of approximately one day. Night-by-night and also intra-night observations were conducted while the source was in view. The details of these observations and results will be discussed in the following sections.

5.3.2 Observations with SCUBA-2

SCUBA-2 ToO observations were conducted at both 450 μm and 850 μm every night between 12 April 2013 (MJD 56394) and 17 April 2013 (MJD 56399). Integration times for each observation were ~ 10 minutes and a total of 16 observations were collected over

MJD	τ	Weather Grade	Flux (Jy)	Obs. Runs
56394	0.06	2	0.28 ± 0.01	1
56395	0.18	4	0.29 ± 0.02	1
56396	0.30	5	0.33 ± 0.06	3
56397	0.16	4	0.33 ± 0.03	6
56398	0.19	4	0.34 ± 0.03	3
56399	0.11	3	0.33 ± 0.02	2

Table 5.5: The daily 850 μm flux measurements of MRK 421 obtained using the JCMT SCUBA-2 instrument over six days between 12 April 2013 (MJD 56394) and 17 April 2013 (MJD 56399). It is noted that each observation run has an integration time of ~ 10 minutes. The flux density quoted is the average flux measured on each night when multiple observation runs were conducted. Opacities (τ) and their corresponding weather grades are quoted for each observation.

the 6-day period, varying between 10 minutes and 60 minutes per night depending on the number of observation runs taken (see Table 5.5).

During the observation period, τ values varied between τ = 0.06 to τ = 0.30, with an average of τ = 0.18. The highest value of τ = 0.30 was encountered on only one night, and these observations were excluded from further analysis.

The average FCF used to analyse the results from these observations was calculated independently using observations of flux calibration sources (see Section 4.3.1), which yielded FCF_{850} = 585 Jy pW^{-1} $beam^{-1}$ at 850 μm. An example of an 850 μm map obtained during an observation run on 15 April is shown in Figure 5.3. The data were analysed to produce daily and intra-night light curves and tested for variability.

5.3.3 Observations with *Fermi*-LAT

The *Fermi*-LAT data from MRK 421 during the period of the flare between 12 April 2013 (MJD 56394) and 17 April 2013 (MJD 56399) were comprised of PASS7REP_V15 data, analysed within a region of interest of 15° centred on the source. Details of how the data were extracted, processed and analysed are described at length in Section 4.6. A summary of the *Fermi*-LAT instrument specification and data selection criteria are shown in Table 5.6.

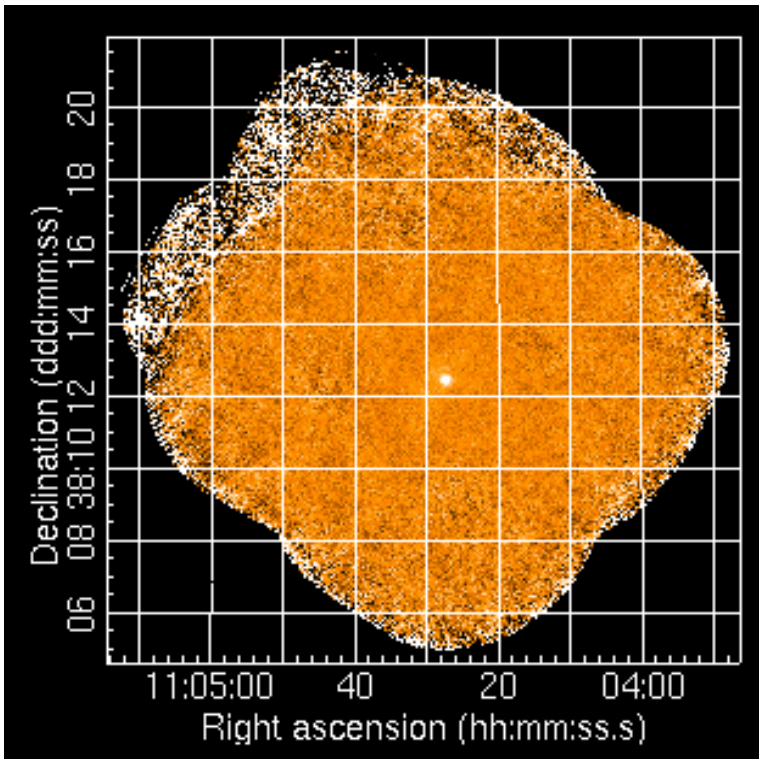

Figure 5.3: MRK 421 as observed on 15 April 2013 at 850 μm at a flux of S = (0.33 $\pm$ 0.03) Jy. Details of the instrument PSF can be found in Section 4.3.1.

Instrument	Selection Criteria
ScieceTools Version	v9r33p0
IRF	Reprocessed PASS7 (PASS7REP)
Event Class	source
Zenith Angle Cuts	100°
Rock-Angle cut	<52°
Energy Range	100 MeV - 100 GeV
Radius of Interest	15° (centred on source)
Likelihood Analysis	Unbinned
Binning Timescale	Daily
TS Threshold	25

Table 5.6: A summary of the *Fermi*-LAT instrument specification and data selection criteria as discussed in Chapter 4.

MJD	Flux (10^{-7} ph cm^{-2} s^{-1})
56394	5.63 $\pm$ 1.45
56395	3.94 $\pm$ 0.35
56396	4.27 $\pm$ 1.25
56397	7.35 $\pm$ 0.27
56398	6.51 $\pm$ 1.86
56399	3.84 $\pm$ 1.27

Table 5.7: The daily *Fermi*-LAT 100 MeV to 100 GeV observations between 12 April 2013 (MJD 56394) and 17 April 2013 (MJD 56399).

Table 5.7 summarises *Fermi*-LAT flux measurements of MRK 421 during the observation period.

5.3.4 Night-by-Night Variability

Observations with SCUBA-2

A summary of the daily average fluxes and opacities is shown in Table 5.5. Figure 5.4 represents the light curve obtained over the entire observation period; for days with multiple observations, the average flux observed on that day was used. The highest averaged flux value was observed on 16 April (MJD 56398) at S = (0.34 $\pm$ 0.03) Jy, with an opacity of τ = 0.19 (see Table 5.5).

The overall average flux, S_{ave}, during the six-day observation period was S_{ave} = (0.31 $\pm$ 0.02) Jy. This was compatible with the known flux of the object at 870 μm at (0.35 $\pm$ 0.03) Jy on 07 December 2013 and (0.31 $\pm$ 0.06) Jy on 4 February 2016 (150) (see Section 5.4.1). The 2013 and 2016 fluxes were obtained using the Submillimeter Array (SMA) near the summit of Mauna Kea, Hawaii [3]. Data from this program are updated regularly and are available at the SMA website[4].

The overall light curve for the duration of 6-day period was analysed to investigate possible night-by-night variability. A χ^2 test based on the null hypothesis that the flux of MRK 421 is constant at S_{ave} produced a reduced χ^2 of 3.11 with a chance probability

[3]MRK 421 is included as an ongoing monitored source with the SMA to determine the fluxes of compact extragalactic radio sources that can be used as calibrators at mm wavelengths (150)

[4]http://sma1.sma.hawaii.edu.callist/callist.html (last viewed 18/03/2016)

Waveband	Average Flux	χ^2	Red. χ^2	V
sub-mm	(0.31 ± 0.02) Jy	12.44 ($< 2\sigma$)	3.11	0.03
γ-ray	$(5.26 \pm 1.07) \times 10^{-7}$ ph cm^{-2} s^{-1}	77.18 (4σ)	15.44	0.16

Table 5.8: Variability analysis and statistics of MRK 421 at sub-mm and γ-ray energies.

of 0.014%. This provides weak evidence at the 2σ level that the 850 μm flux is varying on timescales of approximately five days.

Observations with *Fermi*-LAT

Fermi-LAT observations of MRK 421 during the period of outburst resulted in a maximum flux of $S_{\gamma,max}$ = (7.35 $\pm$ 0.27) $\times 10^{-7}$ ph cm^{-2} s^{-1} on 15 April 2013 (MJD 56397) and a minimum flux of $S_{\gamma,min}$ = (3.84 $\pm$ 1.27) $\times 10^{-7}$ ph cm^{-2} s^{-1} on 17 April 2013 (MJD 56399). The average flux at γ-ray energies during this period was $S_{\gamma,ave}$ = (5.26 $\pm$ 1.07) $\times 10^{-7}$ ph cm^{-2} s^{-1}.

The γ-ray dataset revealed a χ^2 value of 77.18 and a reduced χ^2 of 15.44 (d.o.f. = 5) suggesting variability at the 4σ level. Using the variability index, V (see Section 3.3) to determine the variability yielded V = 0.16. A summary of these results is shown in Table 5.8.

5.3.5 Intra-night Variability

Observations with SCUBA-2

On 15 April (MJD 56397), a set of six observations was conducted between UT 10:37 and 12:30 due to varying levels of opacity[5]. The measured flux varied between S = (0.28 $\pm$ 0.04) Jy and S = (0.38 $\pm$ 0.03) Jy. The opacities fluctuated between τ = 0.16 and τ = 0.17 (see Table 5.9).

The average flux on this day was S = (0.33 $\pm$ 0.03) Jy. The χ^2 test based on the assumption of a constant flux at the average value throughout the two-hour observation results in χ^2 = 9.45 with a reduced χ^2 of 1.89 (d.o.f.= 5). This result shows there is no evidence for variability (9% probability) on a timescale of 2 hours.

[5]SCUBA-2 observations of MRK 421 required a minimum of Grade 4 weather conditions for point source observations. This enabled multiple observations of the source, when opacities were too high (Weather Grades > 3) for SCUBA-2 Legacy Surveys and other observations which required higher opacities.

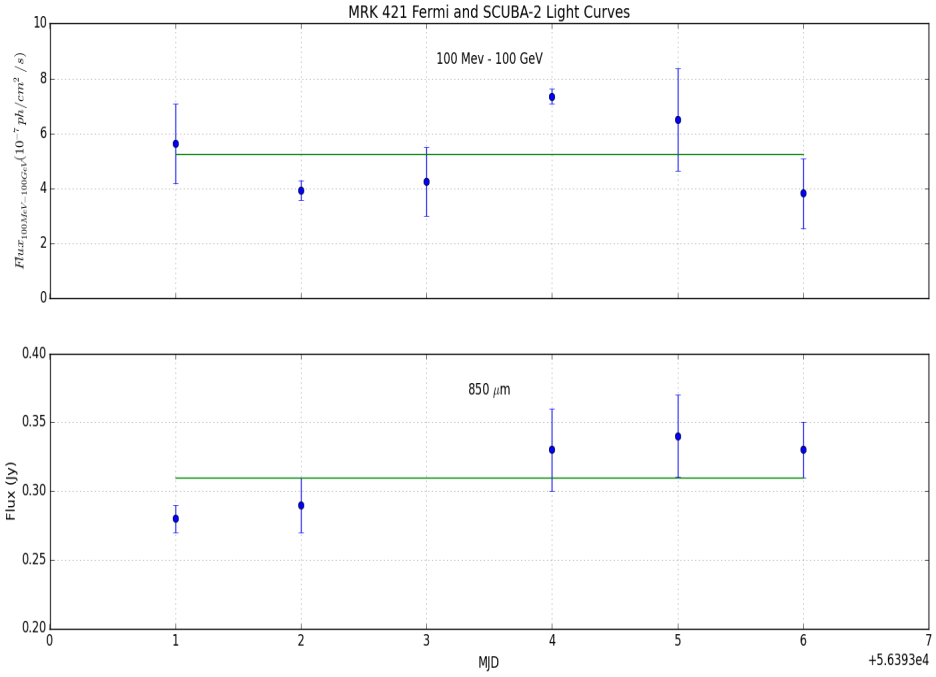

Figure 5.4: The *Fermi*-LAT (top) and SCUBA-2 (bottom) light curve of MRK 421 obtained during the flaring period between 12 April 2013 (MJD 56394) and 17 April 2013 (MJD 56399). Daily observations were obtained for SCUBA-2 while the *Fermi*-LAT observations were binned on daily timescales to match the SCUBA-2 observations. The line (green) in each plot represents the the average flux over observation period.

UT	τ	Weather Grade	Flux (Jy)	Int. Time (min)
10:37:00	0.16	4	0.29 ± 0.02	10
10:49:00	0.15	4	0.38 ± 0.03	10
11:01:00	0.15	4	0.34 ± 0.03	10
12:05:00	0.15	4	0.37 ± 0.04	10
12:17:00	0.16	4	0.28 ± 0.04	10
12:30:00	0.17	4	0.33 ± 0.04	10

Table 5.9: Intra-night 850 μm flux measurements obtained on 15 April 2013 (MJD 56397) over the duration of approximately two hours. The table shows the universal time (UT) at which each observation was conducted, the opacity at the time and the observed flux and error.

UT	Flux (10^{-7} ph cm^{-2} s^{-1})
02:10:00	2.41 $\pm$ 2.52
06:46:00	14.83 $\pm$ 4.61
08:04:00	7.75 $\pm$ 3.63
10:02:00	15.14 $\pm$ 3.59
13:19:00	7.28 $\pm$ 1.89
16:36:00	6.07 $\pm$ 0.83

Table 5.10: The intranight *Fermi*-LAT 100 MeV to 100 GeV light curve observed on 15 April 2013 (MJD 56397). The table shows the universal time (UT) at which the source was observed.

Observations with *Fermi*-LAT

In order to study correlated variability between the intra-night observations obtained with SCUBA-2, *Fermi*-LAT data were binned on timescales of 95 minutes[6]. Table 5.10 shows the flux measurements on 15 April 2013 (MJD 56397). The average flux during this period at *Fermi*-LAT energies was recorded at $S_{\gamma,ave}$ = (8.91 $\pm$ 2.84) $\times 10^{-7}$ ph cm^{-2} s^{-1}. The χ^2 test based on the assumption of a constant flux at the average value on 15 April 2013 results in a χ^2 = 23.87 with a reduced χ^2 of 4.77 (d.o.f.= 5). This shows some evidence for variability at the 3.5σ level. The variability index for the six observations (Table 5.10) is 0.40 indicating weak evidence for variability in agreement with results from the χ^2 analysis.

5.3.6 Variations in Opacity

In order to ascertain whether the atmospheric opacity is causing either the observed night-by-night or intra-night flux variations, the correlation between the measured flux against τ for each individual observation was studied. Figure 5.6 shows the observed flux against τ. The opacities are obtained from the SCUBA-2 observation log and are measured for each observation run based on the method described in Section 4.3.1. It shows that no direct correlation can be observed between these parameters.

[6]In the scanning mode, *Fermi*-LAT alternates pointing above and below the orbital plane providing a uniform sky coverage once the instrument has completed two orbits approximately every three hours. Thus the smallest temporal resolution available ~ 95 minutes.

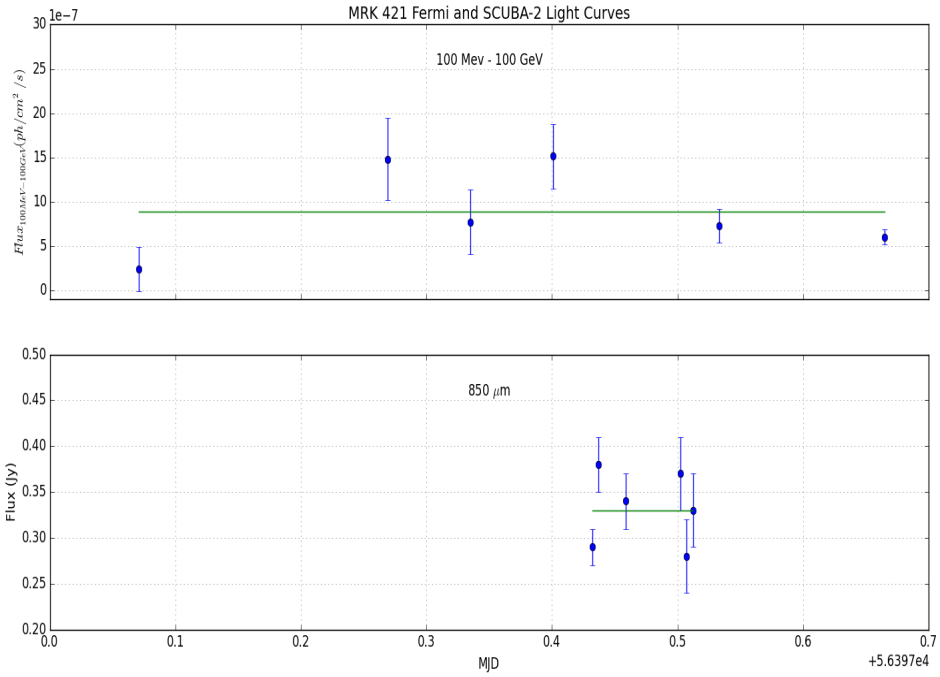

Figure 5.5: This shows the *Fermi*-LAT (top) and SCUBA-2 (bottom) light curve obtained during the 15 April 2013 (MJD 56397). The line (green) in each plot represents the the average flux over observation period.

During the observation period, the errors introduced ranged between 0.06 Jy and 0.07 Jy (typical values for errors are 0.03 Jy) for days on which the opacity reached τ = 0.30. This effect is also seen with the PKS 2155-304 observations when high opacities (τ > 0.2) were recorded.

5.4 Correlation between SCUBA-2 and *Fermi* Observations

As shown in Figure 5.4, no evidence for correlation is observed between the 100 MeV to 100 GeV γ-ray flux and 850 μm sub-mm flux. Further statistical investigation to determine evidence of correlation, including the existence of lags, is limited by the lack of sub-mm data. Also, both light curves only sample a very short period during the flare. There are no observations at 850 μm during the initial stages of the flare nor the decay period. Due to this, further correlation studies between the 850 μm and 100 MeV to 100 GeV γ-ray light curves will not present accurate results. It can be concluded that lim-

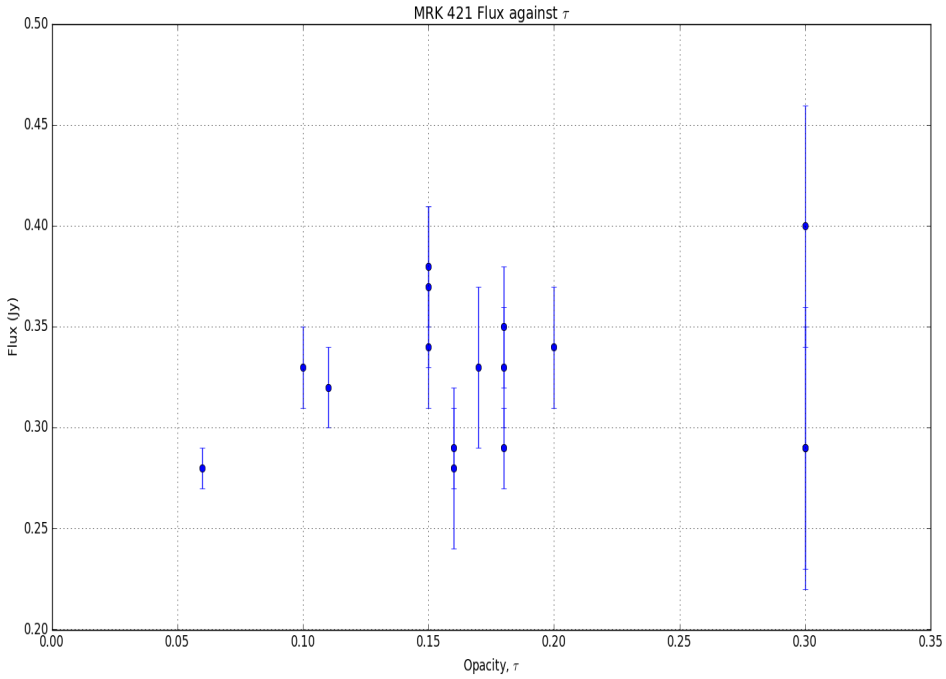

Figure 5.6: Daily measured flux at 850 μm against the opacity, τ, obtained from the SCUBA-2 observation daily observation logs (see Section 4.3.1) between 12 April (MJD 56394) and 17 April (MJD 56399).

iting the datasets to short-term observations between several days to several months, impedes correlation studies. As such, this provides further motivation for the long-term monitoring of sources in an effort to limit the effects of temporal bias on the datasets.

5.4.1 Discussion of the ToO Observations of MRK 421

The flare observed during the spring period of 2013 (155; 68; 257) followed one which occurred in September 2012 as discussed above (e.g.(325; 223)). For this thesis, ToO observations were conducted at 850 μm with SCUBA-2 and 100 MeV to 100 GeV γ-ray observations were made with *Fermi*-LAT between 12 April 2013 (MJD 56394) and 17 April 2013 (MJD 56399). Observations at 850 μm revealed no evidence for variability using both the χ^2 test (with χ^2 and reduced-χ^2 (d.o.f. = 4) values of 12.44 and 3.11) and variability index of $V = 0.03$ which is very low, while observations at γ-ray energies revealed a higher chance of variability compared to the sub-mm flux using the same tests (with

χ^2 and reduced-χ^2 (d.o.f. = 5) values of 77.18 and 15.44 and a variability index of V = 0.16). A summary of these results can be found in Table 5.8.

It was found that the sub-mm flux was compatible with the known flux of the object at 870 μm recorded at (0.35 $\pm$ 0.03) Jy on 7 December 2013 and (0.31 $\pm$ 0.06) Jy on 4 February 2016 (150)[7].

Multiwavelength observations studying the source at γ-ray energies with radio (224) and optical, X-ray and γ-ray energies (142) show that between the higher energy bands and lower energy bands, some level of temporal lag is present. Hovatta et al. (224) showed that there is a lag of 60 to 70 days between the *Fermi*-LAT and radio light curves using cross-correlation methods for observations conducted during the flare in 2013. Lee et al. (142) also showed that there may be evidence for a lag of approximately seven to 10 days between the optical and γ-ray bands with the optical leading the γ-ray band (however, this result was not statistically significant), while there is correlation with zero-lag between the X-ray and γ-ray emission. Results from both these studies indicate that there is a possibility of a lag between emission in the higher and lower energy bands. If temporal lags (> 6 days) are present between emission at γ-ray and sub-mm wavebands, then there may be little or no evidence for correlation during a short simultaneous multiwavelength campaign as presented here.

Thus, the observations must be unbiased and conducted over a longer period, preferably between several months to years, since ongoing multiwavelength studies are showing lags on different timescales depending of the wavelengths observed (224; 142). In Chapter 7, long-term observations of MRK 421 are presented with data obtained from *Fermi*-LAT and SMA, where the long-term behaviour in terms of flares and outbursts are discussed.

5.5 Concluding Remarks on PKS 2155-304 and MRK 421

Based on the results obtained from variability studies, it was found that both the HBLs did not exhibit significant variability on time scales between six days and 66 days during both quiescent and flaring states at sub-mm wavelengths. For the particular case of PKS 2155-304 with observations taken over 66 days, the object was in a quiescent state. This

[7]Although MRK 421 is an SMA calibrator, only four observations were conducted at 870 μm for this source between December 2004 and February 2016, resulting in a lack of a baseline flux estimate.

might result in the source not being very active at sub-mm wavelengths, resulting in a general lack of flux variability, although the γ-ray observations show a higher level of variability compared to the sub-mm the observations and the number of observations were limited. There was also no evidence for correlation between the γ-ray and sub-mm emission. The ToO observations of MRK 421 during a flaring period also revealed similar results although during this period the source was in outburst at γ-ray and X-ray energies. There was very weak evidence for variability on time scales of five days and there was a lack of correlation between the sub-mm and γ-ray wavebands. Both these datasets are limited and target a particular emission state of the respective HBL. This may cause some level of bias to the results produced from the analysis. Due to this, a more consistently sampled dataset over a longer observation period will help bring to light any missing features (i.e. evidence for correlated variability or temporal lags between emission at different wavelengths) of the γ-ray and sub-mm emission.

The following chapters will include long term ($\sim$ 12-year) monitoring datasets from the SMA of a sample of eight sources (with the exception of PKS 2155-304) (see Section 3.7). Once again, the study will aim to understand the behaviour of blazars in the sub-mm and mm regimes, and the connection between emission at (sub-)mm wavelengths to emission at γ-ray energies.

Chapter 6

Sub-mm Observations with the Submillimeter Array (SMA)

As discussed in the previous chapter, PKS 2155-304 was monitored between three- and four-day intervals, over a period of 66 days, which resulted in 15 flux measurements. Statistical studies on the variability and trend of the emission were limited due to the small dataset. A detailed correlation study with γ-ray data on a statistical level were not feasible. MRK 421, on the other hand, was sampled on daily and intraday time scales, providing good temporal resolution for variability and correlation studies. However, the dataset was limited by the duration over which the source was monitored (i.e. over a period of only 6 days). The object at the time was undergoing outburst. However, it was found that the ToO sub-mm observations did not include either the onset or the decay of the flare. In this way, the dataset was rendered incomplete. Thus, information on the nature of variability on daily and weekly time scales as well as correlation with γ-ray emission was in some ways biased as it targeted specific periods during which the objects were either in a quiescent or flaring state.

It became clear that a regularly-sampled light curve with a temporal resolution as small as a day over a period of several years was necessary for this study, as observations in the past have shown that the sub-mm light curves of blazars in general show variability on different time scales from days to weeks (311). In order to investigate this and to study its correlation with the γ-ray waveband a more complete dataset was necessary. These 'improved' datasets should include consistent monitoring over a period of several years. This way the duty cycle[1] of the (sub-)mm emission can be determined, which

[1]The duty cycle of a source is defined here as the period over which the source transitions from a quiescent state to an active state and finally decays back into its quiescent state (see Sections 6.3 and 7.1 for a

will correct any bias in observations determined by the emission state of the object. A long-term dataset will also provide ample data for detailed correlation studies with observations at γ-ray wavelengths. Since γ-ray observations are obtained from *Fermi*-LAT datasets, which can be processed on daily time scales, a similar temporal resolution was necessary for the (sub-)mm datasets.

This led to the SMA Calibrator List datasets which includes several well-monitored blazar sources, spanning a time period of over a decade. In the following sections, the details of the SMA instrument and the datasets within the SMA Calibrator List are discussed. Finally, the SMA light curves for each chosen source are presented along with a summary of key features or periods of interest within these light curves.

6.1 The Submillimeter Array (SMA)

6.1.1 The Instrument

The Submillimeter Array (SMA) was the world's first interferometric telescope functioning at sub-mm wavelengths (11). The SMA is a radio interferometer comprising of eight movable elements[2]. The array operates at 180 GHz to 700 GHz (0.3 mm to 1.7 mm). The SMA is located on Mauna Kea, Hawaii at 4080 m above sea level. Similar to the chosen site of the JCMT, the location of the SMA helps reduce effects of atmospheric extinction (197; 11).

Each dish of this interferometer array is a smooth parabolic reflector, 6 m in diameter and can be arranged into configurations as long as 509 m, positioned along the sides of a Releaux triangle for optimal imaging quality (see Figure 6.1). This produces a synthesised beam of sub-arcsecond width. The array observes simultaneously with two receivers, each having a 2 GHz bandwidth. Signals from the telescope are amplified and combined to produce resolution equivalent to an antenna of 0.5 km across (197; 11).

6.1.2 The SMA Calibrator List and Datasets

The SMA datasets used in this study are obtained from the SMA Calibrator List [3], which consists of phase calibrators for the array. It comprises a collection of bright sources,

complete definition of states at (sub-)mm and γ-ray energies).

[2]https://www.cfa.harvard.edu/sma/general/

[3]http://sma1.sma.hawaii.edu/callist/callist.html (last viewed: 24/08/2015)

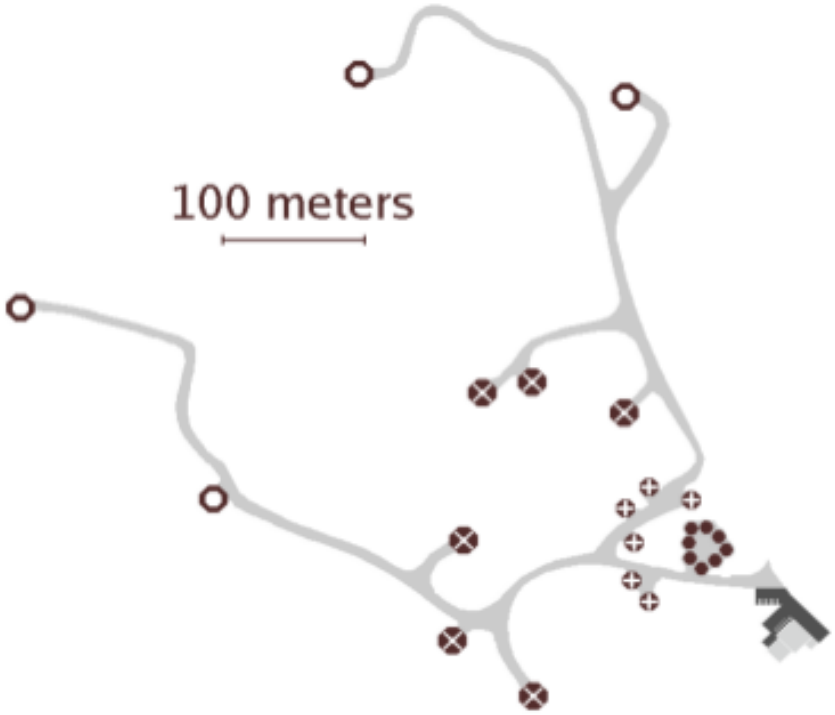

Figure 6.1: Layout of the SMA instrument with antennas configured in one out of four approximately circular rings. The four nested rings consists of 24 pads, shown as the unfilled, crossed and completely filled circular legends. Each ring may accommodate up to eight pads (197) in a Reuleaux triangle. The design optimises uniform sampling within a circular boundary, whose radius determines the angular resolution (197). The maximum baseline lengths of these circular rings are between 25 m and 509 m. This provides angular resolutions between 5 arcseconds to 0.25 arcseconds at 350 GHz (~ 860 μm, optimum frequency of the array for continuum sensitivity). Image obtained from Blundell (11).

typically with flux measurements higher than 750 mJy at 230 GHz (1.3 mm) and 1 Jy at 345 GHz ($\sim$ 870 μm). These sources are generally observed at 870 μm and 1.35 mm during both science observations and dedicated observing tracks (150). Dedicated observing tracks are large scale projects which require observing times in the range of 100 to 1000 hours. Science observations, on the other hand, have time allocations of less than 100 hours. Both of these short and long-term projects require calibration sources in order to calibrate both instrument and flux measurements. Instrument calibration, such as noise introduced by the antenna or other parts of the instrument array, often use bright quasars as a target in order to solve for changes to the frequency and time variations which occur during observations. Solar system bodies are generally used for flux calibration purposes (i.e. to scale the amplitude of the absolute fluxes of observed sources) as these objects have well known flux properties which allow them to be modelled accurately.

The list consists of a total of 234 objects, of which there are 171 sources (35 BLOs and 136 FSRQs) with positive blazar-class identification between Fermi and CGRaBS (45; 150). The datasets include 1.35 mm and 870 μm flux measurements. In these datasets, it is important to note that the 1.35 mm waveband is more regularly sampled (up to daily observations) compared to the 870 μm waveband; however, this greatly differs from source to source. There are several reasons behind the irregularity in sampling at 870 μm compared to the 1.35 mm. The first reason is that atmospheric conditions (with higher opacities) limit the number of calibration observations that are conducted. Thus, in order to maximise the time for science observations, flux calibration is usually done at 1.35 mm rather than 870 μm (as observations at lower frequencies require lower levels of precipitable water vapour (PWV)). The standard values of PWV for different SMA wavelength regimes are shown in Table 6.1. Observations at 1.35 mm also have a higher signal-to-noise ratio (SNR). Finally, the comparatively better sensitivity and that the larger size of the primary beam at 1.35 mm compared to 870 μm makes calibration and pointing at 1.35 mm much easier.

All the light curves presented in this chapter constitute observations of over a decade. These observations date back to 2002, six years prior to the launch of the *Fermi*-LAT instrument. The reason behind including the $\sim$ 12 year long SMA datasets, instead of only including observations which coincide with the *Fermi*-LAT monitoring period, is to

Wavelength (mm)	PWV (mm)
> 0.99	4.0
0.71 - 1.00	2.5

Table 6.1: Summary of the standard values of the precipitable water vapour for the given wavelength regime.

understand to a greater level of detail the typical duty cycles of the (sub-)mm emission from the well-known blazar sources chosen for this study.

6.1.3 The SMA Source Sample and Datasets

Of the many sources in the calibrator list, eight sources were chosen. These include two HBLs, two IBLs, three FSRQs and a radio galaxy. This sample was chosen to include eight well-studied sources (primarily blazars), which were also well-monitored at *Fermi*-LAT energies. This will help build upon previous work within the multi wavelength blazar study literature. Section 3.7 discusses the source sample in detail. Part of the motivation of this study is to investigate the behaviour of these sources at 1.35 mm wavelengths. The small sample of sources is ideal for an in depth source-by-source analysis, which will be presented in the following chapters. The different subclasses will also facilitate a type based qualitative (Chapter 6 and 7) and multi-waveband correlation (Chapter 8) analysis of the different sources.

In this chapter, the (sub-)mm emission will be studied both qualitatively, investigating the different states of emission (i.e. flares, outbursts, high states and flickering) and quantitatively, using the variability index, V. Finally, the correlation between the 1.35 mm emission and the 100 MeV to 100 GeV *Fermi*-LAT γ-ray emission (see Chapter 7) will be presented. In this chapter, discussions will primarily feature the 1.35 mm emission as the sampling is better at this wavelength compared to the 870 μm wavelength. However, maximum and minimum flux measurements observed at both wavelength regimes, including periods of interest (which consists of outbursts or flares) will be summarised in Section 6.4.

In Table 6.2, a summary of the details of each source is presented. These include details on right ascension (RA), declination (Dec.), redshift (z) and the blazar source type.

Name	RA (hh:mm:ss)	Dec. (deg:min:sec)	z	Type
MRK 421	11:04:27	+38:12:32	0.031	HBL
MRK 501	16:53:52	+39:45:37	0.034	HBL
OJ 287	08:54:49	+12:06:31	0.310	IBL/LBL
BL Lacertae	22:02:43	+42:16:40	0.069	IBL/LBL
3C 273	12:29:07	+02:03:09	0.158	FSRQ
3C 279	12:56:11	-05:47:22	0.536	FSRQ
3C 454.3	22:53:58	+16:08:54	0.859	FSRQ
NGC 1275	03:19:48	41:30:42	0.018	Radio Gal.

Table 6.2: A summary of the blazar sources included in this study and details on right ascension (RA), declination (Dec.), redshift (z) and the blazar type.

6.2 SMA Source Light Curves

6.2.1 Producing SMA Light Curves from Processed Data

In order to produce the light curves for each source, the calendar dates (e.g. 12 July 2008) from the SMA Calibrator List were converted to Modified Julian Dates (MJD) using the PYTHON module JDCAL. The GCAL2JD function within this module converts the calendar date (year, month, day) to the Julian Date (JD) for midnight of the given calendar date as well as the MJD. The JD begins at noon on January 1, 4713 B.C. while the MJD begins at midnight instead of noon. This is accounted for by the 0.5 in Equation 6.1. The relationship between the MJD and JD is given by:

$$MJD = JD - 2400000.5 \tag{6.1}$$

The MJD is then adjusted to account for the time of observation. The observation time obtained from the SMA Calibrator List is converted to a fraction of day and added to calculated MJD values.

A Python code was written to complete this task for all the datasets in this study.

6.3 Definitions of Emission States at (Sub-)mm Wavelengths

Each SMA light curve is analysed qualitatively to understand specific periods during which the emission of the source changes or transitions from one state to another. This involves understanding the duty cycle[4] of flares, outbursts, high states and flickering episodes. These will be classified as periods of interest; the duration and features of each of these will be discussed independently, before the connection between these events in the (sub-)mm with events occurring in the γ-ray band is considered (see Chapter 7). It has been found in the course of this research that the nature of the (sub-)mm emission is different from emission at other wavebands (i.e. the HE γ-ray wavebands). Thus, for the sake of simplicity, the definition of some of these features and events specific to the (sub-)mm regime are described here. A separate set of definitions for the different emission states in the γ-ray regime will be addressed in Section 7.1. The main difference between the events in the (sub-)mm and events in γ-ray wavelengths are the timescales on which they occur.

For simplicity, the 1.35 mm light curve of BL Lacertae (see Figure 6.2) was chosen to describe these different emission states present in the SMA datasets, since this source in particular exhibits all the emission states present between 4 February 2008 (MJD 54500) and 31 August 2014 (MJD 56900). It must be cautioned that distinguishing between different emission states is not always straightforward. This may be due to under sampling, such that the onset or decay of a particular state may not be fully sampled. A flare may appear as a high state (see Section 6.3.3), if the entire period of the flare is not evenly sampled (i.e. if the peak of the flare is not sampled). It must also be noted that all four source classes show very different behaviour at (sub-)mm wavelengths (i.e. based either on variability timescales or flux amplitudes), thus the definitions in the following sections were designated based on the overall behaviour of all the sources present in this study. This will assist the qualitative analysis of each source presented in Section 6.4.

Before describing these emission states, a few conventions used to qualitatively analyse the SMA light curves are described as follows:

[4]The duty cycles of emission states represent the period over which each state may evolve, e.g. from the onset to the decay of a flare or outburst. This is similar to the duty cycle of a light curve, in that the latter represents the periodicity of the transition or evolution between emission states in the overall light curve.

- quiescent flux levels - an approximation of the average baseline[5] flux level present when the overall 12 year light curve is considered
- maximum flux level - this is defined as the maximum flux measurement observed in the overall light curve regardless of the emission states present within the light curves.
- minimum flux level - defined as the minimum flux measurement observed in the overall light curve regardless of the emission states present within the light curve.
- brightest source - the brightest source in an emission band is defined as the source which exhibits the highest flux[6] of the eight sources in that emission band.
- faintest source - the faintest source is the source which has the smallest maximum flux[7] throughout the observation period.

6.3.1 Flares

In this study, flares in the (sub-)mm regime begin as an increase in flux levels (i.e. flux levels double or triple). At (sub-)mm wavelengths the onset of a flare typically occurs on timescales ranging between 3 weeks to 5 months. This onset is followed by a peak and decay phase. As such, flares are also identified based on their rise $\rightarrow$ peak $\rightarrow$ decay structure. However, the decay phases of flares in the (sub-)mm waveband usually occur on longer timescales (> 1 month[8] depending on the amplitude[9] and onset timescale of the flare) compared to the onset. An example of a flare is shown in Figure 6.2. The flare is observed between 16 October 2011 (MJD 55850) and 14 March 2012 (MJD 56000). In this particular flare, the source reaches the peak flux within ~ 50 days. The rise and decay timescales of flares at (sub-)mm wavelengths are usually longer than the rise and decay times of flares observed at γ-ray energies.

[5]This is often observed as the flux level the source typically returns to after an active period such as an outburst.

[6]This is based on a single flux measurement, typically obtained during the strongest outburst or flare.

[7]This is a single flux measurement, typically obtained during a flare or an outburst.

[8]The timescales of the decay phases of flares are difficult to determine since some sources do not decay fully before beginning a new flare. This is primarily due to the longer variability timescales observed at longer wavelengths (see Section 3.2.1).

[9]The amplitude of a flare is defined as the difference in the peak flux measurement and the flux observed at the onset of the flare.

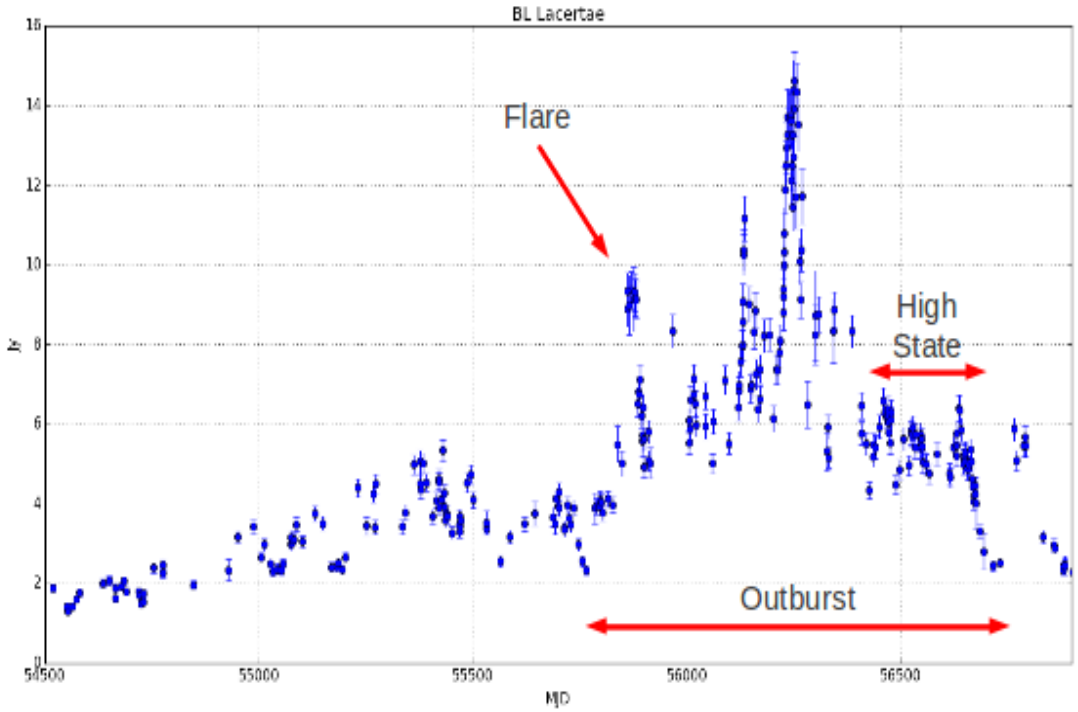

Figure 6.2: A section of the 1.35 mm light curve from BL Lacertae between 4 February 2008 (MJD 54500) and 31 August 2014 (MJD 56900) which shows different types of emission states occurring during an outburst. A flare is observed between 16 October 2011 (MJD 55850) and 14 March 2012 (MJD 56000). An outburst which comprises a progression of two or more flares is observed between 16 October 2011 (MJD 55850) and 12 February 2014 (MJD 56700). A high state and flickering behaviour can be observed between 18 April 2013 (MJD 56400) and 12 February 2014 (MJD 56700). The definitions of these emission states are presented in Sections 6.3.1, 6.3.2, 6.3.3 and 6.3.4.

6.3.2 Outbursts

An object enters a state of outburst when flux levels increase, often doubling or tripling, while beginning a series or progression of flares (two or more flares occurring consecutively[10] or subsequent flares are superposed over previous ones). While the timescales of outbursts vary depending on the type of object, at (sub-)mm energies, they typically extend over periods of approximately two years. This covers the period beginning from the rise of the first flare to the decay of the final flare, after which the flux measurements return to their initial levels recorded before the onset of the outburst. During a typical outburst, flares occur consecutively, often not decaying completely before onset of the following flare. This particular feature of 'superposed' flares is typically seen in the (sub-)mm rather than in the γ-ray wavebands. An example of an outburst can be seen in BL Lacertae between 16 October 2011 (MJD 55850) and 12 February 2014 (MJD 56700) at 1.35 mm (Figure 6.2). The primary difference between a flare and an outburst, is that an outburst consists of a series of flares. A flare, with its distinct structure, may occur independently, although this is rarely observed. This may be due to the sampling resolution or the typical decay timescales which are generally much longer than the rising timescales, as observed in most of the 1.35 mm light curves in which the flares and outbursts are well-sampled. Flares usually form part of an outburst in the (sub-)mm regime and can be distinguished by their relative rise $\rightarrow$ peak $\rightarrow$ decay structure when the entire light curve is observed.

6.3.3 High States

High states are defined as periods of observations during which flux levels either increase or decrease to levels which are at least twice the quiescent flux of the source, followed by a plateau phase at this level. During this plateau stage, flux levels may flicker (see definition of flickering in Section 6.3.4). The duration of a high state may vary between three months to several years. Both these instances have been observed in the source sample. An example of this can be seen in the 1.35 mm light curve from BL Lacertae (Figure 6.2) between 18 April 2013 (MJD 56400) and 12 February 2014 (MJD 56700). In this particular case, the high state occurs during the decay period of an outburst (i.e. flux levels were also higher than quiescent flux levels for this source of ~ 2

[10]The second flare begins when the previous flare has decayed completely.

Jy). The reason this is considered a high state and not a flare is based on the flux levels, i.e. during this period, flux levels vary below the doubling and tripling flux conditions which designate a flare.

It must be cautioned that flares can be misidentified as high states due to the effects of under-sampling. For example, during the high state in BL Lacertae between 18 April 2013 (MJD 56400) and 12 February 2014 (MJD 56700), there were several occasions during which the source was undersampled. However, the possibility of a flare occurring during this period is small due to the general trend of the 1.35 mm which suggests flares generally occur on longer timescales. It was also noted that the gap spans $\sim$ 20 to 50 days, leaving only a small possibility for a flare to occur during this time (see definition of flare in Section 6.3.1).

6.3.4 Flickering

Flickering occurs when the object exhibits small amplitude flux variations (less than double the preceding flux measurement) over a duration of time (between several weeks to months) depending on the wavelength of emission. At (sub-)mm wavelengths, these typically range between several weeks to several months. In order to distinguish between a flickering state or a flare, the flux levels during a flickering episode do not double or triple as they do during flaring periods. This feature typically occurs during quiescent states or during the plateau period of high states. An example of flickering is observed in BL Lacertae between 18 April 2013 (MJD 56400) and 4 November 2013 (MJD 56600) at 1.35 mm when the object was in a high state (Figure 6.2). Both flickering and high states may lack the structure of a flare, which also facilitates distinguishing between these three states.

Due to the complex nature of the (sub-)mm light curves which differ between source types, the process of distinguishing between emission states is equally complex. Thus, each source is analysed using the definitions presented above as a baseline guide.

6.4 Source-by-Source Discussion of the SMA Light Curves

The following sections will aim to highlight features of the 1.35 mm and 870 μm light curves for each source separately, including periods of interest in which the sources un-

Source	Max. Flux (Jy)	Date (max)	Min. Flux (Jy)	Date (min)
MRK 421	0.37 ± 0.05	15/02/2014	0.21 ± 0.07	01/05/2008
MRK 501	0.82 ± 0.07	01/10/2004	0.37 ± 0.04	03/09/2014
OJ 287	8.29 ± 0.43	06/01/2010	0.97 ± 0.06	24/05/2007
BL Lac.	14.63 ± 0.74	20/11/2012	1.19 ± 0.06	13/10/2006
3C 273	17.93 ± 0.93	15/11/2005	2.95 ± 0.15	09/01/2014
3C 279	20.76 ± 1.04	24/05/2012	5.11 ± 0.26	13/05/2009
3C 454.3	51.77 ± 4.31	20/11/2010	0.97 ± 0.05	29/05/2012
NGC 1275	12.67 ± 0.65	11/08/2014	1.86 ± 0.47	09/02/2004

Table 6.3: The table above shows the maximum and minimum flux measurements and their corresponding dates over the monitoring period for each source at 1.35 mm.

dergo flaring, outburst, high states or flickering activity. Tables 6.3 and 6.4 summarise the maximum and minimum flux measurements for each source at 1.35 mm and 870 μm respectively.

Results presented in this chapter will include observations between June 2002 and September 2014 (the monitoring period for each source is noted separately in the sections below). September 2014 was chosen as a period to end this study as this would sufficiently account for any lags present between the SMA and *Fermi*-LAT datasets (*Fermi*-LAT datasets end February 2014 in this study, Chapter 7).

As a guideline, most flux measurements are quoted as they appear in the datasets along with their corresponding calendar and modified Julian dates (MJD). However, due to gaps in sampling, certain features including the start and end times of the onset and decay of flares are difficult to determine. This also makes the actual peak flux values of said flares difficult to ascertain. In such cases, the flux values as they appear in the light curves are quoted.

HBLs

6.4.1 MRK 421

MRK 421 is the least bright of the BLOs at (sub-)mm wavelengths in the sample of sources presented in this study. While the 1.35 mm dataset is under-sampled with ~ 50 observations, it is the least sampled of all the sources studied with only three observa-

Source	Max. Flux (Jy)	Date (max)	Min. Flux (Jy)	Date (min)
MRK 421	0.35 ± 0.03	07/12/2013	0.19 ± 0.06	04/01/2006
MRK 501	0.58 ± 0.08	22/09/2004	0.29 ± 0.08	01/06/2006
OJ 287	6.08 ± 0.31	01/03/2009	0.60 ± 0.06	17/03/2007
BL Lac.	13.99 ± 0.70	09/11/2012	1.13 ± 0.17	08/09/2006
3C 273	13.88 ± 1.55	12/11/2008	2.27 ± 0.23	04/08/2011
3C 279	15.50 ± 3.95	14/01/2007	3.33 ± 0.27	10/01/2003
3C 454.3	40.42 ± 2.02	05/07/2005	2.01 ± 0.11	26/10/2011
NGC 1275	8.49 ± 0.56	29/08/2014	1.33 ± 0.14	15/11/2002

Table 6.4: The table above shows the maximum and minimum flux measurements and their corresponding dates over the monitoring period for each source at 870 μm.

Wavelength	Start Date	Period(s) of Interest
1.35 mm	15/11/2005 - 24/06/2014	N/A
870 μm	30/12/2004 - 07/12/2013	N/A

Table 6.5: Summary of the monitoring period as well as periods of interest (flares, outbursts and high states) of MRK 421.

tions conducted at 870 μm.

At 1.35 mm, flux levels range between (0.21 ± 0.07) Jy and (0.37 ± 0.05) Jy within periods of just over a year with no clear structure in the emission. Although there are occasions in which observations were conducted on consecutive days, the flux levels did not vary significantly within this time period. Any increase or decrease in flux appears to occur gradually over periods of several months. Based on the light curve at 1.35 mm, and taking into account the lack of sampling at this wave band, the emission appears to be flickering throughout the observation period.

6.4.2 MRK 501

While the highest flux for MRK 501 was recorded at (0.82 ± 0.07) Jy on 01 October 2004 (MJD 53279) at 1.35 mm, all other observations range between (0.37 ± 0.04) Jy and (0.55 ± 0.03) Jy, varying between these two values over periods of several years. The highest flux may have been an indication of a flare occurring during the initial period of observation

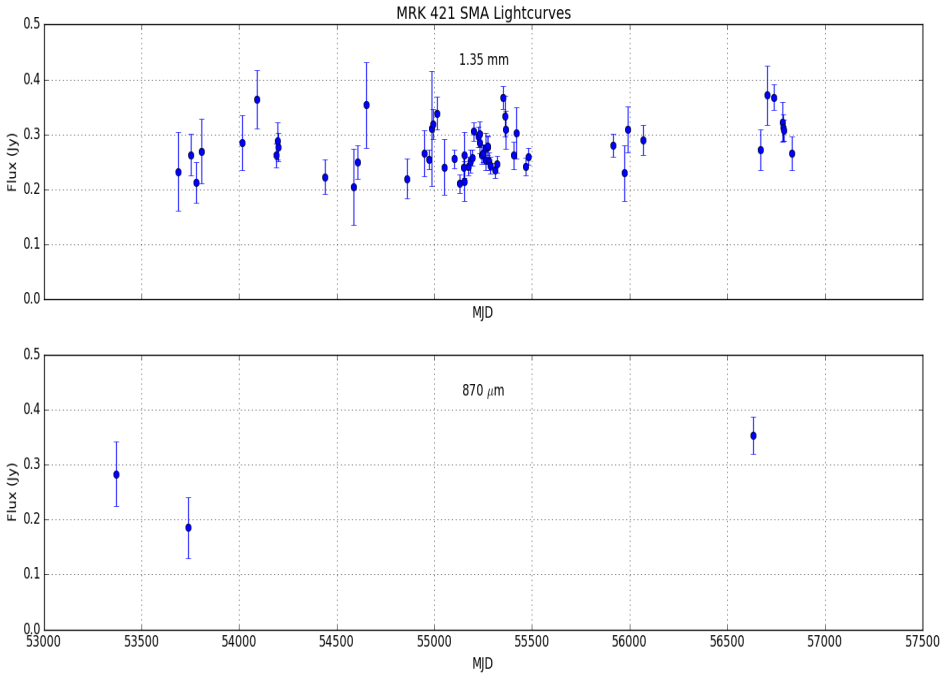

Figure 6.3: The 1.35 mm (top) as well as the 870 μm (bottom) SMA light curves for MRK 421.

Wavelength	Start Date	Period(s) of Interest
1.35 mm	01/10/2004 - 03/09/2014	N/A
870 μm	22/09/2004 - 25/02/2013	N/A

Table 6.6: Summary of the monitoring period as well as periods of interest (flares, outbursts and high states) of MRK 501.

with the SMA. However, no observations were conducted before or after this flux was recorded, making it difficult to draw any conclusions based on this measurement.

IBL

6.4.3 OJ 287

OJ 287 is one of the more variable BLOs at 1.35 mm wavelengths. Between 18 January 2003 (MJD 52657) and approximately 24 May 2007 (MJD 54244) the source goes through a flaring episode in which the flux increases from (1.64 $\pm$ 0.25) Jy to (6.63 $\pm$ 0.51) Jy

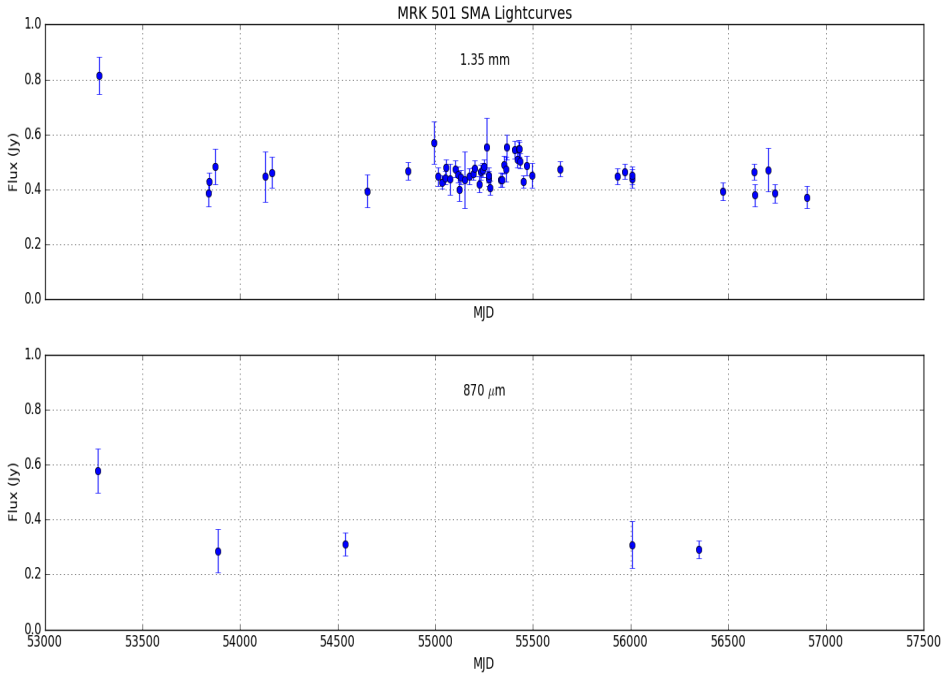

Figure 6.4: The 1.35 mm (top) as well as the 870 μm (bottom) SMA light curves for MRK 501.

Wavelength	Obs. Period	Period(s) of Interest
1.35 mm	18/01/2003 - 30/09/2014	24/05/2007 - 18/06/2010
870 μm	23/11/2002 - 30/04/2012	N/A

Table 6.7: Summary of the monitoring period as well as periods of interest (flares, outbursts and high states) of OJ 287.

within a period of eight months, between 3 June 2003 (MJD 52793) and 5 March 2004 (MJD 53069).

Over the period of $\sim$ 12 years, OJ 287 appears to enter into several periods of outburst (see Figure 6.5). The brightest of these[11] is observed during the middle of the monitoring period with approximately two flares occurring consecutively during this time. It appears that the outburst begins approximately on 18 October 2008 (MJD 54757) with a flux level of (2.73 $\pm$ 0.14) Jy, reaching a peak on 10 February 2009 (MJD 51584) with a flux of (7.02 $\pm$ 0.45) Jy. This shows a rise time of approximately four months during which

[11]The highest flux observed for this source occurs during this period.

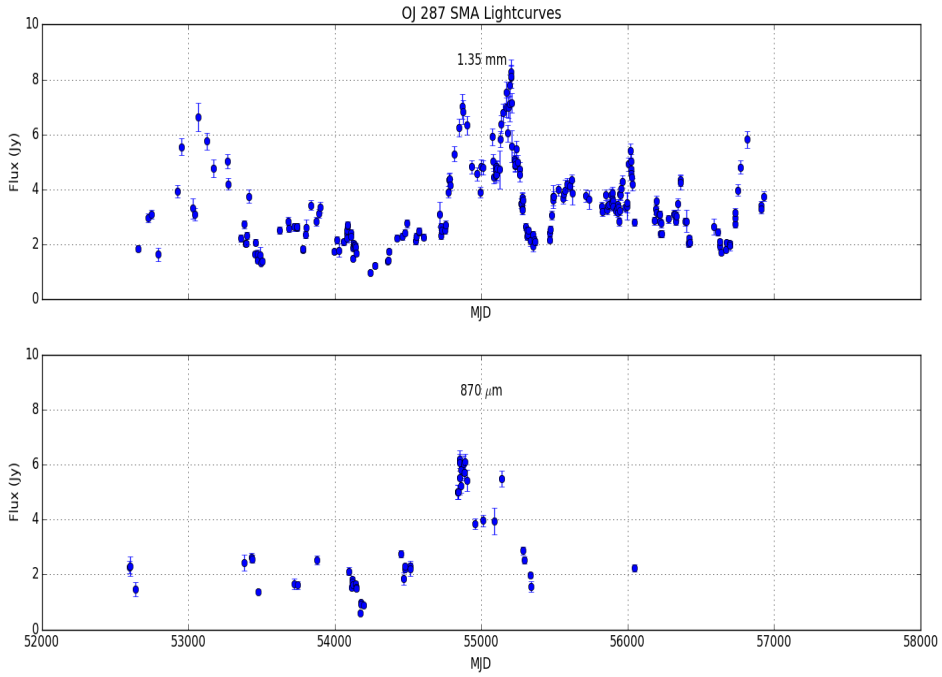

Figure 6.5: The 1.35 mm (top) as well as the 870 μm (bottom) SMA light curves for OJ 287.

the flux approximately triples. This peak is followed by a second peak on 6 January 2010 (MJD 55202) with a flux level of (8.29 ± 0.43) Jy.

This outburst is followed by an active state in which the object increases in flux from ~ 2 Jy to ~ 4 Jy. The flux continues to vary considerably in this phase exhibiting small amplitude flares, rising and decaying within periods of several months.

The 870 μm light curve is under-sampled to the extent that it is difficult to distinguish periods of flares or outbursts from the light curve. However, over the monitoring period, it can be surmised that the flux varies between (0.60 ± 0.06) Jy to (6.08 ± 0.31) Jy within a period of several months. There is good evidence that the outburst observed at 1.35 mm wavelengths is reflected in the light curve at 870 μm, as two similar peaks are observed in the latter (Figure 6.5) on 10 March 2009 (MJD 54900) and 4 January 2010 (MJD 55200). The 1.35 mm light curve leads the 870 μm by approximately 20 days.

Wavelength	Obs. Period	Period(s) of Interest
1.35 mm	11/10/2002 - 24/09/2014	22/07/2011 - 20/04/2015
870 μm	06/06/2002 - 03/12/2013	06/07/2011 - 03/12/2013

Table 6.8: Summary of the monitoring period as well as periods of interest (flares, outbursts and high states) of BL Lacertae.

6.4.4 BL Lacertae

BL Lacertae is the brightest of the BLOs in this source sample. Both the 1.35 mm and 870 μm light curves reveal an interesting phenomenon. For most of the monitoring period between 11 October 2002 (MJD 52558) and 22 July 2011 (MJD 55764) the object remains in a relatively quiescent state with flux levels varying between $\sim$ 2 Jy to $\sim$ 6 Jy on a typical time span of several months. This may represent small-amplitude flares. On approximately 22 July 2011 (MJD 55764) the object entered into an outburst with several flares occurring consecutively during that time (Figure 6.6). The peak flux achieved during this period of outburst is (14.63 $\pm$ 0.74) Jy on 20 November 2012 (MJD 56251), seven times higher than its quiescent level flux observed in the early periods of 2002. This is the only outburst observed in the whole 12-year observation period.

The 870 μm light curve also shows evidence of similar behaviour. Peaks and troughs observed in the 1.35 mm light curve are observed at 870 μm with a slight delay between the two wavelengths (several days). There is also evidence for a much less-sampled (compared to the 1.35 mm light curve) outburst observed between 06 July 2011 (MJD 55748)[12] until the end of the observation period, in which the flux increases to $\sim$ 14 Jy, once again seven times higher than the quiescent level flux of the source.

FSRQ

6.4.5 3C 273

An outburst was observed during the middle of the monitoring period. Here, the object enters into a series of progressive flares, with the entire outburst lasting approximately

[12]The difference in the onset of the outburst at 1.35 mm and 870 μm may be the result of an undersampling of the latter, resulting in the appearance that the onset of the outburst began earlier at 870 μm compared to the 1.35 mm outburst.

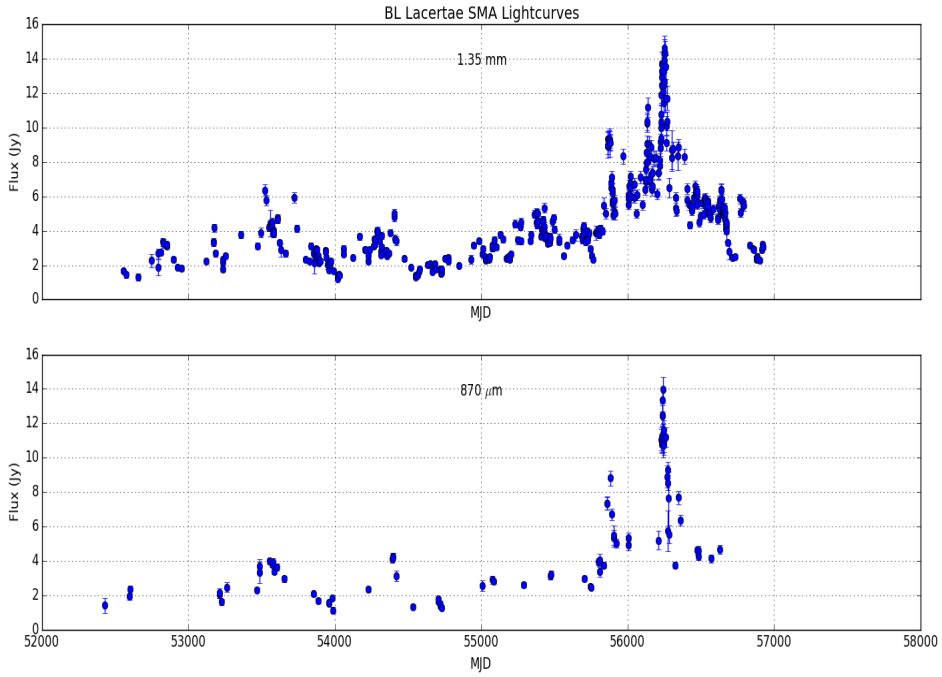

Figure 6.6: The 1.35 mm (top) as well as the 870 μm (bottom) SMA light curves for BL Lacertae.

Wavelength	Obs. Period	Period(s) of Interest
1.35 mm	18/01/2003 - 15/08/2014	15/04/2005 - 05/01/2011
870 μm	06/06/2002 - 04/08/2013	12/05/2005 - 03/11/2010

Table 6.9: Summary of the monitoring period as well as periods of interest (flares, outbursts and high states) of 3C 273.

five years and occurring almost simultaneously at both wavelengths. There are prominent gaps in the observation when the object enters this state of outburst, so the onset may not be accurately determined. Over a period of several months, between 15 April 2005 (MJD 53475) and 15 November 2005 (MJD 53689), the flux levels at 1.35 mm increase from (3.93 $\pm$ 0.20) Jy to (17.93 $\pm$ 0.93) Jy at 1.35 mm.

The 1.35 mm data show approximately six individual flares during the outburst. These flares range in intensity and flux levels. The lifetime of each flare is several months (e.g. 7 months for the second flare) between onset and decay. The rising timescale of each flare is approximately three to five months followed generally by a decay time that

Wavelength	Obs. Period	Period(s) of Interest
1.35 mm	18/01/2003 - 19/07/2014	13/05/2009(onset) - 24/05/2012(peak)
870 μm	03/06/2003 - 15/04/2014	onset and decay undefined

Table 6.10: Summary of the monitoring period as well as periods of interest (flares, outbursts and high states) of 3C 279.

is longer than the rising timescale. The last three flares observed at 1.35 mm show increased intensity, rising to peak flux levels of ~ 16 Jy and ~ 18 Jy. The fourth and fifth flare during this period of outburst occurred in rapid succession between 08 November 2008 (MJD 54778) and 16 December 2008 (MJD 54816), making it seem like one prolonged flare or a high state. The sixth and final prominent flare during this prolonged outburst rises to flux levels of (15.60 $\pm$ 0.78) Jy on 04 November 2009 (MJD 55139).

The outburst observed in the 870 μm light curve exhibits similarities with the flare observed in the 1.35 mm light curve. However, again due to under-sampling, it is difficult to determine individual flaring periods as the available data largely resembles a high state with varying flux levels within the period of outburst as observed at 1.35 mm. The highest flux during this outburst (and the entire observation period) was recorded on 12 November 2008 (MJD 54782) at (13.88 $\pm$ 1.55) Jy. This occurs quasi-simultaneously with the 1.35 mm emission, which recorded its third highest flux state between 08 November 2008 (MJD 54778) and 14 November 2008 (MJD 54784). This suggests that the emission at both the 1.35 mm and 870 μm wavebands may be simultaneous, given random and systematic errors between the datasets and the effects of under-sampling.

After this period of outburst, emission at both wavelengths returned to the initial flux states at an average of ~ 4 Jy beginning 26 August 2011 (MJD 55799) until the end of the observation period, while also exhibiting flickering behaviour.

6.4.6 3C 279

The sampling of the 1.35 mm light curves was irregular, i.e. there were periods during which observations were recorded daily and periods (months) during which no observations were recorded at all (e.g. 9 July 2003 (MJD 52829) to 27 January 2004 (MJD 53031), as shown in Figure 6.8). Due to this, it is difficult to distinguish between the onset and decay of each flare including whether these flares decayed completely before the object

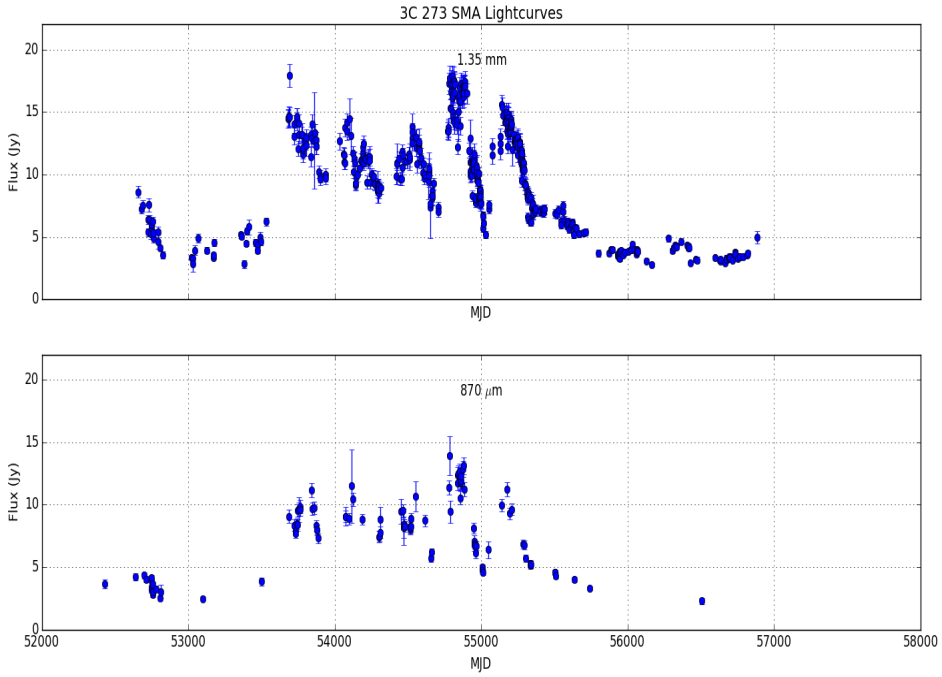

Figure 6.7: The 1.35 mm (top) as well as the 870 μm (bottom) SMA light curves for 3C 273.

entered a new flaring state. As with the other sources, the 870 μm light curve for 3C 279 is generally under-sampled throughout the ~ 12 year observation period.

The 1.35 mm light curve shows at least two periods of outbursts. The first is a less intense outburst estimated to occur between 09 July 2003 (MJD 52829) and 13 May 2009 (MJD 54964) with highest flux measurement reaching (15.65 ± 0.79) Jy on 28 November 2006 (MJD 54067) during this first outburst. This outburst consists of several smaller flares occurring on different timescales, typically several years between onset and decay. It takes a year and more for the object to reach its peak flux level during each flare. Some flares have clearly defined features between onset and decay while others do not seem to decay completely before the object enters into another flaring state. During the first period of outburst, flux levels varied between ~ 6 Jy and ~ 16 Jy.

The second outburst at 1.35 mm, which is the strongest of the two outbursts, starts on 13 May 2009 (MJD 54964) leading to a peak on 24 May 2012 (MJD 56071), after which the object begins to gradually decay through a series of flares and consecutively lower peak flux levels. This decreasing trend continues until the final date of observation presented.

Similar to the first outburst, the time scales of each flare differ, averaging between several months (approximately seven to nine months) to over a year. The shorter flares occur between the onset and the peak flare, while the longer flares occur during the decay phase of the outburst. During the rising trend of each flare, the flux typically oscillates between a range of ~ 3 Jy to ~ 5 Jy, again depending on the flare. This is indicative of a very complex flaring behaviour. Although trends emerge from an overall analysis of the light curve, a more detailed inspection reveals the diverse nature of each individual flare.

At 870 μm, the highest flux observed was (15.50 $\pm$ 3.95) Jy recorded on 14 January 2007 (MJD 54114). The minimum flux was observed on 10 January 2003 (MJD 52649) with a flux of (3.33 $\pm$ 0.27) Jy. As the 870 μm light curve is largely under-sampled compared to the 1.35 mm light curve, it is difficult to distinguish between flaring periods or the presence of outbursts. Observations reveal a flux variability ranging between ~ 3 Jy and ~ 15 Jy over the entire monitoring period. Although, there is evidence[13] which indicates that emission at 870 μm is similar to that of the 1.35 mm, this is difficult to ascertain due to gaps in the observations due to under-sampling. Thus, at 870 μm, the object appears to enter two high states (reflective of the outbursts observed at 1.35 mm) in which the flux levels of the object gradually increase to a peak before beginning to decay. The onset and decay of these apparent high states occur quasi-simultaneously and approximately on the same timescales as that observed in the 1.35 mm light curve.

6.4.7 3C 454.3

3C 454.3 is the brightest of all the sources studied. The datasets, both at 1.35 mm and 870 μm, are relatively well-sampled compared to the other sources. This allowed for a clearer observation of trends in the (sub-)mm flux.

The 1.35 mm data begin at low flux levels fluctuating between ~ 2 Jy and ~ 9 Jy over the period between 11 October 2002 (MJD 52558) and 13 January 2005 (MJD 53383). Between 13 January 2005 (MJD 53383) and 06 May 2005 (MJD 53496), there is a gap in the dataset. During this period of ~ 4 months, however, it appears that the flux more than doubled, increasing from (9.65 $\pm$ 0.49) Jy to (25.93 $\pm$ 1.30) Jy. The object

[13] Peaks and troughs are observed to occur quasi-simultaneously at both wavelengths where observations are present at 870 μm.

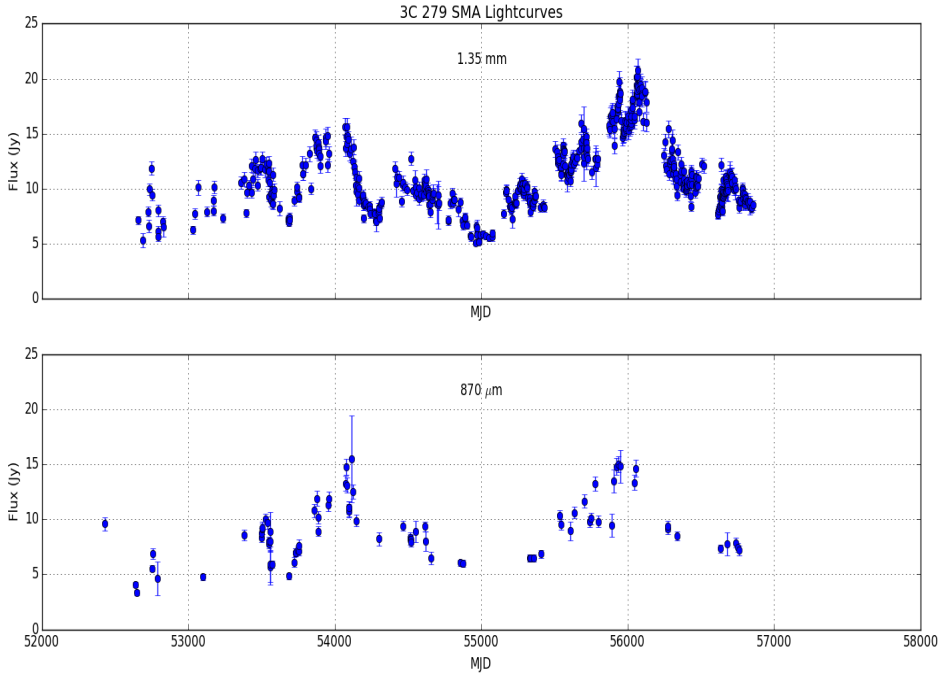

Figure 6.8: These plots show the 1.35 mm (top) as well as the 870 μm (bottom) SMA light curves for 3C 279.

Wavelength	Obs. Period	Period(s) of Interest
1.35 mm	11/10/2002 - 02/10/2014	17/08/2004 - 31/07/2006
1.35 mm	as above	31/07/2006 - 03/04/2009
1.35 mm	as above	03/04/2009 - 29/05/2012
870 μm	06/06/2002 - 17/09/2014	12/08/2004 - 29/12/2006
870 μm	as above	29/12/2006 - 02/05/2009
870 μm	as above	02/05/2009 - 26/10/2011

Table 6.11: Summary of the monitoring period as well as periods of interest (flares, outbursts and high states) of 3C 454.3.

appears to be entering a state of outburst with several flares following this, reaching peak flux levels of ~ 42 Jy. While the period of the outburst lasts for approximately two years, the time between each flare varies between several weeks and several months. The strongest flares recorded during this period appear to be superposed over each other, during which there is a small decay period (flux levels decrease to ~ 32 Jy) of several days before flux levels increase once again to ~ 41 Jy.

The second period of interest observed from July 2006 to April 2009 begins as a flare rising from (5.34 $\pm$ 0.27) Jy on 09 April 2007 (MJD 54199) to (17.88 $\pm$ 0.90) Jy observed on 07 September 2007 (MJD 54350), over a duration of six months. The flux then remains in this high state (flickering between ~ 13 Jy and ~ 18 Jy) for approximately 10 months, from September 2007 ($\sim$ MJD 54358) to June 2008 ($\sim$ MJD 54632). After this period, flux levels rise again to peaks of ~ 27 Jy before decaying to ~ 4 Jy in May 2009 ($\sim$ MJD 54966). The plateau phase of the second high state within this period lasted for the duration of 4 months, between June 2008 ($\sim$ MJD 54632) and October 2008 ($\sim$ MJD 54754).

The third period of interest can be categorised as either a high state or an outburst. First a rise is seen from (3.04 $\pm$ 0.17) Jy, beginning on 03 April 2009 (MJD 54924) to a peak flux of (28.25 $\pm$ 1.42) Jy on 03 October 2009 (MJD 55107). For this particular flare, the doubling timescale is approximately three months. In that same month alone, the flux also triples from the initial (3.04 $\pm$ 0.17) Jy to (10.35 $\pm$ 0.54) Jy on 31 July 2009 (MJD 55043). The source then continues to flicker in this high state until approximately July 2010 ($\sim$ MJD 55392). Following this the object begins a short period of outburst in which the maximum flux of the entire observation period is observed. Several flares are observed during this stage accompanying the maximum peak emission. The period of outburst lasts for 10 months between July 2010 ($\sim$ MJD 55392) to May 2011 ($\sim$ MJD 55696) when the object is seen to decay to ~ 9 Jy.

For the strongest flare observed, the flux increased from (20.624 $\pm$ 1.055) Jy on 30 September 2010 (MJD 55469) to (51.77 $\pm$ 4.31) Jy on 20 November 2010 (MJD 55520) over a period of ~ 50 days, which is a relatively short period for a source to flare to this level at (sub-)mm wavelengths[14]. Following this period of outburst, flux levels fall to the minimum flux of (0.97 $\pm$ 0.05) Jy recorded on 29 May 2012 (MJD 56076). The decay timescale in this particular instance is approximately five months, taking approximately

[14]Most flares for this source and other FSRQs have rising timescales greater than three months

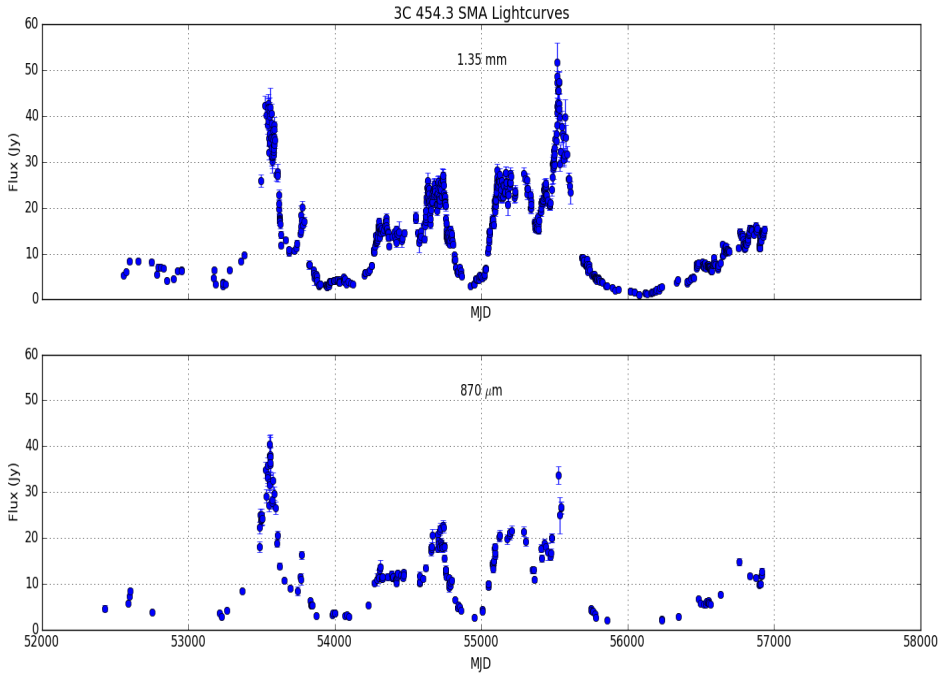

Figure 6.9: These plots show the 1.35 mm (top) as well as the 870 μm (bottom) SMA light curves for 3C 454.3.

two months to initially reduce by half (from ~ 51 Jy to ~ 26 Jy). Towards the end of the monitoring period, the flux levels are observed to be on an increasing trend, which may hint at the onset of another active period.

The 870 μm datasets reflect similar flares and outbursts throughout the period of observations with peaks of flares occurring almost simultaneously. Although, it is observed that the brightest flare at 1.35 mm is not the brightest flare at 870 μm, this is very likely a result of under-sampling, as a gap is observed in the 870 μm dataset between between tens of days to ~ 6 weeks during the brightest flare observed at 1.35 mm.

Radio Galaxy

6.4.8 NGC 1275

NGC 1275 is particularly interesting in that both (sub-)mm light curves show a continuous increasing trend over the entire monitoring period. The 1.35 mm flux show a gradual increase until a sharper rise is seen around May 2009 ($\sim$ MJD 54966). Before this period,

Wavelength	Obs. Period	Period(s) of Interest
1.35 mm	30/10/2002 - 30/09/2014	N/A
870 μm	15/11/2002 - 05/09/2014	N/A

Table 6.12: Summary of the monitoring period as well as periods of interest (flares, outbursts and high states) of NGC 1275

which constitutes the first half of the observation period (approximately six years), the flux level only doubles. In the year preceding May 2009 ($\sim$ MJD 54966), the flux just short of doubles reaching its first peak at (6.90 $\pm$ 0.46) Jy on 01 May 2009 (MJD 54952).

The second half of the observation period, from May 2009 ($\sim$ MJD 54966) to August 2014 ($\sim$ MJD 56884), flux measurements double from $\sim$ 6 Jy to $\sim$ 12 Jy. However, during this time, the 1.35 mm light curve appears more dynamic[15] compared to the first half of the observation period. Although flares and periods of outbursts are difficult to distinguish due to the nature of the light curve, flux levels appear to rise, reach a peak, and then decay. This is different compared to the first half of the observation period because flux measurements did not exhibit prominent peaks or structure and flux levels appeared to simply flicker. In the second half, clear peaks with higher variability amplitudes compared to that observed in the first half of the light curve can be distinguished from the 1.35 mm spectrum.

The 870 μm light curve is under-sampled and thus features of the light curve are less apparent. However, the general increasing trend observed at 1.35 mm is also observed at 870 μm. Once again the 870 μm flux appears to reflect the 1.35 mm emission on very similar timescales. The first peak observed at 1.35 mm on 01 May 2009 (MJD 54952), is also observed at 870 μm, where flux levels increase to (5.23 $\pm$ 0.39) Jy from (2.82 $\pm$ 0.52) Jy observed on 21 July 2008 (MJD 54668). Over the $\sim$ 12 year observation period the flux appears to quadruple at 870 μm.

6.5 Variability of the (Sub-)mm Emission in Blazars

The variability amplitudes were measured for each source at 1.35 mm over the $\sim$ 12 year observation period in order to determine if this parameter was source class dependent.

[15]This constitutes both a steeper rise in flux and an increase in short-term variability amplitudes.

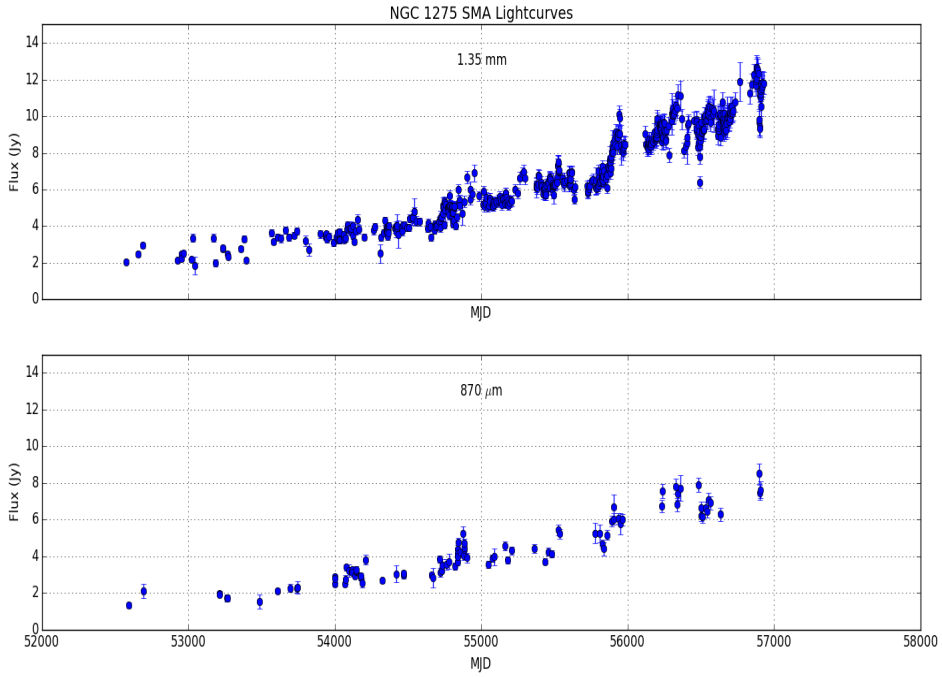

Figure 6.10: These plots show the 1.35 mm (top) as well as the 870 μm (bottom) SMA light curves for NGC 1275.

The variability index, V, calculated using Equation 3.2, is presented in Table 6.13.

It is noted that 1.35 mm and 870 μm observations for both the HBLs presented in this study are limited and clear conclusions cannot be made based on the variability indices calculated for these sources. However, for the remaining sources, it can be seen that 3C 273 and 3C 279 exhibit lower variability indices than both the IBLs. This can be attributed to the difference in the flux levels during quiescent and flaring periods, which is much larger for the IBL sources. All three FSRQs appear to be in a very active state throughout most of the observation period. 3C 454.3, in particular showed the largest difference in flux between its brightest flare and its quiescent state, making it the most variable source in the sample at (sub-)mm wavelengths.

Results of the higher variability indices for both IBLs and FSRQs compared to the HBLs in Table 6.13 are consistent with the findings of a much larger study conducted by Strom et al. (45) which suggests that IBLs tend to behave like FSRQs rather than HBLs. This behaviour will also be addressed in Chapter 7 when the *Fermi*-LAT light curves of each source are presented.

Source	$V_{1.35}$	V_{870}
MRK 421	0.07 ± 0.50	0.14 ± 0.50
MRK 501	0.29 ± 0.25	0.15 ± 0.35
OJ 287	0.77 ± 0.09	0.80 ± 0.11
BL Lacertae	0.84 ± 0.07	0.82 ± 0.07
3C 273	0.70 ± 0.06	0.66 ± 0.10
3C 279	0.57 ± 0.05	0.53 ± 0.15
3C 454.3	0.96 ± 0.06	0.90 ± 0.05
NGC 1275	0.67 ± 0.08	0.69 ± 0.11

Table 6.13: Variability indices at 1.35 mm and 870 μm, $V_{1.35}$ and V_{870} respectively, for each source calculated using Equation 3.2 using the maximum and minimum flux measurements at 1.35 mm over the ~ 12 year observation period. Variability is the strongest when $V \sim 1$.

6.6 On the 1.35 mm and 870 μm Emission of the Source Sample

The (sub-)mm emission for each source can be considered based on the type of activity it exhibits. The lack of data at both SMA energy bands for MRK 421 and MRK 501 limit the conclusions that can be made at (sub-)mm wavebands for the HBL class in general. It is noted however, that small levels of variability exists on timescales of several months (< 1 year) (based on available data). Noting the limited datasets, this appears consistent with the type of variability seen in PKS 2155-304 and MRK 421 discussed in Chapter 5. No clear indication of flares, or outbursts are observed for these sources during the ~ 12 year observation period.

Both OJ 287 and BL Lacertae show episodes of outbursts and flares, with flux levels doubling on timescales of ~ 4 to ~ 7 months. The nature of these sources (such as the onset, progress and decay of outbursts and flares) at (sub-)mm wavelengths most resemble (sub-)mm emission from FSRQs. While both sources show quiescent and flaring periods, OJ 287 appears more variable than BL Lacertae, with several flaring episodes throughout the ~ 12 year observations period, although OJ 287 is fainter than BL Lacertae.

All three FSRQs presented in this study exhibit several periods of outburst, with flux levels doubling or tripling over periods of ~ 2 months (e.g. 3C 454.3) to ~ 7 months. The features of flaring activity are very similar for the FSRQs and IBLs, in which flares

typically have a rapid rise and longer decay period (compared to the rising period).

Finally, the (sub-)mm light curves from NGC 1275 represent a completely different emission pattern. This source exhibits a general rising trend throughout the ~ 12 year observation period, with no particular period of outburst observed. This may be a result of its orientation to the line of sight, suggesting that either the observations probe a different region of the jet compared to observations of the other sources or that the emission is beamed differently (different Doppler factors) compared to the other sources in the sample. Once again, this highlights that the (sub-)mm emission observed exhibits evidence of being source-class dependent.

In conclusion, results from the study of the SMA light curves has brought to light some of the important features in the (sub-)mm emission regime of the eight sources. These can be summarised as below:

- Variability amplitudes are the largest for the FSRQs and IBLs, followed by the radio galaxy and HBLs.
- Flares and outbursts occur over periods of several months to years respectively.
- The behaviour of the (sub-)mm emission appears to be source class dependent when based on the parameters of flare intensity (timescales and flux amplitudes) and behaviour of outbursts.
- The observations of both positive and negative time delays of several days between the 1.35 mm and 870 μm emission for a few of the sources (e.g. OJ 287, BL Lacertae) may be a result of synchrotron self-absorption or the occurrence of forward and reverse shocks.

In the following chapters, the SMA light curves will be presented alongside γ-ray observations from *Fermi*-LAT in order to study the (sub-)mm/γ-ray connection for these sources. As previously stated, the SMA light curves are significantly longer than the *Fermi*-LAT light curves. Due to this, the SMA light curves will be truncated to coincide with the *Fermi*-LAT observations. Details of this can be found in Chapter 7.

Some of the questions that will be addressed in the following chapters are:

- Is the activity in the (sub)-mm regime correlated with activity in the γ-ray regime?

- If the (sub-)mm and γ-ray regimes are correlated, what is the extent of the correlation? Are there temporal lags between events[16] in the γ-ray regime and events in the (sub-)mm regime? Are these source class dependent? These questions will be addressed in Chapter 8 using statistical methods.

[16]Events include emission states such as flares or outbursts.

Chapter 7

The Connection Between the Fermi-LAT and SMA Light Curves

In this chapter, a truncated version of the SMA datasets is presented alongside *Fermi*-LAT light curves for the eight sources over a period of 5.5 years. The aim of this chapter is to determine on a qualitative level the connection between the γ-ray and (sub-)mm emission over the duration stated above by observing the overall light curves (by eye) at γ-ray and 1.35 mm wavelengths. Interesting features in the light curves will be discussed based on flux levels during different emission states.

The discussions presented in this chapter will provide a preliminary qualitative assessment of the behaviour of blazars at γ-ray and (sub-)mm emission bands, in addition to facilitating interpretation of the statistical correlation analysis which will be presented in Chapter 8. A careful qualitative study of each individual light curve for each source will bring to light features that may not be observed using correlation methods alone such as the variability timescales and duty cycles[1] of the eight blazar sources (see Section 8.4).

Analysis methods and selection cuts for the *Fermi*-LAT data are discussed in detail in Section 4.6. A summary of the *Fermi*-LAT data selection cuts used for all eight sources is shown in Table 7.2. Based on a qualitative assessment of all eight *Fermi*-LAT light curves, it was found that two of the fainter sources produced noisier γ-ray light curves than others. A noisy dataset is typically seen as rapid variability on daily timescales which may interfere with the interpretation of the behaviour of the source emission. This is

[1] A duty cycle for the purposes of this study is defined as the period over which the source evolves from a quiescent state to an active state and finally decays back into its quiescent state (see Section 7.1 for a complete definition of states in the γ-ray waveband).

observed most readily in MRK 421 and MRK 501. Figures 7.1 and 7.3 show the light curves of MRK 421 using the *Fermi*-LAT datasets with a TS cutoff of 10 respectively. Figures 7.2 and 7.4 show the light curves of MRK 421 and MRK 501 using *Fermi*-LAT datasets with a TS threshold of 25 respectively. While the noise in MRK 421 appeared as rapid variability on very short timescales at low flux levels ($\sim 2 \times 10^{-7}$ ph cm^{-2} s^{-1}), the noise present in MRK 501 appeared as flux values with large error bars at flux levels as high as 6×10^{-7} ph cm^{-2} s^{-1}.

There are several reasons which may cause HBLs to exhibit noisier datasets compared to the other blazar sub-classes. As discussed in Section 1.3, the high energy peak of the HBL SED predominantly falls in the GeV to TeV range of the electromagnetic spectrum. This suggests that the majority of its energy output falls just outside the 100 MeV to 100 GeV observation range chosen in this study. As a result, HBLs have lower photon counts observed in the 100 MeV to 100 GeV energy range compared to IBLs and FSRQs. The lower photon counts observed for HBLs coupled with the short (daily) temporal bins chosen for this study makes it more likely for the presence of systematic noise to affect the observed number of photon counts in each time bin (i.e. this may also cause an incorrect estimate of the flux errors, as the latter is statistically determined from the number of observed photon counts) (172; 133). Systematic noise in general is the result of uncertainties introduced during photon selection processes and as a result of instrument response functions during data processing and analysis. Uncertainties in photon selection may be introduced during event trigger and event reconstruction processes as well as during the application of various event selection cuts (see Section 4.5 (153)). On the other hand, uncertainties introduced by instrument response functions may be attributed to the discrepancies between observed and simulated (using Monte Carlo methods) data of calibration sources used to produce the instrument response functions (153). As a result, these systematic uncertainties affect flux and spectral measurements of the observed astrophysical sources (153). Increasing the TS threshold to 25 removes time bins with a smaller detection significance. A higher TS also indicates that the photon counts present in the observed sky map (see Chapter 4.6) is more likely due to the source being present in that location rather than contribution from background counts convolved with the instrument response functions. The application of a higher TS threshold for the HBLs improved the light curves by reducing inaccurate flux counts resulting primarily

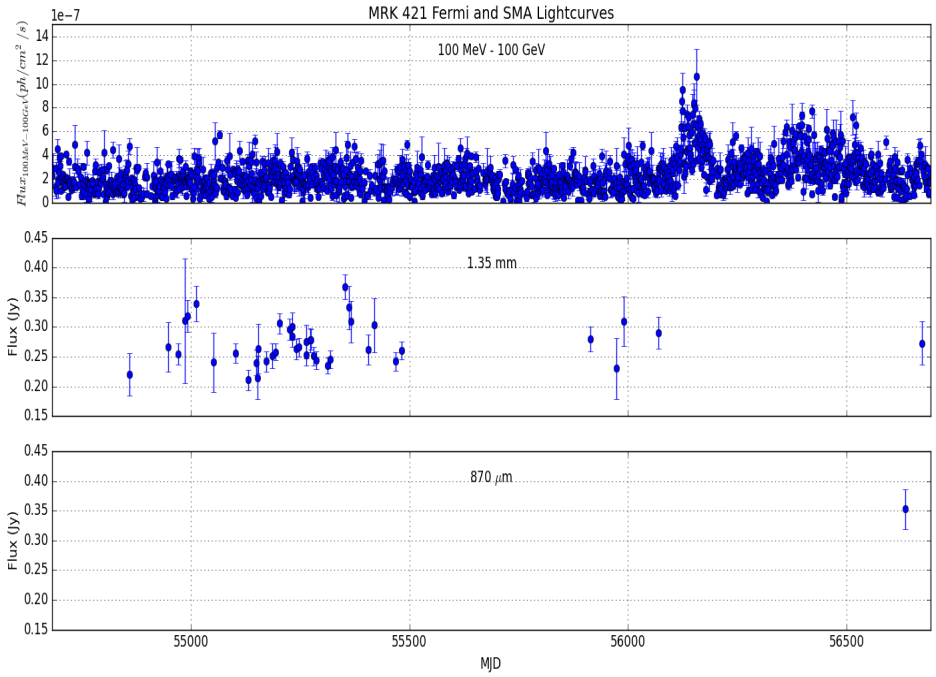

Figure 7.1: The 100 MeV to 100 GeV *Fermi*-LAT light curve with a TS threshold of 10, shown together with the 1.35 mm and 870 μm SMA light curves for MRK 421.

from systematic noise.

For MRK 421, increasing the TS threshold removed some of the rapid flickering that is most likely attributed to systematic noise at flux levels below 2×10^{-7} ph cm^{-2} s^{-1}. However, the general features including the short-term (daily) variability of the light curve was maintained throughout the 5.5 year observation period. For MRK 501, increasing the TS threshold removed data points with large error bars suggesting that these may also be the result of systematic noise due to the faintness of the source (i.e. low photon counts in a particular time bin) and the short daily time bins chosen for the likelihood analysis (see Section 4.6) (172; 133). As such, applying a more stringent TS cutoff improves the accuracy of the light curve. This is also important as incorrect flux estimates affects the accuracy of the DCF analysis (see Section 8.4.1). In Table 7.1, a summary of the source and the TS threshold value used to produce the *Fermi*-LAT light curves is shown.

In order to look for simultaneous or quasi-simultaneous correlation between the γ-ray and (sub)-mm wavebands, the $\sim$ 12 year SMA light curves, shown in Chapter 6,

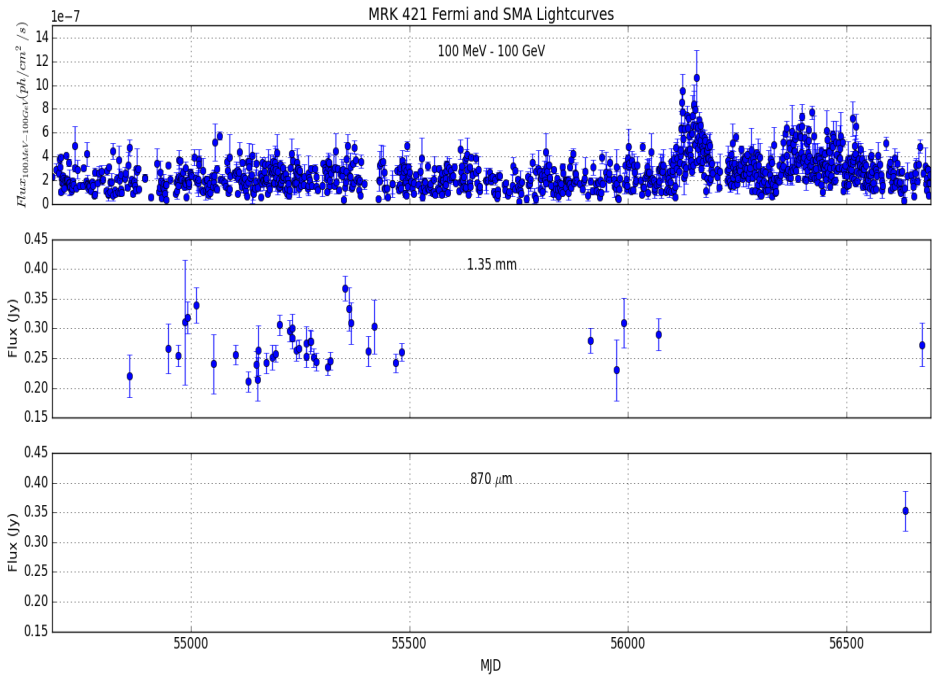

Figure 7.2: The 100 MeV to 100 GeV *Fermi*-LAT light curve with a TS threshold of 25, shown together with the 1.35 mm and 870 μm SMA light curves for MRK 421.

Source	TS Cutoff
MRK 421	25
MRK 501	25
OJ 287	10
BL Lacertae	10
3C 273	10
3C 279	10
3C 454.3	10
NGC 1275	10

Table 7.1: Summary of the *Fermi*-LAT TS threshold values used to produce the light curves for the eight sources.

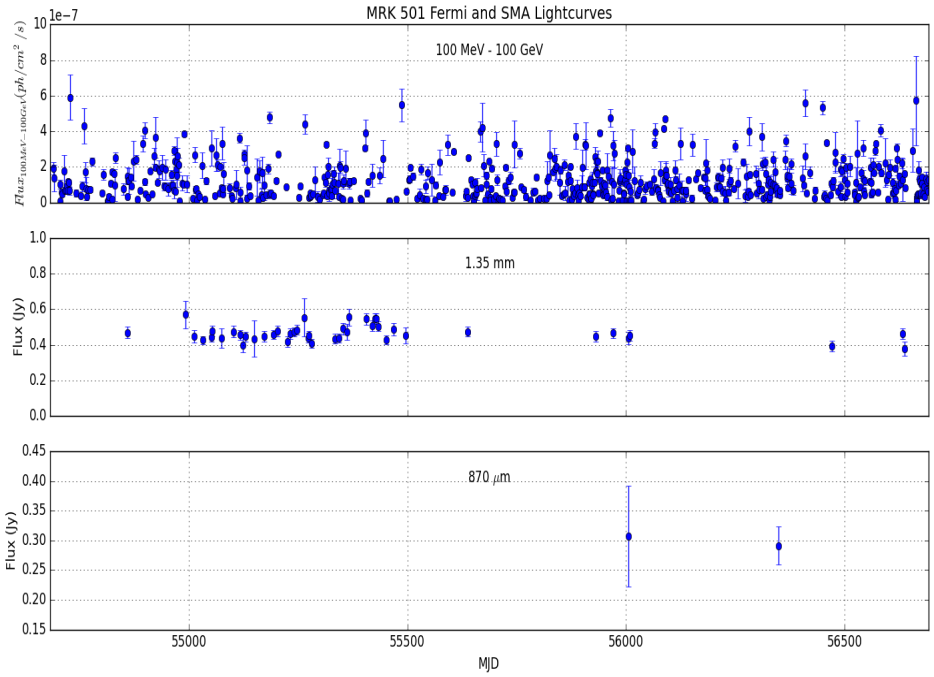

Figure 7.3: The 100 MeV to 100 GeV *Fermi*-LAT light curve with a TS threshold of 10, shown together with the 1.35 mm and 870 μm SMA light curves for MRK 501.

were truncated to the period between 4 August 2008 (MJD 54682) and 4 February 2014 (MJD 56692) to coincide with the *Fermi*-LAT datasets. The discussion in this chapter will also be limited to the connection between the 1.35 mm and 100 MeV to 100 GeV light curves. This is primarily due to the limited sampling at 870 μm.

7.1 Definition of Emission States in the γ-ray Regime

In the following sections, each source will be discussed based on features present in the γ-ray light curves. These features represent different emission states, namely periods of outbursts, flares, high states and flickering. As part of this study, it was found that the emission in the γ-ray and (sub-)mm regimes was markedly different, particularly with respect to the temporal evolution of each state. Due to this, the various states of the object (i.e. outbursts, flares and high states) will be redefined as they appear in the γ-ray regime. It is noted here that this is part of a long-term study, and while some of these sources have been known to exhibit extreme flaring activity with variability observed on

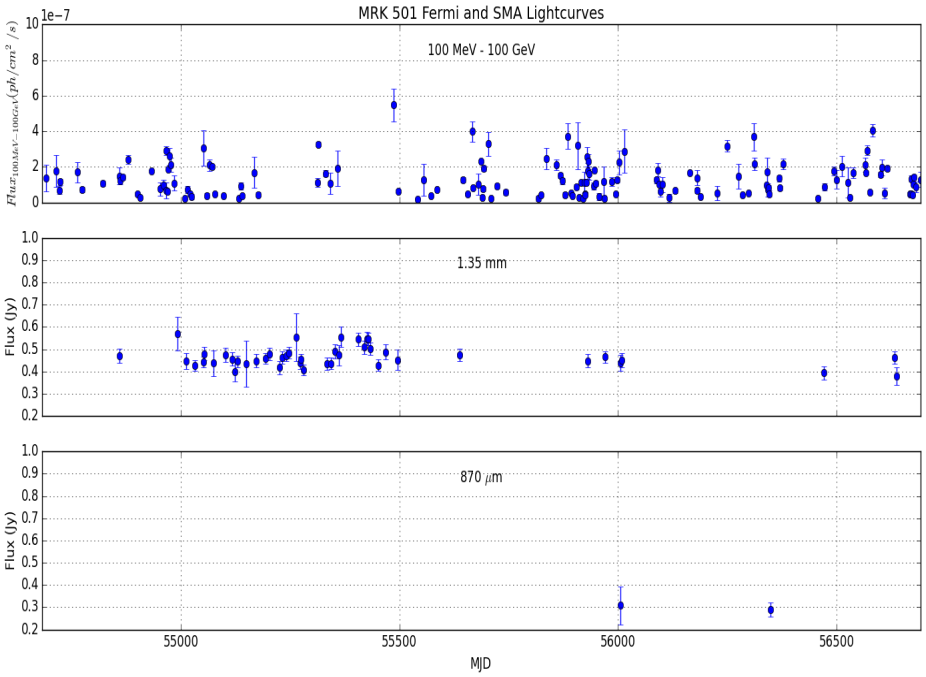

Figure 7.4: The 100 MeV to 100 GeV *Fermi*-LAT light curve with a TS threshold of 25, shown together with the 1.35 mm and 870 μm SMA light curves for MRK 501.

timescales of < 1 hour (2), the definitions here are limited to the binning interval of the *Fermi*-LAT observations presented in this thesis, which are binned on daily timescales to coincide with the temporal resolution available from the SMA datasets.

In addition to this, a note of caution must be included when considering assigning a particular emission state to a source. These definitions were designated a posteriori based on a qualitative analysis of each light curve individually. It was found that the behaviour of γ-ray emission varied from source to source and sometimes from epoch to epoch (see Section 7.3). It was also observed that due to the complex nature of the γ-ray emission certain states such as an outburst include features of other states, including flares and flickering. Thus, distinguishing between states is often done based on the relative states present in a particular light curve.

Instrument	Selection Criteria
ScieceTools Version	v9r33p0
IRF	Reprocessed PASS7 (PASS7REP)
Event Class	source
Zenith Angle Cuts	100°
Rock-Angle cut	<52°
Energy Range	100 MeV - 100 GeV
Radius of Interest	15° (centred on source)
TS Threshold	See Table 7.1
Likelihood Analysis	Unbinned
Binning Timescale	Daily
Start date	MJD 54682 (4 August 2008)
End Date	MJD 56692 (2 April 2014)

Table 7.2: Summary of *Fermi*-LAT instrument specification and data selection cuts for all eight sources.

7.1.1 Flare

In the γ-ray regime, a flare is defined as a rapid increase in flux, often doubling on short timescales. This typically occurs over a duration of one day and several tens of days, varying between sources and individual flaring events. The primary difference between a flare and an outburst is that an outburst is usually made up of a series of flares, with the flares either occurring consecutively (a clear structure of the onset, peak and decay is seen) or a superposition of flares (a second flare is observed before the preceding flare decays completely). In the γ-ray regime, the entire flare (onset $\rightarrow$ peak $\rightarrow$ decay) occurs on timescales of several days (tens of days) to weeks ($\sim$ 3 weeks), after which the object returns to flux levels prior to the onset of the flare[2]. Two examples of flares can be seen in the light curve of 3C 273. The first is observed between 27 December 2009 (MJD 55192) and 24 January 2010 (MJD 55220) followed by a second flare observed between 23 February 2010 (MJD 55250) and 14 April 2010 (MJD 55300), as shown in Figure 7.5. The

[2]Initial flux level is defined as the flux observed before the onset of the flare. This may not be the quiescent flux level if the flare is part of an outburst or the flare transitions into a different emission state, such as a high state.

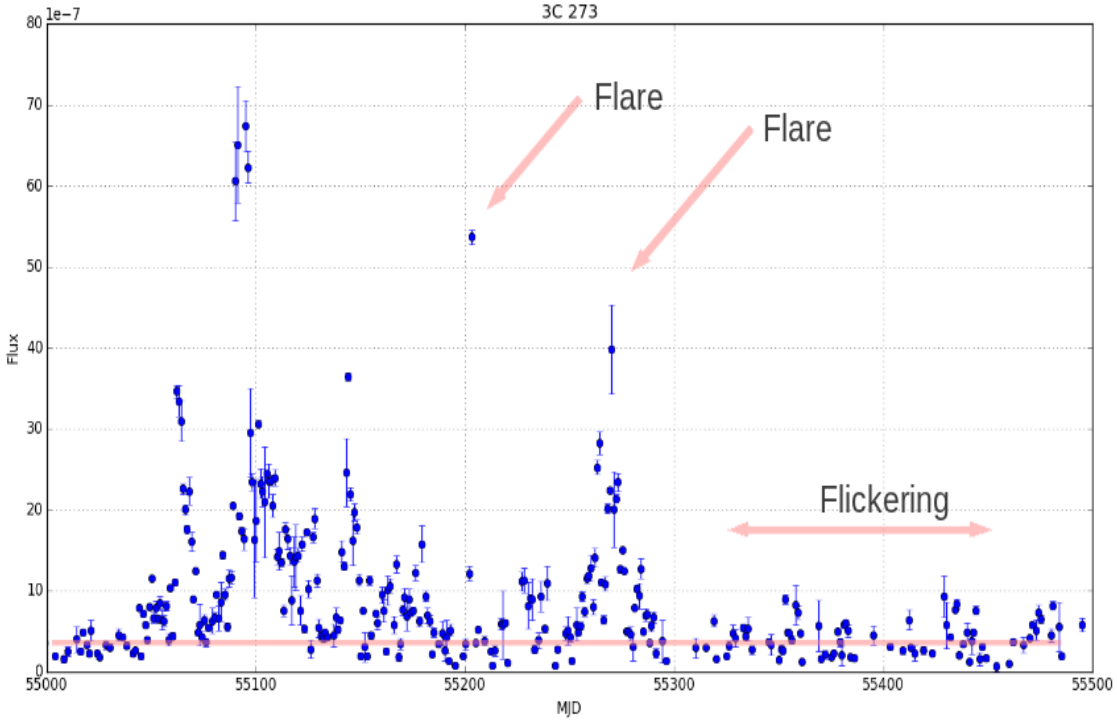

Figure 7.5: This plot shows two examples of flares observed at γ-ray energies (in ph cm^{-2} s^{-1}) in 3C 273. The first is occurs between 27 December 2009 (MJD 55192) and 24 January 2010 (MJD 55220) while a second flare is observed between 23 February 2010 (MJD 55250) and 14 April 2010 (MJD 55300). Flickering can be seen in the flux between 14 May 2010 (MJD 55330) and 11 September 2010 (MJD 55450). For this source the quiescent level flux was $\sim 4 \times 10^{-7}$ ph cm^{-2} s^{-1} (red line) over the 5.5 year monitoring period.

overall trend and structure of the flare shows a clear transition between the onset, peak and decay phases.

7.1.2 Outburst

An outburst in the γ-ray waveband is defined as a period of very intense or high activity. During this state, a significant increase in flux level occurs, doubling or tripling on timescales of several tens of days. An example of this is shown in Figure 7.6 obtained from 3C 279 between 11 October 2008 (MJD 54750) and 30 March 2009 (MJD 54920). An outburst typically appears as an epoch in which the source typically undergoes a series of flares along with rapid variability on daily timescales. Some of these flares may

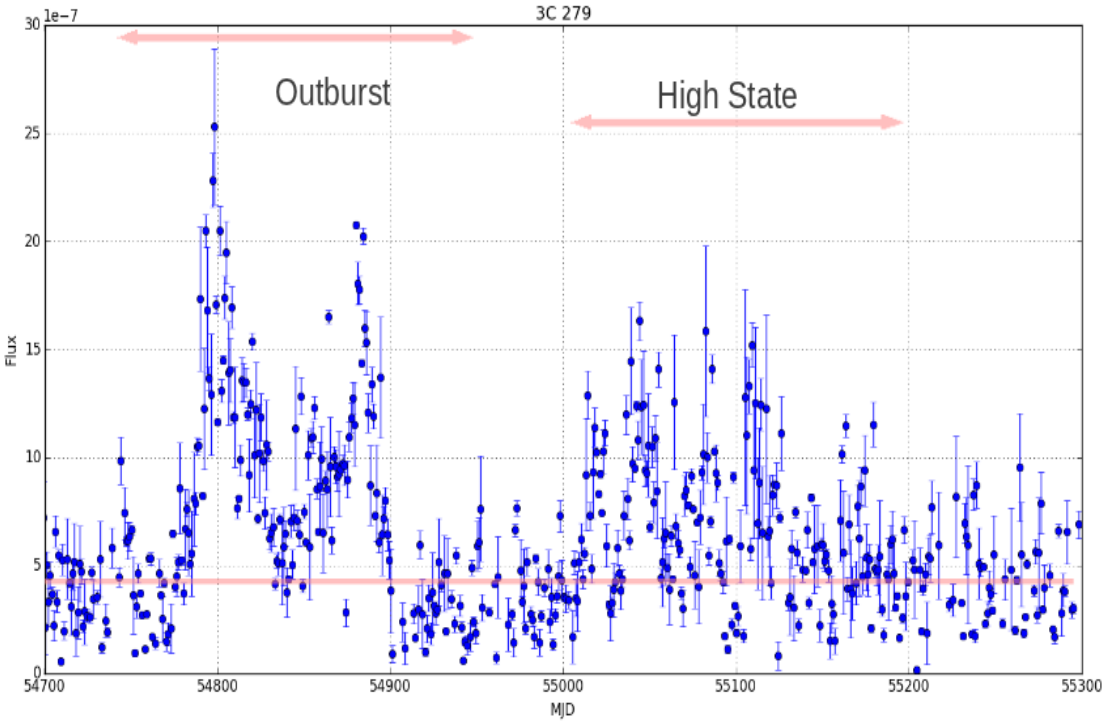

Figure 7.6: This plot represents an example of an outburst observed at γ-ray energies (in ph cm^{-2} s^{-1}) between 11 October 2008 (MJD 54750) and 30 March 2009 (MJD 54920) obtained from the 3C 279 *Fermi*-LAT light curve. A high state is observed at γ-ray energies between 18 June 2009 (MJD 55000) and 15 December 2009 (MJD 55180). The quiescent level flux for 3C 279 is $\sim 3 \times 10^{-7}$ ph cm^{-2} s^{-1} (red line).

appear superposed.

7.1.3 High State

A high state is a lengthened period of time (between several weeks to months) over which the flux remains in a high flux state relative to its quiescent level flux. During this period, the object may remain quiescent or exhibit flickering (see Section 7.1.4). In the γ-ray regime, an object usually enters a high state gradually, increasing over small intervals over periods of several weeks to months followed by a plateau phase (flux remains approximately constant) with comparatively smaller variations in flux than observed during an outburst or flare. An example of this can be seen in the light curve of 3C 279 between 18 June 2009 (MJD 55000) and 15 December 2009 (MJD 55180) shown in Figure

7.6.

At γ-ray energies, it is important to note that high states are at times difficult to differentiate from flares or outbursts due to the intrinsic nature of the γ-ray emission. Flares may be superposed upon each other resulting in the appearance of a high state with flickering flux levels instead of a structured outburst. For the purposes of this study, we define that flares and outbursts both have a distinct structure (onset $\rightarrow$ peak $\rightarrow$ decay) compared to the flickering behaviour observed in a high state which generally lacks structure. High states also do not often reach the peak flux levels observed in an outburst for a given source. This distinction can be seen in Figure 7.6 when the high state observed between 18 June 2009 (MJD 55000) and 15 December 2009 (MJD 55180) is preceded by an outburst observed between 11 October 2008 (MJD 54750) and 30 March 2009 (MJD 54920), which reaches much higher flux levels.

In summary, high states are distinguished from both flares and outbursts primarily by their lack of structure, their more gradual increase to a high state (rise times typically shorter than the rise times of a flare or outburst) and the fact that the maximum flux levels in a high state are typically lower than the the peak flux levels reached during a flare.

7.1.4 Flickering

Flickering is represented by short periods (typically between two and three months) where the flux exhibits small levels of variability ($< 10 \times 10^{-7}$ ph cm^{-2} s^{-1} over the period specified). These often manifest during periods of quiescence or high states. An example of this can be seen in the 3C 273 light curve between 14 May 2010 (MJD 55330) and 11 September 2010 (MJD 55450) shown in Figure 7.5. Flickering episodes can be distinguished from an outburst or flare because flickering is generally small level flux variability which lacks the onset $\rightarrow$ peak $\rightarrow$ decay structures of flares and outbursts. Flickering can be observed during all emission states in the γ-ray regime, but is not a common feature in the (sub-)mm wavebands.

Source	Maximum Flux	Date Observed
MRK 421	10.60 ± 2.33	17/8/12
MRK 501	5.91 ± 1.26	19/9/08
OJ 287	30.68 ± 4.87	4/8/11
BL Lac	22.12 ± 1.11	4/1/13
3C 273	67.47 ± 3.13	21/9/09
3C 279	56.27 ± 2.24	11/10/13
3C 454.3	590.0 ± 6.20	19/11/10
NGC 1275	16.30 ± 2.33	18/8/13

Table 7.3: The maximum fluxes and their corresponding dates observed over the monitoring period for each source at 100 MeV to 100 GeV γ-ray energies. The maximum flux is measured in units of $\times 10^{-7}$ ph cm^{-2} s^{-1}.

7.2 A summary of the *Fermi*-LAT Flux Maxima and Minima

Table 7.3 shows a summary of the maximum and minimum flux levels and their corresponding observation dates for each source at *Fermi*-LAT γ-ray energies, over the duration of the monitoring period. The greatest variability is displayed by 3C 454.3, which has the highest and second lowest fluxes.

7.3 *Fermi*-LAT and SMA Light Curves

High Frequency Peaked BL Lac Objects

7.3.1 MRK 421

The γ-ray light curve shows an outburst which began on 22 June 2012 (MJD 56100) and a high state between 8 January 2013 (MJD 56300) and 27 July 2013 (MJD 56500). Unfortunately, no SMA data were available for either the outburst in 2012 or during the high state in 2013 (see Figure 7.7).

7.3.2 MRK 501

At *Fermi*-LAT energies, no strong outburst was observed. However, the source appears to exhibit flux variability throughout the 5.5 year observation period shown in Figure

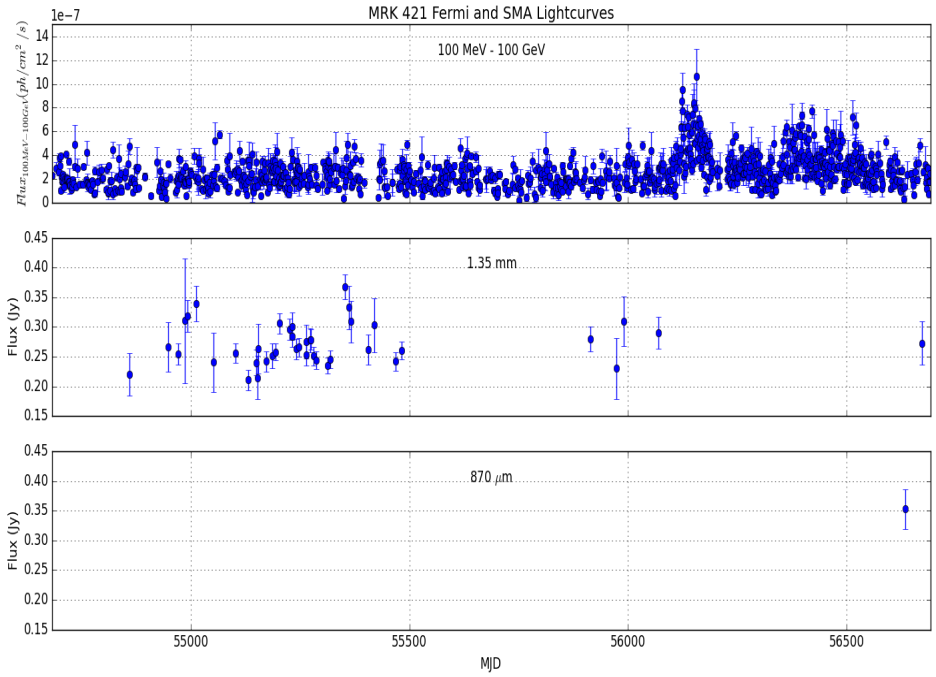

Figure 7.7: The 100 MeV to 100 GeV *Fermi*-LAT light curve together with the 1.35 mm and 870 μm SMA light curves for MRK 421.

7.8. There is no evidence for correlation between the γ-ray and (sub-)mm light curves primarily due to under-sampling in the SMA regime.

7.4 Intermediate Frequency Peaked BL Lac Objects

7.4.1 OJ 287

The 1.35 mm light curve shows two flares. During the second flare, which began on 15 November 2009 (MJD 55150), a flare is also observed in the *Fermi*-LAT light curves (Figure 7.9), though this is not the case during the first flare observed with SMA. While flux levels in the *Fermi*-LAT band return rapidly to the levels observed before the onset of the flare, the 1.35 mm light curve shows a longer period of decay, occurring between 15 March 2010 (MJD 55270) and 11 September 2010 (MJD 55450).

Another flare is observed at *Fermi*-LAT energies on 8 July 2011 (MJD 55750) followed by a high state between 14 March 2012 (MJD 56000) and 30 September 2012 (MJD 56200).

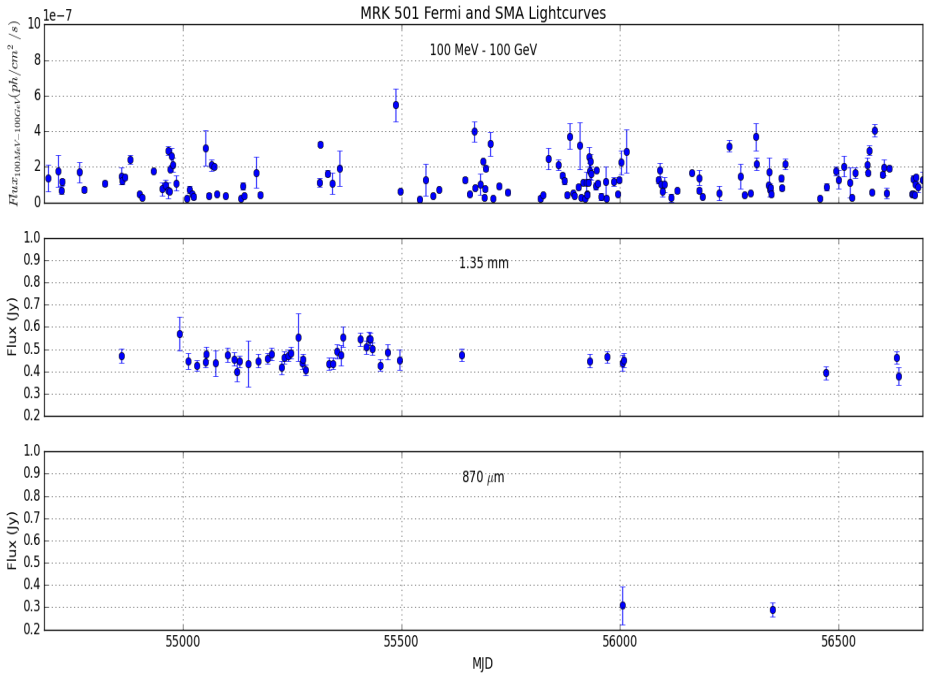

Figure 7.8: The 100 MeV to 100 GeV *Fermi*-LAT light curve together with the 1.35 mm and 870 μm SMA light curves for MRK 501.

However, during this period, no correlated event is seen at 1.35 mm around this period.

A qualitative analysis of the light curves show little evidence for correlation between the γ-ray and (sub-)mm regimes. Throughout the 5.5 year observation period, the 1.35 mm light curve shows the object in an initial flaring state after which the mm emission returns to quiescent levels with very weak flux variability. The γ-ray light curve appears more variable, with small, isolated active periods, one of which occurs during the second high state observed in the 1.35 mm light curve. The active periods in the γ-ray regime therefore do not seem to be directly correlated to the active periods in the mm regime. This may, however, indicate the presence of a time delay between flare events in the two wavebands.

7.4.2 BL Lacertae

The *Fermi*-LAT light curve in Figure 7.10 shows several low-amplitude flares, in which flux levels double within a day during the first half of the observation period. This can

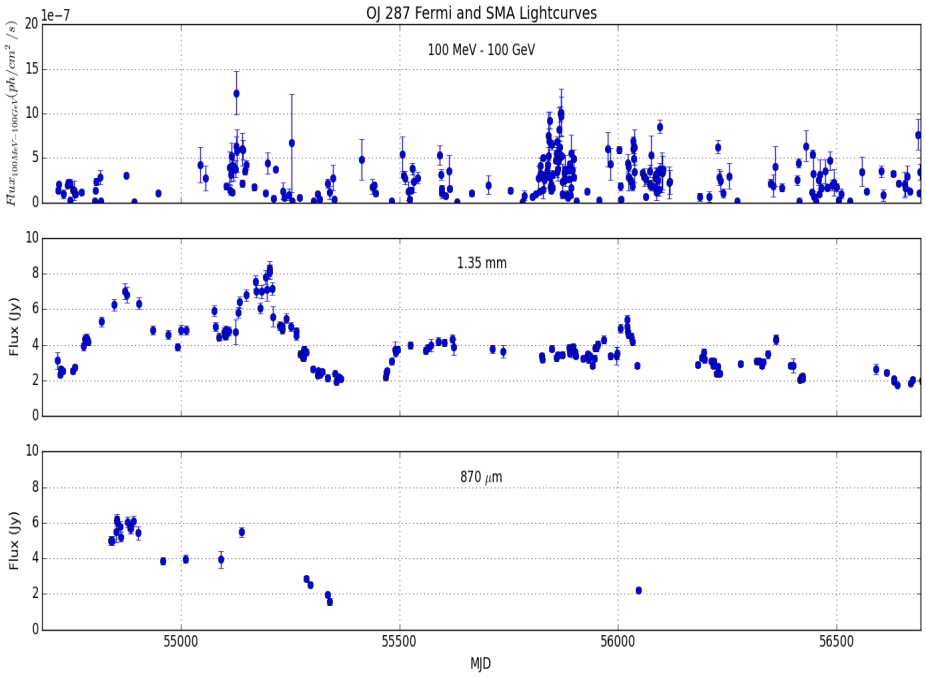

Figure 7.9: The 100 MeV to 100 GeV *Fermi*-LAT light curve together with the 1.35 mm and 870 μm SMA light curves for OJ 287.

be observed (by eye) from the light curve. During this period flux levels reached (12.8 $\pm$ 0.5) $\times 10^{-7}$ ph cm^{-2} s^{-1} on 15 April 2009 (MJD 54936). Analysis of the 1.35 mm light curve for the same period shows similar variability, albeit on longer timescales.

Beginning 29 January 2011 (MJD 55590), the *Fermi*-LAT light curve exhibited a gradual increase in variability amplitudes. This appears to be a prolonged outburst which began to decay on 7 February 2013 (MJD 56330). During this period the onset and decay of flares are not clearly defined. This may imply that either these flares evolve on timescales shorter than a day, or that the flares appear superimposed. Qualitatively, there appears to be some evidence of correlation with the 1.35 mm light curve. The latter also appears to be in a period of prolonged outburst occurring over the same time period.

Another period of interest begins on 27 July 2013 (MJD 56500) and lasts until 4 February 2014 (MJD 56692). During this time, it appears that the *Fermi*-LAT light curve once again shows that BL Lacertae enters into a state of outburst. However, the 1.35 mm emission appears to be decreasing in flux. This may indicate that mm emission may still be in the decay phase of the previous outburst which occurred between 29 January 2011 (MJD

55590) and 7 February 2013 (MJD 56330).

It is also observed that throughout the 5.5 year observation period, the 1.35 mm light curve exhibits an underlying increasing trend. Observations of flares and outbursts are superimposed over this general trend. This trend, however, is not visible in the *Fermi*-LAT light curve. At γ-ray energies, it is observed that only the variability amplitudes increase, as flux levels generally decay to levels observed during quiescent states.

BL Lacertae is the brightest of the IBLs at both γ-ray and (sub-)mm wavelengths. Analysis of *Fermi*-LAT and SMA light curves indicate that the object was in a particularly active state during the second half of the 5.5 year monitoring period. It is also observed that there is a greater level of correlation between the γ-ray and 1.35 mm energy bands compared to both the HBLs and OJ 287. As discussed above, during the first half of the observation period, when the variability amplitudes were lower at γ-ray energies, very little correlation is observed (by eye) with the 1.35 mm band. However, as the object enters into a state of outburst, the correlation becomes increasingly apparent although the nature of the light curves at γ-ray and 1.35 mm wavelengths are different. This will be analysed further using the DCF correlation method in Chapter 8.

7.5 Flat Spectrum Radio Quasars (FSRQs)

7.5.1 3C 273

As shown in Figure 7.11, the γ-ray light curve appears to show 3C 273 in an active state during the first part of the observation period. Beginning 4 August 2008 (MJD 54682), 3C 273 enters into a period of outburst with flux levels reaching (17.71 $\pm$ 2.65) $\times 10^{-7}$ ph cm^{-2} s^{-1}. This is followed by a much brighter outburst occurring between 18 June 2009 (MJD 55000) and 23 July 2010 (MJD 55400). During this period flux levels reach the maximum flux for this source of (67.47 $\pm$ 3.13) $\times 10^{-7}$ ph cm^{-2} s^{-1} (see Table 7.3). Multiple flares occur during this period, with intervals of 10 to 15 days between onset and decay.

Observations of 3C 273 at 1.35 mm also reveal an extended period of intense activity. Between 4 August 2008 (MJD 54682) and 18 June 2009 (MJD 55000), two outbursts are seen in the 1.35 mm light curve. During this stage flux levels reach (17.85 $\pm$ 0.89) Jy on 12 December 2008 (MJD 54812). A third outburst begins at 18 June 2009 (MJD 55000), reach-

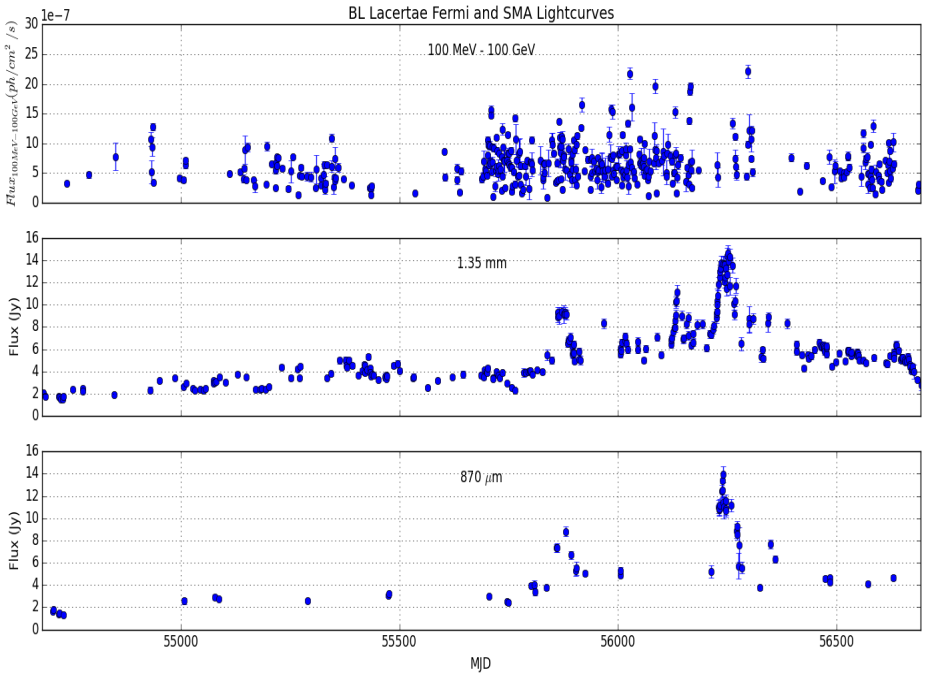

Figure 7.10: The 100 MeV to 100 GeV *Fermi*-LAT light curve together with the 1.35 mm and 870 μm SMA light curves for BL Lacertae.

ing peak flux levels of (15.00 $\pm$ 0.78) Jy on 4 November 2009 (MJD 55139), and continues to decay from its high state reaching flux levels of (6.90 $\pm$ 0.35) Jy on 5 November 2010 (MJD 55505). Following this, the 1.35 mm emission continues to decay for the remainder of the observation period to $\sim$ 3 Jy.

While both the mm and γ-ray light curves show an intense active state between 4 August 2008 (MJD 54682) and 18 June 2009 (MJD 55500), the outbursts observed at both energy regimes occur on different timescales and are not simultaneous. This indicates that there may be a time-delay between correlated events in both energy regimes. The outburst observed at 1.35 mm has rise and decay periods occurring on longer timescales compared to the γ-ray outbursts. Another feature observed at 1.35 mm which is not present in the γ-ray regime is the comparatively longer decay timescales of flares compared to its rising timescales. Flares in the γ-ray regime appear to have approximately similar rise and decay times.

In summary, the preliminary qualitative analysis suggests that while there may be some connection between the γ-ray and mm emission based on occurrence of active pe-

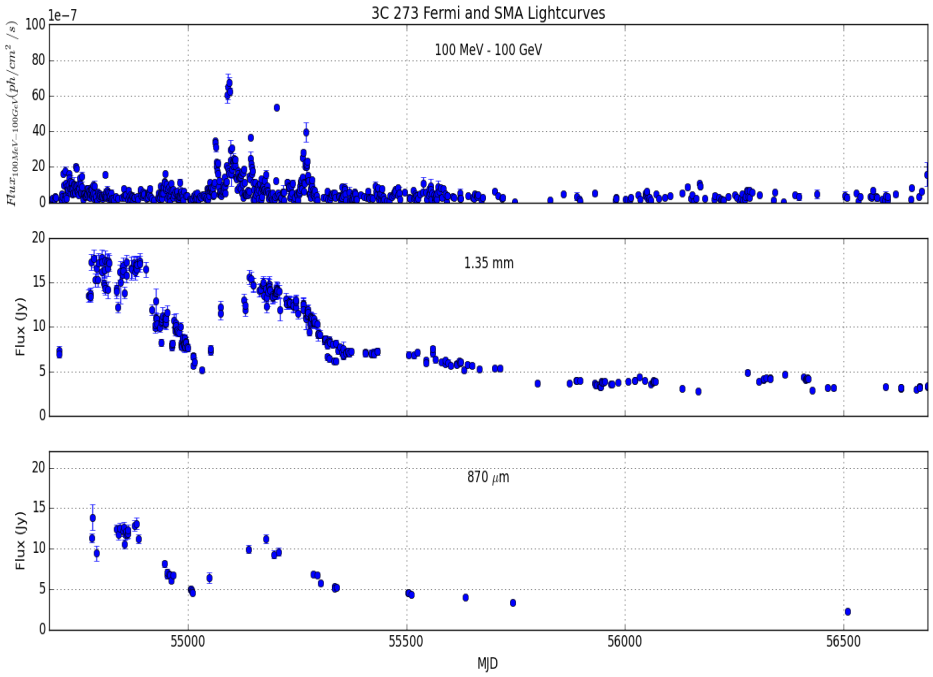

Figure 7.11: The 100 MeV to 100 GeV *Fermi*-LAT light curve together with the 1.35 mm and 870 μm SMA light curves for 3C 273.

riods during the observation period, the difference in timescales of the activity at both energy regimes may suggest that the emission regions are not co-spatial. Nevertheless, the same perturbation might be triggering a rise in activity in the γ-ray and 1.35 mm emission regions. However the delay suggests that either the perturbation triggers an event in the γ-ray region and travels further downstream to trigger emission in the mm region, or the mm emission is observed much later due to the effects of synchrotron opacity (see Chapter 3). This scenario may explain the longer variability timescales resulting from a more extended mm emission region compared to a smaller γ-ray emission region producing the more rapidly varying γ-ray photons.

7.5.2 3C 279

The maximum γ-ray flux of 3C 279 is the lowest of the three FSRQs presented in this study. Beginning 10 November 2008 (MJD 54780), this source entered a period of outburst with two distinct flares occurring consecutively (see Figure 7.12). During this pe-

riod the highest flux was (20.78 $\pm$ 0.13) $\times 10^{-7}$ ph cm^{-2} s^{-1} observed on 18 February 2009 (MJD 54880). This flare was then followed by a high state between 18 June 2009 (MJD 55000) and 14 April 2010 (MJD 55300). During this period, 3C 279 exhibited rapid variability on daily timescales. Following this the source went into several flaring episodes observed between 23 July 2010 (MJD 55400) and 31 October 2010 (MJD 55500), 8 February 2011 (MJD 55600) and 27 August 2011 (MJD 55800) and towards the end of the monitoring period between 26 November 2013 (MJD 56500) and 4 February 2014 (MJD 56692). During this final period of outburst (classified as such because a minimum of two flares was observed during this time), 3C 279 reached its brightest flux level (for the 5.5 year observation period) on 11 October 2013 (MJD 56576) at (56.27 $\pm$ 2.24) $\times 10^{-7}$ ph cm^{-2} s^{-1}. Most of these flaring episodes lasted between 100 to 200 days between onset and decay.

The 1.35 mm dataset, however, reveals a markedly different behaviour. Throughout the 5.5 year monitoring period, the 1.35 mm light curve shows a gradual increase in flux from ~ 5 Jy to ~ 20 Jy between 4 August 2008 (MJD 54680) and 22 June 2012 (MJD 56100). No clear period of outburst or flare is defined (Figure 7.12).

The difference in the nature of the light curves at γ-ray and mm wavelengths highlights the difference in the duty cycle (period of transition between different emission states) of the emission at both these wavelengths. The light curves appear to exhibit different features at both wavebands, and while 3C 279 is the faintest FSRQ (based on the convention defined in Section 7.1) at γ-ray energies, it is the second brightest at 1.35 mm based on the data available.

7.5.3 3C 454.3

This is the brightest source in the sample at both γ-ray and 1.35 mm wavelengths. The *Fermi*-LAT light curve in Figure 7.13 shows three distinct periods of outburst over the 5.5 year monitoring period. The first period of outburst begins on 15 November 2009 (MJD 55150) and lasts until 24 January 2010 (MJD 55220). During this period, the first flare reaches (162.8 $\pm$ 0.19) $\times 10^{-7}$ ph cm^{-2} s^{-1} on 3 December 2009 (MJD 55168). The second flare occurs between 25 March 2010 (MJD 55280) and 24 May 2010 (MJD 55340), reaching a peak flux of (100.3 $\pm$ 11.30) $\times 10^{-7}$ ph cm^{-2} s^{-1} on 4 April 2010 (MJD 55290). Beginning 11 October 2010 (MJD 55480), 3C 454.3 enters an exceptional outburst during

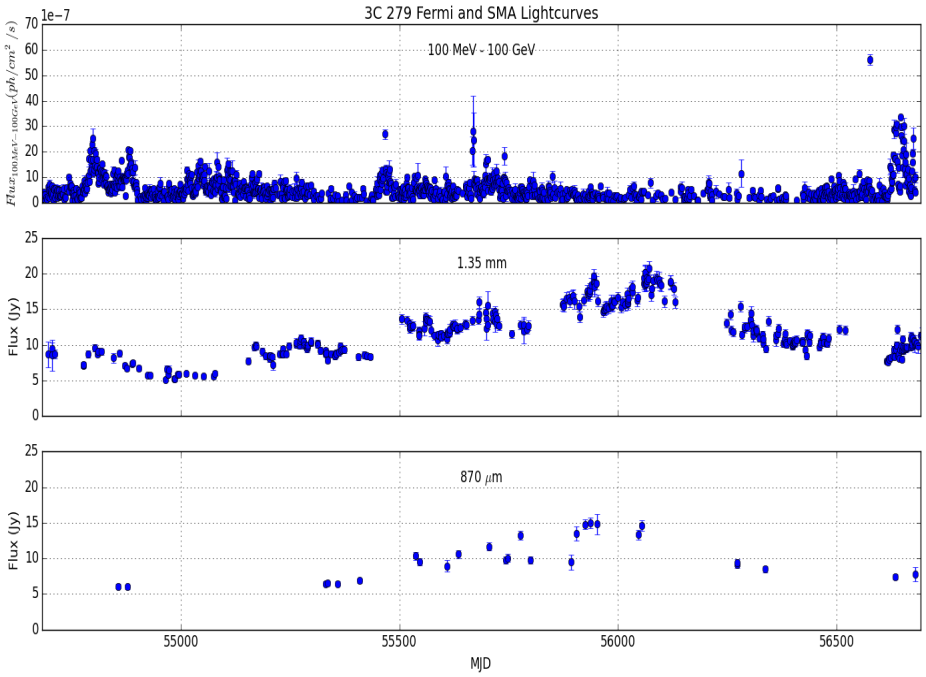

Figure 7.12: The 100 MeV to 100 GeV *Fermi*-LAT light curve together with the 1.35 mm and 870 μm SMA light curves for 3C 279.

which the object reaches (589.8 $\pm$ 6.20) $\times 10^{-7}$ ph cm^{-2} s^{-1} on 19 November 2010 (MJD 55519). During this period the flux level rises from (121.4 $\pm$ 0.27) $\times 10^{-7}$ ph cm^{-2} s^{-1} on 16 November 2010 (MJD 55516) to (404.0 $\pm$ 0.30) $\times 10^{-7}$ ph cm^{-2} s^{-1} on 17 November 2010 (MJD 55517). 3C 454.3 then returns to quiescent flux levels beginning 8 February 2011 (MJD 55600).

The exceptional outburst observed at γ-ray energies was also observed at 1.35 mm. The rise and peak of the outburst occur on similar timescales to those observed at *Fermi*-LAT energies. The peak of the 1.35 mm outburst was recorded at (51.77 $\pm$ 4.31) Jy on 20 November 2010 (MJD 55520), a day after the peak of the third γ-ray outburst. This indicates a quasi-simultaneous outburst in both the γ-ray and mm bands. The difference in the nature of the emission in both energy regimes is that the 1.35 mm data show a more gradual rise to peak flux levels, while the γ-ray data exhibit a sharper increase. The decay period of this particular outburst at 1.35 mm is also longer than the decay observed at γ-ray energies.

Another key difference between the 1.35 mm and γ-ray light curves is that, while

the latter enters into two periods of outburst between 15 November 2009 (MJD 55150) and 24 January 2010 (MJD 55220), and between 25 March 2010 (MJD 55280) and 24 May 2010 (MJD 55340) respectively, neither of these outbursts is observed in the 1.35 mm light curve. Instead, the 1.35 mm light curve suggests that the object was in a high state (given the lack of structure in the 1.35 mm dataset) between 18 June 2009 (MJD 55000) and 23 June 2010 (MJD 55370).

3C 454.3 exhibits periods during which the γ-ray and 1.35 mm regimes were both correlated and uncorrelated throughout the 5.5 year monitoring period. The correlated behaviour observed from the qualitative analysis is similar to other studies, namely those by Raiteri et al. (2008) (59), Jorstad et al. (2010) (214), which found correlation between the optical and mm bands varying between 15 and 60 days, with the higher frequency regimes leading the lower frequency bands. The interesting aspect of this particularly short lag between the γ-ray and 1.35 mm emission bands observed in Figure 7.13 will be explored further in Chapter 8 using a statistical correlation method.

The simultaneity of the correlation between the γ-ray and mm bands may be related to the brightness of the outburst as only the brightest γ-ray outburst appears to correlate with the 1.35 mm emission. This suggests that while there may be regions within the jet that are separate from each other emitting in different energy regimes, there may also emission regions within the jet that are co-spatial. An acceleration mechanism, the rise of a shock for instance, may cause co-spatial regions to radiate simultaneously. Alternatively, a stronger trigger may indicate that the energy transfer propagating through a co-spatial region occurs almost simultaneously.

7.6 Radio Galaxy

7.6.1 NGC 1275

The *Fermi*-LAT light curve for NGC 1275 is particularly interesting. Throughout the 5.5 year monitoring period, the source exhibits no particular periods of outburst or flares. The source however shows rapid variability which gradually increases in amplitude over the 5.5 year period. The 1.35 mm light curve also shows a gradual increase in flux levels over the 5.5 year monitoring period.

The lack of defined emission states observed in both energy regimes for this source

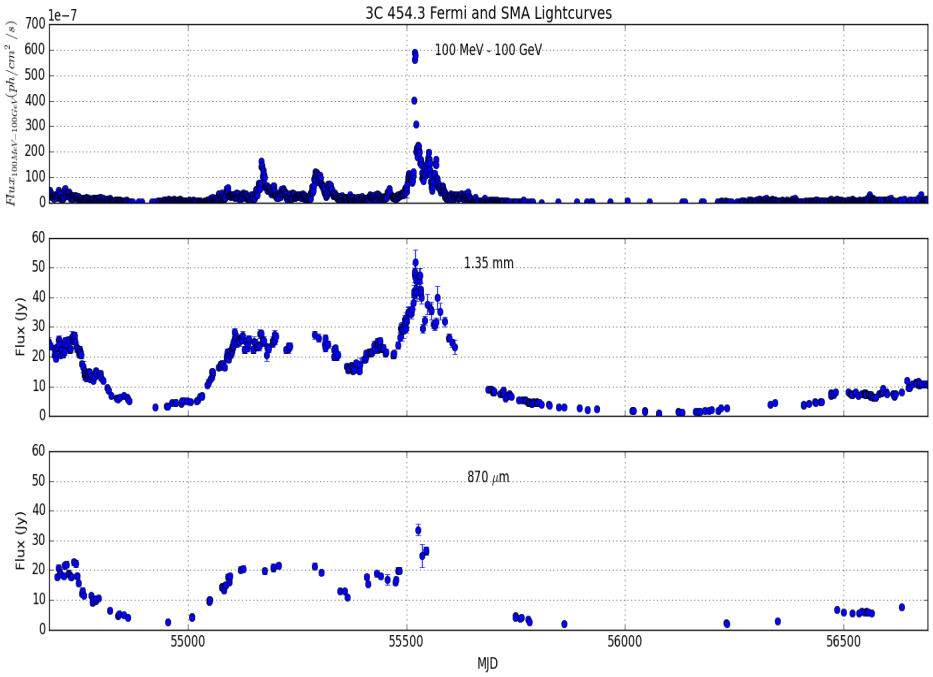

Figure 7.13: The 100 MeV to 100 GeV *Fermi*-LAT light curve together with the 1.35 mm and 870 μm SMA light curves for 3C 454.3.

may be due to its source class. As a radio galaxy, NGC 1275 is not directly aligned to the line-of-sight resulting in the observed emission from both non-thermal and extended thermal components in the host galaxy (120). The contribution to the emission from other structures may 'swamp' jet emission resulting in a lack of structure in the light curves of this source.

7.6.2 General Observations on the γ-ray and (Sub-)mm Emission

The most prominent difference between γ-ray and (sub-)mm emission is the variability amplitude and variability timescales of the radiation. It was found that the variability index, V at γ-ray energies for the 5.5 year observation period for all sources were ~ 1, suggesting that all sources were strongly variable at γ-ray energies. As discussed in Chapter 3, γ-ray emission varies on much shorter timescales with much higher variability amplitudes than emission in the (sub-)mm regimes. During quiescence, γ-ray variability is observed on daily timescales, while the (sub-)mm flux varies on timescales

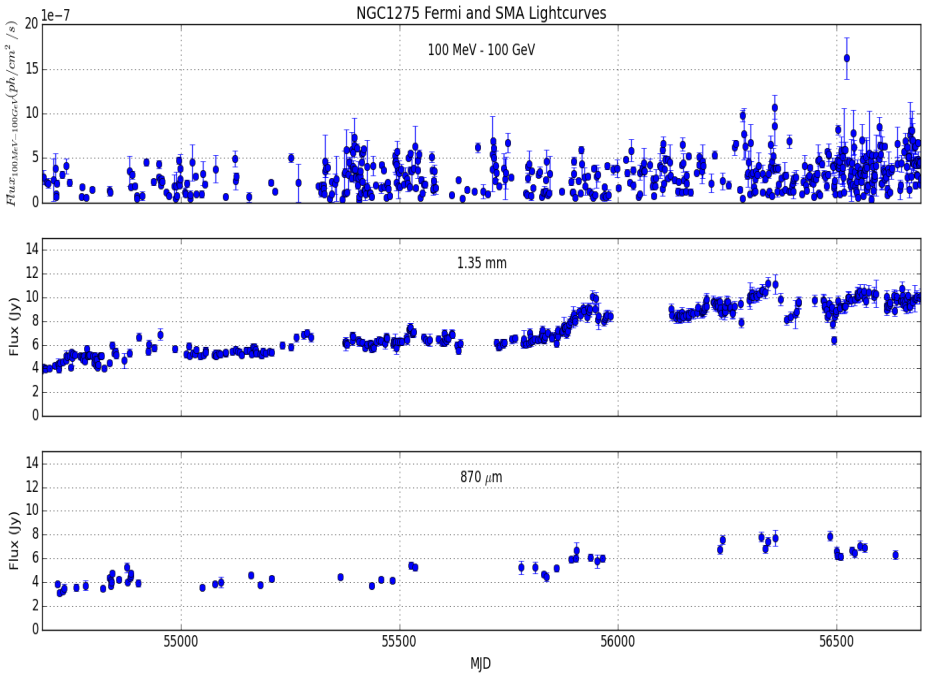

Figure 7.14: These plots show the 100 MeV to 100 GeV *Fermi*-LAT, 1.35 mm and the 870 μm SMA light curves for NGC 1275.

of several weeks to months[3] (e.g. MRK 421, BL Lacertae). As part of this pattern, active emission states including flares and outburst have much shorter rise and decay times at γ-ray energies compared to emission at (sub-)mm wavelengths.

Due to this, new flares in the (sub-)mm regime often emerge before a previous flare has decayed, causing the flares to appear superposed during an outburst (e.g. 3C 273).

The temporal differences in the emission at γ-ray and (sub-)mm wavelengths suggest that the emitting region is much smaller for the former compared to the latter, based on light crossing time arguments (see Section 3.2.3).

[3]While it is possible that the sensitivity of the instrument at (sub-)mm wavelengths may contribute to the lack of variability on daily timescales (the instrument sensitivity at (sub-)mm wavelengths is largely dependent on atmospheric opacities, as discussed in Chapter 4 and 6), other studies have also shown (sub-)mm variability on the timescales of weeks to months (311; 45). This is also in agreement with daily observations of MRK 421 presented in Chapter 5, which showed weak evidence for variability on daily timescales.

7.6.3 Connection between the γ-ray and (Sub-)mm Emission Relative to the Blazar Source Class

The preliminary qualitative analysis of the light curves show that transitions between states are more readily observed in IBLs and FSRQs than HBLs and the radio galaxy studied. For example, the γ-ray and (sub-)mm light curves for 3C 273, 3C 279 and BL Lacertae show periods of outburst and quiescence over the duration of the 5.5 year monitoring period. MRK 501 and NGC 1275, however, exhibit non-periodic, featureless variability at both γ-ray energies and (sub-)mm energies. MRK 421 exhibits one exceptional flare, superimposed on its non-periodic variability observed at γ-ray energies. Based on available data, emission at 1.35 mm of MRK 421 exhibits some structure, however, it was difficult to determine which emission state the source was in due to inconsistent monitoring leading to a general lack of data on this source[4].

Both NGC 1275 and BL Lacertae exhibit possible underlying increasing trends in the γ-ray (NGC 1275) and (sub-)mm (both NGC 1275 and BL Lacertae) emission. This trend appears more prominent at (sub-)mm energies and is more difficult to identify in the γ-ray energy band due to the rapid variability observed in the γ-ray waveband compared to the much lower variability amplitudes at (sub-)mm energies. No other source in the blazar sample exhibited this underlying trend feature.

7.6.4 Concluding Remarks on the Qualitative Analysis of *Fermi*-LAT and SMA Light Curves

The preliminary qualitative analysis in this chapter on the γ-ray and 1.35 mm behaviour, both independently and when considering the correlation between emission at these wavebands have resulted in the following findings:

- The γ-ray and 1.35 mm light curves for each source behave differently. For example, the temporal evolution between states and the transition into different emission states are different and can be observed in almost every source.

- The FSRQs and IBLs exhibit a more dynamic light curve at γ-ray and 1.35 mm energies compared to the IBLs and the radio galaxy. This is seen most clearly in the

[4]The lack of data made it difficult to determine baseline flux levels based on which flares and outbursts are usually distinguished.

IBLs and FSRQs during transition periods between quiescent and flaring states.

- The duty cycle (i.e. the period over which a source transitions from quiescence $\rightarrow$ active state $\rightarrow$ quiescence) of the γ-ray waveband is more easily understood than the duty cycle of the 1.35 mm band. The duty cycle of flares in the 1.35 mm waveband runs for several years. Some sources, namely 3C 273 and 3C 279, have duty cycles longer than 5.5 years, when analysis of the 12 year datasets is considered (see Chapter 6).

- There is some evidence for correlated behaviour for some of the sources in the sample (see Table 7.4). Due to the dynamic nature of the FSRQ and IBL light curves, correlation is also more readily observed as events at both wavebands can be distinguished more easily.

Several of the sources, particularly the IBLs and FSRQs (see Table 7.4), exhibited some level of correlation between the 1.35 mm and γ-ray wavebands. Most of the sources which showed possible correlation did so with the presence of temporal delay (typically between ~ 100 days and several hundreds of days) between events in the γ-ray and 1.35 mm regime (it is difficult at this stage to establish which wavelength may be leading the other) with the exception of 3C 454.3, which exhibited possible simultaneous correlation. This type of behaviour implies that while there may be multiple emission regions within the jet, some of these regions may either be co-spatial, or they may share the same particle population, along with external photon sources feeding into the jet.

The appearance of a shorter time delay between emission in the γ-ray and 1.35 mm wavebands for brighter flares, observed mainly with the FSRQs, suggests that the emission mechanism for both energy regimes may be the same. This would explain the simultaneous correlation between the γ-ray and 1.35 mm wavebands seen in 3C 454.4 light curves. A larger time delay, as observed in 3C 273 and 3C 279, suggests that a flare may propagate along the jet causing different emission regions to flare at different times.

In the following chapter, the level of correlation between the γ-ray and 1.35 mm light curves will be analysed statistically using the discrete correlation function method. This provides further insight into the type of correlation observed (i.e. simultaneous correlation, correlation with lag, anti-correlation or a lack of correlation).

A	B	C
MRK 421	No evidence	N/A
MRK 501	No evidence	N/A
OJ 287	Weak evidence	1.35 leads
BL Lacertae	Some evidence	γ-ray leads
3C 273	Some evidence	1.35 leads
3C 279	Weak evidence	γ-ray leads
3C 454.3	Some evidence	Simultaneous
NGC 1275	Some evidence	γ-ray leads

Table 7.4: Summary of the type (if present) of correlation observed for each source. Column A is the source name, Column B indicates whether evidence of correlation is present for that source and Column C suggests the waveband (either γ-ray or 1.35 mm) that might be leading emission in the other waveband.

Chapter 8

Correlation Between the γ-ray and 1.35 mm Emission in Blazars

In this chapter, a more statistically rigorous approach will be applied to examine if and how correlation may exist between the γ-ray and 1.35 mm light curves of the source sample. Based on the qualitative analysis presented in Chapter 7, it was found that correlation may be present for three out of the eight sources. These three sources are BL Lacertae, 3C 273 and 3C 454.3. The 100 MeV to 100 GeV γ-ray and 1.35 mm light curves from all eight sources will be analysed using the discrete correlation function method (see Section 8.1) in order to quantitatively search for any evidence of correlation between the wavebands. Evidence for correlation and the length of time delay between correlated events will then be used to draw a physical interpretation of the emission regions within blazar jets. First, however, the correlation method applied including the advantages and limitations of this method will be discussed.

8.1 The Discrete Correlation Function (DCF)

The discrete correlation function (DCF) method by Edelson & Krolik (266) was chosen to analyse the correlation between the γ-ray and 1.35 mm light curves due to the uneven sampling present in the 1.35 mm dataset. Apart from the DCF method, other correlation techniques, including cross-correlation (e.g. (239)) and several variations of the DCF method (e.g. ZDCF (3), DCCF (268; 146)), can also be used to study correlated behaviour in AGN. The cross-correlation method was not chosen because this technique relies on interpolating between missing data points. As the 1.35 mm regime was under-sampled for all the sources (primarily when a source was faint or below the horizon), the appli-

cation of this method may not produce accurate results. The DCF method as described by Edelson & Krolik (1988) (266) was chosen instead of variations of this method (e.g. the DCCF method (146)) because the basic DCF method is generally used in most research which studies correlation between the lower and higher energy bands in active galactic nuclei, even alongside variations of the DCF method. As such, applying the DCF method by Edelson & Krolik to this study facilitates direct comparisons with previous or ongoing studies in this area. In addition, this technique also allows time delays between correlated events to be measured based on available data without interpolating between gaps in the dataset. This is very useful, as gaps as long as several months (typically three months) exist in the SMA dataset which would skew the final outcome of the analysis.

8.1.1 Methodology

In order to apply this method, stochastic, statistically stationary[1] datasets are required. The correlation between each pair of points from each dataset (i.e. the γ-ray and 1.35 mm datasets respectively) is calculated based on Equation 8.1 using existing data points within the datasets. This Unbinned Discrete Correlation Function ($UDCF_{ij}$) for two datasets of different lengths is given by:

$$UDCF_{ij} = \frac{(a_i - \bar{a})(b_j - \bar{b})}{\sqrt{(\sigma_a^2 - e_a^2)(\sigma_b^2 - e_b^2)}} \tag{8.1}$$

where a_i and b_j are the i^{th} and j_{th} flux measurements in the 1.35 mm and γ-ray datasets respectively, $\bar{a}$ and $\bar{b}$ are the means of the 1.35 mm and γ-ray datasets respectively, and e_a and e_b are the noise contribution to the datasets, given by the average flux measurement errors of the 1.35 mm and γ-ray datasets respectively. Lastly, σ_a and σ_b represent the standard deviations of the 1.35 mm and γ-ray datasets respectively.

The Discrete Correlation Function ($DCF(\tau)$) parameter is then determined by averaging the $UDCF_{ij}$ values in a given time-lag bin. This is given by Equation 8.2.

$$DCF(\tau) = \frac{1}{M} UDCF_{ij} \tag{8.2}$$

[1]A statistically stationary dataset has the same mean and standard deviation throughout the entire dataset as a result of a stationary process which has no trends and no seasonal periodic fluctuation (see Section 8.4.2 for a detailed explanation).

where M is the number of values in each temporal bin (τ). Thus, the final DCF value is dependent on M which is determined by the size of the temporal bin. Effects of this on the DCF curve will be discussed in Section 8.4.4.

Calculation of the pairwise time delay, δ_t, given by Equation 8.3, uses the convention that the γ-ray observation dates (in MJD) are subtracted from the 1.35 mm observation dates (in MJD). In other words, δ_t is given by the MJD of the j^{th} term in the γ-ray dataset subtracted from the MJD of the i^{th} term in the 1.35 mm dataset. This results in positive delays representing information that the γ-ray emission leads the 1.35 mm by the corresponding time delay, while a negative δ_t indicates that the 1.35 mm emission leads the γ-ray emission.

$$\delta_t = t_i - t_j \tag{8.3}$$

The δ_t values are then binned into 30-day time bins for the length of the entire dataset (see Section 8.4.4). This includes the truncated 1.35 mm and γ-ray datasets presented in Chapter 7. $UDCF_{ij}$ values which fall into each 30-day bin are calculated and then averaged over the number of $UDCF$ values in that bin (i.e. M). This final value is the discrete correlation function, $DCF(\tau)$, which exists for each time bin, with the exception of time bins with no data points (266). $DCF(\tau)$ values are plot for the length of the datasets.

The significance of the DCF results for this study was determined using Monte Carlo methods which are described in Section 8.3.

A summary of the nomenclature used in the DCF study is shown in Table 8.1.

8.2 Testing the DCF Code using Simple Wave Functions

The DCF analysis code was first tested on two simple wave functions shown in Figure 8.1 as a green and blue wave respectively. Each wave is plotted between $\pm 2\pi$ radians and includes 201 data points. The wave functions were offset from each other and the data points within each wave function were spaced at different intervals. Data points in the green wave were spaced three days apart (in arbitrary MJD units) while data points in the blue wave were spaced two days apart (in arbitrary MJD units). The amplitudes of the wave functions were set between arbitrary limits of ± 1. Finally, simulated errors

Symbol	Definition
a_i	i^{th} flux in the 1.35 mm dataset
b_j	j^{th} flux in the γ-ray dataset
$\bar{a}$	mean of the 1.35 mm dataset
$\bar{b}$	mean of the γ-ray dataset
σ_a	standard deviation of the 1.35 mm dataset
σ_b	standard deviation of the γ-ray dataset
e_a	average flux measurement error in the 1.35 mm dataset
e_b	average flux measurement error in the γ-ray dataset
UDCF$_{ij}$	correlation between a_i and b_j
M	number of values present in a temporal bin
DCF(τ)	UDCF$_{ij}$ averaged over M in a temporal bin
δ_t	pairwise time lag between 1.35 mm and γ-ray
t_i	MJD of the i^{th} term in the 1.35 mm dataset
t_j	MJD of the j^{th} term in the γ-ray dataset

Table 8.1: Summary of the nomenclature used in the DCF method.

Details	Wave 1 (blue)	Wave 2 (green)
Data Points	201	201
Period repeat every (radians)	2π	2π
Interval Between Data Points (days)	2	3
Amplitude (arbitrary units)	$\pm$1.5	$\pm$1.5
Arbitrary MJD	2000 to 2400	2000 to 2600

Table 8.2: Details of the two pseudo light curves generated to test the DCF code based on the method described in Section 8.1.1.

were also introduced to the datasets by randomly selecting 201 values between 0.1 (in arbitrary units) and 0.3 (in arbitrary units) for each data point in each curve.

Table 8.2 shows a summary of the details of the two wave functions used in testing the DCF analysis.

Based on the equations presented in Section 8.1.1, a DCF plot was produced (Figure 8.2). The $UDCF_{xy}$ is calculated based on Equation 8.4.

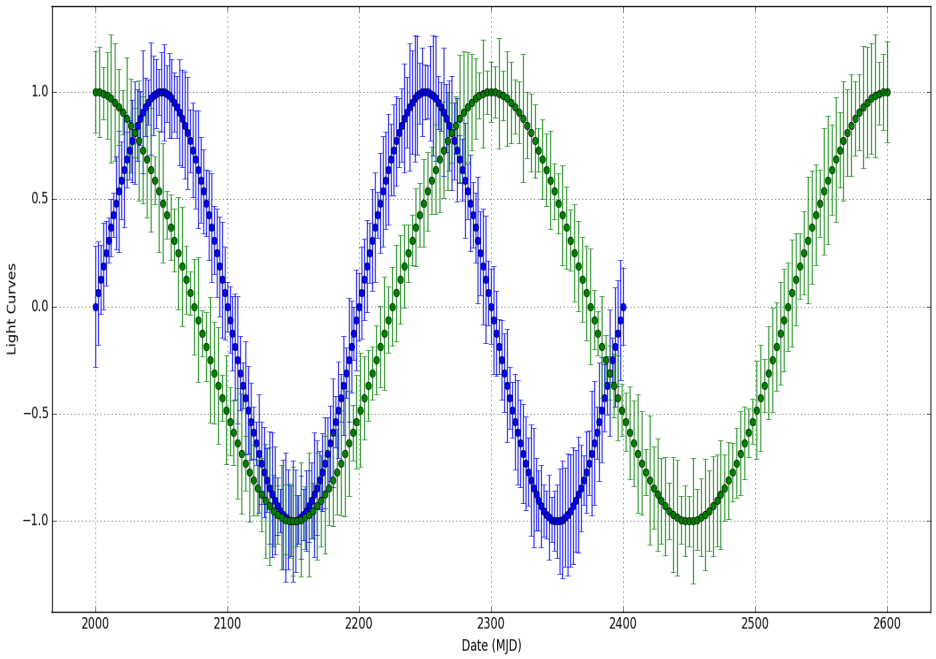

Figure 8.1: This plot shows two arbitrary wave functions offset from each other representing pseudo light curves. Data points in the blue wave are spaced two days apart and while data points in the green wave is spaced three days apart. Both curves were plotted between $\pm 2\pi$ radians. The x-axis represents the pseudo date of observation (in arbitrary MJD units).

$$UDCF_{xy} = \frac{(a_{x(blue)} - \bar{a})(b_{y(green)} - \bar{b})}{\sqrt{(\sigma_a^2 - e_a^2)(\sigma_b^2 - e_b^2)}} \tag{8.4}$$

where the a_i and b_j represent the x^{th} and y^{th} terms in the blue and green wave functions respectively. The pairwise lag for this case is calculated as described in Equation 8.5.

$$\delta_t = t_{x(blue)} - t_{y(green)} \tag{8.5}$$

where t_x and t_y represent the MJD of the x^{th} and y^{th} terms in the blue and green wave functions respectively. A bin size of five days was used. Before the DCF analysis on the test data was carried out, the expected results are summarised as follows:

First, there is a total of four peaks and troughs at both positive and negative am-

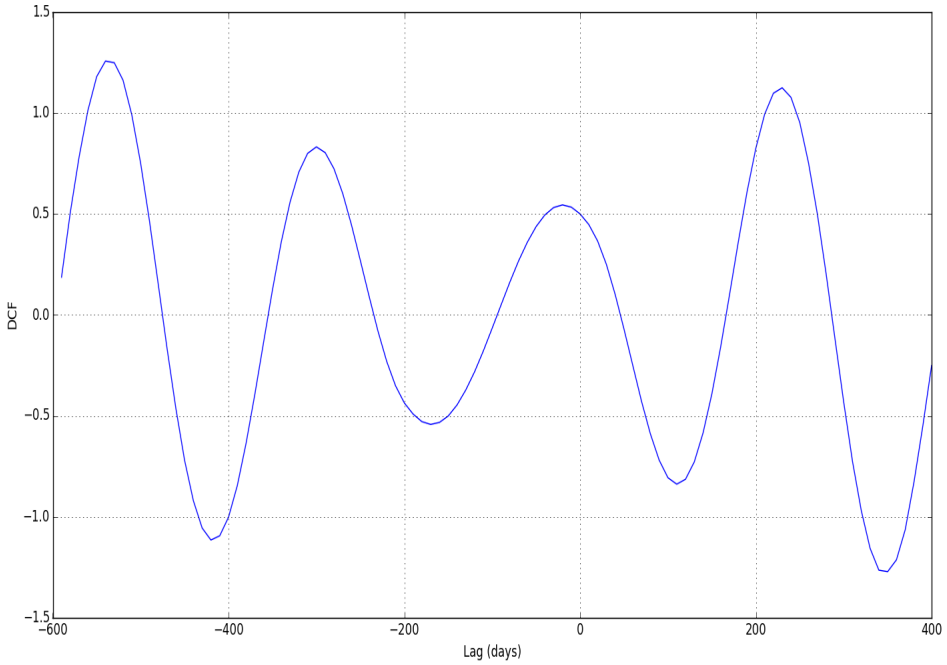

Figure 8.2: The DCF curve based on the method by Edelson & Krolik (266) for the data shown in Figure 8.1.

plitudes in the blue wave function as seen in Figure 8.1. The green wave function, on the other hand, has a total of five peaks and troughs at both positive and negative amplitudes. Thus a total of four positive correlation peaks and four anti-correlation peaks is expected. Based on the DCF method described in Section 8.1.1, positive correlations are expected at both positive and negative lags. These will be at a lag of -30 days, +225 days, -300 days and -550 days. The positive lags (days) represent the blue wave leading the green wave while the negative lags (days) represent the green wave leading the blue wave.

Anti-correlation can be expected when a peak at a positive amplitude correlates with a peak at a negative amplitude (Figure 8.1). These are expected at +125 days, +325 days, -175 days and -425 days.

For this test, the DCF curves produced from the test datasets is assumed to show evidence for correlation or correlation as a function of the temporal lag when the peaks and troughs exceed an arbitrary threshold value of ± 0.5[2]. As expected, positive correlation

[2]The significance of the DCF results for the eight blazar sources, however, are estimated using Monte

peaks are observed at -30 days, +225 days, -300 days and -550 days[3]. The DCF peak at -30 days is the smallest because there are more correlated data points ($UDCF_{xy}$) at this temporal bin than at temporal bins at a lag of +225, -300 and -500 days. This can be observed by eye in Figure 8.1. There is also evidence for anti-correlation at lags of +125 days, +325 days, -175 and -425 days. This also agrees with the expected results. Thus, the DCF code can now be used to analyse correlation between the γ-ray and 1.35 mm light curves presented in Chapter 7.

This test analysis also provides a broad view of some of the shortcomings of the DCF method which must be accounted for while performing the DCF analysis for the eight sources (see Section 8.4).

8.3 Estimating the Significance of the DCF Analysis

The significance of correlation is primarily dependent on the limitations of the DCF method. These are discussed at length in Section 8.4. One of the most common effects of these limitations is the occurrence of spurious correlation peaks. This can be explained as a result of two physically uncorrelated flares, one observed in the γ-ray light curve and the other in the 1.35 mm light curve, which results in a $DCF(\tau)$ peak at the given time lag separating the two flares, as discussed in Fuhrmann et al. (146). The second aspect which affects the significance of the DCF analysis for the datasets presented in this thesis is the variability timescales and duty cycles of the γ-ray and 1.35 mm emission. As discussed in Chapters 6 and 7, the behaviours of the γ-ray and 1.35 mm emission are intrinsically different, as shown by the requirement for separate definitions of states for the two wavelength regimes. One major difference that should be noted is the lack of structure (i.e. distinct transition between emission states, from flares to quiescence) seen particularly in the γ-ray regime for both the HBLs, BL Lacertae and NGC 1275. For NGC 1275 in particular, the 1.35 mm light curve did not show any structure either. Since the DCF method relies on correlating the occurrence of one flare in one wavelength regime to another flare in the second wavelength regime, this will be difficult to achieve when

Carlo simulations of light curves. These are discussed in Section 8.3

[3]The difference observed between these values and that summarised previously as the expected correlated time delay is primarily due to the difference in the intervals between the two datasets analysed, i.e. data in the first and second datasets were spaced at two and three day intervals respectively.

the light curves are intrinsically different (i.e. if distinct structure in the light curve is observed at 1.35 mm while no distinct structure is observed at γ-ray energies).

Estimating the significance of a peak requires an unbiased DCF analysis using particularly uncorrelated datasets. In principle, a significance estimate of a $DCF(\tau)$ peak is determined by estimating the chance probability of obtaining a given correlation value based on the $DCF(\tau)$ amplitude from the distribution of random $DCF(\tau)$ amplitudes at a given time lag when the pairs of simulated light curves are correlated (239; 238; 268). One method of estimating this distribution is by performing a 'mixed source correlation'. This is done by performing the DCF analysis at one wavelength regime for one source with the other wavelength regimes of other sources (268; 146). This method relies on the assumption that variability timescales are the same at the respective wavelengths for the different sources analysed. This, as seen in Chapters 6 and 7, is not a safe assumption to make, as the variability timescale in an emission waveband varies from source to source and from epoch to epoch. This method of significance estimation also requires a large sample of sources.

The significance tests also rely greatly on the number of sources in a sample, and the number of wavelength regimes available for analyses if methods like the mixed source correlation analyses are to be performed. The source sample available for analysis in this thesis is relatively small compared to source sample sizes of > 30 used in other studies, with multi-waveband monitoring (> 3 wavelength regimes) (146; 238; 268). Thus, significance tests conducted with the available source sample and data present in this study may result in inaccuracies in the significance estimates.

For this study, the significance of a correlation coefficient ($DCF(\tau)$) will be estimated using Monte Carlo simulations of γ-ray and 1.35 mm light curves. In order to statistically determine the significance of the DCF results based on the method outlined in Section 8.1.1, an estimate of the significance was obtained using Monte Carlo simulations in which a large number of independent, uncorrelated light curve pairs were generated based on a simple power-law power spectral density (PSD) model for the light curves (261). The DCF analysis was then performed on each light curve pair and the distribution of the resulting random correlation coefficients was determined at their corresponding time lag. Based on this, the chance probability of obtaining a given $DCF(\tau)$ value at a given time lag was estimated. This method is an approximation based primarily on

work presented by Max-Moerbeck et al. (238).

8.3.1 Simulating the γ-ray and 1.35 mm Light Curves

The pairs of independent, uncorrelated light curves were simulated to replicate the aperiodic variability as well as the broad temporal features observed in the γ-ray and 1.35 mm datasets presented in Chapter 7. In order to achieve this, a Fourier Transform was used to generate light curves modelled by a simple power-law PSD ($PSD \propto \nu^{-\alpha}$). Since time variability in blazars (and AGN, in general) are typically modelled after a simple power-law PSD (e.g. (238; 198)) and has been previously measured for several blazar sub-classes at different wavelengths, the values of α have been found to range between $\alpha = (1.4 \pm 0.1)$ and (1.7 ± 0.3) at γ-ray wavelengths (28) to $\alpha = (2.3 \pm 0.5)$ at radio wavelengths (204). The flux for each observation was generated based on the following equation:

$$l(t) \propto \sum_{\nu} \sqrt{P(\nu)} \cos[2\pi\nu - \phi(\nu)] \tag{8.6}$$

where $\phi(\nu)$ is the phase of the signal and is randomised such that $\phi(\nu) \in [0, 2\pi]$. $\sqrt{P(\nu)}$ is the amplitude of the signal in which $P(\nu) \propto \nu^{-\alpha}$ (267). The amplitude of the function is chosen at random from a chi-squared distribution with two degrees of freedom. A constant of proportionality is also introduced into the function, again chosen from a chi-squared distribution with two degrees of freedom. The mean and standard deviation are chosen such that the final resulting amplitude of the signal matches the average flux obtained from a blazar source (~ 30 ph cm^{-2} s^{-1} and ~ 30 Jy from the light curves present in Chapter 7). It was necessary that both the amplitude and constant of proportionality parameters were chosen from a chi-squared distribution as this produced similar aperiodic variability to the original γ-ray and 1.35 mm light curves presented in Chapter 7. This is based on the work by Timmer & Koenig (261). It was found that in order to produce light curves with linear aperiodic signals which exhibit the $P(\nu) \propto \nu^{-\alpha}$ power-law spectrum, the amplitude for each sampling frequency should be obtained from two random numbers that are drawn from a Gaussian distribution. These two numbers represent the real and imaginary parts of the Fourier transform at each given sampling frequency. However, as the sum of the two squared Gaussian distributions follow a chi-squared distribution with two degrees of freedom, the latter was

chosen to produce the amplitude and constant of proportionality for this study (261). Further to this, it was also found that, choosing the amplitude from a different distribution (e.g. Gaussian distribution) instead of a chi-squared distribution produced a more periodic, noisy signal rather than the type of aperiodic variability observed in the original light curves. $l(t)$ is first evaluated and summed for a discrete set of frequencies, ν, such that $\nu = \nu_{min}, 2\nu_{min}, 3\nu_{min}, ..., \nu_{Nyq}$. ν_{Nyq} is the Nyquist frequency and is given by $N/2T$ for a time series sorted in time between 1 and N, while T is given by $N/(t_N - t_1)$ and t_1 and t_N is the first and last date (in MJD) of the simulated datasets (198).

For this work, and based on the light curves presented in Chapter 7 which comprise all three blazar sub-classes, a value for α was chosen such that $\alpha = 2$ for γ-ray light curves while $\alpha = 3$ for 1.35 mm light curves. This is consistent with PSD estimates from studies conducted by Abdo et al. (28), Chatterjee et al. (204) and Max-Moerbeck et al. (239) and will be applicable to a wide range of blazar sources consistent with the range and variety of light curves present in this study.

Figures 8.3 and 8.5 are examples of independent light curve pairs produced using this method. This can be compared to the original light curves of 3C 273 (Figure 8.4) and BL Lacertae (Figure 8.6), reproduced here for convenience.

8.3.2 Significance Estimates

Using the parameters outlined above, 1000 independent and uncorrelated light curve pairs were simulated to represent the γ-ray and 1.35 mm light curves respectively. The DCF analysis based on the method described in 8.1.1 was performed on each light curve pair. For each given time delay, the distribution of the resulting random correlation coefficients obtained from the DCF analysis of the 1000 light curve pairs were recorded in the form of a histogram. Next, the range of correlation coefficients which contained 68.27% of the $DCF(\tau)$ values was determined for each time delay (i.e. for each histogram). This range indicates the 1σ significance level. Similarly, the range of $DCF(\tau)$ which contains 95.45% and 99.73% was determined. These are considered as the 2σ and 3σ significance levels respectively. An example of one of these histograms, for a lag of +440 days between the two simulated light curves is shown in Figures 8.7. Based on Figure 8.7, the 1σ band includes $DCF(\tau)$ values ranging between -0.10 and + 0.10, the 2σ band includes $DCF(\tau)$ values ranging between -0.17 and +0.18, while the 3σ significance band includes

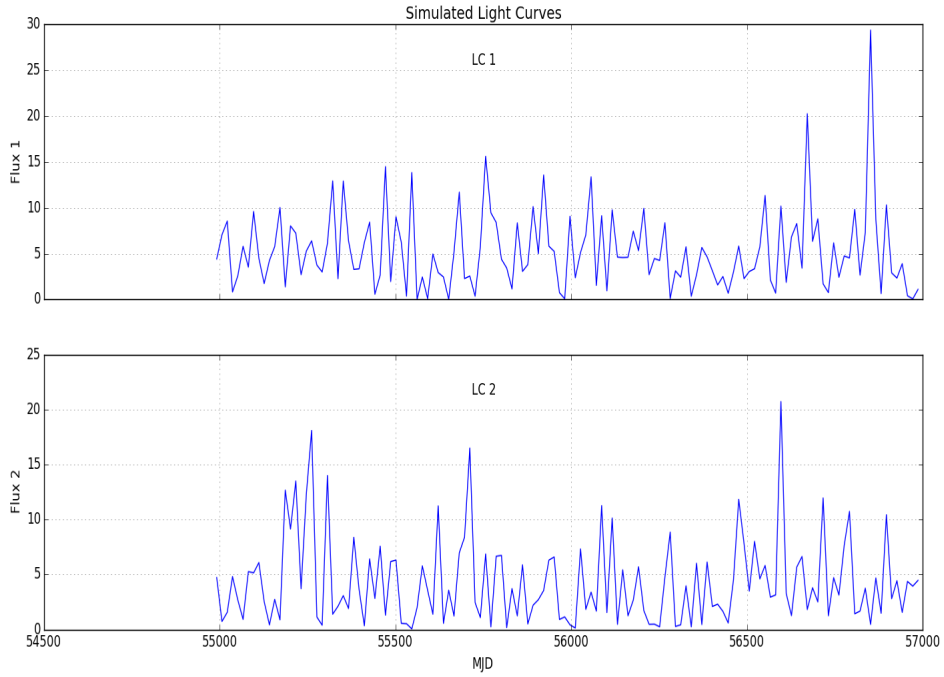

Figure 8.3: Example of a simulated light curve generated based on the method described in Section 8.3. The units of the modelled light curves LC1 and LC2 are ph cm^{-2} s^{-1} and Jy respectively. This is comparable to the light curves of 3C 273 presented in Chapter 7, reproduced here for convenience (Figure 8.4).

$DCF(\tau)$ values ranging between -0.23 and +0.28 (see also Figure 8.8). The significance levels obtained from the DCF analysis of the simulated light curves provide an estimate of the significance of the DCF results in this study. $DCF(\tau)$ values which exceed the 3σ level will be considered as indication of possible evidence for correlation between emission at the γ-ray and 1.35 mm wavebands.

8.4 Caveats Concerning the DCF Method

There are several caveats which could contribute to the uncertainty in the outcome of the $DCF(\tau)$ values. These caveats will be discussed in the following sections.

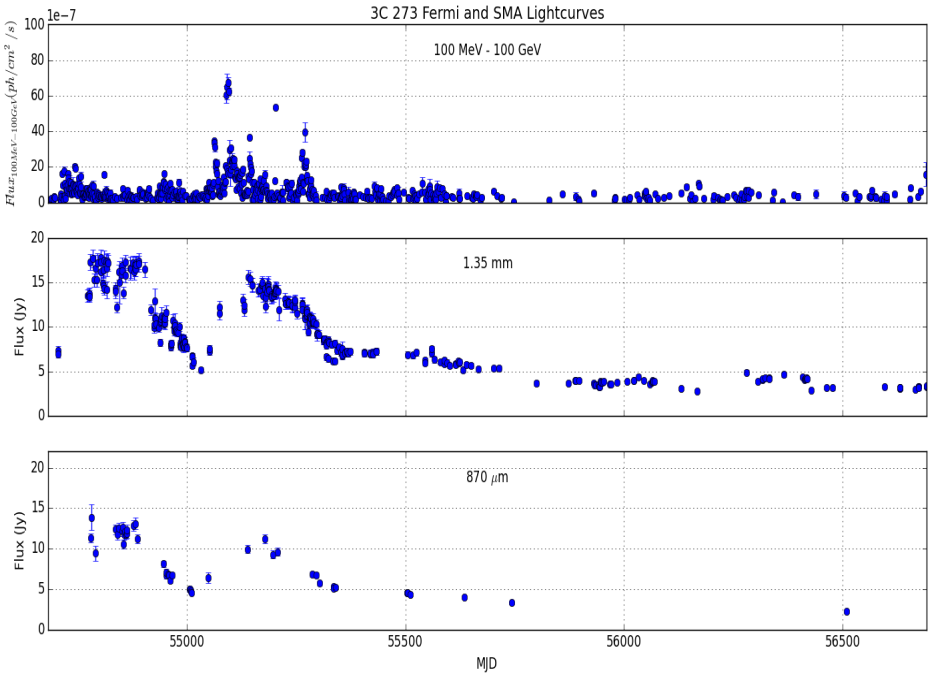

Figure 8.4: *Fermi*-LAT and SMA light curves of 3C 273 reproduced here for comparison with simulated light curves shown in Figure 8.3.

8.4.1 Effects of the *Fermi*-LAT Test Statistic on the DCF Analysis

As discussed in Chapter 7, the high energy (inverse Compton) peaks of the HBL SEDs predominantly fall in the GeV to TeV range of the electromagnetic spectrum. As such, the γ-ray light curves for sources including MRK 421 and MRK 501 exhibited some level of noise. In order to reduce effects of these noise contributions, the TS threshold value was raised from $TS = 10$ to $TS = 25$.

In Figures 8.9 and 8.10, it is observed that increasing the TS threshold increases the values of the $DCF(\tau)$ amplitudes. As observed in Chapter 7, increasing the TS threshold reduces the number of data points present for MRK 421 and MRK 501, thus reducing the number of $UDCF_{ij}$ values present in each bin. This also alters the distribution of $UDCF_{ij}$ and the resulting average (i.e. $DCF(\tau)$ amplitudes) at each time delay. This is readily observed in MRK 501 (Figures 8.11 and 8.12) as there were far fewer data points for MRK 501 at *Fermi*-LAT energies which exceeded the $TS = 25$ threshold. However, the contribution of systematic noise as a result of a lower TS threshold for HBLs may

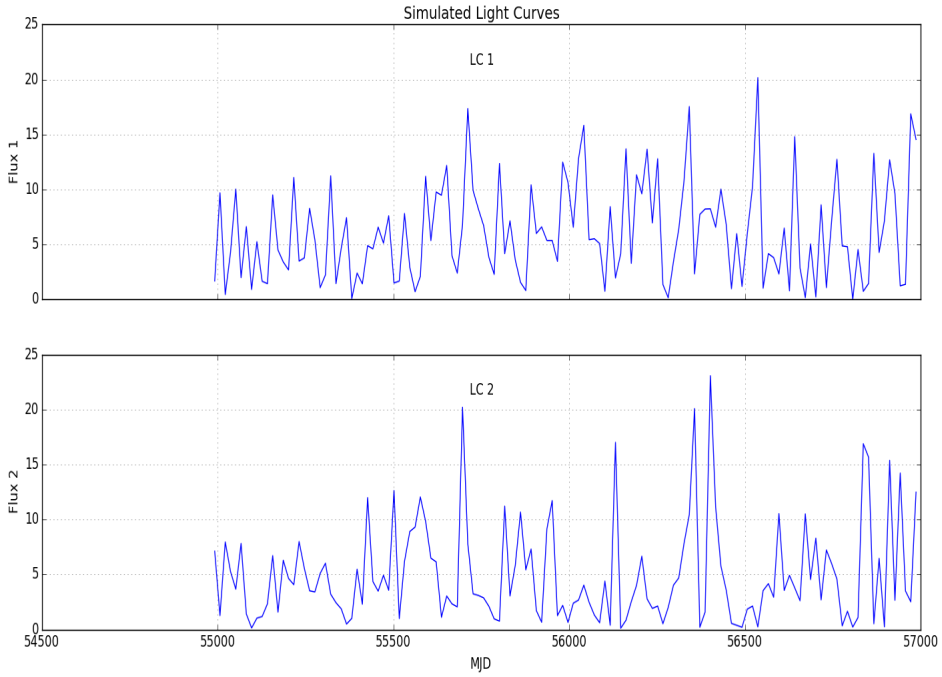

Figure 8.5: Example of a second simulated light curve generated based on the method described in Section 8.3. This is comparable to the light curves of BL Lacertae presented in Chapter 7, reproduced here for convenience (Figure 8.6).

result in a less accurate DCF analysis since the general faintness of the HBLs increases the possibility that *Fermi*-LAT data using TS = 10 may contain incorrect flux measurements which may further affect the accuracy of the DCF analysis. The difference in the DCF analyses for both MRK 421 and MRK 501 using the different TS threshold values demonstrates the sensitivity of DCF analysis to the sampling frequency of a given light curve (see Section 8.4.5). The final DCF analysis produced in this chapter for MRK 421 and MRK 501 will be performed using the TS threshold of 25 as this reduced the presence of systematic noise in the datasets.

8.4.2 'Detrending' 1.35 mm and γ-ray Datasets

Before the DCF method was applied, it was necessary to first determine if both the γ-ray and 1.35 mm datasets were statistically stationary, stochastic functions. The DCF technique relies on the datasets being stationary, i.e. datasets which have no underlying

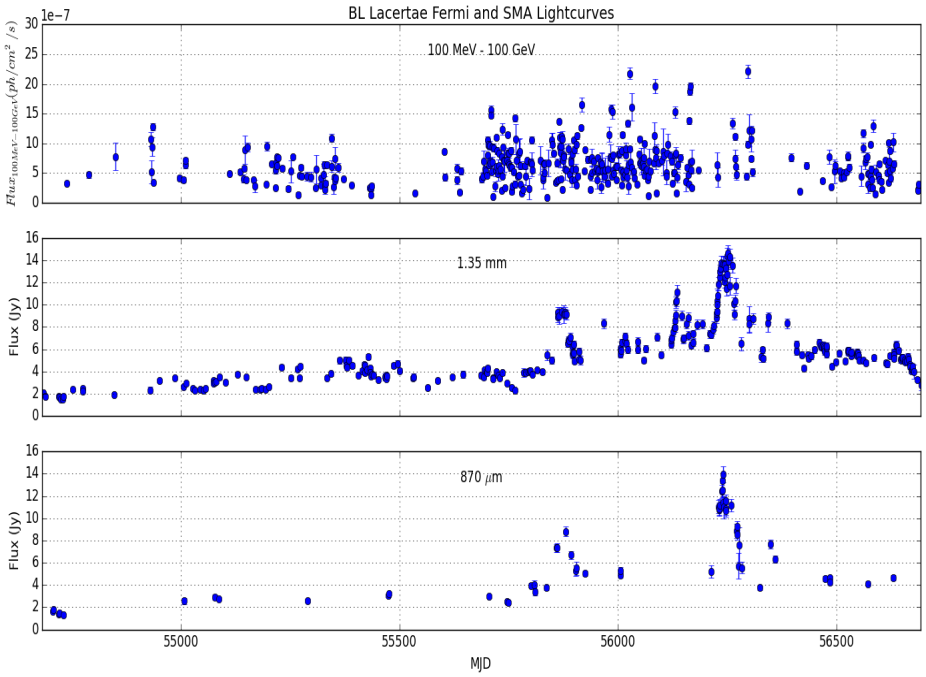

Figure 8.6: *Fermi*-LAT and SMA light curves of BL Lacertae reproduced here for comparison with simulated light curves shown in Figure 8.5.

trend present that would cause the mean and standard deviation to change with time. The datasets available in this study span the length of several years and the variability timescales of the γ-ray and 1.35 mm light curves differ between flaring and quiescent states. This is primarily evident when the emission at a particular wavelength exhibit outbursts or high states for long periods of time without returning to baseline flux levels (see Chapter 7).

As an example, a DCF curve produced using the original non-stationary γ-ray and 1.35 mm light curves of NGC 1275 is shown in Figure 8.14. Due to an underlying rising quadratic trend (this will be discussed in detail below) present in the original datasets (see Figure 8.13 reproduced here from Figure 7.14), this trend is introduced into the DCF curve, producing a broad increase and decrease in the gradient of the overall DCF curve.

Of the eight sources, it was found that only NGC 1275 and BL Lacertae had non-stationary datasets. This is clearly visible in Figures 8.13 and 8.16. In order to determine the underlying trends that feature in the γ-ray and 1.35 mm light curves of BL Lacertae and NGC 1275, each γ-ray and 1.35 mm light curve from each source was fitted using

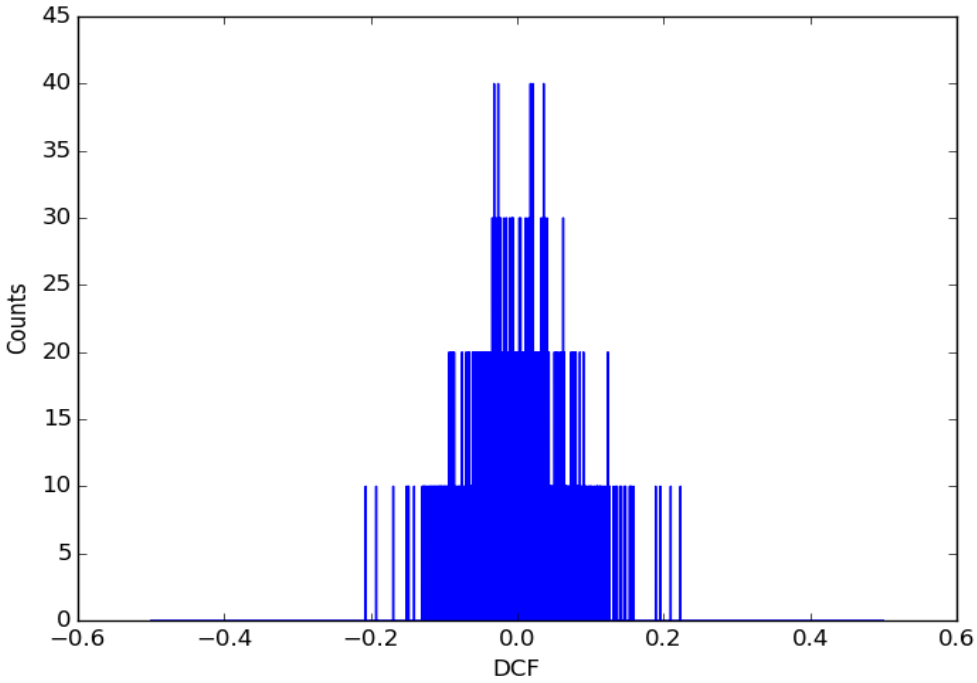

Figure 8.7: Distribution of the $DCF(\tau)$ coefficients at a time delay of +440 days obtained from performing the DCF analysis on 1000 pairs of simulated light curves based on the method described in Section 8.3. The $DCF(\tau)$ range of -0.10 and +0.10 contain 68.27% of the random correlation coefficients. The $DCF(\tau)$ range of -0.17 and +0.18 contain 95.45% of the random correlation coefficients and the $DCF(\tau)$ range of -0.23 and +0.28 contain 99.73% of the random correlation coefficients.

a NUMPY POLYVAL function in the PYTHON environment to evaluate a polynomial (at specific values) which best represents the data. Once the fit is obtained, either linear or quadratic, this 'trend' is then subtracted from the original dataset, leaving behind a 'detrended' residual dataset. The most suitable trend for a given light curve was determined by testing each γ-ray and 1.35 mm dataset from NGC 1275 and BL Lacertae with both linear and quadratic fits individually. The resulting 'detrended' residual datasets are shown in Figures 8.19, 8.20, 8.21, 8.22, 8.23 and 8.24. The residual datasets,which no longer feature any broad rising or falling trends will then be used when performing the DCF analysis.

For NGC 1275, it was determined that a linear trend was present in the γ-ray dataset while a quadratic trend was present in the 1.35 mm dataset. This result is summarised

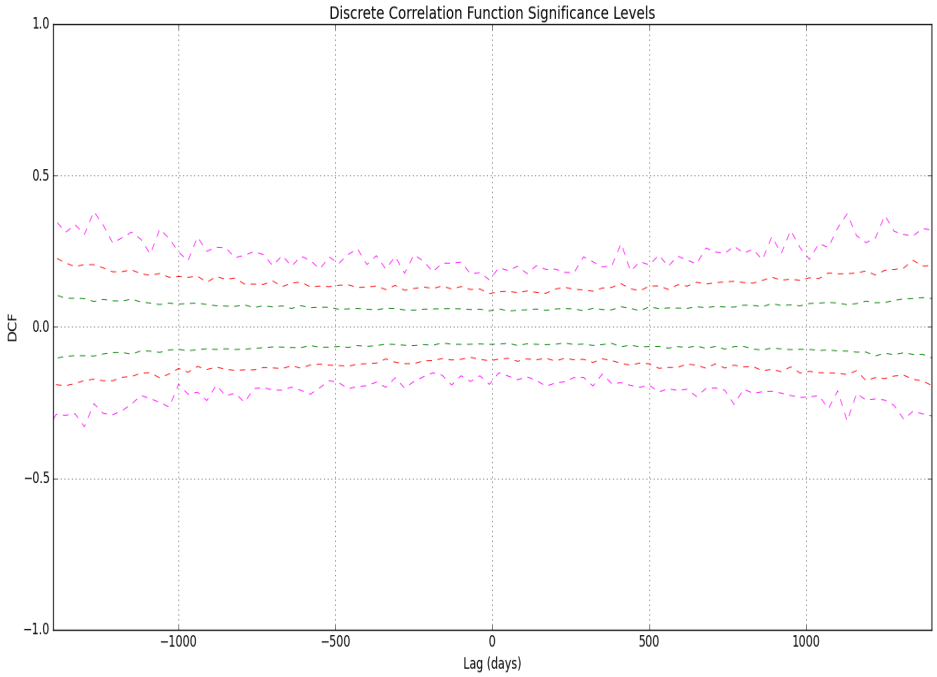

Figure 8.8: The 1σ (green), 2σ (red) and 3σ (magenta) significance levels obtained for the given time delay based on the DCF analysis performed on a large number of simulated γ-ray and 1.35 mm light curve pairs.

in Table 8.3. The resulting DCF curve using the 'detrended' residual NGC 1275 datasets is shown in Figure 8.15, where the overall increase and decrease in gradient is no longer present (compared to Figure 8.14).

The 'detrending' results from BL Lacertae, however, were more complex. First, it was found that the γ-ray dataset did not show any trends from fitting to either a linear or a quadratic trend. However, the 1.35 mm hinted at a linear underlying trend based on available data. When this linear trend was subtracted from the original dataset, the 'detrended' residual featured another trend between MJD 56250 and MJD 56692 (see Figure 8.19). Thus, it can be said that the 1.35 mm light curve has intrinsically two different trends at different epochs within the observation period. Since there is little known about the duty cycle of this source at 1.35 mm wavelengths, it is imperative to account for this anomaly as it will affect the final DCF outcome (146). The effects of linearly 'detrended' 1.35 mm dataset on the final DCF curve were tested. A DCF analysis was performed using both the original 1.35 mm dataset correlated against the original γ-ray

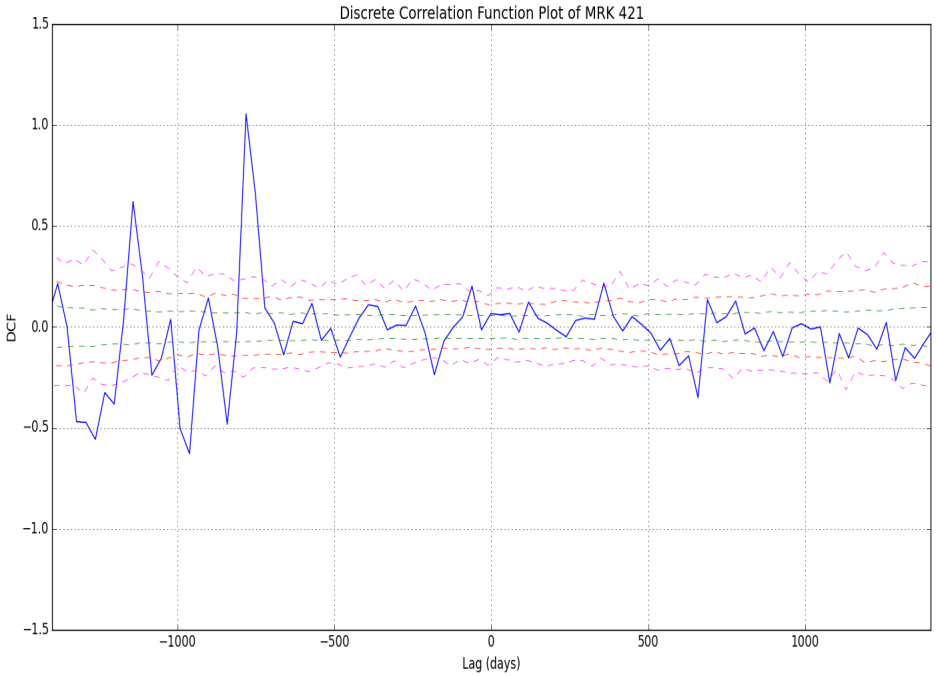

Figure 8.9: DCF analysis of MRK 421 using the *Fermi*-LAT dataset with a TS threshold of 25 and the SMA 1.35 mm dataset shown in Figure 7.7. The fewer data points present in the γ-ray light curve resulted in higher $DCF(\tau)$ amplitudes compared to the DCF analysis performed using the γ-ray light curve of MRK 421 with a TS threshold of 10 (see Figure 8.10).

dataset and a linearly 'detrended' 1.35 mm dataset correlated against the original γ-ray dataset. The results from this are shown in Figures 8.17 and 8.18. Since, the negative gradient linear trend was introduced in the 1.35 mm dataset when the linearly 'detrended' 1.35 mm dataset was used, this introduced a peak at a lag of +1300 days. When the original datasets are used in the DCF analysis, this peak no longer appears and is thus attributed to the new trend in the residual 1.35 mm dataset. Thus, it was found that using the original 1.35 mm dataset on the basis that 'detrending' the dataset results in another 'trended' residual that affects the accuracy of the DCF analysis. Thus, for this thesis, no 'detrending' was used for the final DCF analysis (Table 8.3).

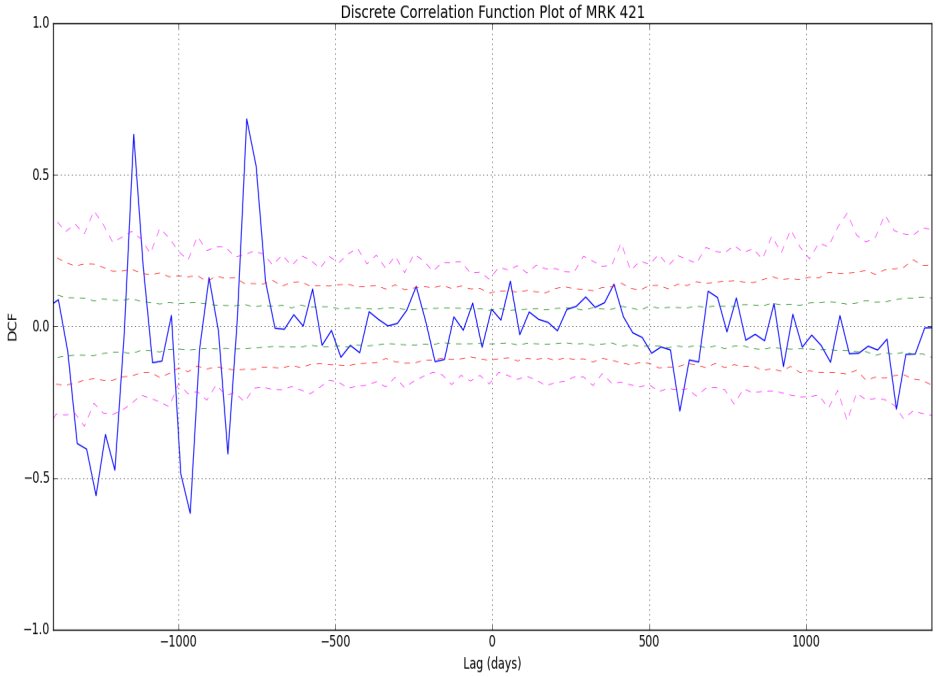

Figure 8.10: DCF analysis of MRK 421 using the *Fermi*-LAT dataset with a TS threshold of 10 and the SMA 1.35 mm dataset shown in Figure 7.1. This DCF curve shows lower $DCF(\tau)$ amplitudes compared to the DCF analysis produced using a γ-ray dataset with a TS threshold of 25 (see Figure 8.9).

Source	Wavelength	'Detrending'
BL Lacertae	γ-ray	N/A
BL Lacertae	1.35 mm	N/A
NGC 1275	γ-ray	linear
NGC 1275	1.35 mm	quadratic

Table 8.3: Functions used to 'detrend' the γ-ray and 1.35 mm light curves of BL Lacertae and NGC 1275 respectively.

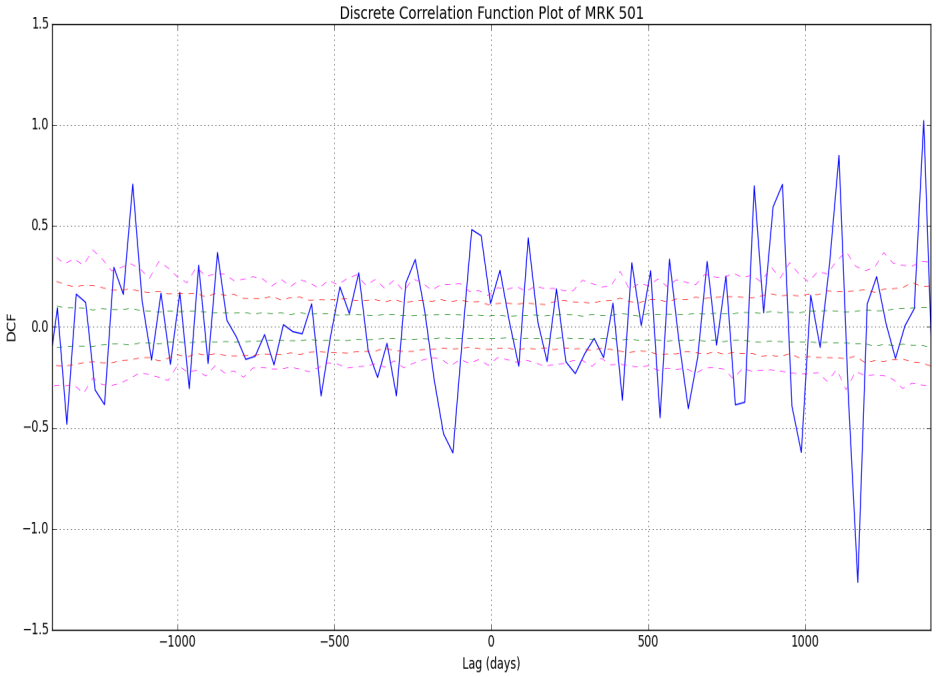

Figure 8.11: DCF analysis of MRK 501 using the *Fermi*-LAT dataset with a TS threshold of 25 and the SMA 1.35 mm dataset shown in Figure 7.8. The fewer data points present in the γ-ray light curve resulted in higher $DCF(\tau)$ amplitudes with a larger number of coefficients exceeding the 3σ significance level compared to the DCF analysis performed using the γ-ray light curve of MRK 501 with a TS threshold of 10 (see Figure 8.12).

8.4.3 Truncated Vs. Original 1.35 mm Datasets

Using the original 12 year 1.35 mm datasets which are twice as long as the 5.5 year γ-ray datasets may result in the appearance of physically uncorrelated DCF peaks. Truncating the longer dataset has also been applied in several other correlation studies which use similar datasets and correlation methods, e.g. in Dutson et al. (141), Max-Moerbeck et al. (239; 238), Larsson (268) and Fuhrmann et al. (146). In order to limit the uncertainty caused by a largely biased sampling (see also Sections 8.4.1 and 8.4.5 for examples of the effects of biased sampling), the DCF analysis here will use truncated 5.5 year 1.35 mm datasets to study its correlation with the 5.5 year γ-ray datasets.

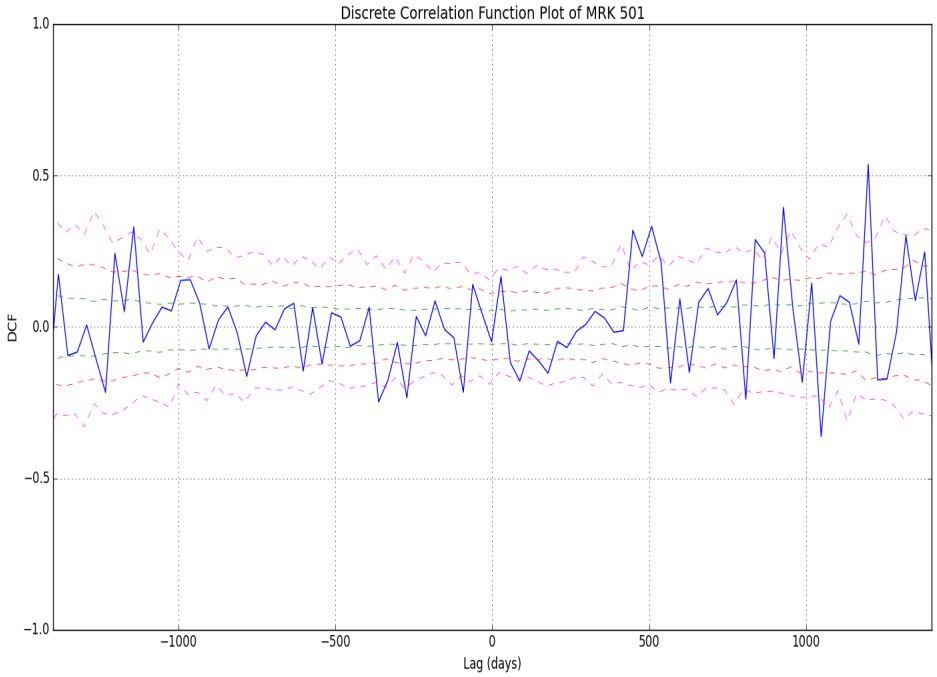

Figure 8.12: DCF analysis of MRK 501 using the *Fermi*-LAT dataset with a TS threshold of 10 and the SMA 1.35 mm dataset shown in Figure 7.3. This DCF curve shows lower $DCF(\tau)$ amplitudes compared to the DCF analysis produced using a γ-ray dataset with a TS threshold of 25 (see Figure 8.9).

8.4.4 Choice of the Temporal Bin Size

Based on Equation 8.2, it is clear that the number of values in each temporal bin affects the final DCF value, i.e. $DCF(\tau)$ is the average of the $UDCF_{ij}$ values in each time bin (266). Thus, choosing an appropriate bin size, which shows good resolution in the final DCF curve without producing a spurious correlation peak, is an important aspect of the study. For example, while a smaller bin size increases the resolution of the DCF plot, there will inevitably be fewer $UDCF_{ij}$ values in each bin. This will increase the final $DCF(\tau)$, leading to a spurious DCF peak in the curve. Increasing the bin size will reduce the average of $UDCF_{ij}$, resulting in a lower $DCF(\tau)$ outcome. In other words, a larger bin size will reduce the sensitivity of the DCF analysis in general. In addition, since the variability timescales and duty cycles of these sources are still largely unknown at the 1.35 mm wavelengths, it is important to choose a reasonably small bin-size in or-

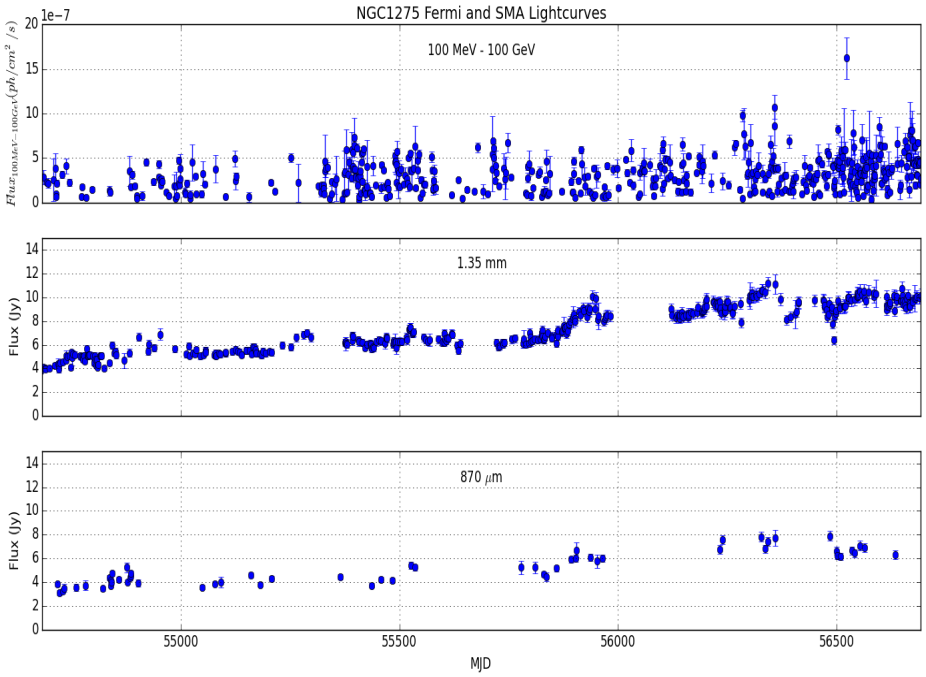

Figure 8.13: The 100 MeV to 100 GeV *Fermi*-LAT, 1.35 mm and the 870 μm SMA light curves for NGC 1275. Both light curves show evidence for underlying trends given by the constant rise in flux throughout the duration of the 5.5 year observation period, i.e. the mean and standard deviation of each dataset varies over this period.

der to retain important information on the correlated duty cycles of these sources. In order to determine a suitable bin size, the DCF analysis was performed using several bin-sizes and the resulting DCF curves were compared to each other. The bin sizes used in the tests were 15 days, 30 days, 50 days, 75 days and 100 days. The DCF plot using a 15-day bin size produced curves with spurious peaks as a result of fewer $UDCF_{ij}$ values present within each bin to be averaged over for the final $DCF(\tau)$ amplitude. This effect is shown in Figures 8.25 and 8.26, when a DCF curve using a 15-day and 30-day bin size respectively are compared. Although this study includes a significance test on the $DCF(\tau)$ amplitudes, a correlation peak is sometimes difficult to differentiate relative to the peaks which occur as a result of a limited $UDCF_{ij}$ count in a particular bin. It is difficult to assess the ideal number of values per bin, as this depends on the structure (number and frequency of events present) of each light curve being correlated and the sampling frequency of the source at both wavebands. White & Peterson (299) suggested

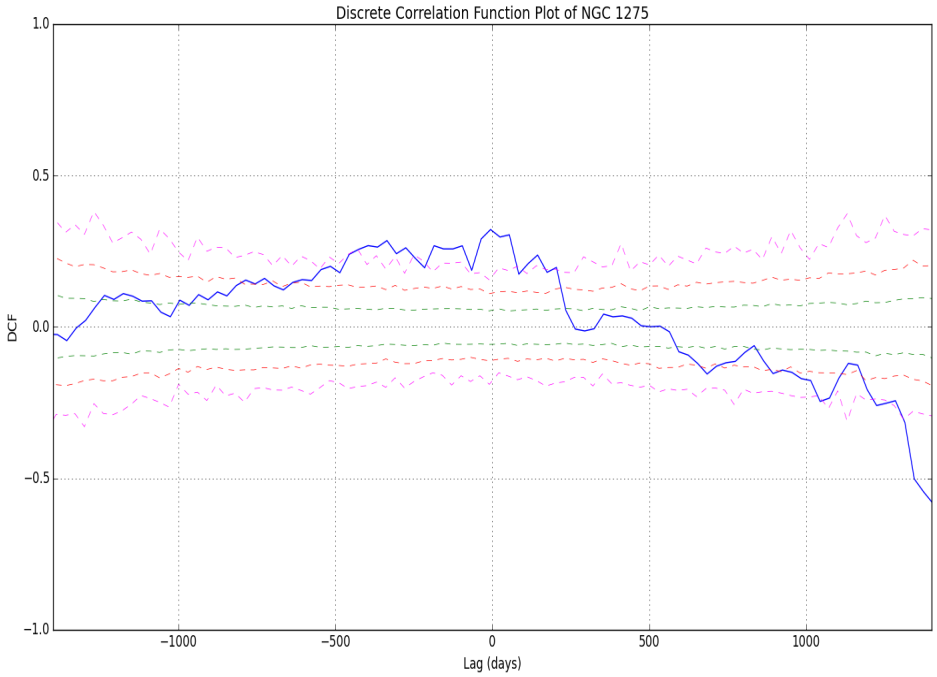

Figure 8.14: An example of a DCF curve produced using the non-stationary dataset of NGC 1275 at both γ-ray and 1.35 mm shown in Figure 8.13. The DCF amplitudes reflect the underlying trend present in the light curves given by the broad rise and fall observed as a function of the time delay.

that a good bin-size is typically the minimum sampling interval between observations[4]. In the case of 1.35 mm observations, however, most sources, with the exception of MRK 421 and MRK 501[5], are sampled on daily timescales, unless the source is below the horizon. However, this will cause some level of uncertainty to the final $DCF(\tau)$ amplitude in some of the time-bins, the time span in which data is present on daily timescales is considerably larger than the time-span during which the source is below the horizon. Thus, a temporal bin of 30 days will better retain the information necessary without incurring too high an uncertainty to the DCF results (as seen in the effects of biased sampling).

[4]This must be treated with caution, since the minimum sampling interval for the 1.35 mm datasets in this source sample range from several days to several years, depending on the source. Thus a sufficiently good bin-size is a compromise between the smaller intervals present which can range from several days to several months.

[5]Sources like OJ 287 are unevenly sampled such that the intervals between observations are larger than the FSRQs.

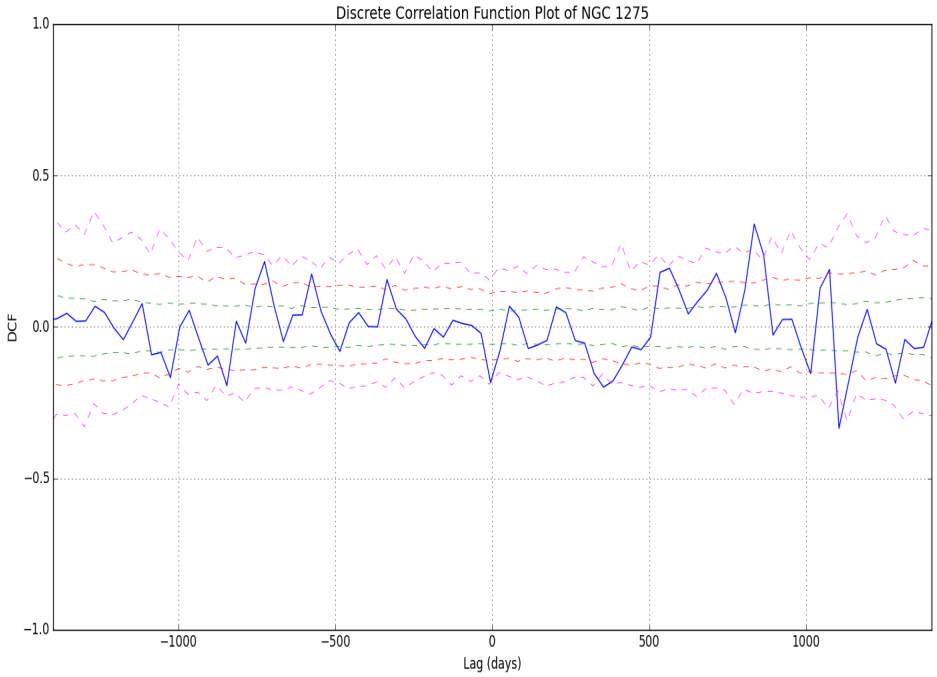

Figure 8.15: DCF curve for NGC 1275 using a 30-day bin size produced using the linearly 'detrended' γ-ray and quadratically 'detrended' 1.35 mm light curves presented in Chapter 7.

In order to illustrate this, results using a 30-day and a 100-day bin-size are shown in Figures 8.27 and 8.28. The 30-day bin-size offers better temporal resolution, while applying a 100-day time bin does not provide the temporal resolution necessary for this study.

Choosing the best temporal bin size is a fair compromise between obtaining good temporal resolution on the delay between events and maintaining the accuracy of the DCF curve without producing spurious correlation peaks. However, that this can be improved by employing a more rigorous approach in determining the significance of the peaks produced (Sections 8.5 and 8.11).

8.4.5 Edge Effects

Edge effects primarily occur as a result of there being too few $UDCF_{ij}$ values in a time-bin which is physically uncorrelated. The number of $UDCF_{ij}$ present in each temporal

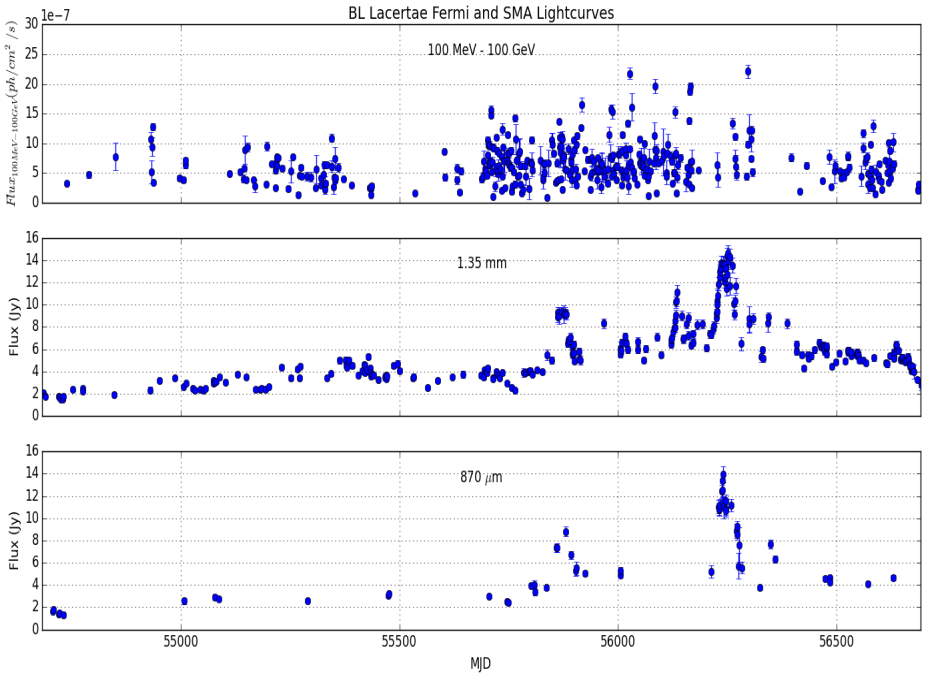

Figure 8.16: The 100 MeV to 100 GeV *Fermi*-LAT, 1.35 mm and the 870 μm SMA light curves for BL Lacertae.

bin depends on the frequency of sampling of each light curve (Section 8.1.1). Unevenly sampled datasets, and choosing small temporal bins, results in there being a range of $UDCF_{ij}$ values in each bin typically between several $\sim$ 10s to several thousands (for well-sampled datasets). As the datasets present in this study (particularly in the 1.35 mm regime) do not all have the same sampling frequency, it is difficult to place a minimum count on the values that are present in each bin, which ideally would be consistent throughout the 5.5 year observation period considered. Several, methods can be employed to reduce edge effects. Using truncated 1.35 mm datasets, along with a 30-day bin size, will ensure a reasonable number of $UDCF_{ij}$ values per bin, reducing the likelihood of bins with only 5 or 10 $UDCF_{ij}$ values.

Based on the DCF curves from all eight sources, it was found that an appropriate range for the time delay was $\pm$1400 days. This depended primarily on the length of the individual datasets. Employing this cutoff reduced the possibility of time-delay bins with comparatively fewer counts (less than 300 for well-sampled datasets which can typically have several thousand counts per bin). Since, the values in each time-bin depended

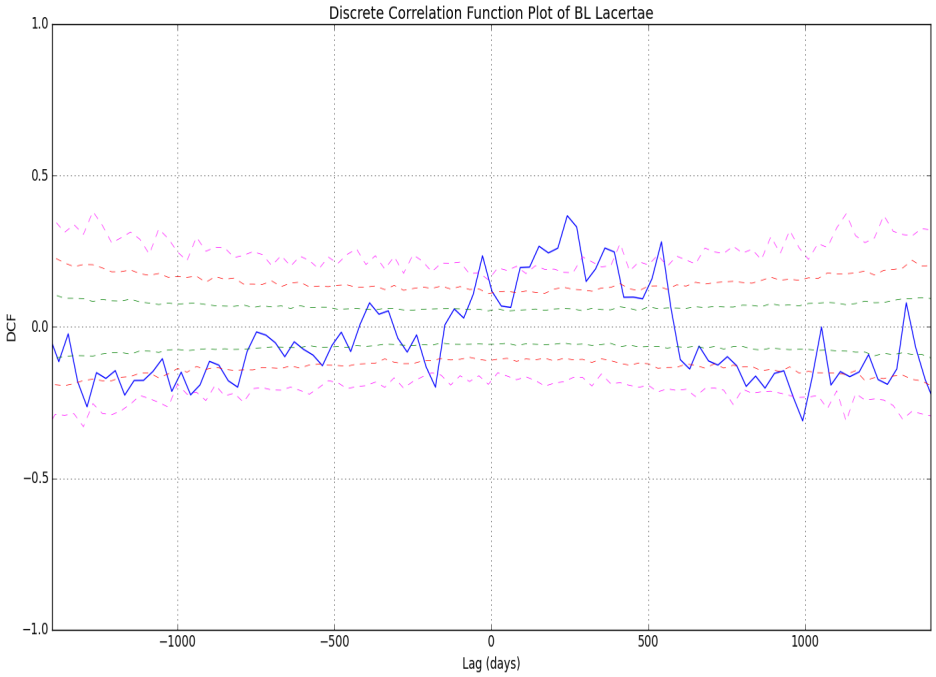

Figure 8.17: DCF analysis using the original γ-ray and 1.35 mm datasets of BL Lacertae.

primarily on the length of the individual datasets some of the sources, i.e. MRK 421 (Figure 8.30) and MRK 501 (Figure 8.31), have visible edge effects within the $\pm$1400 lag cutoff, attributed to the largely undersampled 1.35 mm datasets for both these sources.

In addition to this, cutoff range can also be specified based on the physical separation implied by the observed time delay. This will remove the presence of physically uncorrelated $DCF(\tau)$ peaks from being considered in the final interpretation of the results. For a source at an average redshift of 0.3 (based on the source sample), a time delay of ~ 1400 days will imply a separation of > 200 pc[6] between the γ-ray and 1.35 mm emission regions. This is a large separation when effects due to adiabatic losses and various other possible interactions of the jet (or emission region) with ambient matter are considered. The likelihood of events being correlated at distances ~ 200 pc is very low.

[6]This value applies for a *Fermi* bright blazar using the same parameters (e.g. jet speed and Doppler factors) specified in Section 8.5.1.

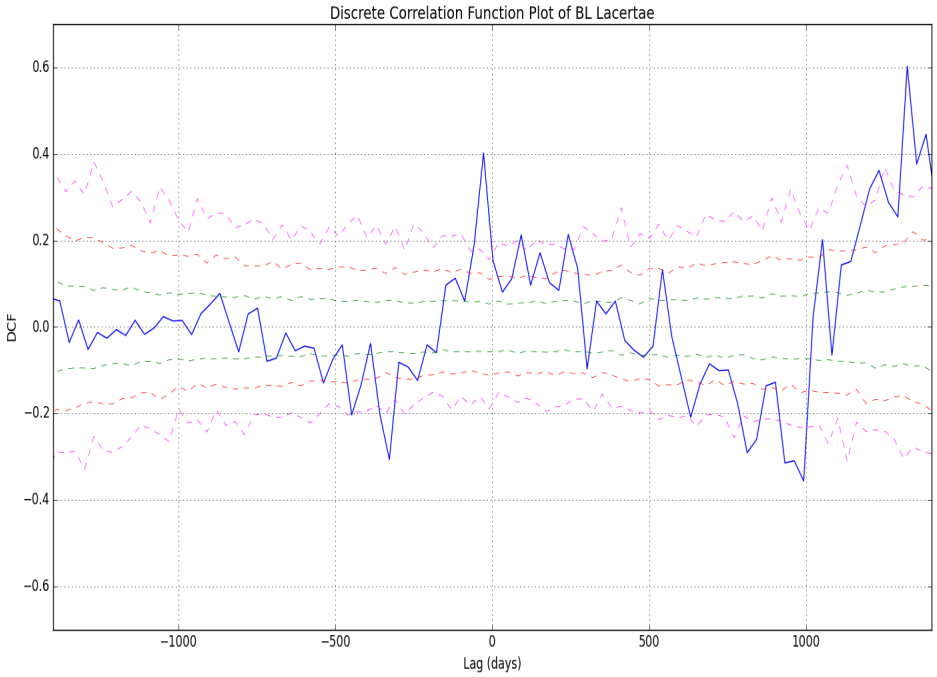

Figure 8.18: DCF analysis using the original γ-ray and the linearly detrended 1.35 mm dataset of BL Lacertae.

8.5 Results of the DCF Analysis

Based on the method described in Section 8.1.1, the DCF analysis was performed for all eight sources using the 100 MeV to 100 GeV *Fermi*-LAT datasets and the truncated 1.35 mm SMA datasets presented in Chapter 7. In this section, results of the DCF analysis are presented by source type followed by a discussion of the key features present in the DCF plots.

Improvements to the method used in this DCF analysis will be discussed in Section 8.11. In Table 8.4, a summary of the DCF analysis criteria is presented.

8.5.1 Physical Interpretation of the DCF Analysis

Results of possible correlation as a function of time delay are used to understand the physical structure of emission regions within the jet. In addition, the distances between the γ-ray and 1.35 mm emission regions, Δr (Figure 8.29), are estimated based on the method described in Section 3.6.1. The time delay between emission in the γ-ray and 1.35

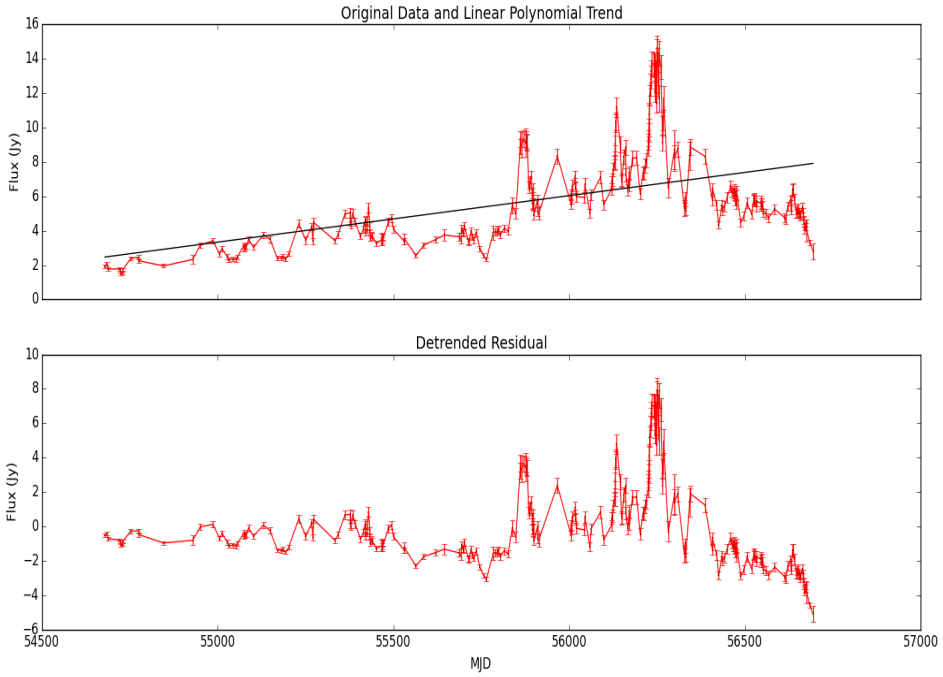

Figure 8.19: The linearly 'detrended' 1.35 mm light curve of BL Lacertae.

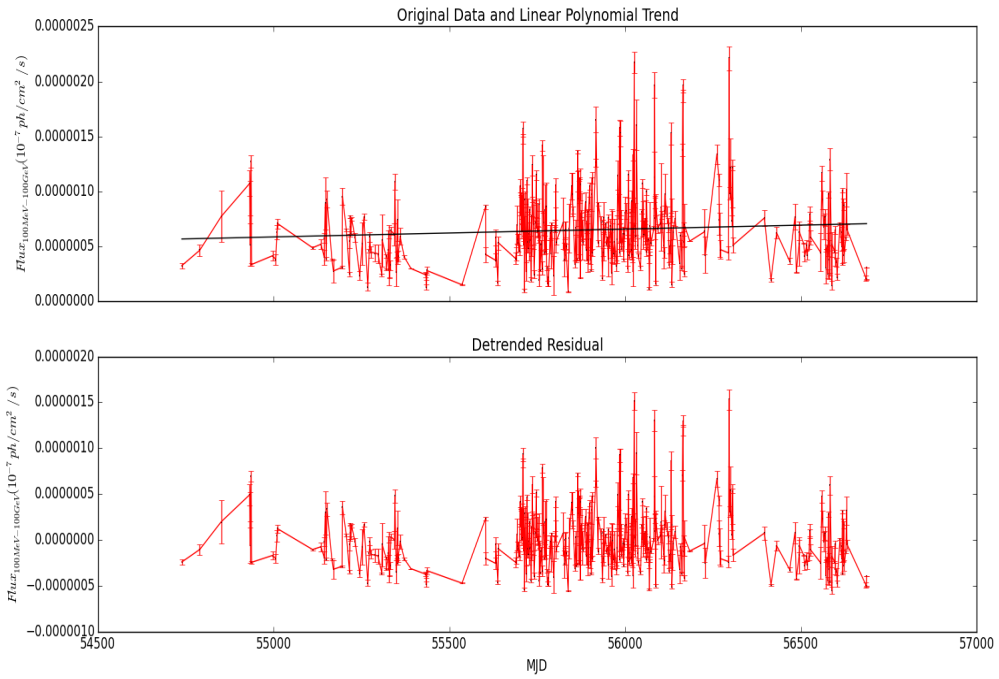

Figure 8.20: The linearly 'detrended' γ-ray light curve of BL Lacertae.

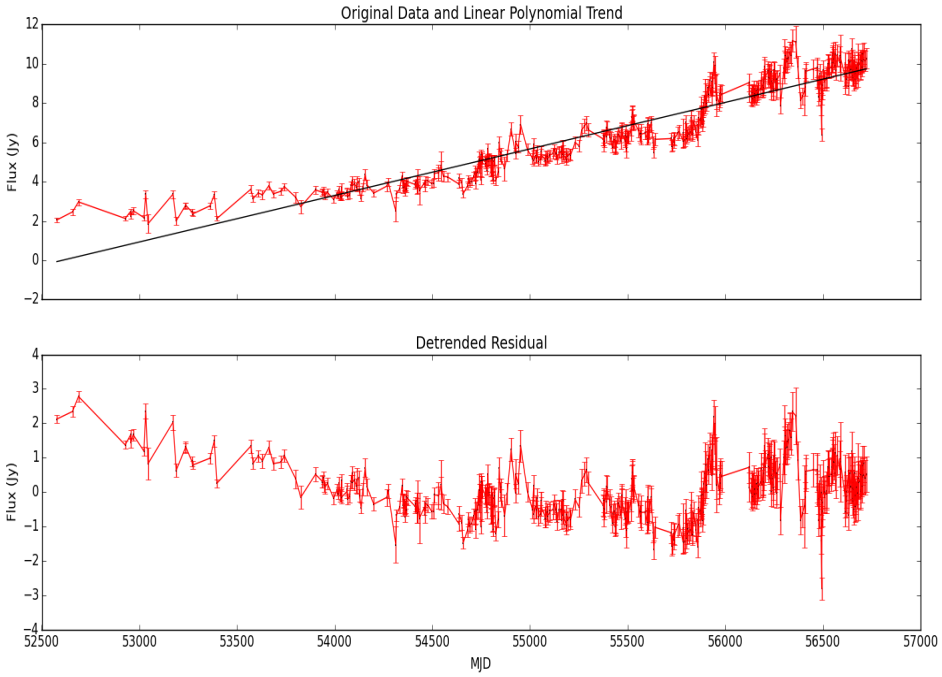

Figure 8.21: The linearly 'detrended' 1.35 mm light curve of NGC 1275.

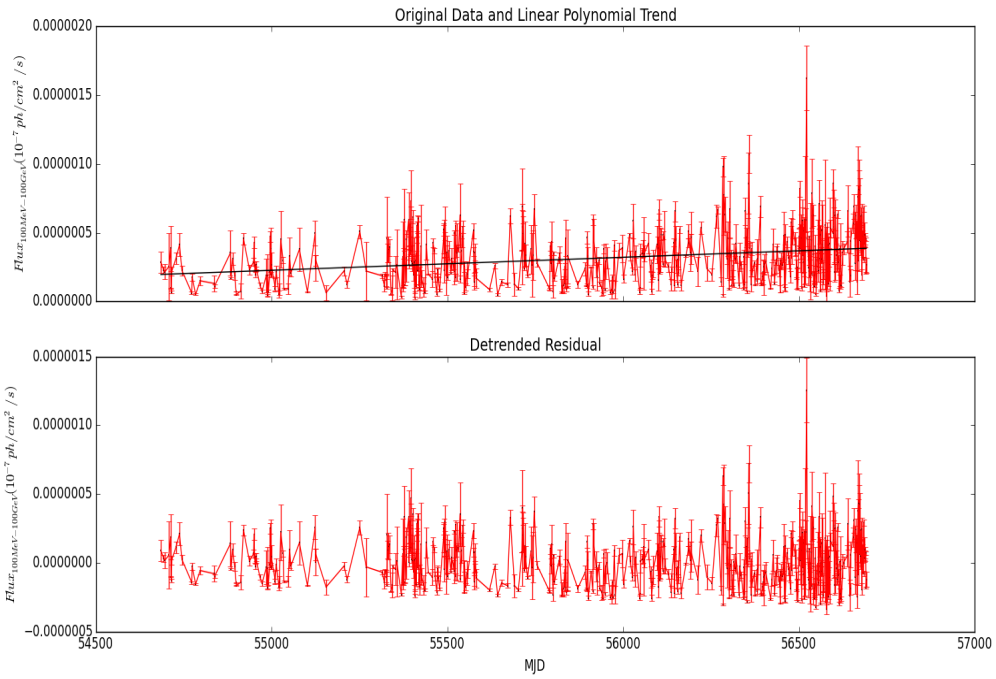

Figure 8.22: The linearly 'detrended' γ-ray light curve of NGC 1275

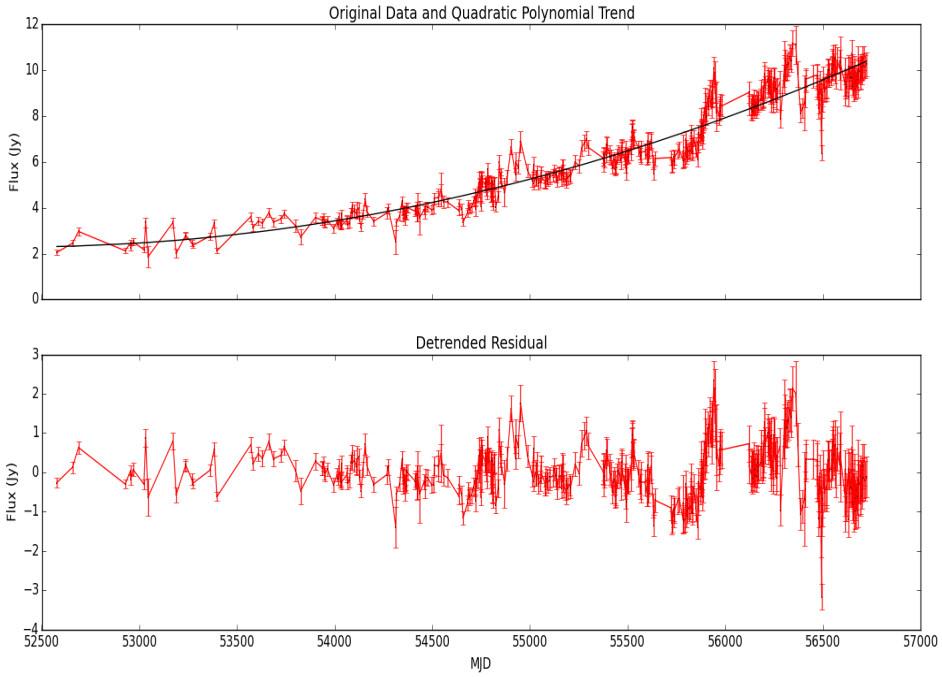

Figure 8.23: The quadratically 'detrended' 1.35 mm light curve of NGC 1275.

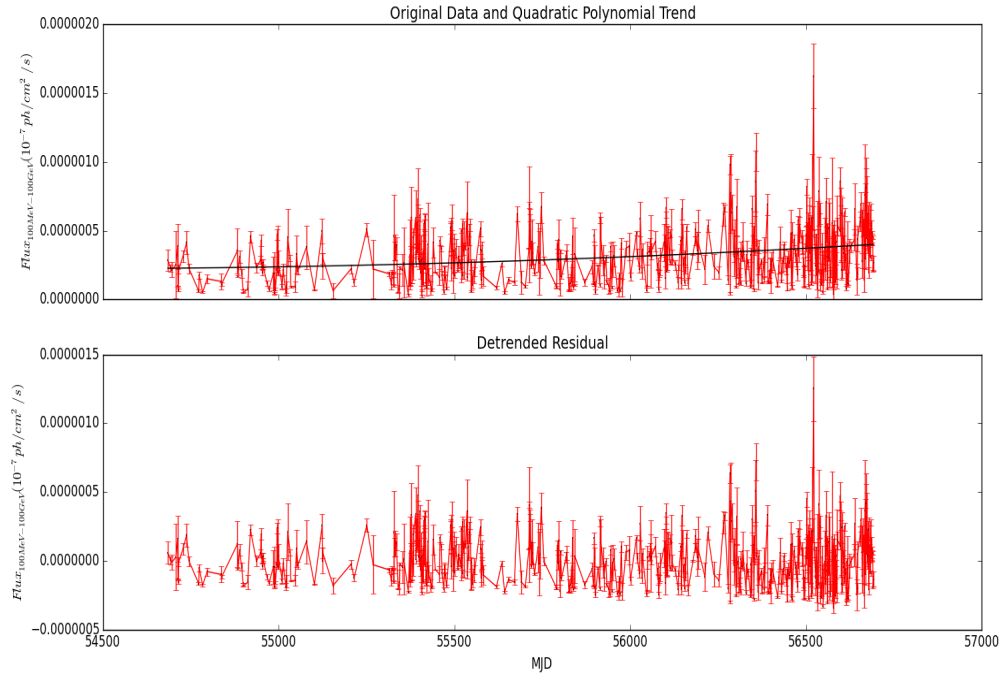

Figure 8.24: The quadratically 'detrended' γ-ray light curve of NGC 1275

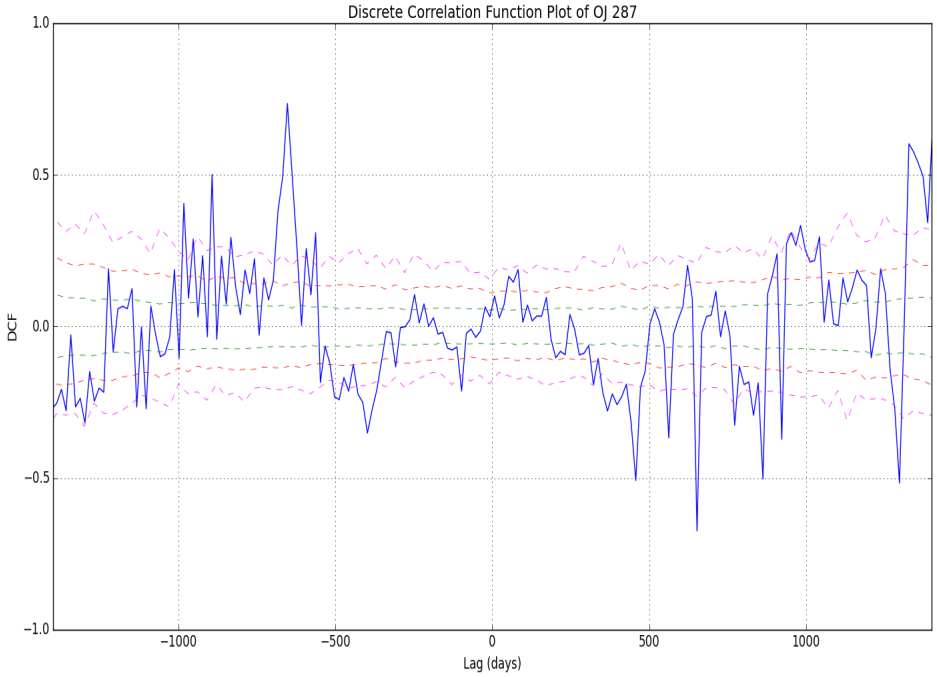

Figure 8.25: DCF curve of OJ 287 using a 15-day bin size based on the *Fermi*-LAT and 1.35 mm light curves shown in Figure 7.9. The number of $UDCF_{ij}$ values in each bin ranged from 5 to 300, decreasing the accuracy of some of the peaks produced in the DCF curve. This can be compared to Figure 8.26 which has comparatively fewer peaks.

DCF criteria	Details
Lag Cutoff (days)	$\pm$1400
Length of γ-ray dataset	5.5 years
Length of 1.35 mm dataset	5.5 years
DCF value considered significant	$> \pm 3\sigma$
Temporal Bin Size (days)	30

Table 8.4: Summary of the DCF analysis criteria for the eight sources used in this study.

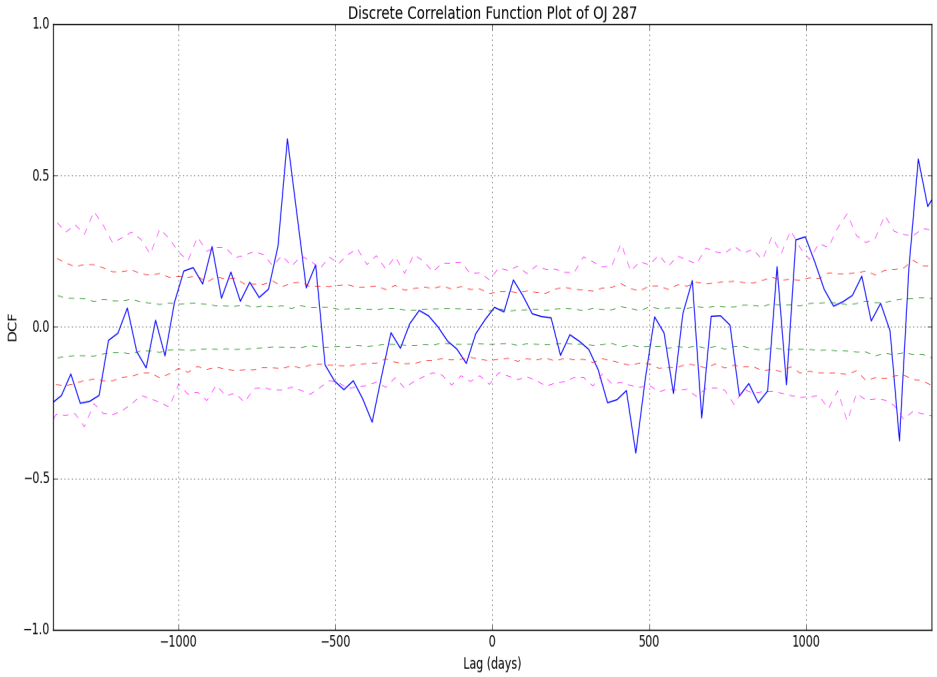

Figure 8.26: DCF curve of OJ 287 using a 30-day bin size based on the *Fermi*-LAT and 1.35 mm light curves shown in Figure 7.9. The chosen bin size is a compromise between obtaining good temporal resolution on the DCF curve and limiting the occurrence or spurious correlation due to physically uncorrelated events in the γ-ray and 1.35 mm regimes.

mm regimes in the rest frame of the source, $\mathrm{tl}^{src}_{mm-\gamma}$, and the Δr parameters (Equation 3.5) are presented in the following sections. The Δr parameters are evaluated based on the parameters estimated for a *Fermi*-LAT, bright γ-ray blazar which has a typical viewing angle of $\theta = 3.6^{\circ}$ (35) and an apparent angular jet speed, $\beta_{app} = 15$ (161; 36).

There are four possible outcomes of the DCF analysis. First, the presence or lack of evidence for correlation is ascertained based on the significance estimates (see Section 8.3). Next, the positive and negative convention of the delay based on the summary provided in Table 8.5 is determined. The delay conventions primarily suggest that emission at one of the two wavelength regimes precedes or follows emission produced in the other wavelength regime. There are two possible conservative assumptions that may be invoked in order to interpret these results under the current blazar jet paradigm. In the first scenario, the γ-ray region is thought to be located close to the central engine,

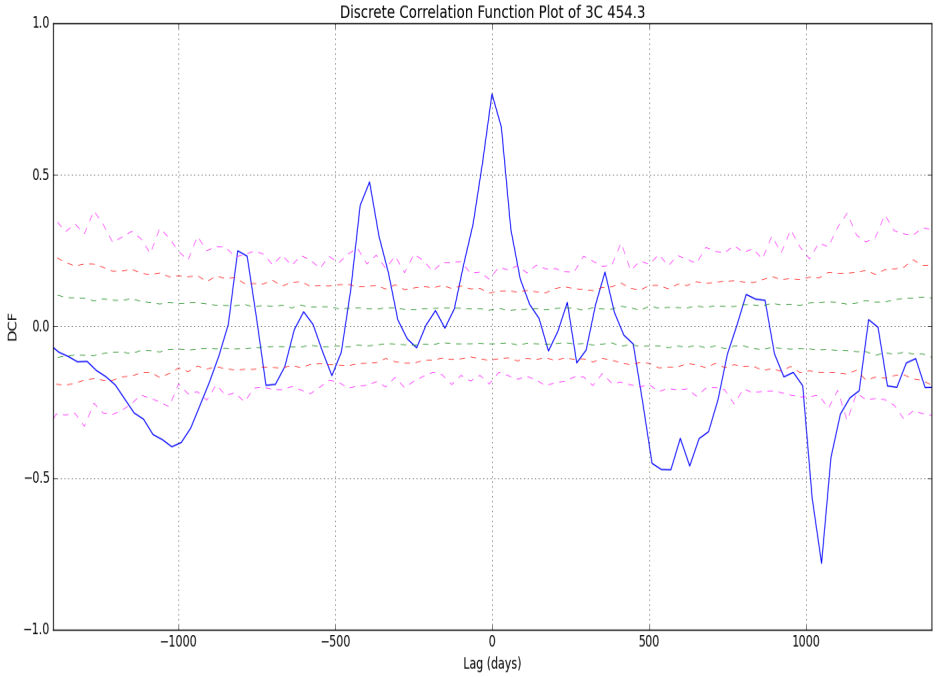

Figure 8.27: DCF curve for 3C 454.3 using a 30-day bin size showing good temporal resolution and the peaks are easily identified. The DCF analysis was performed using *Fermi*-LAT and 1.35 mm light curves shown in Figure 7.13.

DCF	Delay	Interpretation
+ve	+ve	correlation with γ-rays leading 1.35 mm
+ve	-ve	correlation with 1.35 mm leading γ-rays
-ve	+ve	anti-correlation with γ-rays leading 1.35 mm
-ve	-ve	anti-correlation with 1.35 mm leading γ-rays

Table 8.5: Summary of the conventions used based on the DCF method which indicate the physical significance of positive or negative time delays.

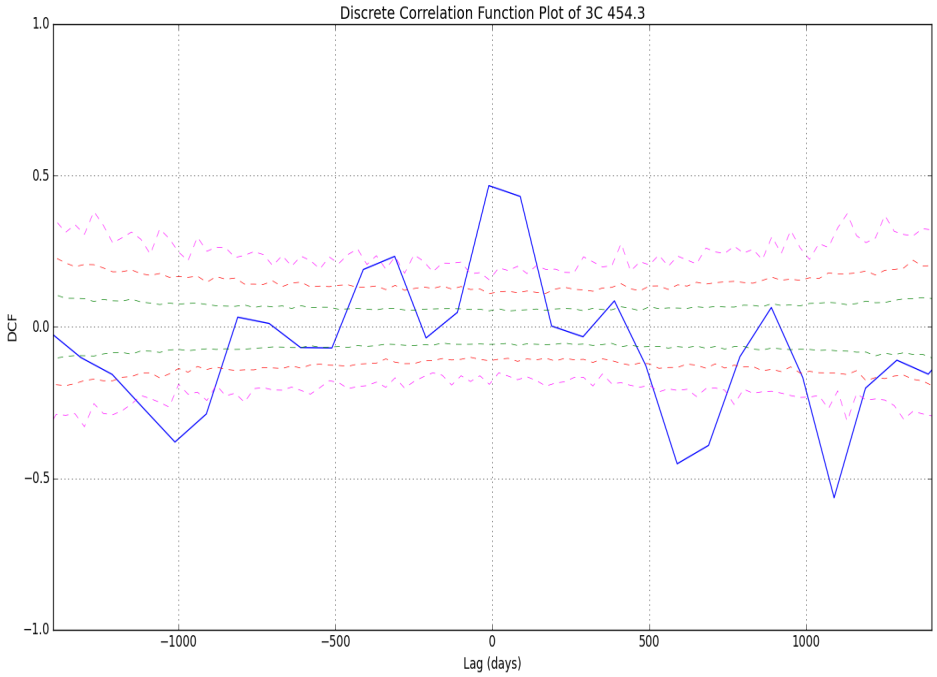

Figure 8.28: DCF curve for 3C 454.3 using a 100-day bin size based on the *Fermi*-LAT and 1.35 mm light curves shown in Figure 7.13. The $DCF(\tau)$ amplitudes are now much lower compared to those observed in Figure 8.27, in addition to the lack of temporal resolution present in the DCF curve.

while the 1.35 mm emission region is thought to be located downstream from the γ-ray emission site. In the second conservative scenario, it may be assumed that the 1.35 mm emission region is located closer to the central engine, while the γ-ray emission region is assumed to be located downstream from the 1.35 mm emission site (see Figure 8.29).

Another important aspect of correlation studies concerns the length of time delays observed between emission at different wavelengths and their corresponding Δr separation. While the purpose of the significance estimates was to identify the likelihood of obtaining a particular correlation at a given time delay based on simulated light curves (see Section 8.3), it is important to note that given the extreme energetics of blazar jets, correlation at shorter time delays may be a more likely occurrence compared to correlation observed between events at longer delays. For example, if a perturbation in the plasma (e.g a flare produced by a shock within the plasma) occurs in γ-ray region close to the central engine, a stronger correlation is more likely to occur at a smaller separation

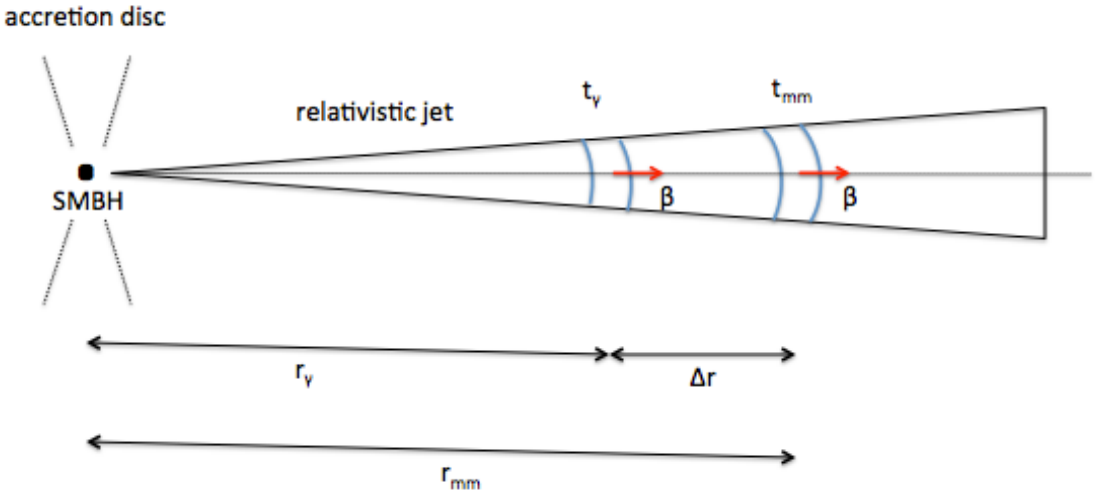

Figure 8.29: Schematic of a jet showing the region where γ-rays may be produced (indicated by r_γ) along with the mm-wave core (indicated by r_{mm}). Δr shows the distance between the observed γ-ray site and the mm-wave core. The plasma or induced shock propagates downstream at speed β, leading to γ-ray events being observed at time, t_γ (MJD) while mm events are observed at time, t_{mm} (MJD). The mm-wave core appears further downstream compared to the γ-ray wave core due to synchrotron opacities which limit the observation of mm wave photons to optically thin regions.

distance from the location of the γ-ray emission site that produced the perturbation compared to a longer separation distance. This is because, at larger separations, the original perturbation giving rise to the event (e.g. flare, outburst) might be interrupted by other events (e.g. collisions with other regions either within or external to the jet). This may lead to the introduction of either forward or reverse shocks which may further alter the characteristic features (e.g. particle population, energy of the particle population) of the original event that had occurred, thus reducing the strength of correlation or altering it completely. Other scenarios that may lead to the absence or disturbance of correlated events are the effects of adiabatic losses when emission from a smaller region of the jet propagates to regions with larger opening angles. The DCF results presented in the following sections will therefore be discussed based on the amplitude of the observed correlation, the length and convention of the observed time delay, and the possible physical interpretation of the result.

8.6 HBLs

8.6.1 MRK 421 and MRK 501

The DCF analysis for MRK 421 and MRK 501 was greatly limited by the lack of data at 1.35 mm (see Figure 7.7). In addition, the γ-ray datasets had a smaller signal to noise ratio, due to the faintness of HBL sources in general. Based on Figure 8.30, the $DCF(\tau)$ coefficients of MRK 421 which exceed the 3σ significance threshold may be the result of correlation between the active period, i.e. outburst observed on 22 June 2012 (MJD 56100) and the period during which SMA data was available at 1.35 mm (see Figure 7.7). However, due to limited sampling at 1.35 mm for this source it cannot be ascertained if the 1.35 mm emission was also in outburst during that time. A similar DCF curve was also observed for MRK 501 (see Figure 8.31). The presence of both positive and negative correlation at both positive and negative delays for MRK 421 and MRK 501 show that the dramatic difference in the sampling frequency of the two light curves greatly affects the results of the DCF analysis. It must be noted that, while ideally the sampling of simulated light curves used to produce the significance estimates should replicate the sampling of the observed light curves, this was not possible for both MRK 421 and MRK 501 as these sources had minimal and largely inconsistent monitoring (i.e. < 40 observations) throughout the 5.5 year observation period (see Figures 7.7 and 7.8). Thus, producing significance estimates based on light curves with drastically different sampling frequencies will largely bias the outcome of the DCF analysis (see Sections 8.4.1 and 8.4.5 for examples of the effects of biased sampling). Thus, maintaining a regular and consistent sampling frequency for the simulated light curves was necessary to maintain the accuracy of the significance estimates.

8.7 IBLs

8.7.1 OJ 287

The light curves of OJ 287 in Figure 7.9 show periods of activity at both γ-ray and 1.35 mm wavelengths although the sampling of the source was inconsistent during parts of the observation period (see Figure 7.9). While there were several flaring periods in the γ-ray regime, emission in the 1.35 mm waveband showed two distinct periods of activity

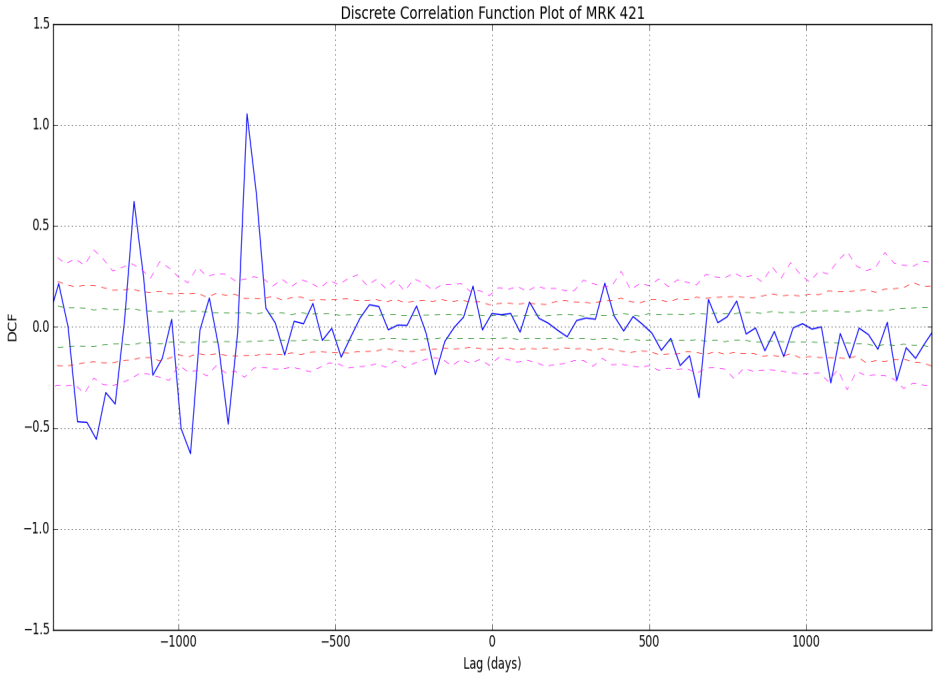

Figure 8.30: DCF curve for MRK 421 using a 30-day bin size produced using the γ-ray and 1.35 mm light curves presented in Figure 7.7.

which mainly occurred in the first half of the observation period.

The DCF analysis of OJ 287 (Figure 8.32) shows evidence for strong correlation ($DCF(\tau) = 0.62$) at a lag of ~ -21.7 months (~ -652 days) in the rest frame of the observer, corresponding to a Δr of ~ 97 pc between the emission regions. For this correlated event, the 1.35 mm emission leads the γ-ray emission. The DCF curve also shows weak evidence for possible anti-correlation ($DCF(\tau)$ = 0.30) at a lag of ~ 22.3 (~ 668 days) months in the rest frame of the observer.

The remaining (anti-)correlated events shown in Table 8.6 show evidence for (anti-)correlation at distances > 150 pc, which suggests that these results may not represent physically correlated events.

8.7.2 BL Lacertae

The DCF plot for BL Lacertae shown in Figure 8.33 exhibits weak evidence for correlation at a delay ranging between ~ -0.9 months (~ -27 days) to $\sim +18.1$ months ($\sim +542$

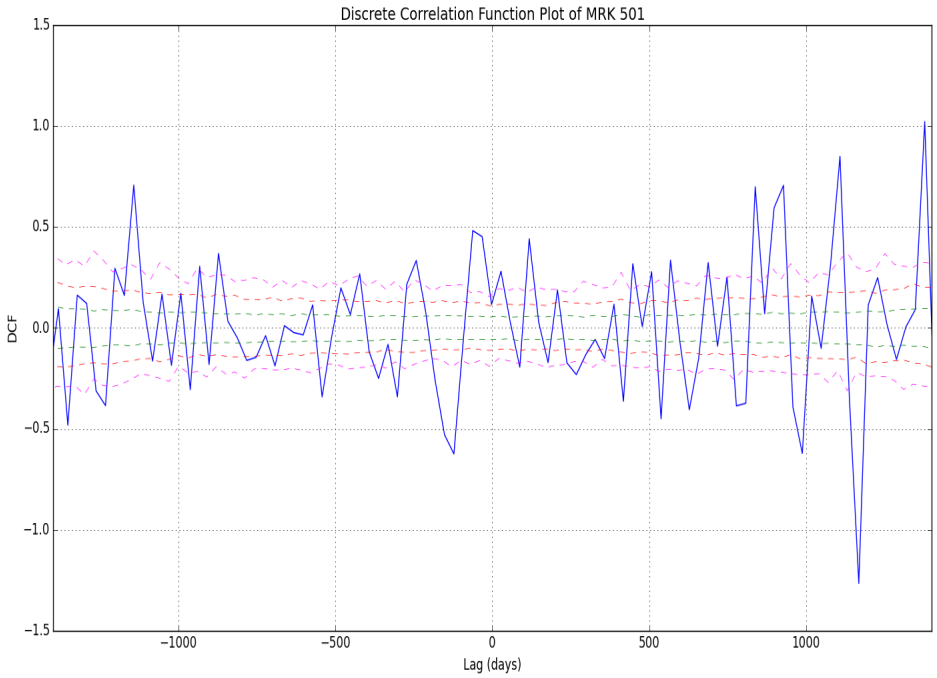

Figure 8.31: DCF curve for MRK 501 using a 30-day bin size produced using the γ-ray and 1.35 mm light curves presented in Figure 7.8.

DCF	$\mathrm{tl}^{obs}_{mm-\gamma}$	$\mathrm{tl}^{src}_{mm-\gamma}$	Δr
0.62	-21.7	-16.6	~ 97
-0.31	-12.7	-9.7	~ 57
-0.42	15.2	11.6	~ 68
-0.30	22.3	16.6	~ 97
-0.25	28.3	21.6	~ 126
-0.38	43.2	33.0	~ 193
0.56	45.2	34.5	~ 201

Table 8.6: Evidence for correlation between the γ-ray and 1.35 mm light curves for OJ 287 (z = 0.310). The $DCF(\tau)$ is peak amplitude of the correlation coefficient. $\mathrm{tl}^{obs}_{mm-\gamma}$ and $\mathrm{tl}^{src}_{mm-\gamma}$ are the corresponding average delay (in months) between emission in the 1.35 mm and γ-ray wavebands in the rest frame of the observer and the source respectively. Δr is the estimated distance (in pc) between the γ-ray and 1.35 mm regions based on the observed delay in the rest frame of the source.

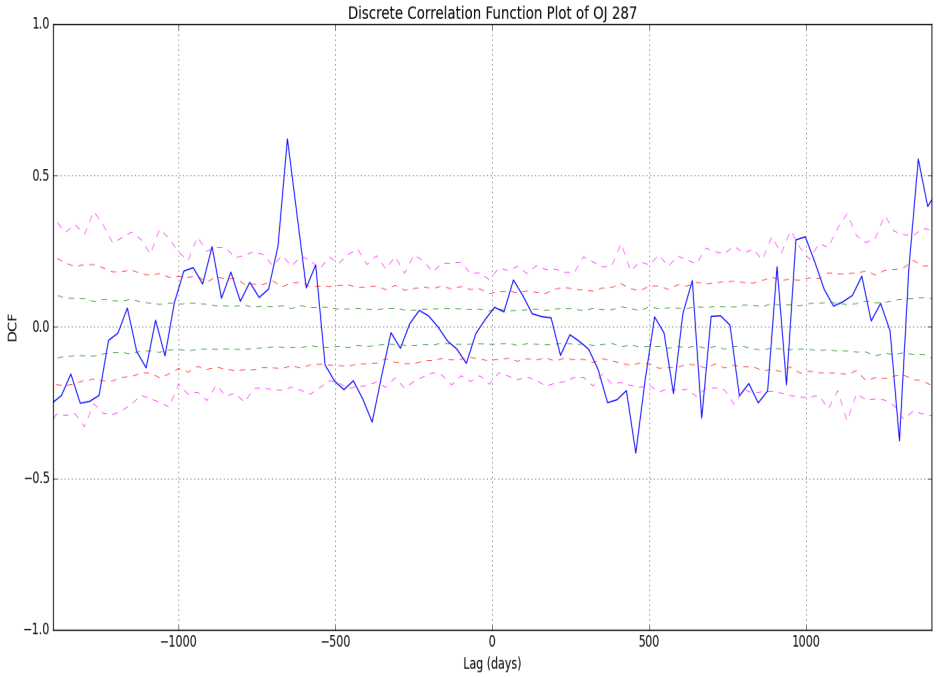

Figure 8.32: DCF curve for OJ 287 using a 30-day bin size produced using the γ-ray and 1.35 mm light curves presented in Figure 7.9.

days). These delays correspond to Δrs that range from $\sim$ 5 pc to $\sim$ 99 pc with the strongest positive correlation corresponding to a Δr separation of $\sim$ 44 pc between the γ-ray and 1.35 mm emission zones. The observation of correlated behaviour (see Table 8.7) is in general agreement with the analysis 'by eye' presented in Chapter 7 as the active periods in the γ-ray waveband occur during similar periods at 1.35 mm wavelengths.

Although evidence for correlation was observed for BL Lacertae above the 3σ significance threshold, the amplitude of the $DCF(\tau)$ correlation coefficients were weaker than OJ 287 and the FSRQs.

Remarks on IBLs

While OJ 287 is fainter than BL Lacertae at both γ-ray and 1.35 mm wavelengths, stronger evidence for correlation is seen for OJ 287 compared to BL Lacertae. This is primarily due to the intrinsic nature of the γ-ray emission for both sources. OJ 287 appears to exhibit various emission states (i.e. quiescent periods and flares) throughout the 5.5 year mon-

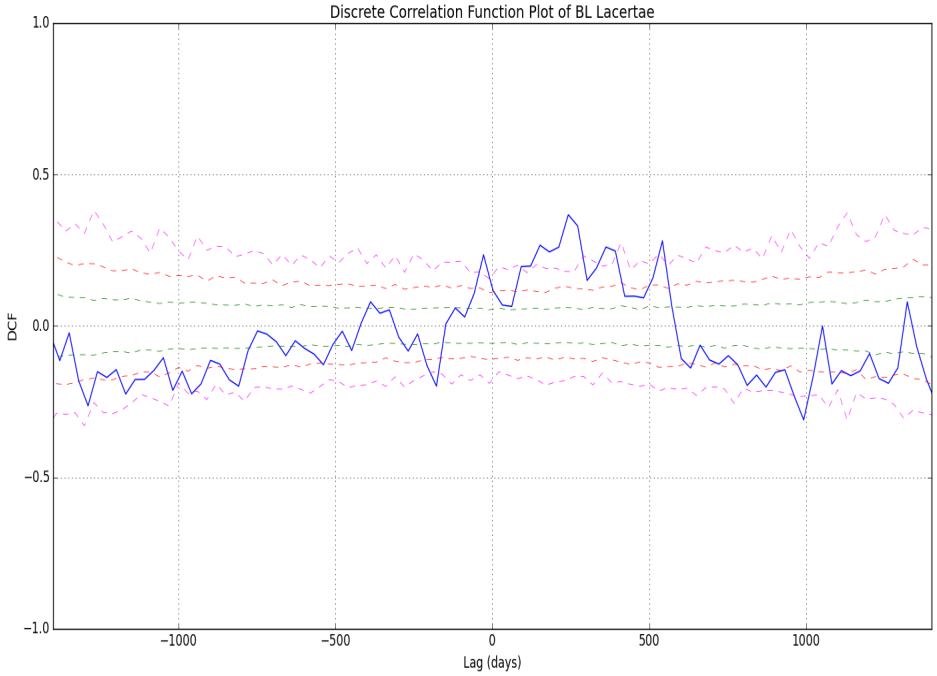

Figure 8.33: DCF curve for BL Lacertae using a 30-day bin size produced using the γ-ray and 1.35 mm light curves presented in Figure 7.10.

DCF	$\mathrm{tl}^{obs}_{mm-\gamma}$	$\mathrm{tl}^{src}_{mm-\gamma}$	Δr
-0.20	-5.9	-5.5	~ 32
0.24	-0.9	-0.8	~ 5
0.37	8.1	7.5	~ 44
0.28	18.1	16.9	~ 99
-0.31	33.1	30.9	~ 180

Table 8.7: Evidence for correlation between the γ-ray and 1.35 mm light curves for BL Lacertae (z = 0.069). The $DCF(\tau)$ is peak amplitude of the correlation coefficient. $\mathrm{tl}^{obs}_{mm-\gamma}$ and $\mathrm{tl}^{src}_{mm-\gamma}$ are the corresponding average delay (in months) between emission in the 1.35 mm and γ-ray wavebands in the rest frame of the observer and the source respectively. Δr is the estimated distance (in pc) between the γ-ray and 1.35 mm regions based on the observed delay in the rest frame of the source.

DCF	$tl^{obs}_{mm-\gamma}$	$tl^{src}_{mm-\gamma}$	Δr
-0.31	-26.2	-22.6	~ 153
0.49	-9.2	-7.9	~ 46
0.36	3.8	3.3	~ 19
-0.63	28.8	24.4	~ 142
-0.38	32.8	28.3	~ 165
-0.33	40.8	35.2	~ 206
-0.58	44.8	38.7	~ 226

Table 8.8: Evidence for correlation between the γ-ray and 1.35 mm light curves for 3C 273 (z = 0.158). The $DCF(\tau)$ is peak amplitude of the correlation coefficient. $tl^{obs}_{mm-\gamma}$ and $tl^{src}_{mm-\gamma}$ are the corresponding average delay (in months) between emission in the 1.35 mm and γ-ray wavebands in the rest frame of the observer and the source respectively. Δr is the estimated distance (in pc) between the γ-ray and 1.35 mm regions based on the observed delay in the rest frame of the source.

itoring period at *Fermi*-LAT energies. BL Lacertae, however, shows rapid variability at γ-ray energies throughout the monitoring period. The only indication that the object was entering an outburst were observations of increasing variability amplitudes during the second half of the monitoring period (see Figure 7.10). Since the DCF technique attempts to correlate flares in one dataset to flares in the other dataset, this general increase in variability amplitude at both wavelengths is not as easily observed resulting in the weaker correlation coefficients found for BL Lacertae.

8.8 FSRQs

8.8.1 3C 273

The DCF analysis of 3C 273 (Figure 8.34) shows the presence of strong positive and negative correlation at both positive and negative delays (summarised in Table 8.8). These results are in agreement with the qualitative analysis presented in Chapter 7 based on Figure 7.11. The anti-correlations observed may be attributed to the presence of longer decay periods at 1.35 mm being correlated with the shorter rising periods observed at γ-ray energies for this source.

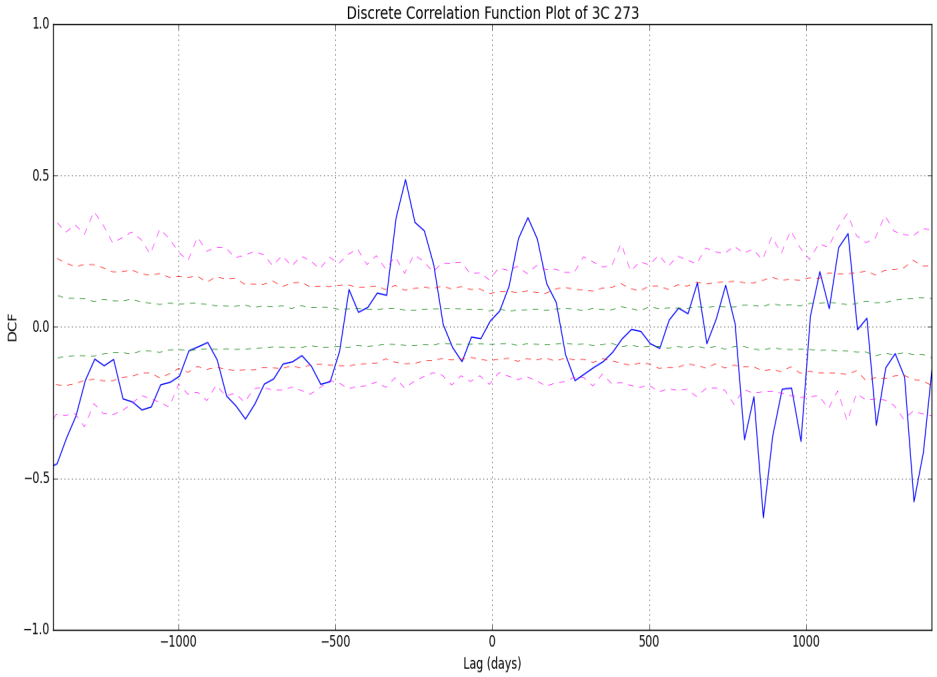

Figure 8.34: DCF curve for 3C 273 using a 30-day bin size produced using the γ-ray and 1.35 mm light curves presented in Figure 7.11.

The shortest correlated delay observed for this source corresponds to a Δr separation distance of $\sim$ 19 pc with a $DCF(\tau)$ amplitude of 0.36 in which the γ-ray emission leads the 1.35 mm emission. A longer correlated delay, which corresponds to a Δr separation of $\sim$ 46 pc with a stronger $DCF(\tau)$ amplitude of 0.46 suggests the 1.35 mm emission leads the γ-ray emission is also present. The presence of correlation with both positive and negative delays suggest that 3C 273 may have a more complex emission mechanism active within the jet (see Section 8.10).

8.8.2 3C 279

The DCF analysis of 3C 279 shown in Figure 8.35 exhibits predominantly positive correlation at negative time delays, which suggests that for this source, the 1.35 mm emission leads the γ-ray emission where the separation between the emission regions corresponds to an average of $\sim$ 80 pc. However, the strongest of these is observed at a negative delay of ~ -22.8 months (~ -685 days). 3C 279 also exhibits weak quasi-simultaneous

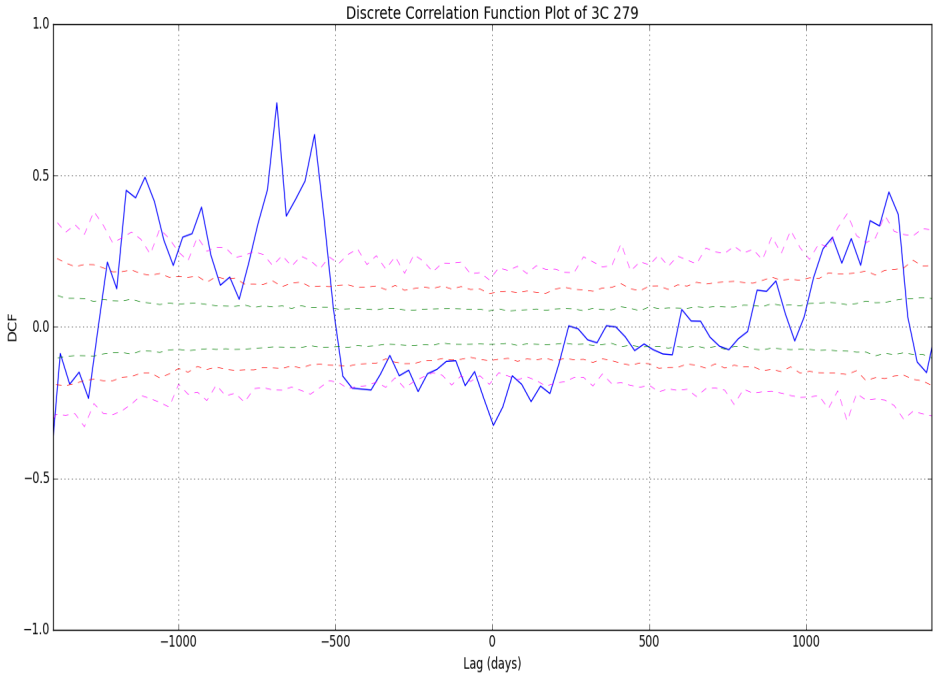

Figure 8.35: DCF curve for 3C 279 using a 30-day bin size produced using the γ-ray and 1.35 mm light curves presented in Figure 7.12.

anti-correlation at a lag of ~ 0.13 months (~ 4 days) in the rest frame of the observer.

8.8.3 3C 454.3

The DCF analysis of 3C 454.3 (Figure 8.36) shows evidence for strong correlation ($DCF(\tau)$ = 0.77) at a lag of ~ 0.02 months (~ 0.6 days) in the rest frame of the observer suggesting simultaneous emission at γ-ray and 1.35 mm wavelengths. This corresponds to a separation distance of < 0.1 pc between the emission zones. This is consistent with the qualitative analysis of the light curve presented in Section 7.5.3. The peak of the exceptional outburst observed on MJD 55519 at γ-ray energies was followed closely by the peak of the strongest outburst at 1.35 mm wavelengths on MJD 55520, suggesting that the 1.35 mm emission lagged the γ-ray emission by ~ 1 day in the rest frame of the observer for this particular event.

This source also exhibits anti-correlation at positive time delays of ~ 19 months and ~ 35 months in the rest frame of the observer.

DCF	$\mathrm{tl}^{obs}_{mm-\gamma}$	$\mathrm{tl}^{src}_{mm-\gamma}$	Δr
0.50	-36.8	-24.0	~ 140
0.40	-30.8	-20.1	~ 117
0.74	-22.8	-14.9	~ 87
0.64	-18.8	-12.3	~ 72
-0.33	0.13	0.08	~ 0.5
0.45	42.1	27.4	~ 160

Table 8.9: Evidence for correlation between the γ-ray and 1.35 mm light curves for 3C 279 (z = 0.536). The $DCF(\tau)$ is peak amplitude of the correlation coefficient. $\mathrm{tl}^{obs}_{mm-\gamma}$ and $\mathrm{tl}^{src}_{mm-\gamma}$ are the corresponding average delay (in months) between emission in the 1.35 mm and γ-ray wavebands in the rest frame of the observer and the source respectively. Δr is the estimated distance (in pc) between the γ-ray and 1.35 mm regions based on the observed delay in the rest frame of the source.

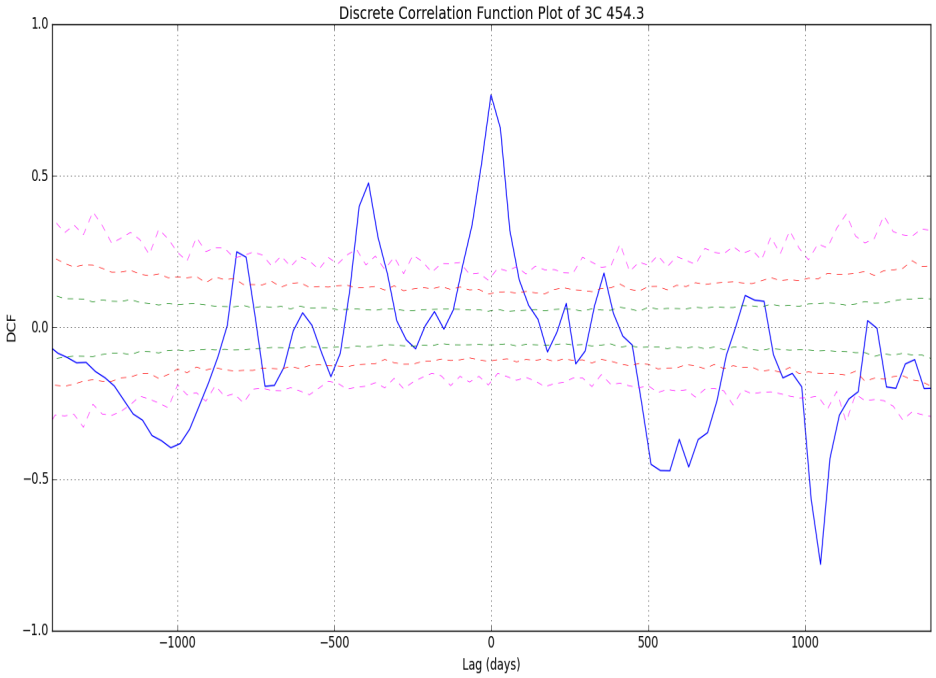

Figure 8.36: DCF curve for 3C 454.3 using a 30-day bin size produced using the γ-ray and 1.35 mm light curves presented in Figure 7.13.

DCF	$tl^{obs}_{mm-\gamma}$	$tl^{src}_{mm-\gamma}$	Δr
-0.40	-34.0	-18.3	~ 107
0.48	-13.0	-7.0	~ 41
0.77	0.02	0.01	~ 0.1
-0.47	19.0	10.2	~ 60
-0.78	35.0	18.8	~ 110

Table 8.10: Evidence for correlation between the γ-ray and 1.35 mm light curves for 3C 454.3 (z = 0.859). The $DCF(\tau)$ is peak amplitude of the correlation coefficient. $tl^{obs}_{mm-\gamma}$ and $tl^{src}_{mm-\gamma}$ are the corresponding average delay (in months) between emission in the 1.35 mm and γ-ray wavebands in the rest frame of the observer and the source respectively. Δr is the estimated distance (in pc) between the γ-ray and 1.35 mm regions based on the observed delay in the rest frame of the source.

Remarks on FSRQs

All three FSRQs show evidence for possible correlation. This agrees broadly with results from the qualitative study presented in Chapter 7. FSRQs were the brightest sources at both γ-ray and 1.35 mm wavelengths, and the strongest evidence for correlation at the shortest time delay was observed for 3C 454.3 which was the brightest source in the blazar sample. 3C 273 exhibits lower amplitude correlation at both positive and negative delays compared to 3C 379. The latter on the other hand exhibited predominantly positive correlation at only negative time delays. It is also highlighted here that while 3C 279 was brighter than 3C 273 at 1.35 mm, the opposite was true at γ-ray energies based on the datasets used in this study.

The three FSRQs presented in this study also show individually distinct behaviour not only in the intrinsic pattern of emission at γ-ray and 1.35 mm wavelengths (see Chapter 7) but also in the type and level of correlation observed between emission bands. Although this study is restricted to three FSRQ sources, it can also be seen why multi-wavelength studies conducted on blazars must account for the individual properties of the source.

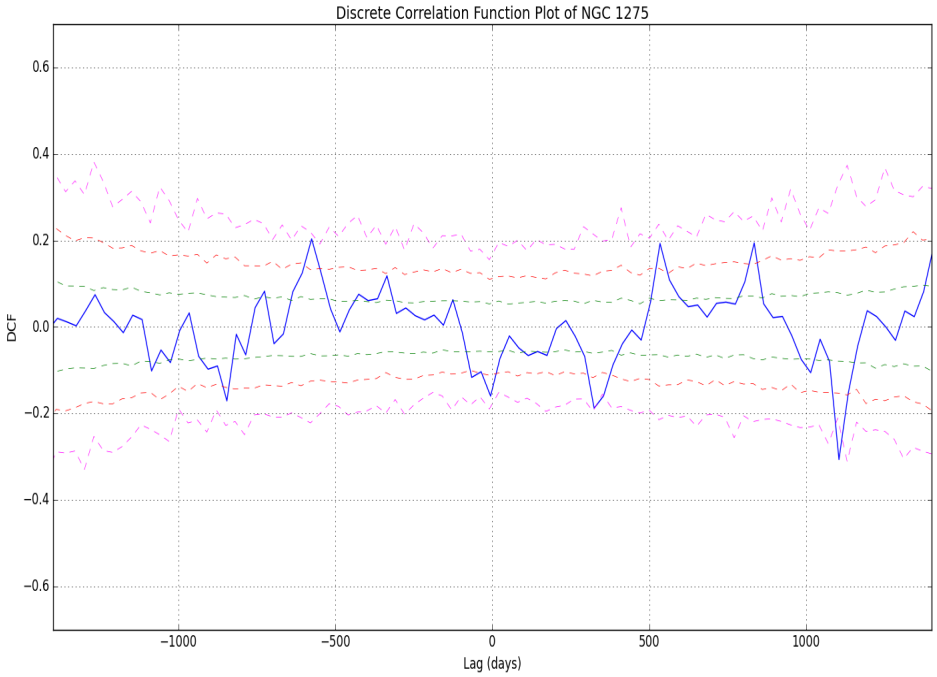

Figure 8.37: DCF curve for NGC 1275 using a 30-day bin size produced using the γ-ray and 1.35 mm light curves presented in Figure 7.14.

8.9 Radio Galaxy

8.9.1 NGC 1275

The DCF curve of NGC 1275 (Figure 8.37) shows a lack of evidence for significant correlation between the γ-ray and 1.35 mm wavelength regimes.

In 2014, Dutson et al. (141) presented a similar study of NGC 1275 investigating the connection between the *Fermi*-LAT γ-ray and SMA 1.35 mm emission of this source. Some key differences exist between the plot produced in this study and the plot produced by Dutson et al. (141). The main difference to note is the binning timescale used in processing raw *Fermi*-LAT data. While Dutson et al. used a fortnightly-binned *Fermi*-LAT dataset for the DCF analysis, data used in this thesis were binned on daily timescales. The latter resulted in a larger number of $UDCF_{ij}$ values in each bin, which then reduced the average value represented by $DCF(\tau)$ based on Equation 8.2.

In order to test this, a DCF analysis was conducted using a fortnightly-binned *Fermi*-LAT dataset, truncated to the same monitoring period used in Dutson et al.. The 1.35 mm

datasets were 'detrended' using a linear trend instead of a quadratic to match the dataset presented in Dutson et al.. Figures 8.37 and 8.38 show that similar peaks are observed at similar time-lags when compared to Dutson et al. (Figure 8.39), but the DCF values are much smaller in this recreation. Comparisons made between Figures 8.37 and 8.38 exhibit several key differences. These differences may be attributed to the analysis methods used in processing raw *Fermi*-LAT data. While the method employed by Dutson et al. uses aperture photometry, the method used in this thesis is the unbinned maximum likelihood method (see Section 4.6). While both likelihood analysis and aperture photometry are used to produce light curves from *Fermi*-LAT datasets, the likelihood analysis applies a more rigorous approach compared to the aperture photometry method. As such, the likelihood analysis provides more accurate flux measurements. This includes removing background contributions using XML models (see Section 4.6) applying more detailed source models to the dataset when the likelihood analysis is performed. Aperture photometry, on the other hand, provides model-independent flux measurements, is less computationally intensive and does not require time-bins to contain a sufficient number of photons for analysis (unlike the likelihood method). The difference in the *Fermi*-LAT analysis methods most likely contribute to the difference observed in the DCF plots in Figures 8.37 and 8.38. For comparison, the $DCF(\tau)$ curve published in Dutson et al. (141) is shown in Figure 8.39.

As discussed in Section 8.4.2, the γ-ray and 1.35 mm light curves have linear and quadratic trends respectively. This is particularly interesting as none of the other sources exhibit this feature, apart from BL Lacertae whose 1.35 mm dataset revealed complex trend patterns during the 5.5 year observation period.

This difference in trends in the γ-ray and 1.35 mm emission bands may be a result of the orientation of the source's emission regions with respect to the line-of-sight of the observer. This orientation may cause emission in the 1.35 mm region of the jet to be boosted by a different Doppler factor from emission in the γ-ray region, resulting in the varying trends seen in different wavebands. Another possibility is that the γ-ray emission is 'swamped' by emission from other sources (i.e. contribution to the γ-ray emission from regions outside the jet).

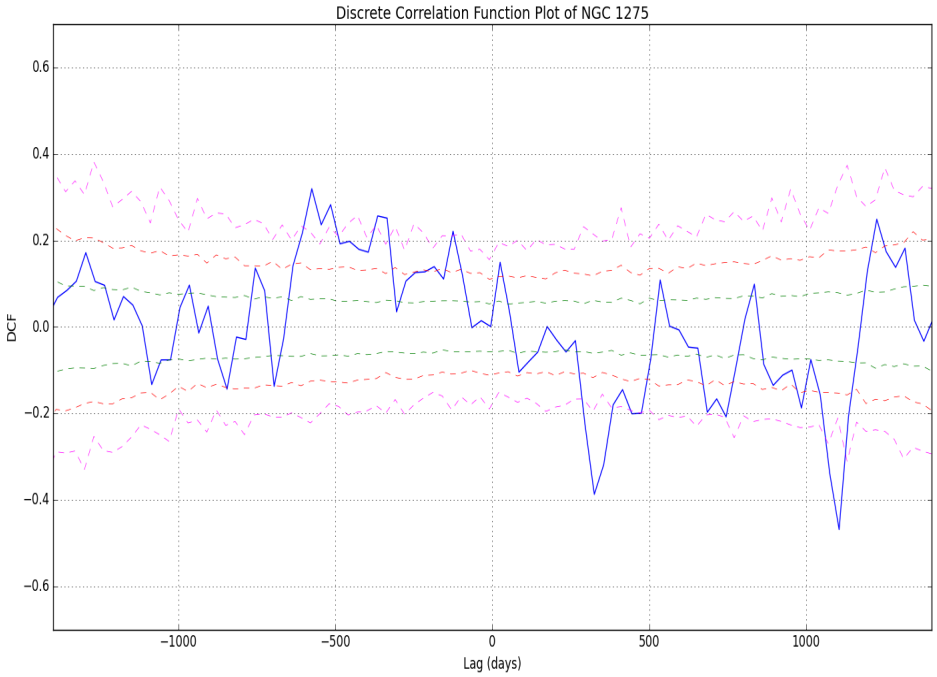

Figure 8.38: DCF curve for NGC 1275 using a fortnightly binned γ-ray dataset along with 1.35 mm dataset over the period specified in (141).

8.10 Implications of DCF Results on the Structure of Emission Zones in Blazar Jets

It was found that 3C 454.3 was the only source in the sample exhibiting simultaneous correlation between emission at the γ-ray and 1.35 mm wavebands (see Figure 8.36). This suggests that for this particular event, the emission zones may have been co-spatial or partially co-spatial (i.e. a separation distance of ~ 0.1 pc between the emission regions). BL Lacertae also exhibited evidence of similar quasi-simultaneous correlation with a time delay of ~ -0.9 months (~ -27 days) in the rest frame of the observer. 3C 273 exhibited a longer positive correlated delay of ~ 3.8 months (~ 114 days) in the rest frame of the observer. The Δr separations observed for 3C 454.3 (~ 0.1 pc), BL Lacertae (~ 5 pc) and 3C 273 (~ 19 pc) appear to agree with results in the literature (114; 36; 59; 42; 327). Studies quoted in the latter were based on a sample of bright AGN sources (primarily blazars) which show time delays ranging from several days (214; 59) to ~ 10 months (42; 327; 36) between the radio and γ-ray wavebands. In addition to this,

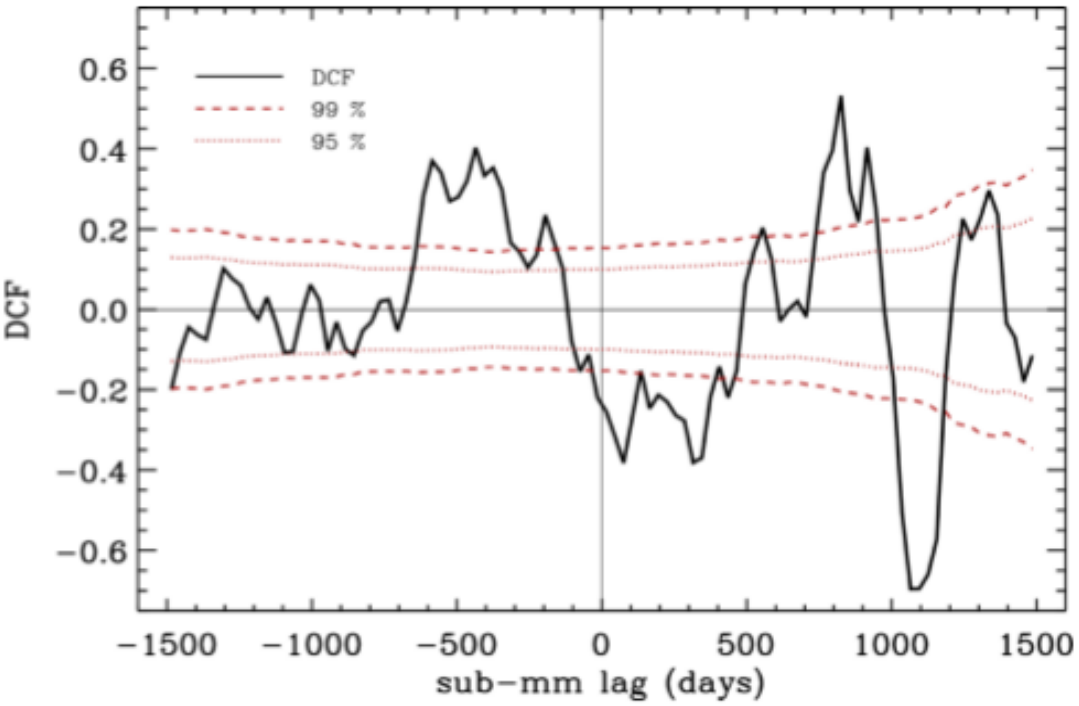

Figure 8.39: DCF curve of NGC 1275 obtained from Dutson et al. (141). The dashed and dotted red lines represent the 99% and 95% confidence intervals respectively.

a study conducted by Max-Moerbeck in 2014 (239) investigating the time-correlation between the γ-ray and radio emission regimes of *Fermi*-LAT blazars revealed time delays ranging between (40 $\pm$ 13) days and (150 $\pm$ 8) days in the rest frame of the observer, during which the γ-ray emission led the 15 GHz radio emission. A similar study conducted by Furhmann et al. (146), found correlated time delays between (7 $\pm$ 9) days and (76 $\pm$ 23) days in the source frame, once again with radio events lagging the γ-ray events. Both these results are compatible with the delays observed for 3C 273 and 3C 454.3 respectively, and are in agreement with the current jet paradigm presented Section 2.5 and Chapter 3.

The second aspect of multiwavelength correlation analysis is the convention of the observed delays. The correlated time delays (i.e. positive or negative delays) for sources such as 3C 273, 3C 279 and BL Lacertae, require the invocation of two different jet scenarios. In 3C 273, the shorter time delay observed was positive, suggesting that if a conservative assumption was invoked (i.e. the γ-ray emission site is located close to the central engine), the separation distance will constrain the 1.35 mm emission site to a distance of

~ 19 pc from the γ-ray emission region. The negative correlated delay also observed in 3C 273 however, implies that a different jet scenario may be in place. The conservative assumption in this case, would be that the 1.35 mm emission site is produced close to the central engine while the γ-ray emission is produced at distances of ~ 46 pc from the 1.35 mm emission site. While there is evidence that the γ-ray emission region is located within the sub-parsec scale of the jet (208; 16), Agudo et al. (114) have found evidence for the production of γ-rays at distances > 14 pc from the central engine. In a later study of an outburst (June 2014) in 3C 454.3 by Coogan et al. (208), evidence for the location of the γ-ray emission at distances of ~ 0.5 pc from the central engine were found. Both these delay conventions (i.e. the location of the 1.35 mm and γ-ray emission sites may both be within the sub-parsec regime of the jet) are in agreement with several published work (278; 36; 59; 42; 327; 208; 16). The evidence for both types of correlated delay conventions present in the same source (e.g. 3C 273) may also suggest a more complex multi-zone jet scenario. However, this is difficult to determine with the limited scope of the information that may be learned from the DCF analysis alone. It must also be cautioned, that one of the correlated peaks may be the result of a physically correlated event while the other may be the result of a spurious correlation. If this scenario is true, the multi-zone jet paradigm may be a better approximation to modelling blazar structure or specific blazar emission events. This may indicate that while there are emission regions within the jet that produce correlated events, other independent regions also exist. This is consistent with the multi-zone jet models described in Section 2.6.

The Δr separation estimated for sources like 3C 279 (between ~ 70 pc and ~ 160 pc) and OJ 287 ($> \sim 97$ pc) in this study, however, imply that a large separation is present between the γ-ray and 1.35 mm regions. While Δr values of ~ 97 pc are within the Mpc scale dimension of the jet, evidence of correlated events between emission zones separated by large distances may not be a reasonable scenario. If an event produced by a perturbation in the plasma propagates from one emission zone to another, the propagation of the perturbation may be interrupted by a variety of events that may occur within the jet environment (e.g. between different regions of jet or with ambient matter or radiation fields external to the jet). Firstly, as the plasma propagates downstream, the emission suffers adiabatic losses (moving from a smaller emission zone to wider zones present further down the jet). The perturbation may also come into contact with ambient

matter and radiation fields causing a distortion to the original perturbation (e.g. change in size of the emission region, radiation pressure and magnetic fields). Other effects that may cause changes to a perturbed shocked plasma at pc scales are the gradual bending of jets (209; 132; 255; 287) which may cause changes to the magnetic field configuration as well as the structure of the emission zone. All of these factors make correlation over very large distances (e.g. > 100 pc) difficult to achieve. In addition, the large Δrs observed for 3C 279 and OJ 287 also show negative delays. While other studies of γ-ray loud AGN by Pushkarev et al. (36) and blazars by Sokolov et al. (53) have found significant positive and negative time delays between γ-ray and radio wavelengths, the delays observed were on much shorter timescales (between 1 to 8 months (36)) suggesting Δr of ~ 7 pc between the radio and γ-ray emission bands.

In summary, the results of the implied locations of the γ-ray and 1.35 mm emission sites may, in turn, suggest one of two scenarios:

- The emission mechanisms which result in outbursts may be intrinsically different for individual cases (i.e. the production of each outburst is different from the other, although they are produced within the same source).

- the jet is made of multiwavelength emission zones outside the radio-wave core (i.e. the location of emission regions are not confined to a given position within the jet).

Without further evidence to support the correlation obtained from DCF methods alone (e.g. VLBI observations which will provide information on the location of the mm-wave core (36)) it is difficult to understand whether the Δr parameter represents a true physical interpretation of the source or is the result of a spurious correlation. This provides strong motivation for further multi-pronged approaches to blazar studies, which would explore various aspects of blazar behaviour (e.g. temporal and spectral evolution of the source).

8.11 Improvements to the DCF Analysis

There are several improvements that could be made to both the analysis and the observation strategy that may improve the accuracy of the DCF results.

Improvements on the observation strategy by, for example, monitoring the sources regularly, is imperative. While gaps in monitoring due to a source being below the horizon are unavoidable, a consistent unbiased sampling during other periods is important in order to obtain a more accurate correlation result. Targeted observations of sources during a particular emission state will bias the final outcome of correlation studies.

Secondly, a more rigorous significance estimate on the resulting $DCF(\tau)$ amplitudes can help to further constrain the validity the observed results. The model-dependent Monte Carlo simulation method described in Section 8.3 may be improved so that the simulated light curves account for the presence of noise, variability timescales and duty cycles observed in each wavelength regime (268; 239; 238). As observed in Chapters 6 and 7, variability timescales and duty cycles vary from epoch to epoch, making it difficult to determine a predominant mode of emission during long-term studies for individual sources. For example, BL Lacertae and NGC 1275 had different underlying trends for the two wavelengths sampled. In addition to this, the γ-ray light curve of BL Lacertae showed the presence of different trends during different epochs of the 5.5 year observation period (see Section 8.4.2). As the variability timescales and duty cycles are not well-determined especially at (sub-)mm wavelengths, the significance test using simulated light curves without careful consideration of the source-type dependent variability timescales and intrinsic trends will reduce the accuracy of the significance estimate. As such, further research into the properties of the (sub-)mm emission for a larger sample of sources is necessary. A more thorough estimate on the blazar PSD for the three types of blazar sub-classes used in this study will also improve the significance estimates as the model parameters of the simulated light curves will be more accurate. Similar work on this have been published by Uttley et al. (198).

Another method through which the significance of the DCF results can be determined is through 'mixed source analysis' (see Section 8.5). There are several caveats to this method. First, the small sample size present in this study limits the accuracy of the 'mixed source analysis' that can be performed. In addition to this, only the γ-ray and 1.35 mm wavelengths were sampled which again limits the number of mixed source analyses that are available for analysis. Ideally the mixed source correlation requires the correlation to be performed N times, where N for an accurate statistical estimate, should be > 2000 times (238; 239; 268). It was also observed that at 1.35 mm wavelengths, flares

are often superposed (i.e. second flare often occur before first flare decays during periods of outburst (see Chapter 6 and 7)). This again will reduce the overall accuracy of the significance study based on a mixed source analyses method.

Finally, the non-stationarity of datasets is an important aspect of this study (268) and there are improvements that can be made to this. As discussed in Section 8.4.2, it was found that the light curve of each source is complex. This is demonstrated by the 1.35 mm light curve of BL Lacertae which exhibited two different intrinsic trends at different epochs in its light curve. As a result, an attempt to 'detrend' the 1.35 mm light curve resulted in the introduction of a new trend at $\sim$MJD 56250 to $\sim$MJD 56692. This introduced an inaccuracy in the DCF which resulted in a spurious peak at a lag of +1300 days (see Figure 8.18). In order to circumvent this problem, a variation of the DCF method can be used in which a new mean and standard deviation (which are the criteria necessary for stationary datasets) is estimated for each time bin and the $UDCF_{ij}$ (Equation 8.1) is calculated based on the respective mean and standard deviation obtained for each bin. Another concern relevant to this study is the length of the datasets (5.5 years) used in the DCF analysis. These are particularly long, and while this length is sufficient to assess variability timescales at γ-ray energies and 1.35 mm wavelengths, it may not be long enough to estimate the duty cycles of the emission which determines the underlying trend of the dataset. This in turn imposes a limitation on the DCF analysis. Thus, 'detrending' long-term datasets must be done cautiously.

8.12 Conclusion

All sources in the sample, excluding the HBLs (due to the lack of data at 1.35 mm which may have affected the results of the DCF analysis) exhibit some level of correlation between the γ-ray and 1.35 mm wavelengths. However, the amplitudes and delay conventions of these differ for each source. Of the eight sources, 3C 454.3 shows evidence for simultaneous correlation while 3C 273 and BL Lacertae show evidence for correlation at both short positive and negative delays (< 4 months in the rest frame of the observer). This short delay suggests that correlation observed in these cases are more likely due to a physically correlated event rather than a spurious correlation or caveats of the DCF analysis. OJ 287 and 3C 279 on the other hand, exhibit correlation with predominantly

longer delays. For these cases, it is difficult to determine if correlation observed at these large delays are physically possible with limited datasets and analysis methods.

While general evidence for correlated behaviour is observed for IBLs and FSRQs, all of these sources exhibit different types of correlation throughout the monitoring period. It is difficult to determine which wavelength might be leading the other - there is evidence for both existing in sources like 3C 273 and 3C 454.3. This study has shown that the behaviour of some of these sources is highly complex, with evidence for correlation suggesting the presence of multiple emission zones. Some of these zones may be co-spatial while others may not. A trigger, such as a shock or 'knot', might cause particles within different emission zones to be excited resulting in flares and outbursts. Emission produced at γ-ray energies might then rise and decay on shorter timescales than emission at 1.35 mm. This trigger could propagate along the jet resulting in a change in emission in the different regions located along the jet. This may explain the lags observed in sources like 3C 273.

Several factors affect the study of correlation for BLOs, in particular MRK 421, MRK 501 and BL Lacertae. In the case of MRK 421 and MRK 501, under-sampling at 1.35 mm is an important factor. It was also observed that the light curves of these sources at γ-ray energies were in general featureless with the exception of an extreme outburst seen in MRK 421. The lack of data at 1.35 mm made it difficult to see if this is also the case at 1.35 mm. The *Fermi*-LAT light curve of BL Lacertae is also generally featureless, and any evidence for activity is seen as a rise in the variability amplitude. At 1.35 mm, BL Lacertae shows clear transitions between quiescent states and outbursts. While this difference between emission at γ-ray and 1.35 mm can be observed by eye, the nature of the DCF analysis does not take this into account. Another interesting feature of BL Lacertae is that both the γ-ray and 1.35 mm wavebands have an underlying trend. This feature is also seen in NGC 1275. However, in the case of NGC 1275, the γ-ray light curve has an underlying linear trend while the 1.35 mm waveband has an underlying quadratic trend. These features which exists within each source class suggest that the emission of each blazar at a particular wavelength is intrinsically different. The classification scheme which may apply to one waveband might not apply to another waveband.

This study has also highlighted the need for consistently sampled datasets over periods of several years. Based on the analysis performed in Chapter 7 and 8, the duty

cycles of some of these sources occur over periods of several years. A consistently sampled dataset would improve the accuracy of multiwavelength correlation studies.

Chapter 9

Conclusions and Further Work

This chapter briefly summarises the research produced in this thesis. The study of AGN and in particular blazars have long been a subject of great interest; the observational, geometric and evolutionary properties of these objects forming a key motivation behind blazar studies.

While blazars have been the subject of extensive multiwavelength campaigns (e.g. (179; 102; 232)) which monitor these objects from radio to γ-ray energies, observation campaigns which include consistently monitored (sub-)mm wavebands have been poor, mainly due to limited instrument resources and time (i.e. the SCUBA-1 instrument, the predecessor to SCUBA-2, was out of commission since 2005 which subsequently led to the drop in access to (sub-)mm observations). However, the more recent advances in instrumentation techniques and access to databases which catalogue these sources regularly (such as the SMA instrument) have provided a wealth of data on blazars and other AGN sub-classes at (sub-)mm wavelengths.

A primary motivation of this research was to study emission in the (sub-)mm waveband in tandem with emission in the HE γ-ray band. The temporal evolution of the blazar broadband emission allows inferences to be made on the physical and geometrical properties of blazar jets. For example, flares observed simultaneously or quasi-simultaneously at different wavelengths may indicate the presence of co-spatial emission regions. On the other hand, the presence of temporal delays between events at different wavelengths may allow further constraints on the physical separation between the emission zones. The nature of the emission during different emission states, such as flares and quiescent states, provides further constraints on the physical parameters (e.g. magnetic field strengths, bulk Lorentz factors, Γ, Doppler factors δ, etc.) which are used in blazar emission models. In this particular work, the connection between the

γ-ray and (sub-)mm emission was explored using both short- and long-term monitoring campaigns. The light curves, which show the emission of the source during different emission states, were analysed both qualitatively and quantitatively to determine the extent of the relationship between the emission at different wavelengths. The purpose behind this was to understand the implications of the observed emission on the physical properties of the relativistic jet (e.g the jet geometry) and to distinguish between emission models.

In the current blazar jet paradigm, leptonic scenarios be it SSC or EC models, are thought to dominate under the simple approach that less energy is required to accelerate an electron to relativistic speeds compared to the energy it takes to accelerate a more massive proton to similar relativistic speeds. While the leptonic framework has been able to explain the emission and variability observed from blazar SEDs, there are aspects of this framework that are still a subject of ongoing research. For example, to what extent do leptonic scenarios dominate if they do in fact dominate emission processes in the jet? How are the emission zone(s) within the jet oriented and located? Some of the models described in Section 2.7 suggest that homogeneous single-zone models are far too simple, and that other more complex scenarios such as the spine-sheath model, or the discontinuous jet model are more realistic scenarios when a relativistically moving stream of plasma is being considered. There are also models which address this issue by invoking different configurations of magnetic fields within the jet.

9.1 On the γ-ray (Sub-)mm Connection in Blazars

Scenarios exist in which different emission bands may exhibit some degree of correlation with one another (36; 141; 115; 46) or, alternatively, an absence of correlation may be found during different epochs or emission states (195; 218; 149). Both the existence or absence of correlation indicate different possible configurations of the geometric structure and the emission mechanisms present in the jet.

As described in Section 2.5, relativistic jets of blazars are highly complex structures which span Mpc scales. Interpreting results from these multiwavelength campaigns is therefore also complex. For example, the highly variable nature of the jet and the extreme environments present in the jet may give rise to physically uncorrelated events occurring

at similar times.

Temporal delays, in general, can be attributed to several factors:

- The activity of the central engine (e.g. change in the magnetic field configuration at the base of the jet or an actively feeding SMBH) may result in progressive delays in different regions of the jet.
- The geometric structure of the γ-ray emission region within the jet is different from that in the region producing the (sub-)mm emission.
- Synchrotron self-absorption may result in emission from the synchrotron component only becoming visible when it reaches optically thin regions (usually described as the radio- or mm-wave cores), while higher energy emission escapes immediately from the jet.
- Interaction of a shocked region within the jet with ambient regions (such as BLR clouds entering the jet). Such interactions may lead to the observation of a flare in one wavelength before another, when the result of the collision propagates downstream or results, alternatively, in forward and reverse shocks.
- Difference in decay times of the synchrotron and IC emission with respect to the apparent crossing time between the two regions. This particular feature may produce positive or negative time delays between the observed energy bands. If the decay time of the synchrotron emission is longer than the apparent crossing time, the synchrotron flare will appear after the high energy flare. Since the decay times are dependent on the wavelength of observation, it can be deduced that at sufficiently high energies of the synchrotron component and sufficiently low energies of the IC component, the decay times of the IC component will be longer than the apparent crossing time. This will result in flares observed in the lower energy regime before they are observed in the higher energy regime.

It is often difficult to distinguish between a physically correlated and a physically uncorrelated event without a multi-pronged approach, i.e. investigating various observational features and structural features at the same time. This method helps constrain the possible scenarios which may produce the different types of correlation observed. For example, some campaigns involve large source samples which include various AGN

Name	RA (hh:mm:ss)	dec. (deg:min:sec)	z	Type
PKS 2155-304	21:58:53	-30:13:18	0.116	HBL
MRK 421	11:04:27	+38:12:32	0.031	HBL
MRK 501	16:53:52	+39:45:37	0.034	HBL
OJ 287	08:54:49	+12:06:31	0.310	IBL/LBL
BL Lacertae	22:02:43	+42:16:40	0.069	IBL/LBL
3C 273	12:29:07	+02:03:09	0.158	FSRQ
3C 279	12:56:11	-05:47:22	0.536	FSRQ
3C 454.3	22:53:58	+16:08:54	0.859	FSRQ
NGC 1275	03:19:48	41:30:42	0.018	Radio Gal.

Table 9.1: Summary of the eight sources included in this study and details on their right ascension (RA), declination (dec.), redshift (z) and the source type.

sub-classes. Other campaigns study various aspects of a given emission band, from flux variability to the evolution of the spectral index. When information from various studies is combined, a detailed view of the AGN may be understood.

The initial part of this work focussed predominantly on the sub-mm and γ-ray observations of HBLs. These were short-term observations of MRK 421 and PKS 2155-304 using *Fermi*-LAT and SCUBA-2 which lasted between six days to approximately three months during both quiescent and flaring periods. Results from this study did not provide enough evidence for variability or any correlation between the wavebands, suggesting that longer-term campaigns are needed.

Thus, the research was expanded to include a larger source sample from three blazar sub-classes and a radio galaxy (Table 9.1). In order to obtain an in-depth understanding of each source and its intrinsic behaviour at the respective wavelengths monitored, a sample size of eight was chosen. Data were then selected from the SMA Calibrator List and the *Fermi*-LAT datasets. This constituted a $\sim$ 12-year monitoring period with the SMA instrument and a 5.5 year monitoring period with *Fermi*-LAT.

9.1.1 Correlation studies on the γ-ray and 1.35 mm Emission in Different Blazar Sub-classes

Studying the connection between the γ-ray and (sub-)mm wavebands was improved with the more well-sampled database of sources over longer monitoring periods (i.e. regular daily, or weekly monitoring over periods of at least several years) using data from the SMA Calibration List. The correlation studies presented in Chapters 7 and 8 revealed interesting features in the emission at both these wavebands.

Some of the key findings are summarised here:

- In general, emission in the γ-ray wavebands was more variable, i.e. with higher variability amplitudes and shorter variability timescales, than emission in the (sub-)mm wavebands.

- Although the sample was quite small, it was apparent that the overall emission at both γ-ray and (sub-)mm wavebands was different for different source classes. FSRQs appear to show a clear transition between emission states from quiescence to outburst, indicating that FSRQs are the most variable of the blazar sub-class, followed by IBLs which also appear to exhibit structure in the temporal evolution of the flux over the 5.5 year observation period. However, unlike the FSRQs, the γ-ray emission in the IBL sub-class did not always exhibit similar behaviour to that of the 1.35 mm emission as seen in BL Lacertae. This source had a clear structure in the transition between emission states in at 1.35 mm but a less well-defined γ-ray light curve. The latter is similar to the generally featureless spectrum observed in HBLs.

- Most of the correlations observed in FSRQs showed possible positive and negative lags between the two emission bands. In other words, both possibilities (i.e. γ-ray emission leading the 1.35 mm emission and 1.35 mm emission leading the γ-ray emission) may be part of the blazar jet model in FSRQs. It must be cautioned, however, evidence for both these scenarios could also be an effect of the limitations in the DCF method which may produce spurious correlation peaks. Since all the FSRQs presented in this study showed light curves with multiple peaks and troughs in the DCF curve, a more stringent significance test must be applied in order to

further determine the validity of the correlation measured, including whether a particular time delay is more favoured than the other.

- Both IBL sources also showed evidence for possible correlation with positive and negative delays. However, the correlation observed with BL Lacertae corresponds to a shorter delay between emission at the γ-ray and 1.35 mm wavebands compared to OJ 287. While both OJ 287 and BL Lacertae are classified as IBLs, the intrinsic nature of the light curves of both these sources differ. While the 1.35 mm light curve of BL Lacertae showed clear structure and transition between emission states, its γ-ray light curve was generally featureless throughout the observation period with only increase in variability amplitudes suggesting any form of increase in activity of the source in the γ-ray emission band.

- A similar behaviour to that in BL Lacertae was also observed for the radio galaxy, NGC 1275, which showed an intrinsic *linear* trend in the γ-ray band while its 1.35 mm emission exhibited an intrinsic *quadratic* trend.

- It was also particularly interesting that only 3C 454.3 in the eight source sample exhibited strong simultaneous correlation between the γ-ray and 1.35 mm wavebands. None of the other FSRQs or IBLs showed this level of simultaneity in the emission at the γ-ray and 1.35 mm wavebands.

These results show that, while each source behaves differently from the other, namely in aspects of variability timescales, the nature of the correlation between the higher and lower energy bands, some general trends appear to be based on their source class. For instance, HBLs have generally featureless spectra, while the IBLs and FSRQs have clear structure as the source transitions between emission states at both wavebands. This suggests that at some level, the blazar sequence has an important effect on the temporal evolution of light curves. It can also be suggested that the intrinsic difference between these sources may be the result of the physical geometry of the emission regions within the jet and the type of emission mechanisms contributing to the emission observed. Some of these will be discussed in the following section.

9.1.2 Physical Interpretation of Correlation Studies and Implications to the Blazar Sequence

The correlation studies of the eight sources led to four possible outcomes. This is illustrated in Figure 9.2. In the first level of outcomes, there is either the possibility of correlation or lack of correlation between the wavebands. Correlated behaviour can be one of three types. The first is either simultaneous or quasi-simultaneous correlation between the emission bands analysed. This particular type of correlation was observed in 3C 454.3 in which the 1.35 mm emission lagged the γ-ray emission within ~ 0.02 months (~ 0.6 days) in the rest frame of the observer, corresponding to a separation distance of ~ 0.1 pc. This suggests that for this particular event, the emission regions may have been co-spatial. A longer quasi-simultaneous correlation was observed in BL Lacertae with a time delay of ~ -0.9 months (~ -27 days) in the rest frame of the observer, corresponding to a separation distance of ~ 5 pc between the emission regions. 3C 273 exhibited correlation at a delay of ~ 3.8 months (~ 114 days) in the rest frame of the observer. This results in a separation distance of ~ 19 pc between the γ-ray and 1.35 mm emission regions. All of these results agree with results from previous studies conducted on a sample of bright AGN sources (mostly blazars) which show time delays ranging between several days (214; 59) and ~ 10 months (42; 327; 36) between the radio and γ-ray wavebands. It may be important to note that of these three sources, 3C 454.3 was the brightest in the source sample and recorded the highest amplitude for an outburst compared to the other sources. However, it is unclear if the brightness of the flare or outburst affects the level or lag in the correlation observed, since there was no trend which linked the brightness of an outburst to observed temporal delays in any of the other sources.

The physical feasibility of an observed correlation can be further explored using the convention of the observed time delays (i.e. positive or negative delays). For example, the presence of both negative and positive correlated delays observed in 3C 273 may be considered. The delay convention for this source requires the invocation of two different jet scenarios. The shorter positive delay observed in 3C 273, suggests that if a conservative assumption was invoked (i.e. the γ-ray emission site located close to the central engine), the separation distance will constrain the 1.35 mm emission region site to ~ 19 pc from the γ-ray emission region. 3C 273 also showed evidence for a negative correlated delay which implied that a different jet scenario may also be possible for this

source. For the longer negative delay, the conservative assumption would be that the 1.35 mm emission region located close to the central engine. This will then constrains the γ-ray emission region to a distance of ~ 46 pc from the 1.35 mm emission site. While previous studies have shown evidence for both the γ-ray and the 1.35 mm waveband regions to be located within the sub-parsec region of the jet (278; 36; 59; 42; 327; 208; 16), studies conducted by Agudo et al. (114) have found evidence for the γ-ray region to be localised at distances > 14 pc from the central engine.

Further to this, sources like 3C 279 and OJ 287 exhibited evidence for relatively long correlated delays (between ~ 20 months and ~ 40 months in the rest frame of the observer) which corresponded to large Δr separations between the γ-ray and 1.35 mm emission regions. For example, the Δr separation for 3C 279 was estimated to lie between ~ 70 pc and ~ 160 pc while Δr for OJ 287 was estimated to be > 97 pc). Although, separation distances of ~ 97 pc are within the Mpc scales of the jet, evidence for strong correlated events separated by large distances as that observed in 3C 279 may not be a reasonable scenario. At vast distances, the propagation of a shocked plasma region along the jet may be subject to a variety of scenarios. Some of these include changes to the magnetic field configuration, possible bending of jets and adiabatic losses incurred during propagation. This reduces the possibility of strong or significant correlation as observed for 3C 279 (~ 0.74) and OJ 287 (~ 0.62). The large time delays observed for OJ 287 and 3C 279 are also inconsistent with results from similar multiwavelength correlation studies (36; 222) which showed shorter delays between radio, optical and γ-ray emission bands (between one to eight months (36) and up to ~ 10 months (42; 327; 222)). Based on comparisons with results in the literature and the implied large distances suggests that the observed correlated delay in OJ 287 and 3C 279 were more likely caused by spurious correlation rather than a representation of the blazar jet scenario.

It is clear that the structure, geometry and dynamics of the jet are very complex. The emission mechanisms or processes which dominate in one source may not dominate emission in the other. It is very likely that all eight sources behave differently simply because the dominant modes of emission and the location of the emission regions during the time of observation are different from one to the other. This does not mean however that these sources are intrinsically different, only that there is a variety of possible events which may occur in the prodigiously energetic regions of the inner jet. This then may

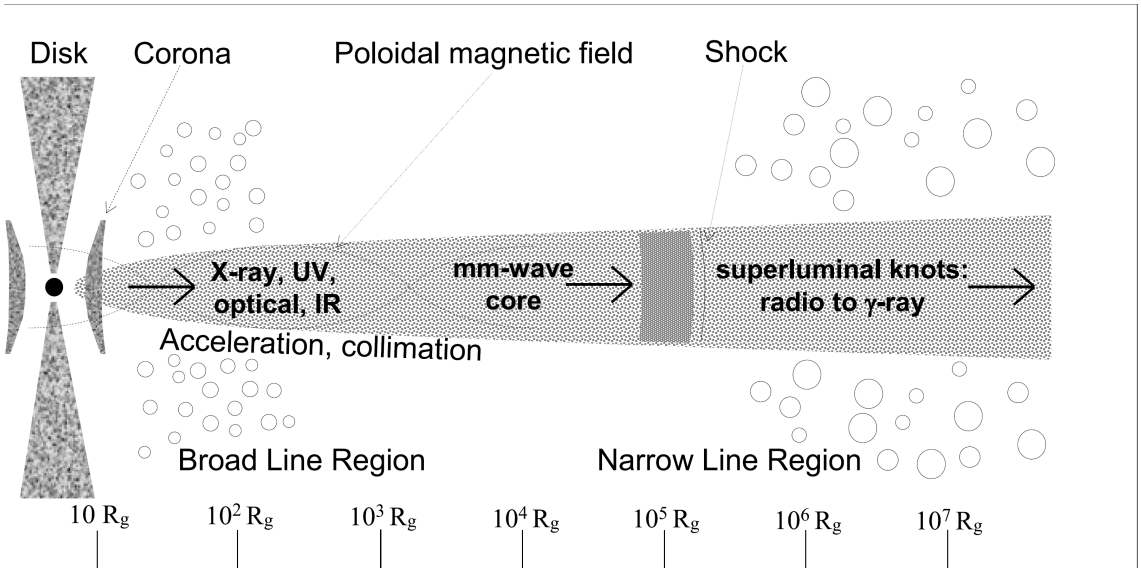

Figure 9.1: Schematic of a quasar jet and regions where emission at different wavebands are thought to originate. R_g represents the gravitational or Schwarzschild radius of the SMBH ($R_g \sim \frac{GM}{c^2}$, where G is the gravitational constant, M is the mass of the SMBH, and c is the speed of light). For an SMBH of $\sim 10^9$ solar masses, R_g is estimated at $\sim 5 \times 10^{-5}$ pc. The scale in the figure is logarithmic beyond 10 R_g. At distances of 10^3 R_g, the jets become visible at radio wavelengths. The broad line region (BLR) typically lies within the sub-parsec region of the jet, while the NLR regions lie at distances > 1 pc (286). This is based on the schematic adapted from Marscher 2005 (278) and Lobanov 2007 (271). Image credit Karouzos et al. (169).

result in the different types of correlations observed (either through variations in the strength of correlation or in the time delay present between correlated events from one source to another). It was also noted that the level of correlation based on the amplitude of the DCF is predominantly stronger for FSRQs than IBLs (the two source types in which correlation was observed). This suggests that when considering correlation between the higher and lower energy bands, the blazar sequence which suggests a progressive link from FSRQs $\rightarrow$ IBLs $\rightarrow$ HBLs $\rightarrow$ may be present based on the sources observed in this study. The correlation observed for HBLs on the other hand may be spurious mainly due to the lack of sampling at 1.35 mm wavelengths (e.g. MRK 421).

It is also clear that more extensive analyses of these sources are necessary to determine their intrinsic characteristics and features.

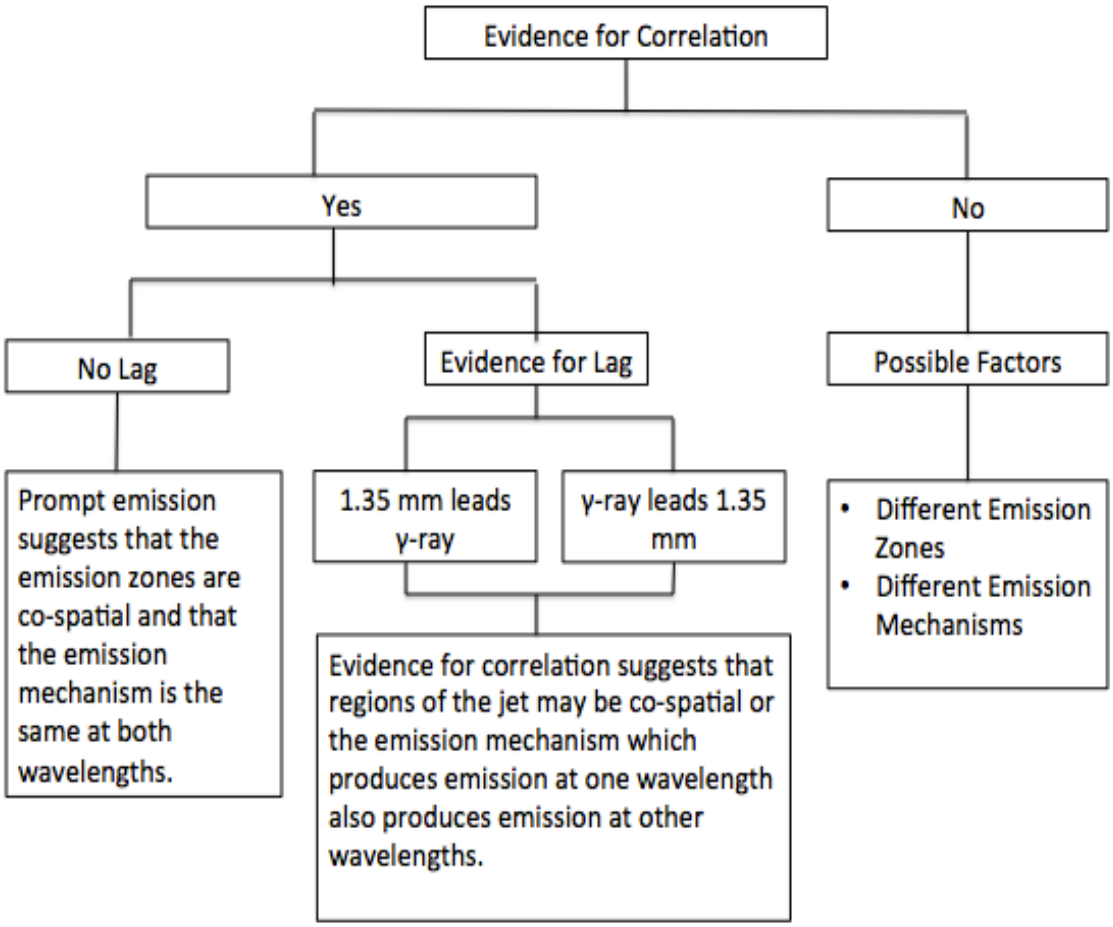

Figure 9.2: This chart represents the physical implications of finding evidence which support or negate correlation between the high-energy γ-ray and 1.35 mm wavebands.

9.2 Improvements to the Methodology and Analysis Methods and Further Work

There are two main factors which limit the research conducted in this thesis. These are the observation methodology and the type of correlation analysis employed. Improvements in both these regards will vastly improve the information obtained from these sources.

One of the key features which limited information from observation is biased sampling. This can be due to targeted observations, such as limiting observations to particular emission states. This not only limits the types of analysis that can be conducted on the dataset, it also gives a biased view of emission from the source. Another problem

with this is the loss of relevant information on duty cycles (i.e. phases between the onset, peak and decay of an event and the transition between states), especially since very little is known of the properties of these sources in the (sub-)mm regimes. It was only determined after the ~ 12-year SMA datasets were analysed that the (sub-)mm emission of each source varied differently between the different blazar sub-classes.

In this regard it can be seen that long-term, unbiased monitoring campaigns are an important aspects of blazar studies. It is also clear that the variability amplitudes and timescales differ from source to source and between the higher and lower emission bands. Monitoring campaigns must be organised to take into account the difference in the variability timescales. If ToO observations are conducted, such as those performed using SCUBA-2 on MRK 421 (see Chapter 5), these must also take into account the temporal lag which may be present between emission bands. Since this is difficult to determine based on previous and ongoing research in this area, unbiased long-term campaigns are needed to circumvent this problem.

Thus, it would be ideal for future observation campaigns to run over the duration of several years, with daily monitoring programs. These campaigns should also cover all wavelength regimes, including the data from VLBI imaging observations. The latter will provide further constraints on the possible location of the (sub-)mm wave core. The research presented in this thesis has brought to light the highly complex nature of blazars (in particular at (sub-)mm wavelengths) and that they vary greatly from source to source while maintaining some general trends which appear source-class dependent. In addition, it was observed that different wavelength regimes of the same source can produce different emission trends (e.g. the γ-ray and 1.35 mm light curves of NGC 1275 displayed linear and quadratic underlying trends respectively during the 5.5-year observation period). This suggests that there is still much to be discovered in these sources, and that blazar classification schemes may need to be improved to accommodate these features. In order to do this, an extensive well-monitored database of a good selection of sources is necessary. Future work may be done to address this in order to improve our understanding of the nature and evolution of these sources.

The second aspect of this study which could be improved involves the type of correlation method employed. As discussed in detail in Chapter 8, the DCF method employed in this thesis can be improved by refining and employing a more rigorous statistical sig-

nificance test. This can be achieved by correlating observed light curves with simulated ones (rather than observed light curves at different wavebands). The former ensures that significance estimates are not affected by intrinsic differences present in light curves in the different wavebands of the same source, i.e. difference in variability timescales and underlying trends at different wavebands. It may also be prudent to extend this correlation method to include other correlation techniques which may account for the difference in the intrinsic trends present in some of these sources. Due to the complex nature of these light curves, the DCF method may fall short when searching for correlated events between the emission bands. Variations to the DCF method, such as the ZDCF (3) and DCCF methods (268; 146), will allow for a more accurate assessment of correlation. Unlike the DCF technique, the ZDCF and DCCF methods make no assumption of the trends present in the dataset.

9.3 Concluding Remarks

Blazars are some of the most interesting sources in the observable universe offering a wealth of information on the nature and evolution of AGNs in general. Due to their alignment to the observer, they provide a particularly helpful way of studying relativistic jets, the mechanisms and structure of these sources. With the continuous advances in instrumentation and technology, more and more of these sources are being discovered and consistently monitored, opening up new windows into some of the more energetic phenomena in the universe. As more and more of these sources are studied, more information about the mechanics of the central engines which hold these galaxies together can be obtained. This will then contribute to a holistic understanding of galactic evolution schemes.

Bibliography

[1] A. Caproni & Z. Abraham. Precession in the inner jet of 3C 345. *ApJ*, 602:625–634, 2004.

[2] A. M. Brown & J. Adams. High-energy gamma-ray properties of the Fanaroff-Riley type 1 radio galaxy NGC 1275. *MNRAS*, 413:2785–2790, 2011.

[3] T. Alexander. Is AGN variability correlated with other AGN properties? ZDCF analysis of small samples of sparse light curves. *Astronomical Time Series in Eds. D. Maoz, A. Sternberg and E. M. Leibowitz (Dordrecht: Kluwer)*, 218:163, 1997.

[4] R. Antonucci. Unified models for active galactic nuclei and quasars. *Ann. Rev. A & A*, 31:473–521, 1993.

[5] T. Arlen. Rapid TeV gamma-ray flaring of BL Lacertae. *ApJ*, 762:92–104, 2013.

[6] E. L. Zirbel & S. A. Baum. On the FR I/FR II dichotomy in powerful radio sources: Analysis of their emission-line and radio luminosities. *ApJ*, 448:521–547, 1995.

[7] J. H. Beall & W. Bednarek. On the hadronic beam model for gamma-ray production in blazars. *ApJ*, 510:188–196, 1999.

[8] A. R. Bell. The acceleration of cosmic rays in shock fronts. I. *MNRAS*, 182:147–156, 1978.

[9] A. R. Bell. The acceleration of cosmic rays in shock fronts. II. *MNRAS*, 182:443–455, 1978.

[10] D. F. Cioffi & J. M. Blondin. The evolution of cocoons surrounding light, extragalactic jets. *ApJ*, 392:458–464, 1992.

[11] R. Blundell. The Submillimeter Array. *IEEE MTT-S International Microwave Symposium Digest*, Jul.:1857–1860, 2007.

[12] M. Boettcher. Modelling the emission processes in blazars. *Astrophysics and Space Science*, 309:95–104, 2007.

[13] M. Böttcher. Modelling the emission processes in blazars. *Astrophysics and Space Science*, 309:95–104, 2007.

[14] H. Bradt. *Astrophysical Processes*. Cambridge University Press, Cambridge, 2008.

[15] A. H. Bridle. Extragalactic jets - Trends and correlations. *Can. J. Phys.*, 64:353–361, 1986.

[16] A. M. Brown. Locating the gamma-ray emission region of the Flat Spectrum Radio Quasar PKS 1510-089. *MNRAS*, 431:824–835, 2013.

[17] A. Hewitt & G. Burbidge. A revised and updated catalog of quasi-stellar objects. *ApJS*, 87:451, 1993.

[18] G. R. Burbidge. On the synchrotron radiation from Messier 87. *ApJ*, 124:416–429, 1956.

[19] P. M. Chadwick. VHE gamma rays from PKS 2155-304. *ICRC Proc.*, 3:338, 1999.

[20] M. C. Begelman & D. F. Cioffi. Overpressured cocoons in extragalactic radio sources. *ApJ*, 345:21–24, 1989.

[21] H. D. Curtis. Descriptions of 762 Nebulae and clusters photographed with the Crossley Reflector. *Publ. Lick Obs.*, 13:9–42, 1918.

[22] G. de Vaucouleurs et al. Third Reference Catalogue of Bright Galaxies. Volume I: Explanations and references. Volume II: Data for galaxies between 0 h and 12 h. Volume III: Data for galaxies between 12 h and 24 h. *Third Reference Catalogue of Bright Galaxies*, pages Volume I – III, 1991.

[23] J. D. Finke & C. D. Dermer. On the break in the *Fermi* - Large Area Telescope Spectrum of 3C 454.3. *ApJ Lett.*, 714:L303–L307, 2010.

[24] D. Sanchez & L. Escande. *Fermi*-LAT detection of a rapid and extraordinary GeV outburst from 3C 454.3. *ATel*, page 3041, 2010.

[25] A. A. Abdo et al. Bright active galactic nuclei source list from the first three months of the *Fermi* Large Area Telescope all-sky survey. *ApJ*, 700:597–622, 2009.

[26] A. A. Abdo et al. *Fermi* discovery of gamma-ray emission from NGC 1275. *ApJ*, 699:31–39, 2009.

[27] A. A. Abdo et al. The first catalog of active galactic nuclei detected by the *Fermi* Large Area Telescope. *ApJ*, 715:429–457, 2010.

[28] A. A. Abdo et al. Gamma-ray light curves and variability of bright *Fermi*-detected blazars. *ApJ*, 722:520–542, 2010.

[29] A. A. Abdo et al. Spectral energy distribution of *Fermi* bright blazars. *ApJ*, 716:30–70, 2010.

[30] A. A. Abdo et al. Spectral properties of bright *Fermi*-detected blazars in the gamma-ray band. *ApJ*, 707:1271–1285, 2010.

[31] A. A. Abdo et al. *Fermi* Large Area Telescope observations of Markarian 421: The missing piece of its spectral energy distribution. *ApJ*, 736:131–153, 2011.

[32] A. A. Moiseev et al. Observation and simulations of the backsplash effects in high-energy gamma-ray telescopes containing a massive calorimeter. *Astroparticle Physics*, 22:275–283, 2004.

[33] A. Abramowski et al. Flux upper limits for 47 AGN observed with H.E.S.S. in 2004-2011. *A & A*, 564:A9–A19, 2014.

[34] A. Abramowski et al. Long-term monitoring of PKS 2155-304 with *ATOM* and H.E.S.S.: Investigation of optical/gamma-ray correlations in different spectral states. *A & A*, 571:A39–A49, 2014.

[35] A. B. Pushkarev et al. Jet opening angles and gamma-ray brightness of AGN. *A & A*, 507:L33–L36, 2009.

[36] A. B. Pushkarev et al. Radio/gamma-ray time delay in the parsec-scale cores of active galactic nuclei. *ApJL*, 722:L7–L11, 2010.

[37] A. C. Fabian et al. A wide Chandra view of the core of the Perseus cluster. *MNRAS*, 418:2154–2164, 2011.

[38] A. C. Gupta et al. Simultaneous multi-wavelength observations of the tev blazar MRK 421 during February March, 2003: X-ray and NIR correlated variability. *Chin. Journ. Astron. Astrophys.*, 8:395–403, 2008.

[39] A. C. S. Readhead et al. Bent beams and the overall size of extragalactic radio sources. *Nature*, 276:768–771, 1978.

[40] A. Celotti et al. A model for the spectral variability of bl lacertae objects at high frequencies. *ApJ*, 377:403–416, 1991.

[41] A. Celotti et al. Jets and accretion processes in active galactic nuclei: Further clues. *MNRAS*, 286:415–424, 1997.

[42] A. E. Vol'vach et al. Correlations between the development of a flare in the blazar 3C 454.3 in the radio and optical. *Astronomy Reports*, 52:867–874, 2008.

[43] A. E. Vol'vach et al. Multi-frequency studies of the non-stationary radiation of the blazar 3C 454.3. *Astronomy Reports*, 55:608–615, 2011.

[44] A. E. Wehrle et al. Multiwavelength variations of 3C 454.3 during the 2010 November to 2011 January outburst. *ApJ*, 758:72–93, 2012.

[45] A. L. Strom et al. Submillimeter variability and the gamma-ray connection in *Fermi* blazars. *American Astronomical Society*, 42:376, 2010.

[46] A. P. Marscher et al. Relative timing of variability of blazars at X-ray and lower frequencies. *American Inst. Phys. Conf. Ser.*, 714:167–173, 2004.

[47] A. P. Marscher et al. Probing the inner jets of the quasar PKS 1510-089 with multi-waveband monitoring during strong gamma-ray activity. *ApJ Lett.*, 710:L126–L131, 2010.

[48] A. P. Marscher et al. Relation between events in the millimeter-wave core and gamma-ray outbursts in blazar jets. *ArXiv*, 1204:6707:1–6, 2012.

[49] A. Paggi et al. SSC radiation in BL Lacertae sources, the end of the tether. *A & A*, 504:821–828, 2009.

[50] A. Pedlar et al. The radio structure of NGC 1275. *MNRAS*, 246:477, 1990.

[51] A. Sillanpaa et al. OJ 287 - Binary pair of supermassive black holes. *ApJ*, 325:628–634, 1988.

[52] A. Sillanpaa et al. Confirmation of the 12-year optical outburst cycle in blazar OJ 287. *A & A*, 305:L17, 1996.

[53] A. Sokolov et al. Synchrotron self-compton model for rapid nonthermal flares in blazars with frequency-dependent time lags. *ApJ*, 613:725–746, 2004.

[54] B. Balmaverde et al. The Chandra view of the 3C/FR I sample of low luminosity radio-galaxies. *A & A*, 451:35–44, 2006.

[55] B. G. Piner et al. The fastest relativistic jets: VLBA observations of blazars with apparent speeds exceeding 25c. *ApJ*, 640:196–203, 2006.

[56] B. Rani et al. Constraining the location of rapid gamma-ray flares in the Flat Spectrum Radio Quasar 3C 273. *A & A*, 557:A71–A82, 2013.

[57] C. D. Dermer et al. High-energy gamma radiation from extragalactic radio sources. *A & A*, 256:L27–L30, 1992.

[58] C. D. Dermer et al. The *Fermi* second Large Area Telescope AGN catalog (2LAC). *AAS*, 219:id. 305.04, 2012.

[59] C. M. Raiteri et al. A new activity phase of the blazar 3C 454.3 multifrequency observations by the WEBT and *XMM-Newton* in 2007-2008. *A & A*, 491:755–766, 2008.

[60] C. M. Raiteri et al. WEBT multiwavelength monitoring and xmm-newton observations of BL Lacertae in 2007-2008. Unveiling different emission components. *A & A*, 507:769–779, 2009.

[61] C. M. Raiteri et al. Another look at the BL Lacertae flux and spectral variability. observations by GASP-WEBT, *XMM-Newton* and *Swift* in 2008-2009. *A & A*, 524:A43–A55, 2010.

[62] C. M. Raiteri et al. The spectrum and magnitude of the galaxy associated with BL Lacertae. *MNRAS*, 436:1530–1545, 2013.

[63] C. R. Lynds et al. New spectroscope observations of quasi-stellar sources. *ApJ*, 142:1667, 1965.

[64] C. Tanihata et al. Evolution of the synchrotron spectrum in Markarian 421 during the 1998 campaign. *ApJ*, 601:759–770, 2004.

[65] C.D. Dermer et al. Nonthermal Compton and synchrotron processes in the jets of active galactic nuclei. *ApJ Supp.*, 109:103, 1997.

[66] D. Gasparrini et al. The 3rd catalog of AGN detected by the *Fermi* LAT. *astro-PH*, arXiv:1508.05301, 2015.

[67] D. Giannios et al. Fast TeV variability in blazars: Jets in a jet. *MNRAS*, 395:L29–L33, 2009.

[68] D. Paneque et al. *Fermi*-LAT and *Swift-XRT* observe exceptionally high activity from the nearby TeV blazar MRK 421. *ATel*, page 4977, 2013.

[69] D. Sanchez et al. Multiwavelength campaign on the HBL PKS 2155-304: A new insight on its spectral energy distribution. *arXiv*, page arXiv:1502.02915, 2015.

[70] E. B. Fomalont et al. The VSOP 5 GHz continuum survey: The prelaunch VLBA observations. *ApJS*, 131:95–183, 2000.

[71] E. Churazov et al. *XMM-Newton* observations of the Perseus cluster. I. the temperature and surface brightness structure. *ApJ*, 590:225–237, 2003.

[72] E. E. Epstein et al. Quenchings and outbursts of extragalactic radio sources: Nine years of 3.3 mm measurements and comparisons with centimeter-wave variations. *AJ*, 87:449–461, 1982.

[73] E. I. Robson et al. The infrared-millimetre-centimetre flaring behaviour of the quasar 3C 273. *MNRAS*, 262:249–272, 1993.

[74] E. Idesawa et al. X-ray observations of the BL Lacertae object OJ 287 with *ASCA*. *PASJ*, 49:631–637, 1997.

[75] E. L. Chapin et al. SCUBA-2: Iterative map-making with the Sub-Millimetre User Reduction Facility. *MNRAS*, 430:2545–2573, 2013.

[76] E. Massaro et al. Log-parabolic spectra and particle acceleration in blazars. II. The *BeppoSAX* wide band X-ray spectra of MRK 501. *A & A*, 422:103–111, 2004.

[77] E. Nieppola et al. Spectral energy distributions of a large sample of BL Lacertae objects. *A & A*, 445:441–450, 2006.

[78] E. Nieppola et al. Correlation between *Fermi*/LAT gamma-ray and 37 GHz radio properties of northern AGN averaged over 11 months. *A & A*, 535:A69–A80, 2011.

[79] E. Pian et al. *BeppoSAX* observations of unprecedented synchrotron activity in the BL Lacertae object Markarian 501. *ApJ*, 492:L17–L20, 1998.

[80] E. Semkov et al. Recent optical activity of MRK 421. *ATel*, page 4972, 2013.

[81] E. Striani et al. *AGILE* detects another extraordinary gamma-ray flare from the blazar 3C 454.3. *ATel*, page 2988, 2010.

[82] F. A. Aharonian et al. The temporal characteristics of the TeV gamma-radiation from MKN 501 in 1997. I. data from the Stereoscopic Imaging Atmospheric Cherenkov Telescope System HEGRA. *A & A*, 342:69–86, 1999.

[83] F. Acero et al. *Fermi* Large Area Telescope third source catalogue. *ApJS*, 218:23, 2015.

[84] F. Aharonian et al. Multi-wavelength observations of PKS 2155-304 with HESS. *A & A*, 442:895–907, 2005b.

[85] F. Aharonian et al. An exceptional very high energy gamma-ray flare of PKS 2155-304. *ApJ*, 664:L71–L74, 2007.

[86] F. Aharonian et al. Simultaneous observations of PKS 2155-304 with H.E.S.S., *Fermi*, RXTE, and ATOM: Spectral energy distributions and variability in a low state. *ApJ Letters*, 696:L150–L155, 2009.

[87] F. Aharonian et al. Simultaneous observations of PKS 2155-304 with HESS, *Fermi*, *RXTE*, and Atom: Spectral energy distributions and variability in a low state. *ApJ Letters*, 696:L150–L155, 2009a.

[88] F. K. Lie et al. The long-term optical behavior of MKN 421. *A & A*, 123:569–574, 1997.

[89] F. K. Schinzel et al. The long-term evolution of the parsec scale jet of quasar 3C 345. *Journal of Physics: Conf. Ser.*, 372:id. 012070, 2012.

[90] F. K. Schinzel et al. Relativistic outflow drives gamma-ray emission in 3C 345. *A & A*, 537:A70–A79, 2012.

[91] F. Tavecchio et al. Theoretical implications from the spectral evolution of Markarian 501 observed with *BeppoSAX*. *ApJ*, 554:725–733, 2001.

[92] F. Tavecchio et al. The intergalactic magnetic field constrained by *Fermi*/Large Area Telescope observations of the TeV blazar 1ES 0229+200. *MNRAS*, 406:L70–L74, 2010.

[93] G. Fossati et al. A unifying view of the spectral energy distributions of blazars. *MNRAS*, 299:433–448, 1998.

[94] G. Fossati et al. Multiwavelength observations of Markarian 421 in 2001 March: An unprecedented view on the X-ray/TeV correlated variability. *ApJ*, 677:906–925, 2008.

[95] G. G. Lichti et al. *INTEGRAL* observations of the blazar MRK 421 in outburst. results of a multi-wavelength campaign. *A & A*, 486:721–734, 2008.

[96] G. Ghirlanda et al. The radio-gamma-ray connectionin *Fermi* blazars. *MNRAS*, 413:852–862, 2011.

[97] G. Ghisellini et al. Inhomogeneous synchrotron-self-compton models and the problem of relativistic beaming of BL Lac objects. *A & A*, 146:204–212, 1985.

[98] G. H. Rieke et al. Determining star formation rates for infrared galaxies. *ApJ*, 692:556–573, 2009.

[99] G. T. Richards et al. Spectral energy distributions and multiwavelength selection of Type 1 quasars. *ApJS*, 166:470–497, 2006.

[100] H. C. Spruit et al. Large scale magnetic fields and their dissipation in GRB fireballs. *A & A*, 369:694–705, 2001.

[101] H. D. Aller et al. Spectra and linear polarizations of extragalactic variable sources at centimeter wavelengths. *ApJS*, 59:513–768, 1985.

[102] H. Gaur et al. Multiwavelength variability of the blazars MRK 421 and 3C 454.3 in the high state. *ApJ*, 143:23–35, 2012.

[103] H. Gaur et al. Optical and radio variability of BL Lacertae. *A & A*, 582:103–111, 2015.

[104] H. Krawczynski et al. X-ray/TeV gamma-ray observations of several strong flares of MKN 501 during 1997 and implications. *A & A*, 353:97–107, 2000.

[105] H. Krawczynski et al. Simultaneous X-ray and TeV gamma-ray observation of the TeV blazar Markarian 421 during 2000 February and May. *ApJ*, 559:187–195, 2001.

[106] H. Landt et al. A physical classification scheme of blazars. *MNRAS*, 351:83–100, 2004.

[107] H. Nagai et al. VLBI monitoring of 3C 84 (NGC 1275) in early phase of the 2005 outburst. *Publ. Astron. Soc. Japan*, 62:L11–L15, 2010.

[108] H. Nagai et al. VLBI and single dish monitoring of 3C 84 for the period 2009-2011. *MNRAS*, 423:L122–L126, 2012.

[109] H. Negoro et al. *MAXI* observations of a bright X-ray flare with multiple peaks from MRK 421. *ATel*, page 4978, 2013.

[110] H.-R. Kloeckner et al. Investigation of the obscuring circumnuclear torus in the active galaxy MRK 231. *Nature*, 421:821–823, 2003.

[111] H. Seta et al. *Suzaku* and multi-wavelength observations of OJ 287 during the periodic optical outburst in 2007. *PASJ*, 61:1011–1022, 2009.

[112] H. Teräsranta et al. Twenty years monitoring of extragalactic sources at 22, 37 and 87 GHz. *A & A*, 427:409–410, 2004.

[113] H. Teräsranta et al. 4 year monitoring of extragalactic sources at 22 and 37 GHz. *ApJ*, 440:409–410, 2005.

[114] I. Agudo et al. Location of the gamma-ray flare emission in the jet of BL Lacertae object OJ 287 more than 14 pc from the central engine. *ApJ Lett.*, 726:L13, 2011.

[115] I. McHardy et al. Simultaneous X-ray and IR variability in the quasar 3C 273. *MNRAS*, 310:571–576, 1999.

[116] J. A. Gaidos et al. Extremely rapid bursts of TeV photons from the active galaxy Markarian 421. *Nature*, 383:319–320, 1996.

[117] J. A. Stevens et al. Multifrequency observations of blazars. 5: Long-term millimeter, submillimeter, and infrared monitoring. *ApJ*, 437:91–107, 1994.

[118] J. Albert et al. Unfolding of differential energy spectra in the *MAGIC* experiment. *Nuclear Instruments and Methods in Physics Research*, 583:494–506, 2007.

[119] J. Aleksić et al. MAGIC observations and multiwavelength properties of the quasar 3C 279 in 2007 and 2009. *A & A*, 530:A4, 2011.

[120] J. Aleksic et al. Contemporaneous observations of the radio galaxy NGC 1275 from radio to very high energy gamma-rays. *A & A*, 564:A5–A17, 2014.

[121] J. Aleksic et al. The 2009 multiwavelength campaign on MRK 421: Variability and correlation studies. *A & A*, 576:A126–A143, 2015.

[122] J. Aleksic et al. Multiwavelength observations of MRK 501 in 2008. *A & A*, 573:A50–A62, 2015.

[123] J. Aleksic et al. Multiwavelength observations of MRK 501 in 2008. *A & A*, 573:A50–A62, 2015.

[124] J. Chevalier et al. Long term variability of the blazar PKS 2155-304. *ArXiv*, 1509.03104:1–9, 2015.

[125] J. Kataoka et al. High-energy emission from the TeV blazar Markarian 501 during multiwavelength observations in 1996. *ApJ*, 514:138–147, 1999.

[126] J. Kataoka et al. *RTXE* observations of 3C 273 between 1996 and 2000: Variability time-scales and jet power. *MNRAS*, 336:932–944, 2002.

[127] J. Kataoka et al. Gamma-ray spectral evolution of NGC 1275 observed with *Fermi* Large Area Telescope. *ApJ*, 715:554–560, 2010.

[128] J. Leó-Tavares et al. The connection between gamma-ray emission and millimeter flares in *Fermi*/LAT blazars. *A & A*, 532:A146, 2011.

[129] J. León-Tavares et al. Exploring the relation between (sub-)millimeter radiation and gamma-ray emission in blazars with *Planck* and *Fermi*. *ApJ*, 754:23–37, 2012.

[130] J. M. Rueda-Becerril et al. The influence of the magnetic field on the spectral properties of blazars. *MNRAS*, 438:1856–1869, 2014.

[131] J. Quinn et al. Detection of gamma-rays with E $>$ 300 GeV from Markarian 421. *ApJ Letters*, 456:L83, 1996.

[132] J. R. Herrnstein et al. Discovery of a subparsec jet 4000 Schwarzschild radii away from the central engine of NGC 4258. *ApJ*, 475:17–20, 1997.

[133] J. R. Mattox et al. The likelihood analysis of *EGRET* data. *ApJ*, 461:396–407, 1996.

[134] J. R. Mattox et al. A quantitative evaluation of potential radio identification for 3EG EGRET sources. *ApJ*, 135:155–175, 2001.

[135] J. S. Miller et al. The spectrum and magnitude of the galaxy associated with BL Lacertae. *ApJ Letters*, 219:L85–L87, 1978.

[136] J. T. Dempsey et al. SCUBA-2: on-sky calibration using submillimetre standard sources. *MNRAS*, 430:2534–2544, 2013.

[137] J.P. Rachen et al. Radio-submm flares from blazars in a discontinuous jet model. *arXiv*, 2010arXiv1006.5364R, 2010.

[138] K. Asada et al. The expanding radio lobe of 3C 84 revealed by VSOP observations. *Publ. Astron. Soc. of Japan*, 58:261–270, 2006.

[139] K. I. Kellermann et al. VLA observations of objects in the *Palomar* bright quasar survey. *ApJ*, 98:1195–1207, 1989.

[140] K. I. Kellermann et al. The radio structure of radio loud and radio quiet quasars in the *Palomar* bright quasar survey. *ApJ*, 108:1163–1177, 1994.

[141] K. L. Dutson et al. A non-thermal study of the brightest cluster galaxy NGC 1275 - the gamma-radio connection over four decades. *MNRAS*, 442:2048–2057, 2014.

[142] K. Lee et al. Optical, gamma-ray and x-ray monitoring of Markarian 421 in the 2005-2006 season. *ASP Conf. Series*, 386:507, 2008.

[143] K. Nilsson et al. H-alpha monitoring of OJ 287 in 2005-08. *A & A*, 516:A60–A65, 2010.

[144] L. Chiappetti et al. Spectral evolution of PKS 2155-304 observed with *BeppoSAX* during an active gamma-ray phase. *ApJ*, 521:552–560, 1999.

[145] L. Foschini et al. Does the gamma-ray flux of the blazar 3C 454.3 vary of sub-hour time-scales. *MNRAS*, 408:448–451, 2010.

[146] L. Fuhrmann et al. Detection of significant cm to sub-mm band radio and gamma-ray correlated variability in *Fermi* bright blazars. *MNRAS*, 441:1899–1909, 2014.

[147] L. Maraschi et al. A jet model for the gamma-ray emitting blazar 3C 279. *ApJ*, 397:L5–L9, 1992.

[148] L. Maraschi et al. Simultaneous X-ray and TeV observations of a rapid flare from Markarian 421. *ApJ*, 526:L81–L84, 1999.

[149] L. Pacciani et al. High energy variability of 3C 273 during the *AGILE* multiwavelength campaign of December 2007-January 2008. *A & A*, 494:49–61, 2009.

[150] M. A. Gurwell et al. Monitoring phase calibrators at submillimeter wavelengths. *ASP COnf. Ser. Proc.*, 375:234, 2007.

[151] M. A. Osterman et al. New multiwavelength observations of PKS 2155-304 and implications for the coordinated variability patterns of blazars. *ApJ*, 671:97–103, 2007.

[152] M. Ackermann et al. The radio/gamma-ray connection in active galactic nuclei in the era of the *Fermi* Large Area Telescope. *ApJ*, 741:30–50, 2011.

[153] M. Ackermann et al. The *Fermi* Large Area Telescope on orbit: Event classification, instrument response functions, and calibration. *ApJS*, 203:4–74, 2012.

[154] M. Ajello et al. Galaxy clusters in the *Swift*/Burst Alert Telescope era: Hard X-rays in the intracluster medium. *ApJ*, 690:367–388, 2009.

[155] M. Balokovic et al. *NuSTAR* detects extreme X-ray flaring of MRK 421. *ATel*, page 4974, 2013.

[156] M. Boettcher et al. *Relativistic Jets from Active Galactic Nuclei*. Wiley-VCH, Germany, 2012.

[157] M. Böttcher et al. Coordinated multiwavelength observations of BL Lacertae in 2000. *ApJ*, 596:847–859, 2003.

[158] M. C. Begelman et al. Theory of extragalactic radio sources. *Reviews of Modern Physics*, 56:255–351, 1984.

[159] M. C. Begelman et al. Implications of very rapid tev variability in blazars. *MNRAS*, 384:L19–L23, 2008.

[160] M. F. Aller et al. Constraining the physical conditions in the jets of gamma-ray flaring blazars using centimeter-band polarimetry and radiative transfer simulations. I. data and models for 0420-014, OJ 287, and 1156 + 295. *ApJ*, 791:53–66, 2014.

[161] M. H. Cohen et al. Relativistic beaming and the intrinsic properties of extragalactic radio jets. *ApJ*, 658:232–244, 2007.

[162] M.-H. Ulrich et al. Nonthermal continuum radiation in three elliptical galaxies. *Astrophysical Journal*, 198:261–266, 1975.

[163] M. Hayashida et al. Multiwavelength observation from radio through very-high-energy gamma-ray of OJ 287 during the 12-year cycle flare in 2007. *arXiv*, arXiv:0907.1343:1–4, 2009.

[164] M. Hayashida et al. Rapid variability of blazar 3C 279 during flaring states in 2013-2014 with joint *Fermi*-LAT, *NuSTAR*, *SWIFT*, and ground based multi-wavelength observations. *ApJ*, 807:79–96, 2015.

[165] M. J. M. Marcha et al. Optical spectroscopy and polarisation of a new sample of optically bright Flat Radio Spectrum Sources. *MNRAS*, 281:425–448, 1996.

[166] M. J. Valtonen et al. The 2005 November outburst in OJ 287 and the binary black hole model. *ApJ*, 643:L9–L12, 2006.

[167] M. Janiak et al. Application of the spine-layer jet radiation model to outbursts in the broad-line radio galaxy 3C 120. *arXiv*, arXiv:1508.06500, 2015.

[168] M. K. Daniel et al. Spectrum of very high energy gamma-rays from the blazar 1ES 1959+650 during flaring activity in 2002. *ApJ*, 621:181–187, 2005.

[169] M. Karouzos et al. AGN jets under the microscope: A divide? *Astron. Nachr.*, 333:417, 2012.

[170] M. Orienti et al. On the connection between radio and gamma-rays. Variability and polarization properties in relativistic jets. *The Innermost Regions of Relativistic Jets and Their Magnetic Fields EPJ Web Conf.*, 61:id. 04009, 2013.

[171] M. Punch et al. Detection of TeV photons from the active galaxy Markarian 421. *Nature*, 358:477–478, 1992.

[172] M. Selig et al. The denoised, deconvolved, and decomposed fermi γ-ray sky. an application of the d^{3}po algorithm. *A & A*, 581:A126, 2015.

[173] M. Sikora et al. Comptonisation of diffuse ambient radiation by a relativistic jet: The source of the gamma-rays from blazars? *ApJ*, 421:153–162, 1994.

[174] M. Spada et al. Internal shocks in the jets of radio loud quasars. *MNRAS*, 325:1559–1570, 2001.

[175] M. Tornikoski et al. The high radio frequency spectra and variability of southern Flat-Spectrum Radio Sources. *AJ*, 120:2278 – 2283, 2000.

[176] M. Türler et al. 30 years of multi-wavelength observations of 3C 273. *A & A*, 134:89–101, 1999.

[177] M. Türler et al. Modelling 20 years of synchrotron flaring in the jet of 3C 273. *A & A*, 361:850–862, 2000.

[178] M. Valtonen et al. The structure of the october-november 2005 outburst in oj 287 and the precessing binary black hole model. *A & A*, 477:407–412, 2008.

[179] M. Villata et al. The WEBT BL Lacertae campaign 2000. *A & A*, 390:407–421, 2002.

[180] M. Villata et al. The correlated optical and radio variability of BL Lacertae. WEBT data analysis 1994-2005. *A & A*, 501:455–460, 2009.

[181] N. Isobe et al. *ASCA* observations of the BL Lacertae object OJ 287 in 1997 April and November. *PASJ*, 53:79–84, 2001.

[182] N. R. MacDonald et al. Through the ring of fire: Gamma-ray variability in blazars by a moving plasmoid passing a local source of seed photons. *ApJ*, 804:111, 2015.

[183] P. A. Hughes et al. Polarized radio outbursts in BL Lacertae. II. The flux and polarization of a pis ton-driven shock. *ApJ*, 298:301–315, 1985.

[184] P. A. Hughes et al. Constraining the physical conditions in the jets of gamma-ray flaring blazars using centimeter-band polarimetry and radiative transfer simulations. II. Exploring parameter space and implications. *ApJ*, 799:207–222, 2015.

[185] P. C. Waggett et al. NGC 6251, a very large radio galaxy with and exceptional jet. *MNRAS*, 181:465–474, 1977.

[186] P. F. Michelson et al. Markarian 421, PKS 0537-441, QSO 0716+714. *IAU Circ.*, 5470:2, 1992.

[187] P. F. Rebillot et al. Multiwavelength observations of the blazar Markarian 421 in 2002 December and 2003 January. *ApJ*, 641:740–925, 2006.

[188] P. Giommi et al. Parameter correlations and cosmological properties of BL Lac objects. *in Blazar Astrophys. BappoSAX and Other Observatories*, eds. P. Giommi, E. Massaro, G. Palumbo:133, 2002.

[189] P. Giommi et al. The sedentary survey of extreme high energy peaked BL Lacs. *A & A*, 434:385–396, 2005.

[190] P. Giommi et al. A simplified view of blazars: Clearing the fog around long standing selection effects. *MNRAS*, 420:2899–2911, 2012.

[191] P. Giommi et al. Simultaneous Planck, Swift, and *Fermi* observations of X-ray and gamma-ray selected blazars. *A & A*, 541:A160–A219, 2012.

[192] P. L. Nolan et al. *Fermi* Large Area Telescope Second Source Catalog. *ApJS*, 199:31–77, 2012.

[193] P. M. Chadwick et al. PKS 2155-304 - a source of VHE gamma-rays. *Astroparticle Physics*, 11:145–148, 1999.

[194] P. M. Chadwick et al. Very high energy gamma rays from PKS 2155-304. *ApJ*, 513:161–167, 1999.

[195] P. M. Ogle et al. Blazar 3C 454.3 in outburst and quiescence during 2005-2007: Two variable synchrotron emission peaks. *ApJ Suppl.*, 195:19–39, 2011.

[196] P. Padovani et al. BeppoSAX obervations of synchrotron X-ray emission from radio quasars. *ApJ*, 581:895–911, 2002.

[197] P. T. Ho et al. The Submillimeter Array. *ApJ*, 616:L1–L6, 2004.

[198] P. Uttley et al. Measuring the broad-band power spectra of active galactic nuclei with rxte. *MNRAS*, 332:231–250, 2002.

[199] R. C. Hartman et al. Detection of the high-energy gamma radiation from quasar 3C 279 by the *EGRET* telescope on the Compton Gamma Ray Observatory. *ApJ*, 385:1, 1992.

[200] R. C. Hartman et al. The third *EGRET* catalogue of high-energy gamma-ray sources. *ApJ Suppl.*, 123:79–202, 1999.

[201] R. C. Hartman et al. Day-scale variability of 3C 279 and searches for correlations in the gamma-ray, X-ray and optical bands. *ApJ*, 558:583–589, 2001.

[202] R. C. Hartman et al. Multiepoch multiwavelength spectra and models for blazar 3C 279. *ApJ*, 553:683–694, 2001.

[203] R. C. Vermeulen et al. Discovery of a nuclear counterjet in NGC 1275: A new way to probe the parsec-scale environment. *ApJ*, 430:L41–L44, 1994.

[204] R. Chatterjee et al. Correlated multi-wave band variability in the blazar 3C 279 from 1996 to 2007. *ApJ*, 689:79–94, 2008.

[205] R. J. H. Dunn et al. Precession of the super-massive black hole in NGC 1275 (3C 84)? *MNRAS*, 366:758–766, 2006.

[206] R. Landau et al. Active extragalactic sources - Nearly simultaneous observations from 20 centimeters to 1400 A. *ApJ*, 308:78–92, 1986.

[207] R. M. Sambruna et al. Correlated intense X-ray and TeV activity of Markarian 501 in 1998 June. *ApJ*, 538:127–133, 2000.

[208] R. T. Coogan et al. Localising the gamma-ray emission region during the June 2014 outburst of 3C 454.3. *arXiv*, 1601.07180:1–12, 2016.

[209] S. Appl et al. Misalignment and curvature effects in extragalactic radio sources. *A & A*, 310:419–437, 1996.

[210] S. Archambault et al. Upper limits from five years of blazar observations with the *VERITAS* Cherenkov telescopes. *arXiv*, page 1603.02410, 2016.

[211] S. Croke et al. Multi-frequency multi-epoch VLBA polarisation observations of MRK 501. *Baltic Astronomy*, 14:367–370, 2005.

[212] S. G. Jorstad et al. Multiepoch Very Long Baseline Array observations of *EGRET*-detected quasars and BL Lacertae objects: Connection between superluminal ejections and gamma-ray flares in blazars. *ApJ*, 556:738–748, 2001.

[213] S. G. Jorstad et al. Polarimetric observations of 15 Active Galactic Nuclei at high frequencies: Jet kinematics from bimonthly monitoring with the Very Long Baseline Array. *The Astronomical Journal*, 130:1418–1465, 2005.

[214] S. G. Jorstad et al. Flaring behaviour of the quasar 3C 454.3 across the electromagnetic spectrum. *ApJ*, 715:362–384, 2010.

[215] S. Jorstad et al. The gamma-ray activity of the high-z quasar 0836+71. *European Physical Journal Web of Conferences*, 61:No. 04003, 2013.

[216] S. Lorenzo et al. Relativistic jets shine through shocks or magnetic reconnection? *MNRAS*, 450:183–191, 2015.

[217] S. Sahu et al. Hadronic-origin orphan TeV flare from 1ES 1959+650. *Physical Rev. D*, 87:103015, 2013.

[218] S. Soldi et al. The multiwavelength variability of 3C 273. *A & A*, 486:411–425, 2008.

[219] S. Vaughan et al. On characterising variability properties of X-ray light curves from active galaxies. *MNRAS*, 345:1271, 2003.

[220] S. Vercellone et al. The brightest gamma-ray flaring blazar in the sky: *AGILE* and multi-wavelength observations of 3C 454.3 during 2010 November. *ApJ Lett.*, 736:L38–L45, 2011.

[221] T. An et al. Extreme superluminal motion in the curved jet of PKS 1502+106. *A & A*, 421:839–846, 2004.

[222] T. Hovatta et al. Long-term radio variability of AGN: flare characteristics. *A & A*, 485:51–61, 2008.

[223] T. Hovatta et al. A major 15 GHz radio flare in the blazar MRK 421. *ATel*, 4451:1, 2012.

[224] T. Hovatta et al. A combined radio and GeV gamma-ray view of the 2012 and 2013 flares of MRK 421. *MNRAS*, 448:3121–3131, 2015.

[225] T. J. L. Courvoisier et al. The radio to X-ray continuum emission of the quasar 3C 273 and its temporal variations. *A & A*, 176:197–209, 1987.

[226] T. J. L. Courvoisier et al. Multi-wavelength observations of 3C 273. II - 1986-1988. *A & A*, 234:73–83, 1990.

[227] T. Jenness et al. Developments in the STARLINK software collection. *ASP Conf. Ser.*, 411:418, 2009.

[228] T. P. Krichbaum et al. The evolution of the sub-parsec structure of 3C 84 at 43 GHz. *A & A*, 260:33–48, 1992.

[229] T. Plewa et al. Bending relativistic jets in AGN. *arXiv*, pages astro–ph/9706124, 1997.

[230] T. Pursimo et al. Intensive monitoring of OJ 287. *A & AS*, 146:141, 2000.

[231] T. Takahashi et al. Complex spectral variability from intensive multiwavelength monitoring of Markarian 421 in 1998. *ApJ*, 542:L105–L109, 2000.

[232] U. Bach et al. Structure and flux variability in the VLBI jet of BL Lacertae during the WEBT campaigns (1995-2004). *A & A*, 456:105–115, 2006.

[233] V. A. Acciari et al. Spectral energy distribution of Markarian 501: Quiescent state versus extreme outburst. *ApJ*, 729:2–10, 2011.

[234] V. S. Paliya et al. Multi-wavelength observations of 3C 279 during the extremely bright gamma-ray flare in 2014 March-April. *ApJ*, 803:15–28, 2015.

[235] V. S. Paliya et al. The violent hard X-ray variability of MRK 421 observed by *NuSTAR* in 2013 April. *ApJ*, 811:143–149, 2015.

[236] W. B. Atwood et al. The Large Area Telescope on the *Fermi* gamma-ray space telescope mission. *ApJ*, 697:1071–1102, 2009.

[237] W. K. Gear et al. A comparison of the radio/submillimetre spectra of BL Lacertae objects and Flat Spectrum Radio Quasars. *MNRAS*, 267:167, 1994.

[238] W. Max-Moerbeck et al. A method for the estimation of the significance of cross-correlations in unevenly sampled red-noise time series. *MNRAS*, 445:437–459, 2014.

[239] W. Max-Moerbeck et al. Time correlation between the radio and gamma-ray activity in blazars and the production site of the gamma-ray emission. *MNRAS*, 445:428, 2014.

[240] W. S. Holland et al. SCUBA-2 : the 10 000 pixel bolometer camera on the James Clerk Maxwell Telescope. *MNRAS*, 430:2513–2533, 2013.

[241] Y. C. Lin et al. Detection of high-energy gamma-ray emission from the BL Lacertae object Markarian 421 by the *EGRET* telescope on the Compton Observatory. *ApJ Letters*, 401:L61–L64, 1992.

[242] Y. G. Zhang et al. Multiwavelength variability in PKS 2155-304. *Journ. Astrophys. Astron.*, 32:327–330, 2011.

[243] A. Abramowski et al. (H.E.S.S.). A multiwavelength view of the flaring state of PKS 2155-304 in 2006. *A & A*, 539:A149–A170, 2012.

[244] F. Aharonian et al. (H.E.S.S.). H.E.S.S. observations of PKS 2155-304. *A & A*, 430:865–875, 2005a.

[245] C. Xinwu & G. Minfeng F. Zhonghui. A test of external compton models for gamma-ray active galactic nuclei. *ApJ*, 646:8–15, 2006.

[246] E. Fermi. On the origin of cosmic radiation. *Phys. Rev.*, 75:1169–1174, 1949.

[247] J. D. Finke. Compton dominance and the blazar sequence. *ApJ*, 763:134–145, 2013.

[248] F. Hoyle & W. A. Fowler. On the nature of strong radio sources. *MNRAS*, 125:169–176, 1963.

[249] A. P. Marscher & W. K. Gear. Models for high-frequency radio outbursts in extragalactic sources, with applica tion to the early 1983 millimeter-to-infrared flare of 3C 273. *ApJ*, 298:114–127, 1985.

[250] M. Georganopoulos. Understanding the Chandra detected X-ray emission of the knots and hot spots of powerful extragalactic jets. *Chinese Journal of Astronomy & Astrophysics Suppl.*, 3:404–414, 2003.

[251] F. Tavecchio & G. Ghisellini. Spine-sheath layer radiative interplay in subparsec-scale jets and the TeV emission from M87. *MNRAS*, 385:L98–L102, 2008.

[252] P. Padovani & P. Giommi. The connection between X-ray and radio-selected BL Lacertae objects. *ApJ*, 444:567–581, 1995.

[253] M. Gliozzi. Long-term X-ray and TeV variability of MRK 501. *ApJ*, 646:61–75, 2006.

[254] M. R. Calabretta & E. W. Greisen. Representation of celestial coordinates in FITS. *A & A*, 395:1077–1122, 2002.

[255] P. E. Hardee. Parsec-scale radio jets. *Cambridge University Press*, eds. J. A. Zensus & T. J. Pearson:266, 1990.

[256] H. Alfvén & N. Herlofson. Cosmic radiation and radio stars. *Phys. Rev.*, 78:616–616, 1950.

[257] J. Cortina & J. Holder. *MAGIC* and *VERITAS* detect an unprecedented flaring activity from MRK 421 in VHE gamma-rays. *ATel*, page 4976, 2013.

[258] T. W. Jones. Numerical modelling of compact radio jet dynamics. *BAAS*, 14:963–977, 1982.

[259] M. Georganopoulos & D. Kazanas. Decelerating flows in TeV blazars: A resolution to the BL Lacertae - FR I unification problem. *ApJ Lett.*, 594:L27–L30, 2003.

[260] M. Georganopoulos & D. Kazanas. Witnessing the gradual slowdown of powerful extragalactic jets: The X-ray-optical-radio connection. *ApJ Lett.*, 604:L81–L84, 2004.

[261] J. Timmer & M. Koenig. On generating power-law noise. *A & A*, 300:707, 1995.

[262] R. D. Blandford & A. Koenigl. Relativistic jets as compact radio sources. *ApJ*, 232:34–48, 1979.

[263] A. Königl. Relativistic jets as X-ray and gamma-ray sources. *ApJ*, 243:700–709, 1981.

[264] F. Melia & A. Königl. The radiative deceleration of ultrarelativistic jets in active galactic nuclei. *ApJ*, 340:162–180, 1989.

[265] J. H. Krolik. *Active Galactic Nuclei: From the Central Black Hole to the Galactic Environment*. Princeton University Press, Princeton, USA, 1999.

[266] R. A. Edelson & J. H. Krolik. The discrete correlation function - A new method for analyzing unevenly sampled variability data. *ApJ*, 333:646–659, 1988.

[267] P. Lachowicz. Wavelet analysis: A new significance test for signals dominated by intrinsic red-noise variability. *arXiv*, 0906.4176:0906.4176, 2009.

[268] S. Larsson. Statistical analysis of multiwavelength light curves. *arXiv*, 1207:1459:1–6, 2012.

[269] R. D. Blandford & A. Levinson. Pair cascades in extragalactic jets. 1: Gamma-rays. *ApJ*, 441:79=95, 1995.

[270] G. B. Rybicki & A. P. Lightman. *Radiative processes in astrophysics*. Wiley-Interscience, New York, 1979.

[271] A. Lobanov. Compact radio jets and nuclear regions in active galaxies. *arXiv*, 0708.4280, 2007.

[272] M. S. Longair. *High Energy Astrophysics*. Cambridge University Press, Cambridge, 2011.

[273] R. V. E. Lovelace. Dynamo model of double radio sources. *Nature*, 262:649–652, 1976.

[274] D. Lynden-Bell. Galactic nuclei as collapsed old quasars. *Nature*, 223:690–694, 1969.

[275] C. R. Lynds. New spectroscopic observations of twenty quasi-stellar sources. *ApJ*, 147:837–840, 1967.

[276] A. P. Marscher. Relativistic jets and the continuum emission in QSOs. *ApJ*, 235:386–391, 1982.

[277] A. P. Marscher. Compact extragalactic radio jets. *Astrophysical Jets Meeting*, 00:73–94, 1993.

[278] A. P. Marscher. Multiband impressions of active galactic nuclei. *Mem. Soc. Atron. It.*, 76:168, 2005.

[279] A. P. Marscher. Turbulent extreme multi-zone model for multi-waveband variations in blazars. *ArXiv*, 1304.2064:1–6, 2012.

[280] A. P. Marscher. Turbulent, extreme multi-zone model for simulating flux and polarization variability in blazars. *ApJ*, 780:87–97, 2014.

[281] A. Sokolov & A.P. Marscher. External Compton radiation from rapid nonthermal flares in blazars. *ApJ*, 629:52–60, 2005.

[282] F. Melia. *High-Energy Astrophysics*. Princeton Series in Astrophysics, Princeton, 2009.

[283] C. D. Dermer & G. Menon. *High Energy Radiation from Black Holes*. Princeton University Press, Princeton, 2009.

[284] H. R. Miller. B2 1101+38: a BL Lacertae object. *ApJ*, 201:L109–L111, 1975.

[285] W. Baade & R. Minskowski. Identification of te radio sources in Cassiopeia, Cygnus A and Puppis A. *ApJ*, 119:206–214, 1954.

[286] H. Netzer. *The Physics and Evolution of Active Galactic Nuclei*. Cambridge University Press, Cambridge, 2013.

[287] P. E. Hardee & M. L. Norman. Asymmetric morphology of the propagating jet. *ApJ*, 365:134–158, 1990.

[288] Ya. B. Zel'Dovich & I. D. Novikov. Relativistic astrophysics, part i. *Soviet Astrophys. - Uspekhi*, 7:763–788, 1965.

[289] D. E. Osterbrock. Active galactic nuclei. *Re. Prog. Phys.*, 54:579–633, 1991.

[290] C. M. Urry & P. Padovani. Unified schemes for radio-loud active galactic nuclei. *Publ. Aston. Soc. Pac.*, 107:803, 1995.

[291] P. Padovani. The blazar sequence: Validity and predictions. *Astrophys. & Space Sci.*, 309:63–71, 2007.

[292] P. Padovani. The discovery of high-power high synchrotron peak blazars. *MNRAS*, 422:48–52, 2012.

[293] D. Eckert & S. Paltani. *INTEGRAL* observations of the Perseus cluster. *A & A*, 495:415–420, 2009.

[294] P. Grandi & G. G. C. Palumbo. Jet and accretion-disk emission untangled in 3C 273. *Science*, 306:998–1002, 2004.

[295] R. D. Blandford & D. G. Payne. Hydromagnetic flows from accretion discs and the production of radio jets. *MNRAS*, 199:883–903, 1982.

[296] A. H. Bridle & R. A. Perley. Extragalactic radio jets. *A & A Annu. Rev.*, 22:319–358, 1984.

[297] B. M. Peterson. *An Introduction to Active Galactic Nuclei*. Cambridge University Press, Cambridge, 1997.

[298] B. M. Peterson. The broad-line region in active galactic nuclei. *Lecture Notes in Physics, Berlin Springer Verlag*, 693:77, 2006.

[299] R. J. White & B. M. Peterson. Comments on cross-correlation methodology in variability studies of active galactic nuclei. *PASP*, 106:879–889, 1994.

[300] D. Petry. Multiwavelength observations of Markarian 501 during the 1997 high state. *ApJ*, 536:742–755, 2000.

[301] P. G. Edwards & B. G. Piner. The subluminal parsec-scale jet of Markarian 501. *ApJ*, 579:L67–L70, 2002.

[302] P. T. Wallace R. F. Warren-Smith. The STARLINK software collection. *ASP Conf. Ser.*, 52:229, 1993.

[303] J. P. Rachen. Hadronic blazar models and the correlated X-ray/TeV flares. *AIP Conf. Ser.*, 515:41–52, 2000.

[304] M. J. Rees. New interpretation of extragalactic radio sources. *Nature*, 229:312–317, 1971.

[305] M. J. Rees. The M87 jet - Internal shocks in a plasma beam. *MNRAS*, 184:61–65, 1978.

[306] R. D. Blandford & M. J. Rees. A 'twin-exhaust' model for double radio sources. *MNRAS*, 169:395–415, 1974.

[307] R. D. Blandford & M. J. Rees. Some comments on radiation mechanisms in Lacertids. *University of Pittsburgh Press*, A79:328–341, 1978.

[308] A. Reimer. On the physics of hadronic blazar emission models. *Journal of Physics Conf. Ser.*, 355:012011, 2012.

[309] S. P. Reynolds. Theoretical studies of compact radio sources. I - Synchrotron radiation from relativistic flows. *ApJ*, 256:13–37, 1982.

[310] B. L. Fanaroff & J. M. Riley. The morphology of the extragalactic radio sources of high and low luminosity. *MNRAS*, 167:31–35, 1974.

[311] I. Robson. Submillimeter and infrared variability of blazars. *ASP Conf. Ser.*, 110:175–189, 1996.

[312] G. Henri & L. Saugé. The bulk lorentz factor crisis of TeV blazars: Evidence for an inhomogeneous pileup energy distribution? *ApJ*, 640:185–195, 2006.

[313] P. A. G. Scheuer. Models of extragalactic radio sources with a continuous energy supply from a central object. *MNRAS*, 166:513–528, 1974.

[314] C.D. Dermer & R. Schlickeiser. Model for the high-energy emission from blazars. *ApJ*, 416:458, 1993.

[315] M. Schmidt. 3C 273: A star-like object with large red-shift. *Nature*, 197:1040–1043, 1963.

[316] I. S. Shklovsky. Optical emission from the Crab Nebula in the continuous spectrum. *Proc. Acad. Sci. U.S.S.R.*, 91:475, 1953.

[317] M. C. Begelman & M. Sikora. Inverse Compton scattering of ambient radiation by a cold relativistic jet - A source of beamed, polarised, continuum in blazars? *ApJ*, 322:650–661, 1987.

[318] A. Sillanpaa. Double-peak structure in the cycle optical outbursts of blazar OJ 287. *A & A*, 315:L13–L16, 1996.

[319] J. E. Baldwin & F. G. Smith. Radio emission from the extragalactic nebula M 87. *The Observatory*, 76:141–144, 1956.

[320] G. Drenkhahn & H. C. Spruit. Efficient acceleration and radiation in Poynting flux powered GRB outflows. *A & A*, 391:1141–1153, 2002.

[321] L. O. Takalo. OJ 287: The rosetta stone of blazars. *Vistas in Astron.*, 38:77, 1994.

[322] G. Ghisellini & F. Tavecchio. Structured jets in TeV BL Lac objects and radio galaxies. Implications for the observed properties. *A & A*, 432:401–410, 2005.

[323] G. Ghisellini & F. Tavecchio. Rapid variability in TeV blazars: the case of PKS 2155-304. *MNRAS*, 386:L28–L32, 2008.

[324] S. Vercellone; (AGILE Team). Long-term gamma-ray and multi wavelength observations of 3C 454.3 (a.k.a. the "Crazy Diamond"). *Proc. Conf. Como, Italy, June 2009*, Accretion and Ejection in AGN: A Global View edt. L. Maraschi et al.:257, 2010.

[325] F. D'Ammando & M. Orienti (*Fermi* LAT Collaboration. *Fermi* LAT detection of a GeV flare from the BL Lac object MRK 421. *ATel*, 4261:1, 2012.

[326] C. M. Urry. Multiwavelength properties of blazars. *Advances in Space Research*, 21:89–100, 1998.

[327] A. Lahteenmaki & E. Valtaoja. Testing the inverse Compton models for active galactic nuclei with gamma-ray and radio observations. *ApJ*, 590:95–108, 2003.

[328] P. Sreekumar & W. T. Vestrand. PKS 2155-304. *IAU Circ.*, 6774:2, 1997.

[329] A. E. Vol'vach. Results of long-term monitoring of 3C 273 over a wide range of wavelengths. *Astronomy Reports*, 57:34–45, 2013.

[330] R. C. Walker. Detection of a VLBI counterjet in NGC 1275: A possible probe of the parsec-scale accretion region. *ApJ*, 430:L45–L48, 1994.

[331] J. H. Oort & T. H. Walraven. Polarisation and composition of the Crab Nebula. *Bull. Astron. Inst. Netherl.*, 12:285–308, 1956.

[332] D. G. Wentzel. Coronal heating by Alfven waves. *Solar Physics*, 39:129–140, 1974.

[333] www.slac.stanford.edu/exp/glast/groups/canda/archive/p7rep_v15/lat_Performance.htm. (last viewed: 11/04/2016).

[334] R. D. Blandford & R. Znajek. Electromagnetic extraction of energy from Kerr black holes. *MNRAS*, 179:433–456, 1977.